# Surface Engineering of Zirconium for Tribological Properties Enhancement

Abdulkarim Alansari

A thesis submitted to De Montfort University in partial fulfillment of the requirement for the degree of Doctor of Philosophy at De Montfort University

School of Engineering and Sustainable Development
Faculty of Computing, Engineering and Media
De Montfort University
Leicester
UK

March 31, 2019

# Declaration

This thesis is submitted for the degree of Doctor of Philosophy (Ph.D) in the school of Engineering and Sustainable Development, Faculty of computing, Engineering and media at De Montfort University (DMU) of Leicester under the supervision of Dr. Yong Sun. I declare that the work is my own and nothing in this work has been submitted in any other university or in any other degree. The work of this submission is all original and any work or idea that is used has been referenced.

# Authorship Attribution Statement

This thesis contains material from three papers published in the following peer-reviewed journals and a paper presented at an international symposium, where I was the first author.

1. Chapter 4: presented by myself at the 4th International Symposium on Surface Hardening of Corrosion Resistant Materials, June 2016, Malta.

2. Chapter 5: published as A. Alansari, Y. Sun, Effect of oxidation time on the tribological behavior of thermally oxidized commercially pure zirconium under dry sliding conditions, Surface and Coatings Technology, 309 (2017) 195-202. http:// dx.doi.org/10.1016/j.surfcoat.2016.11.070.

3. Chapter 6: published as A. Alansari, Y. Sun, Surface finish effect on dry sliding wear behaviour of thermally oxidized commercially pure zirconium, Transactions of Nonferrous Metal Society of China, 29(2019) 88-97. DOI:/10.1016/S1003-6326(18)64918-0.

4. Chapter 7: published as A. Alansari, Y. Sun, A comparative study of the mechanical behaviour of thermally oxidised commercially pure titanium and zirconium, Journal of the Mechanical Behavior of Biomedical Materials, 74 (2017) 221–231. http://dx.doi.org/10.1016/j.jmbbm.2017.06.011.

# Acknowledgement

First of all I thank Allah (God) for blessing me to reach to this stage. I would like to express my sincere gratitude to my supervisor, Dr. Yong Sun, who has supported me throughout my PhD project with his knowledge, experience and patience. He allowed me to learn and use all materials lab equipments freely, I could not ask for a better or more experienced supervisor.

I would like to thank De Montfort university for giving me the access to all the available facilities. I would like to thank Paul Dean, Paul Taylor and all of the technicians of the mechanical workshop, who were always ready to help and share their knowledge.

I would like to thank Dr. X.Y.Li of the University of Birmingham for allowing me to experience and use GDOS for samples characterisation.

I would love to thank my family and my love for supporting me emotionally and financially throughout my life and studies, without them this project would have been impossible. I finally would like to thank my best friends for supporting me emotionally throughout all the time in my project.

# Abbreviations

| | |
|---|---|
| BCC | Body Centered Cubic |
| $BaCO_3$ | Barium Carbonate |
| $CaCO_3$ | Calcium Carbonate |
| COF | Coefficient Of Friction |
| CP-Ti | Commercially Pure Titanium |
| CP-Zr | Commercially Pure Zirconium |
| EDX | Energy Dispersive X-ray |
| FC | Furnace Cooling |
| FCC | Face Centered Cubic |
| GDOS | Glow Discharge Optical Spectrometry |
| HCP | Hexagonal Closed Pack |
| HV | Hardness Vickers |
| $Na_2CO_3$ | Sodium Carbonate |
| O | Oxygen |
| OCP | Open Circuit Potential |
| ODZ | Oxygen Diffusion Zone |
| OL | Oxide Layer |
| OxZr | Oxidised Zirconium |
| PC | Pack Carburising |
| PE | Polyethylene |
| POD | Pin On Disk |
| SEC | Saturated Calomel Electrode |
| SEM | Scanning Electron Microscope |
| Ti | Titanium |
| TiC | Titanium Carbide |
| $TiO_2$ | Titanium Dioxide |
| TML | Total Material Loss |
| TMLR | Total Material Lost Rate |
| TO | Thermal Oxidation |
| TO Zr | Thermal Oxidised Zirconium |
| XRD | X-ray Diffraction |
| Zr | Zirconium |
| ZrC | Zirconium Carbide |
| $ZrO_2$ | Zirconium Dioxide |

# List Of Symbols

| | | |
|---|---|---|
| $E$ | Young Modulus | Gpa |
| $Zr - \alpha$ | Alpha Zirconium Phase | - |
| $\alpha(\beta - Zr)$ | Alpha-Beta Zirconium Phase | - |
| $A_o$ | Area After Treatment | $mm^2$ |
| $Zr - \beta$ | Beta Zirconium Phase | - |
| t | Coating Thickness | $\mu$m |
| $k_d$ | Coefficient Of Dimensional Wear | $mm^3N^{-1}m^{-1}$ |
| $\rho$ | Density | $gcm^{-3}$ |
| L | Distance Of Total Sliding | m |
| $\rho$ | Electrical Resistivity | $\Omega m$ |
| $\mu$ | Friction Coefficient | - |
| F | Friction Force | N |
| H | Hardness | HV |
| $P_{max}$ | Maximum Pressure | Gpa |
| $F_n$ | Normal Applied Load | N |
| $v_1, v_2$ | Poissons Ratios | - |
| G | Shear Modulus | Gpa |
| c | Specific Heat Capacity | $Jg^{-1}K^{-1}$ |
| $\sigma_T$ | Tensil Strength | MPa |
| $\gamma$ | Thermal Conductivity | $Wm^{-1}K^{-1}$ |
| $\alpha$ | Thermal Expansion Coefficient | $K^{-1}$ |
| V | Wear Track Volume | $mm^3m^{-1}$ |
| $\sigma_Y$ | Yield Strength | MPa |

# Abstract

Zirconium and its alloys have found increasing applications in several industrial sectors including the nuclear power generation, the chemical processing and the biomedical industries, mainly due to the combination properties of neutron transparency, excellent corrosion resistance and good biocompatibility [1] [2] [3]. However, with a base hardness of about 200 HV, zirconium and its alloys have poor tribological properties and find limited applications in other fields of engineering [4]. Efforts have been made in this work to develop surface engineering techniques to enhance the tribological properties of commercially pure zirconium (CP-Zr) and to characterise the structures and properties of surface engineered CP-Zr. It can be stated that there is limitation in the current research, no sufficient information on thermal oxidation and carburising of Zr has been released in open literature. In this research better wear resistances have been achieved for surface engineered zirconium using Thermal Oxidation (TO) and Pack Carburising (PC) treatments.

Two surface engineering techniques have been investigated in this work. One is thermal oxidation (TO) and another is pack carburising (PC). Both processes have been investigated under a wide range of processing conditions, including processing temperature, time, surface roughness and compositions. The structures and compositions of the resultant surface and subsurface layers have been characterised using a variety of analytical and experimental techniques, including metallography, scanning electron microscope, X-ray diffraction, glow discharge spectrometer and ball-cratering. The properties of the surface engineered CP-Zr have been characterised by microhardness testing, scratch testing, and tribological testing under both dry, unlubricated and simulated body fluids (Ringer's solution) conditions. The results show that TO is a very effective surface engineering technique to enhance the tribological properties of CP-Zr. TO produces a hard $ZrO_2$ oxide layer (OL) of 5 to 12 microns on the surface and an oxygen diffusion zone (ODZ) of a few microns in the subsurface. The OL offers good wear resistance while the ODZ provides load

bearing capacity. Thus, the combination of the OL and ODZ offers CP-Zr excellent tribological properties under high contact loads. However, the performance of TO CP-Zr depends on the TO process conditions and the surface roughness of the TO surface. This work investigated the effect of TO temperature, time, initial surface toughness and roughness after TO, on the tribological performance. It has been determined that the optimum TO temperature is $650^oC$ and optimum time is 6 h. Too high a temperature and too long a TO time can lead to the formation of pores and cracks in the OL, leading to deterioration in tribological properties. This happens due to the fact that the created OL using those conditions can be poor, damaged and flakes off easily. It has also been found that a slightly rough surface before and/or after TO is beneficial in delaying crack formation in the OL during sliding and enhancing the load bearing capacity of TO CP-Zr. This happens because there is minimal contact between the alumina ball and surface of the sample during friction and wear testing.

A further investigation has been conducted to compare TO Zr with TO Ti. Both Zr and Ti are important biometals used in medical implants. But they show very different TO characteristics in terms of OL growth kinetics and mechanical properties. This investigation has shown that TO produces a much thicker OL on Zr than on Ti and the OL on Zr is very adherent to the substrate. As a result, the TO Zr performs much better during sliding tests under dry conditions and in Ringer's solution.

Another surface engineering technique investigated is pack carburising (PC). Although very few work has been reported on carburising of zirconium, there have been some reports on pack carburising of titanium. It is thus necessary to investigate the feasibility of pack carburising CP-Zr in this work. PC was conducted at various temperatures ($825 - 980^oC$) and for various duration (3-40 h) and with different pack compositions. The results show that CP-Zr can be effectively carburised at temperatures higher than $900^oC$ for sufficiently long duration (more than 10 h). Low temperatures and short duration favour oxidation rather than carburisation. Successfully carburised CP-Zr comprises a ZrC carbide layer of a few microns on the surface, followed by a thick diffusion zone (200 microns) containing oxygen and carbon in the subsurface. The carburised CP-Zr offers enhanced tribological properties, but is not as effective as thermal oxidised CP-Zr.

# Contents

# List of Figures

# Chapter 1

# Introduction

## 1.1 Background

Zirconium is an engineering metal widely used in nuclear power industry because of the ability of resisting hydrogen [11]. Due to its extremely good corrosion resistance and biocompactivity, it is also found that Zr has common uses in the biomedical field, such as in artificial hip and knee joints [12]. However, Zr is a relative soft metal and suffers from high friction and wear [13].

Therefore efforts have been made to improve the tribological behaviour of Zr, mainly by thermal oxidation [14]. Unfortunately, unlike thermal oxidation of titanium which has been investigated widely in detail [15], no sufficient information on thermal oxidation of Zr has been released in open literature [16]. Furthermore, very little work has been reported regarding carburising of Zr, although recent work done at De Montfort University showed that carburising can be used to improve the surface properties of titanium [17]. Therefore it is necessary and timely to have a detailed study on process optimisation of thermal oxidation of Zr and on carburising of Zr, and further to study the structure and properties of surface engineered Zr for general engineering and biomedical application.

Efforts have been made by other investigators to improve the wear resistance of zirconium through extending the oxide film on the surface, mainly by thermal oxidation [4][14] [18] [19] [20] and plasma electrolytic oxidation [21] [22][23]. With a bulk hardness of 1200 to 1300HV, a sufficiently thick $ZrO_2$ film can provide zirconium with excelent resistance to abrasion and wear [4][14] [18] [19] [21] [22].

Thermal oxidation is thus an effective surface engineering technique to harden the surfaces of zirconium (Zr) and its alloys for improvement in friction and wear performance. Unlike thermal oxidation of titanium where the rutile oxide layer

formed tends to be fragile and flake off easily when it is thicker than about 2$\mu$m [15][24], thermal oxidation of zirconium can produce a thick and adherent $ZrO_2$ layer without the danger of flaking off [25] [26][27][28][29]. The adherent and protective nature of the thick oxide layer on zirconium can be explained by the plasticity of zirconium oxide at elevated temperatures [30].

Indeed, oxidized zirconium (OxZr) has recently been introduced as an alternative bearing in total joint arthroplasty for artificial hip and knee joints [3][16] [19] [31] [32] [33] [34]. OxZr possesses a good combination of a ceramic bearing surface to resist wear and a tough metallic core to resist fracture. Both in vivo and in vitro tests demonstrate that, as compared to the most commonly used Co-Cr bearing, OxZr with a $ZrO_2$ layer about 5$\mu$m thick offers several advantages, including reducing polyethylene (PE) wear and enhanced resistance to surface roughening caused by third body particles [33] [35] [36] [37] [38]. Most of the published reports on clinic use of OxZr is based on the commercial process, OXINIUM (Smith and Nephew Inc.), which produces an $ZrO_2$ layer about 5$\mu$m thick and an oxygen diffusion zone (ODZ) of 1.5 to 2$\mu$m thick on Zr-2.5 wt% Nb alloy. The thicknesses of the oxide layer and ODZ, which can be controlled easily by altering processing conditions, are expected to have significant effects on the tribological and load bearing properties of OxZr. However, information in this respect is limited in open literature. Thus, it is necessary to investigate the details of the effect of processing parameters and surface conditions on the response of Zr to thermal oxidation.

In a recent investigation [15][17] [39][40], it is found that CP-Ti can be carburised in a carburising pack containing a mixture of charcoal and carbonates to produce a titanium carbide layer of more than 10 micron thick on the surface and a thick oxygen diffusion zone up to 400 microns thick in the subsurface. Such pack carburised CP-Ti possesses extremely good tribological properties under high contact loads. It has been reported by Bailey and Sun [39], that carburised CP-Ti performs much better than oxidised CP-Ti and even better than bearing steel under dry sliding conditions. However, very few work has been reported on carburising Zr [41][42][43],and no report has been found on pack carburising Zr. The promising results from pack carburising CP-Ti suggest that it is possible to employ the same technique to Zr to achieve enhanced tribological properties.

## 1.2 Objectives

The aim of this work is therefore to develop surface engineering techniques to achieve enhanced tribological properties of CP-Zr. Two techniques have been investigated, i.e. thermal oxidation (TO) and pack carburising (PC). The objectives are as follows:

- To optimise the TO process through detailed investigation on the effect of temperature, time and surface roughness.
- To explore the feasibility of pack carburising Zr and its impact on tribological properties.
- To characterise the structures and properties of surface engineered zirconium using a variety of experimental and analytical techniques.
- To compare surface engineered zirconium with surface engineered titanium and identify its application potentials in biomedical and general engineering sectors.

## 1.3 Research Plan

The research involves surface engineering processing, structural and properties characterisation and theoretical analysis. Investigation was conducted in several stages, as described below.

1. Thermal oxidation of Zr was investigated first in terms of process optimisation. The effect of oxidation temperature and time is studied in details. A high temperature furnace available in the Materials Lab DMU was used.
2. The oxidised Zr was then characterised to study the composition, structure and surface properties as a function of oxidising conditions. A variety of measurement and testing techniques has been used, such as optical microscopes, scanning electron microscopes, microhardness tester and surface roughness tester. All these facilities are available in DMU.
3. The oxidised Zr was tested by friction and wear tests, corrosion tests and tribocorrosion tests. The wear mechanisms were analysed and studied in details. The Materials Lab houses all these surface properties testing facilities. Mechanism study was aided by microscopic techniques.

4. In the second stage, carburising of Zr was investigated. The carburised Zr was then optimised and characterised as in 1-3 above. Pack carburising method was used, which can be carried out using a high temperature furnace and a custom designed container to be manufactured in the mechanical workshop.

## 1.4 Thesis Organisation

This thesis contains nine chapters:

- Chapter 1 gives a brief introduction to the background information relevant to this research and defines the aim, objectives and the work to be conducted.
- Chapter 2: presents an literature survey on subject matters related to this work.
- Chapter 3: describes the experimental techniques and methodology used in this work.
- Chapter 4: based on a paper I presented at an international symposium, presents the results and discussion on the effect of TO temperature and initial surface roughness on the structures and tribological performance.
- Chapter 5: based on the paper I published in Surface and Coatings Technology, presents the results and discussion on the effect of TO time at a specific temperature of $650^oC$.
- Chapter 6: based on the paper I published in Transations of the Non-ferrous Metal Society of China, presents the results and discussion on the effect of surface roughness after TO.
- Chapter 7: based on the paper I published in Journal of the Mechanical Behavior of Biomedical Materials, compares the response of CP-Zr to thermal oxidation with that of CP-Ti .
- Chapter 8: presents the results on pack carburising of CP-Zr.
- Chapter 9: contains main conclusions that can be drawn from this work and recommendations for future work.

# Chapter 2

# Literature Survey

## 2.1 Zirconium

### 2.1.1 General properties and Applications

In the field of biomedical engineering and science, zirconium alloys have been used and investigated in many orthopaedics applications. Zirconium was discovered to the world in 1789 by a Klaproth [44][45][46], who isolated zirconium oxide from a sample of zircon ($ZrSiO_4$), zircon or zargun as it was called by Arabs which was known as a gemstone in past. However when Neils Bohr [47][48] was working on the atomic theory he was sure that both Hafnium and Zirconium were rare to find on earth, meaning that it actually comprises 0.016 percent of crustal rocks on earth. In fact the researches show that only Iron, Titanium and Manganese are more abundant than zirconium. The main minerals in zirconium element are baddeleyite ($ZrO_2$) and zircon ($ZrSiO_4$) which can be found mostly in Australia, United States and South Africa [49]. Zirconium commercial production was intended by the Kroll process which uses magnesium (Mg) to reduce minerals [50]. However removing oxygen and nitrogen is also another way which was called the Arkel-de Boer process [51][52][53]. In this method a vessel with a little amount of iodine is used to heat the crude zirconium and the temperature can go up to $200^oC$ for the volatilization of $ZrI_4$ to provide pure zirconium. The properties of zirconium make it one of most wanted materials due to the low density and good strength beside the very good resistance against corrosion (see table 2.1).

Table 2.1: Properties of commercially pure zirconium

| Property | value |
|---|---|
| Young modulus | 88 GPa |
| Thermal conductivity | 22.6 $Wm^{-1}K^{-1}$ |
| Density | $6.53gcm^{-3}$ |
| Electrical resistivity | $4.21x10^{-7}$ $\Omega m$ |
| Specific heat capacity | $0.278Jg^{-1}K^{-1}$ |
| Tensile strength | 330 MPa |
| Yield strength | 230 MPa |
| Poisson's Ratio | 0.34 |
| Thermal expansion coefficient | $5.8x10^{-10}K^{-1}$ |

Due to its extremely good corrosion resistance and the ability to resist hydrogen, zirconium has been used in nuclear industry, for example creating the cans that holds bars of fuel reactors and in pressure tubes in some of the nuclear reactors [54][55]. One of the important uses of zirconium is that when combined with magnesium which will give it more strength, which helps reducing the fuel consumption as well as reduction air pollution when it is used in aircrafts [56][57][58]. More recently zirconium has found interesting biomedical uses particularly for making hip and knee joints replacement or in other word orthopaedics applications [59].

Zirconium has also found applications in many other sectors of industry. Table 2.2 summarises typical applications in industry for making various components.

Table 2.2: Typical applications of zirconium and its alloys

| Industry | Components | Useful properties |
|---|---|---|
| Nuclear industry | nuclear reactors, Nuclear power stations, cladding of fuel rods and sheathing of nuclear power rods . | Corrosion resistance, low neutron capture, thermal conductivity and hydrogen embrittlement or absorption. |
| Chemical industry | Heat exchangers, acid pipes, pressure vessels, vacuum tubes, reboilers, evaporators and Fittings. | Corrosion resistance, difficult to ignite and has heat resistance, resistance to acids alkalis and seawater, low toxicity. |
| Space and aeronautic | Space vehicle, grinding wheels, flash bulbs, gas turbines and jet engine blades. | Low cost, High temperatures or heat resistance, water resistance biocompatible. |
| Biomedical | Hips and knee joints replacement and dental implants and Hemofiltration(Kidney injuries). | Corrosion resistance, does not get effected in room temperature and it is non-toxic and has low radiation. |

### 2.1.2 Zirconium Crystal Structure

Zirconium has a hexagonal closed pack structure (HCP) and this is from the Tetragonal phase family [60][61]. Similar to titanium, zirconium has the same crystal structure and similar atomic size. There are three polymorphic forms of zirconium: alpha zirconium ($\alpha$-Zr), beta zirconium ($\beta$-Zr) and alpha-beta zirconium ($\alpha$-($\beta$-Zr) [17][62]. However this is dependent on thermal and thermo-chemical treatments, which mean that the microstructure can be modified and controlled for various applications [63][64]. The allotropic phase transformation of commercially pure zir-

conium starts at temperature of $1170^oC$; this is where the structure changes from the hexagonal closed-pack phase ($\alpha_{HCP}$) to the body-centered cubic phase ($\beta_{BCC}$). The hexagonal closed-pack structure of the $\alpha$-Zr phase has lattice parameters of a=3.25Å and c=5.14Å, which result in c/a of 1.582 [65]. Figure 2.1 shows a comparison of the temperature dependence of c and a.

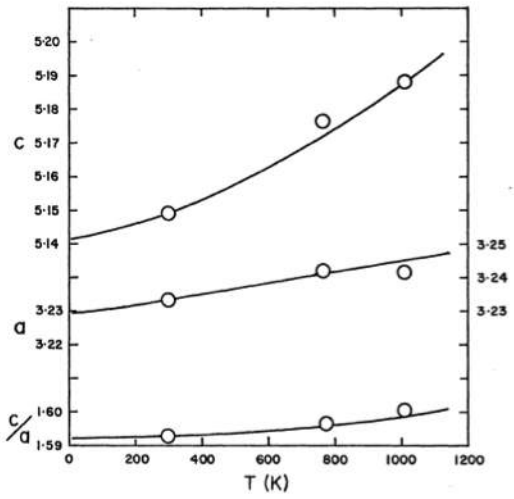


Figure 2.1: comparison of the temperature dependence of c and a

The hexagonal closed-pack structure of the $\alpha$-Zr phase can actually be seen in a schematic diagram as shown in figure 2.2a, which shows the most densely packed lattice planes highlighted with the crystal system directions. When the transformation starts from the $\alpha$-Zr phase to the $\beta$-Zr phase, the crystal structure changes to body-centered cubic (BCC) with lattice parameter of a=3.25Å.

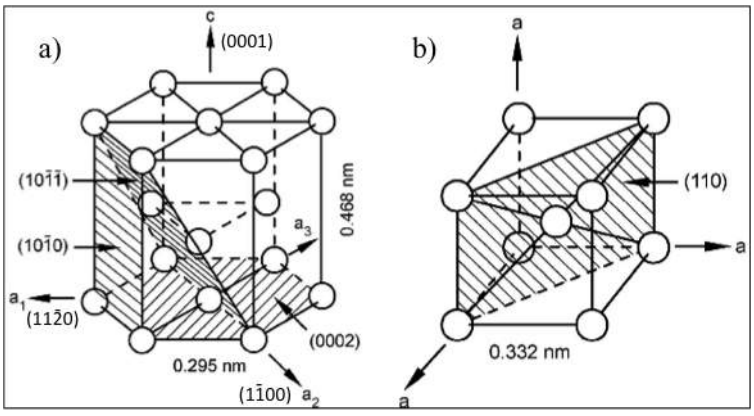


Figure 2.2: The unit cell crystal structure of (a) $\alpha$-Zr planes and (b) $\beta$-Zr planes [5]

Figure 2.2b shows the unit cell crystal structure of $\beta$-planes. The densely packed

plane in this phase is [110] plane as highlighted. The transition temperature after changing from HCP structure to BCC structure is dependent on the composition of zirconium. In some cases there is a possibility to stabilise the $\beta$ phase of zirconium in room temperature.

In general the ideal c/a ratio of Hexagonal closed-pack structure is about 1.633. In hexagonal closed-pack metals, a slip normally starts in the bergers vector ($\overrightarrow{a}$) or in $<11\bar{2}0>$ direction. Figure 2.3 shows the slip planes, it shows that the slip planes can be basal (0002) or prism ($10\bar{1}0$) with two independent planes of slip. A pyramidal slip $<10\bar{1}1>$ could appear due to the impact made by basal slip and prism slip. However this will result in the existence of four different slip systems [17] [66] [67]. Since the c/a ratio of zirconium ($\alpha$-Zr) is less than the ideal value, this will lead in having large gaps or spaces between the prism planes. The spacing between planes will result in the packing density of planes, and it will increase relative to the basal plane (0002). This means that the slip will favour prismatic plane more than basal planes[68].

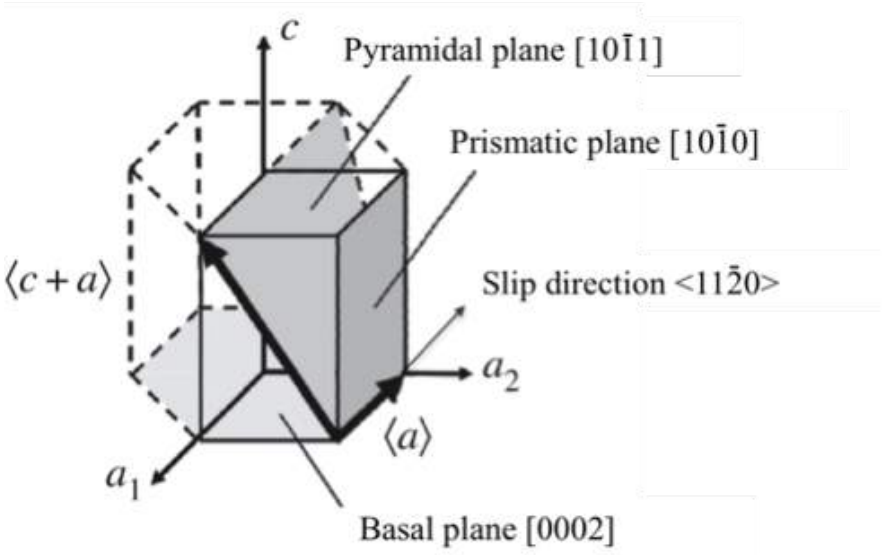


Figure 2.3: HCP crystal lattices slip systems

The requirement of Von Mises principle is to have five independent slip systems for the plastic deformation to occur [69][70]. For hexagonal closed-pack systems, another slip system is required to reach good ductility. For homogenous deformation to happen, strain in the $\overrightarrow{c}$ direction is necessary along with $\overrightarrow{a}$. This new slip can be represented as $\overrightarrow{a}+\overrightarrow{c}$ slip $<11\bar{2}3>$. This slip will help in providing five independent systems as listed in table 2.3 [66][68].

Table 2.3: HCP crystal lattices slip systems

| Slip System | Bergers Vector | Slip plane | Slip direction | Number of slip systems | |
|---|---|---|---|---|---|
| | | | | Total | Independent |
| 1 | $\overrightarrow{a}$ | [0002] | $<11\bar{2}0>$ | 3 | 2 |
| 2 | $\overrightarrow{a}$ | $[10\bar{1}0]$ | $<11\bar{2}0>$ | 3 | 2 |
| 3 | $\overrightarrow{a}$ | $[10\bar{1}1]$ | $<11\bar{2}0>$ | 6 | 4 |
| 4 | $\overrightarrow{a}+\overrightarrow{c}$ | $[10\bar{1}1]$ | $<11\bar{2}3>$ | 12 | 5 |

## 2.2 Zirconium Oxide ($ZrO_2$)

### 2.2.1 General properties

Zirconium dioxide is mainly used for ceramic materials. This compound can naturally be found in the earth crust with small percentage (0.016%). It has many good mechanical properties such as hardness, high melting point and low reactivity. $ZrO_2$ is produced from zirconium mineral concentrates, by chloride and sulphate process [71][72][73][74]. The chloride process includes natural rutile that is then converted to $ZrCl_4$. Zirconium chloride ($ZrCl_4$) is different to Titanium chloride ($TiCl_4$), because it has a polymeric structure [75][76]. Another difference is that $ZrCl_4$ has a solid structure, where $TiCl_4$ is distillable. However, when $ZrCl_4$ is oxidized at high temperature (1000$^o$C) this will result in $ZrO_2$. This new compound is then cleaned from chloride and hydrochloric acid residuals that were formed during the process. On the other hand, in sulphate process zirconium slag reacts with sulphuric acid. Zirconium hydroxide ($ZrO(OH)_2$) is then formed through hydrolysis, which is cleaned after [17] [77]. Both processes can produce $ZrO_2$. In the final stage $ZrO_2$ is milled to provide a controlled particle size. After that the surface is coated to improve the functional behaviour in many applications.

Zirconium dioxide is widely used but mainly for producing hard ceramics [78][79]. $ZrO_2$ is also used in nuclear power industry and biomedical industry such as hips and knee joints replacements. $ZrO_2$ can also be used on oxygen sensors because it has the ability to let oxygen move freely through the crystal structure at high temperatures [80]. Furthermore, zirconium dioxide is one of the most important electroceramics and it can be used as solid electrolyte in electro-chromic machines [81][82]. Zirconium dioxide has a great mechanical, thermal and electrochemical properties as listed in table 2.4.

Table 2.4: Zirconium dioxide properties

| Properties | ,Value |
|---|---|
| Density | 5.68 g $cm^{-3}$ |
| Hardness | 1350 HV |
| Poisson's Ratio | 0.3 |
| Shear modulus | 85 GPa |
| Young's modulus | 210 GPa |
| Thermal conductivity | 4.3 W/mK |
| Liner thermal expansion coefficient | 10 x $10^{-6}$ $K^{-1}$ |
| Melting point | 2700$^oC$ |
| Specific heat capacity | 540$Jkg^{-1}K$ |
| Electrical resistivity | 4.5 x $10^{18}\Omega$ m |
| Offset yield strength | 350 MPa |
| Ultimate,tensile strength | 450 MPa |

### 2.2.2 Zirconium Oxide Crystal Structure

There are three crystallographic phases of zirconium dioxide: Monoclinic phase (M), Tetragonal phase (T) and Cubic phase (C) [83][84][85][86]. The monoclinic phase comes in the form of deformed prism with parallel-piped sides and it is stable at temperature of 1170$^oC$. It has lower mechanical properties and this is due to the reduction of ceramic particles cohesion. The tetragonal phase comes in the form of a straight prism that has rectangular sides and it is stable between temperatures of 1170$^oC$ and 2370$^oC$ with good mechanical properties. Finally the cubic phase, which comes in the shape of straight prism with square sides and it is stable above temperature of 2370$^oC$ with sufficient mechanical properties [87] [88][89]. Figure 2.4 shows the temperature range for the three phases.


Figure 2.4: Crystallographic phases of $ZrO_2$

Figure 2.5 shows the crystal structure for (a) monoclinic, (b) tetragonal and (c) cubic phases. Both monoclinic and tetragonal structures have six oxygen atoms and each atom is bonded to three Zr atoms. Where cubic structure has seven fold coordination or oxygen atoms ($Zr^{4+}$). The distance between Zr and O is about 0.216nm. Monoclinic phase has a Baddeleyite structure type and this type the crystals are commonly tabular on 100 and it is elongated on [010] or short to long

prismatic along $< 001 >$. The prism faces are parallel to [001]. Tetragonal phase has a rutile structure type, which means that it is commonly observed to exhibit a prismatic growth habit along the c axis direction [001]. Cubic phase has a fluorite structure type; this means that zirconium atoms are situated at the corners of the cubic elementary cell also at the center of $< 110 >$ directions. This also means that the oxygen atoms lie on the quarters of $< 111 >$ directions [87][90][91]. Zirconium dioxide crystals are in two different directions of $1\bar{1}0$ and $\bar{1}\ \bar{1}1$. This gives two different slip systems: primary slip system (001)[110] and secondary slip system such as $(1\ \bar{1}\ \bar{1})[101]$ and $(1\bar{1}1)$ [011] [92].

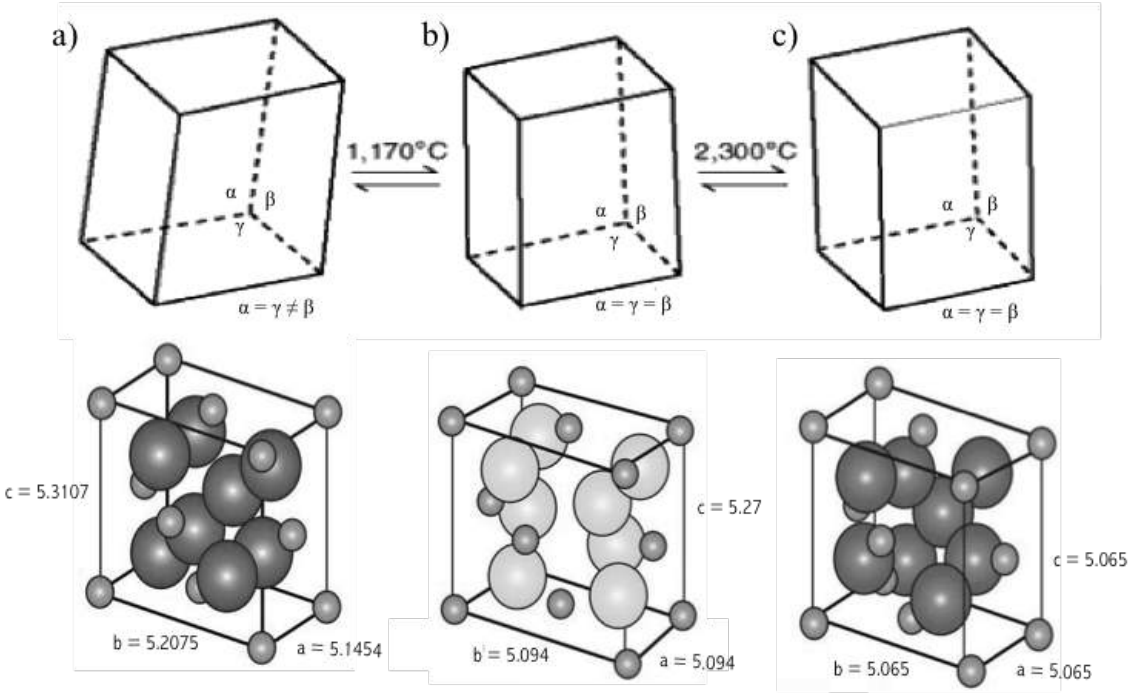


Figure 2.5: The unit cell crystal structure of a) monoclinic, b) tetragonal and c) cubic

## 2.3 Zirconium Carbide (ZrC)

### 2.3.1 General properties

Zirconium Carbide (ZrC) is a very hard ceramic material and it is commonly used to make cutting tools [93]. This type of material has great hardness, high melting point, high strength and good electrical conductivity. However, in industrial field, Zirconium carbide is produced through sintering process [94][95]. ZrC is one of the most important and widely used ceramic, and it comes in the appearance of dark

Table 2.5: Zirconium Carbide properties

| Properties | ,Value |
|---|---|
| Density | 6.73 g $cm^{-3}$ |
| Hardness | 3000 HV |
| Poisson's Ratio | 0.25 |
| Shear modulus | 175 GPa |
| Young's modulus | 430 GPa |
| Thermal conductivity | 25 W/mK |
| Liner thermal expansion coefficient | 6.8 x $10^{-6}$ $K^{-1}$ |
| Melting point | $3250^oC$ |
| Specific heat capacity | $368Jkg^{-1}K$ |
| Electrical resistivity | 82 x $10^{-8}\Omega$ m |
| Offset yield strength | 790 MPa |
| Ultimate,tensile strength | 875 MPa |

Table 2.6: Zirconium Carbide crystal structure properties

| Properties | Value |
|---|---|
| Crystal,structure | Cubic, cF8 |
| Space group | $Fm\bar{3}m$ |
| Lattice parameters | a=b=c= 5.065Å<br>$\alpha = \beta = \lambda = 90^o$ |

grey metallic powder. It is mainly used in commercial applications (prototypes) and in nuclear industry (coating of nuclear power reactors) [96]. In the biomedical field, the interest of zirconium carbide has increased. This is due to the great mechanical, physical, chemical and thermal properties as shown in Table 2.5 [97].

Zirconium carbide is similar to most carbides of refractory metals. It is a sub-stoichiometric, which means that it contains carbon atoms. However, the carbon content is higher with higher temperature [98][99].

### 2.3.2 Zirconium Carbide Crystal Structure

Zirconium carbide has face centered cubic crystal (FCC) structure [100][101][102]. The parameters of ZrC crystal structure are as listed in Table 2.6 and it is also represented graphically in Figure 2.6. The cubic crystal structure has unit cell in the shape of cube, this is one of the simplest crystal structures.

Similar to most transition carbides, zirconium carbide is dominated by slip of $[111] < 1\bar{1}0 >$ and $[110] < 1\bar{1}0 >$. The slip occurs in the [111] planes; which gives twelve slip planes. At very high temperatures the $[111] < 1\bar{1}0 >$ slip occurs [17] [62].

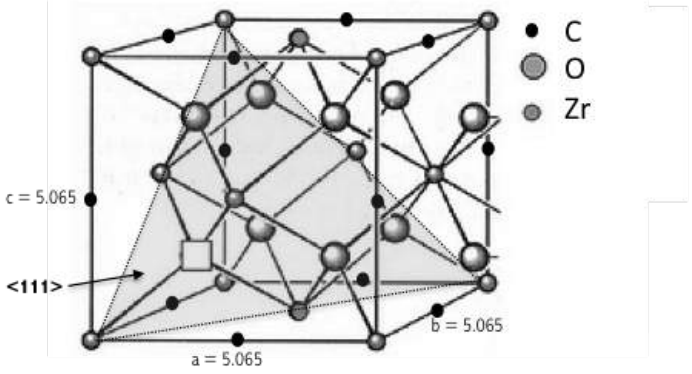


Figure 2.6: The unit cell crystal structure of Zirconium Carbide

## 2.4 Zirconium Surface Modification

As can be seen from Table 2.1, zirconium has a relevily low strength [103][104]. Under tribological conditions, zirconium is expected to suffer from high friction and wear. Surface engineering is the most effective to improve surface properties of engineering materials, such as wear resistance and corrosion resistance. Surface modification can be applied with many techniques to modify the surface properties of zirconium and fight in having high friction or wear and other galling issues that is linked with zirconium. These techniques can include coating of the surface, heat treatments, chemical treatments and treating the surface by improved chemical bonding or thermochemical technique [99][105]. Typical thermochemical treatments includes thermal oxidation and carburising, which are discussed further below for zirconium.

### 2.4.1 Oxidation

Oxidation is a treatment that is applied to increase the surface hardness and corrosion resistance of zirconium. This will creat a film that is $1.2 - 12\mu m$(more or less) thick on zironium's surface [28][106][107]. While knowing that the chemical environment can have a significant effect on zirconium, oxidation can help to improve the chemical properties. There are many techniques that were implemented to provide a solution such as forming a thin oxidised film on the surface of zirconium by using thermal oxidation or anodising or in other word the growth of anodic film[28]. Oxidation also includes effective techniques such as oxygen diffusion[108], plasma electrolytic oxidation[109]. Thermal oxidation is the cheapest method offering very

good results in terms of improving the surface of zirconium against friction, wear and corrosion[40].

### 2.4.2 Thermal oxidation

Thermal oxidation is normally to create a thin oxide layer on a metal surface [110][111][112]. This technique uses reletevly high temperatures and as the temperature increases the oxide layer becomes thicker. For zirconium, thermal oxidation is normally curried out between 500 and 1200$^o$C for several hours. Former studies have shown that thermal oxidation creates multilayer structure on the surface of the material. This is because when the oxide layer forms on the surface, there is a process of oxygen diffusion as well as absorption, producing an oxygen diffusion zone(ODZ) beneath the oxide layer[111]. Once the oxygen diffusion zone occurs at the required level this will give zirconium dioxide layer($ZrO_2$). Normally the surface will be darker and this process will give zirconium better resistance against corrosion, friction and wear[15][110]. Figure 2.7 is a schematic diagram showing the structure of typically thermal oxidised zirconium, comprising a $ZrO_2$ layer on top of an oxygen diffusion zone.

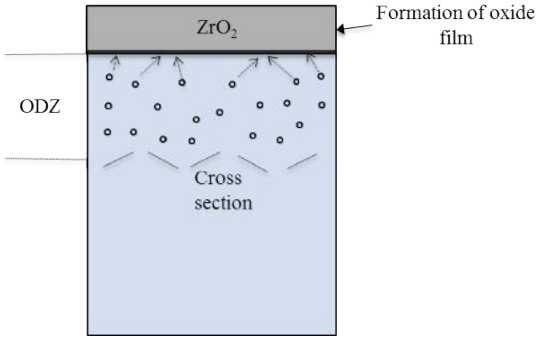


Figure 2.7: Schematic diagram for zirconium thermal oxidation structure

Although there are very few reports on the effect of TO parameters on Zr for biomedical applications, there are many reports on the oxidation behaviour of Zr and its alloys in nuclear reactors which involve exposure to high temperatures and long duration [113][114][115][116]. A very important phenomenon observed is oxidation breakway, which marks the transition from parabolic growth governed by solid state diffusion to linear growth governed by the formation of pores and cracks in the oxide layer. Figure 2.8 shows typical examples of oxide layer after oxidation breakway [6][25][29][117][118].

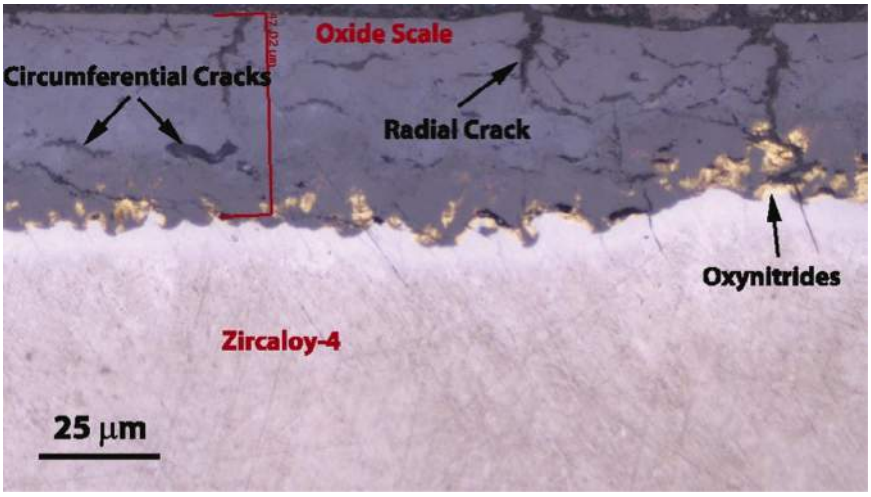


Figure 2.8: Cross section of a oxidised Zr at $900^oC$ for 30 min, showing formation of pores and cracks in the OL due to oxidation breakway [6]

Before breakway, the oxide layer formed is compact, dense and adherent to the substrate [6][119][120]. After breakway, the oxide layer becomes porous, cracked and crumbly, and tends to flake from the substrate. The breakway is favours by high temperature and long time oxidation and is associated with the formation of oxygen gases inside the oxide layer and the build up of residual stress [6][121][122]. Formation of gases inside the OL leads to the formation of pores, while larger residual stresses can lead to the formation of cracks in the OL. It is thus very important that TO of Zr for tribological applications should be carried out under conditions that oxidation breakway does not occur. This is to ensure that a dense and adherent OL is formed to provide protection to Zr. The formation of pore and cracks in the OL is expected to deteriorate the tribological performance and load bearing capacity of TO-Zr [6].

### 2.4.3 Carburising

Carburising is a technique used to improve the wear resistance and fatigue strength of steels. It has been used recently to improve the wear resistance of titanium[39]. Since then carburising has been applied to zirconium [123]. It has been shown that zirconium carbide ($ZrCO_2$) has linear type of reaction, combining it with a layer of boron oxide will give zirconium diboride ($ZrB_2O_2$) which will increase wear resistance [124]. Zirconium carburisation has been realised using plasma carburising[125]. Plasma carburising is a thermochemical technique used to improve metal hardness and wear properties. During this process there are gaseous reactant that produce

heat on the surface of the metal. This technique creates a carburised layer on the surface of the metal, improving wear and corrosion resistance. The carburising in[125] was carried out in a vacuum chamber with $1 \times 10^{-2} mbar$ vacuum level. The chamber was filled with pure methane gas. The gas was ionised in a plasma with a high density of $10^{25} \sim 10^{26} \frac{ions}{m^3}$ and high ion energy of $1 \sim 2keV$. This process produced a thermally effected layer of about $80\mu m$ with a surface hardness up to $8.5GPa$. However, very few studies have been conducted on carburising Zr using other conventional and industrial processes, such as gas carburising and pack carburising.

## 2.5 Tribology

Tribology is known as the technology of interacting surfaces in relative motion and it also can be defined as the technology of friction, wear and lubrication [126][127]. Materials surfaces are not perfectly flat, so when two surfaces are in contact only small percentage of the apparent surface area is actually supporting the load; this will result in high contact stress which will lead to increase of friction and wear [128].

### 2.5.1 Friction

Friction is the resistance to motion when two bodies in contact are forced to move relative to each other. It is associated with any wear mechanism that may be operated with a lubricant or surface films that may be present as well as the surface topographies [128]. From the frictional interaction heat can be generated and it can affect the performance of the lubricants and change the properties of the contacting materials or their films and in some cases it can change the properties of the product being processed. Furthermore any of these frictional heating can cause a safety problem because of the danger of mechanical failure of components such as fire or explosion [8][126][128]. Thus, friction reduction becomes one of the main tasks of surface engineering of materials.

#### The Friction Law

Under the conditions of sliding, the coefficient of friction ($\mu$) for a given pair of materials and fixed conditions of lubrication may be almost constant. This observation led to two realistic laws of sliding friction, which was discovered in 1699 by Leonardo Da Vinci. The laws of friction are then stated as follows[8]:

1. The friction force is proportional to the load.
2. The friction force is independent of the apparent area of contact.
3. The friction force is independent of the sliding velocity.

**Friction Coefficient**

As shown in figure 2.9,in both ideal rolling and sliding, a tangential force F is needed to move the upper body over the stationary counter-face.

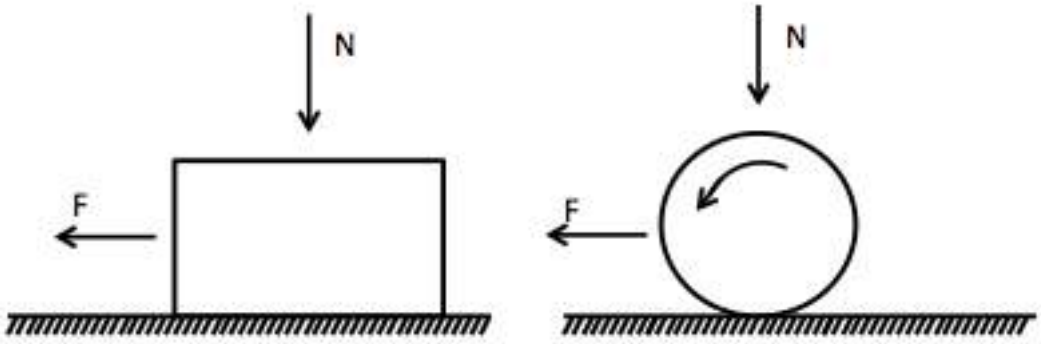


Figure 2.9: Friction force (F) is needed to cause motion by rolling and sliding

It is very important to separate the various terms and concepts associated with friction such as:

1. Friction force.
2. Friction Coefficient.
3. Frictional energy.
4. Frictional heating.

These four issues are defined as the context of solid friction, which also can be defined as the resistance to movement of one solid body over another. This movement can be sliding or rolling. When two bodies are forced to move to each other, the friction force (F) is tangential force that must be overcome in order for one solid contacting body to slide over another. It acts in the plane of the surfaces and is usually proportional to the Normal load N, as seen in Equation 2.1 [8][126][128].

$$F = \mu N \tag{2.1}$$

The frictional constant is known as the friction coefficient ($\mu$) and therefore the equation can be expressed as:

$$\mu = \frac{F}{N} \tag{2.2}$$

**Factors that affect friction**

Controlling friction between two contacting bodies is possible, but it can be controlled with specific conditions. There are many factors that affect friction such as:

- The nature of the surface.
- The load applied.
- Surface finishing.
- Temperature.
- Nature of relative motion.
- Characteristic of lubricants.

### 2.5.2 Wear

In general wear is defined as the damage to a solid surface caused by the removal or displacement of material by the mechanical action of a contacting solid, liquid or a gas. Wear is usually observed when there is friction; wear can be achieved through the physical contact of material in motion. In most cases wear can cause material loss which at the end will lead to failure [126][128][129]. When there are two materials in contact specifically sliding contact, then this will cause material degradation. However the sliding movement will affect the material, since some material will be lost or removed. This wear loss can be expressed in equation 2.3, which can help to calculate the rate of abrasive wear for the softer material during the contact [17]

$$\frac{V}{L} = K\frac{F_n}{H} \tag{2.3}$$

where:

V=material lost volume, L=Distance of total sliding, $F_n$=Normal applied load, H=Hardness of the softer material, K=coefficient of wear.

By rearranging Equation 2.3 and $\frac{K}{H}$ can be made the subject, which is known as the coefficient of dimensional wear ($k_d$) with the unit of ($mm^3N^{-1}m^{-1}$). The coefficient of dimensional wear helps in finding the removed material volume, per unit distance, per unit load, as shown in Equation 2.4 [8][17].

$$k_d = \frac{V}{LF_n} \tag{2.4}$$

### Wear Mechanisms

Wear is classified in many different ways. For example, it can be classified as lubricated wear and non-lubricated wear or in other words dry wear. However the common practice is classifying the wear mechanism that is operating. In practice wear involves more than one mechanism or multi-mechanisms operating in the same time, which makes it hard to tell the differences between wear types. However, this motivated researches to develop methods to understand types of wear, which was introduced by Budinski. In his approach he classified the creation of wear into four different categories: Abrasion, erosion (corrosive), adhesion and surface fatigue. These four types are as shown in Figure 2.10. [17][128].

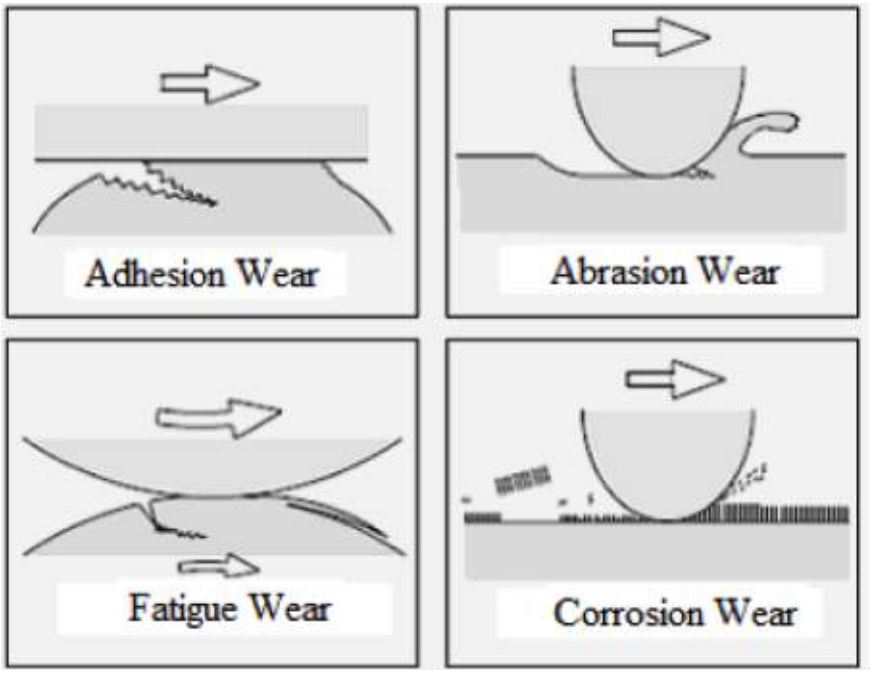


Figure 2.10: Four types of wear [7]

### Abrasive wear

Abrasive wear occurs when forcing hard or rough surface to move against a solid surface. This wear type is identified by noticing the scratches (grooves) on the softer material surface. When a harder material moves over a softer material, the softer material is abraded, and this is known as the two body wear, There are however an observation of wear particles formation. The creation of wear particles introduces a different mode of wear which is known as the three body wear. Abrasive wear can be avoided by the right selection of material and by surface engineering treatment to increase surface hardness. Generally, when talking about the abrasive wear, it can be separated into four different categories depending on the type of contact happening [17][128]:

- **Low-stress abrasion;** this type of abrasion occurs due to the light rubbing contact to the metal surface under a low contact stress and minimal plastic deformation if there is any. However, wear is noticed when scratches appear on the surface of the metal or specifically on the wear track.
- **High-stress abrasion;** this type of abrasion occurs due to the high strain hardening on the surface of the metal under high contact stress which is enough to damage the surface due to severe plastic deformation and scoring.
- **Gouging Abrasion;** this type of abrasion involves very high stress which results in having big grooves or houges. In this type of abrasion strain hardening and plastic deformation are involved and they are both leading factors.
- **Polishing wear;** this type of wear is a very mild form as it is hard for scratches to be observed. The surface of this type of wear is usually smooth and bright due to the polishing effect of the counterface or abrasives.

### Adhesive wear

Adhesive wear can be introduced as the removal of material from surface and transfer to another. This is due to cold welded junctions, which is formed between two surfaces during relative motion or in sliding motion. In this case, usually the removed material from the soft body sticks on the surface of the harder body. Since material transfer is involved in the wear process, if the removal is in larger scale this will cause large removal and material tearing. This type of wear will have a big issue if the contacting surfaces are both from the same material. However there are other

factors that can also cause issues such as high temperatures, poor lubrication, high loads and high sliding speed which can cause galling which can be easily visible on both surfaces. To avoid adhesive wear it is better if the two contacting surfaces are not from the same material, also it is necessary to avoid sliding hard material against another hard material, and finally by lubrication since it will reduce wear. [17][128].

#### Erosion wear (Corrosive)

This type of wear occurs when the sliding contact is running in a corrosive environment. Erosion wear is also known as the material chemical degradation when both wear and corrosion are included in the process [128]. The present of fluids can have lubricating effects, which is something hard to avoid. On the other hand, to avoid erosion wear some methods were investigated such as reducing the temperature, speed of sliding and load. If the sliding process was done in a corrosive environment and using a passive material, this will lead to:

- The formation of the lubricating film in the contact zone, which will reduce wear and corrosion.
- Producing a weak film, that will be removed continuously and will result in increasing the wear rate.
- The formation of protective film on the surface, which will produce pitting on the surface [17].

#### Surface fatigue wear

This type of wear is associated with continuous sliding and rolling of one body over another, which will cause the subsurface to be cyclically stressed or in other words it can result in micro-cracking and cycle stresses to the subsurface. This high stress that the subsurface has experienced will produce plastic deformation. These factors will change the structure of the material and will create visible larger cracks and cause fracture.

### 2.5.3 Surface Roughness

In general no surface is perfectly flat, and to prove that a microscope is needed. In fact even polished samples are not flat and they have surface irregularities or surface

roughness. The profilometer can help in describing the surface's topography in a single direction but the graph will be hard to read and the measurements are not always accurate. The material's surface roughness can be identified in equation 2.5. This equation is working by using a centre line average and the height (y) above the mean line in order to calculate the average roughness ($R_a$) over a length (L). The mean line is constant so when the equal areas can lie above and below the line as shown in figure 2.11. When the average roughness fails to produce information of the differences between spiky surfaces and smoother surfaces, the root mean square roughness r.m.s ($R_q$) offers a better significance to various surfaces as shown in equation 2.6 [8]:

$$R_a = \frac{1}{L}\int_0^L |y(x)|dx \tag{2.5}$$

$$R_q = \frac{1}{L}\sqrt{\int_0^L y^2(x)dx} \tag{2.6}$$

However for majority of surfaces the value of root mean square roughness is nearly similar to the value of the average roughness, and in some of the cases such as the distribution of Gaussian of height of surfaces $R_q = 1.25R_a$[8].

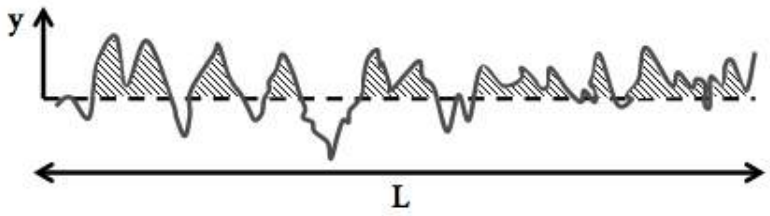


Figure 2.11: The profile of a surface showing the height of the surface with relation to centre line average

### 2.5.4 Lubrication

One of the best solutions to reduce wear is lubrication. Friction can also be reduced by applying lubricants between the two surfaces. Lubrication helps in reducing the consumption of power which is needed to overcome the friction and this will help both sliding and rolling process when two materials are in contact. In general lubricants help in reducing wear but not eliminating it, so wear always occurs when two contacting bodies have relative motion [8].

### Lubrication types

There are many ways of lubrication such that the surfaces is separated by a lubricant; which could be solid or semi solid, liquid or even gas. When lubrication is included, then the value of Lambda ($\lambda$) helps in measuring the contact of asperities during sliding process, expressed in equation 2.7 [17].

$$\lambda = h_{min}/\sigma^{x} \tag{2.7}$$

where $h_{min}$ is the thickness of the minimum film and $\sigma^{x}$ is root mean square surface roughness of the two surfaces in contact ,which is expressed in equation 2.8.

$$\sigma^{x2} = (R^2)_{q1} + (R^2)_{q2} \tag{2.8}$$

where $(R^2)_{q1}$ and $(R^2)_{q1}$ are the root mean square surface roughness for both the first and second surfaces. The value of lambda will help identifying the type of lubrication between the two surfaces. There are four situations that lambda could be located in between the contacting surfaces:

- **Hydrodynamic lubrication;** in this case there is a full film of fluid which will detach the surfaces from each other. This will help to gain low friction and low wear. Therefore this situation can be achieved when $\lambda > 5$.
- **Elastohydrodynamic lubrication;** in this type of lubrication there is less wear and friction, because there is no high pressure between the two surfaces. However there could be a concentrated contact in some of the areas on one surface or maybe both. This type of lubrication can be gained when $3 < \lambda < 5$.
- **Mixed elastohydrodynamic lubrication;** in this situation there is contact between the asperities even when there is a film between the surfaces. This situation also has a reduction in both wear and friction and it is more realistic comparing with hydrodynamic lubrication. Therefore this situation can be achieved when $1 < \lambda < 3$.
- **Boundary lubrication;** in this type of lubrication there is a high pressure which can create pitting or pockets full of locked lubricants between the two surfaces. There is damage on the material due to the high load or low sliding speed, therefore $\lambda < 1$.

These lubrication boundary conditions can be related to a parameter of lubrication, which is proportional to the viscosity of the lubricant ($\eta$) and the surface's speed ($\omega$) and the inverse of the pressure ($\rho$), as expressed in equation 2.9 [8].

$$Parameter of Lubrication = \frac{\eta\omega}{\rho} \tag{2.9}$$

The four types of lubrications can be represented graphically in a Stribeck curve diagram as shown in figure 2.12. The diagram expresses the boundary limitation of each type of lubrication and also presents the amount of friction on the surface for each stage during the surface contact. It can be seen that as the speed increases the film is starting to be created. In some points the lubrication will give the best conditions with minimum amount of friction. However when the viscosity of the lubricant increases this will lead to the increase the friction coefficient.

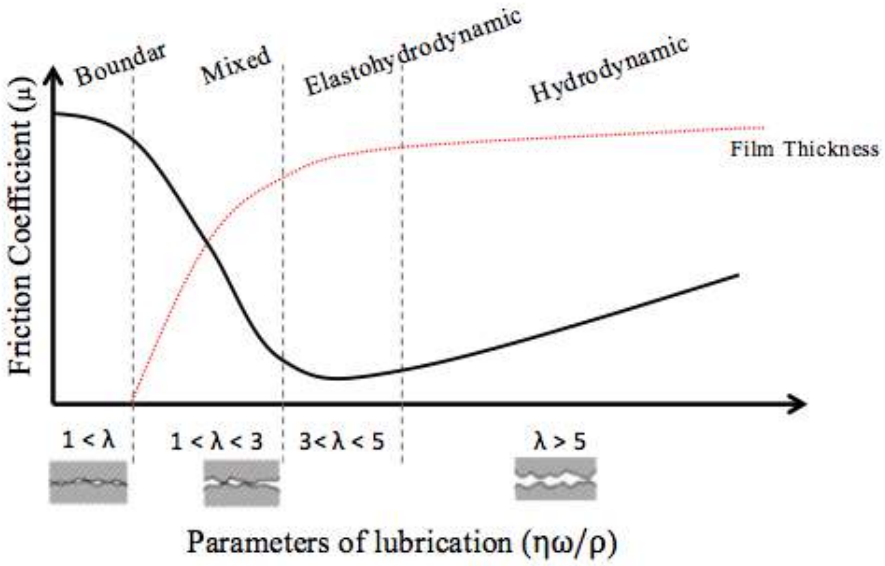


Figure 2.12: The Stribeck Curve [8]

## 2.6 Corrosion

Each year, corrosion and wear or the combined effects costs hundreds of billions of dollars in many industrial economies around the world. Corrosion and wear damage can be reduced with surface engineering such that engineering components can perform functions that are distinct from the bulk of the material. Metal corrosion is known as chemical or electrochemical processes where the exposed surface is in

contact with a corrosive environment [128][130].

### 2.6.1 Electrochemical Corrosion

When Electrochemical corrosion is involved with an active metal, no matter what environment involved (in water or not), there will always be an electricity flow from a metal to other metal, or from a metal surface to the other part of the same metal's surface [131]. Electrons loss occurs when the metal is in an electrolytic solution, leading to the formation of metal ions and thus corrosion. When the reaction of corrosion is applied to the atoms of a metal, these atoms will be converted to ions, because of the loss of electrons to the corrosive medium as described in equation 2.10 [17][128].

$$M \rightarrow M^{n+} + ne^{-} \tag{2.10}$$

knowing that: $M = Metal, n = Valence, e = Electron$. This reaction is known as the anodic reaction or oxidation, causing the metal to be oxidised as there is a transmission of electrons. However this movement of electrons must be followed by a cathodic reaction called reduction. This cathodic reaction will cause the electrons to be consumed, thus maintaining mass conservation. It is possible to have both anode and cathode existing in the same metal, where the cathode is linked to the anode, in other words cathode is followed by anode and they produce what is called a wet corrosion cell when they are electrical contact in an electrolyte [17].What is common in most corrosion reaction is that oxidation and reduction are always in different locations on the metal, the reason being that metals are in general conductive. It is clear that for corrosion to happen both anodic and cathodic reactions must be included and if one or both are not included this will stop corrosion from happening [128][132].

### 2.6.2 Corrosion forms and Mechanisms

In general, corrosion is known as the change of material from its original state after a long period which makes it less desirable and the material will no longer function properly, which can lead to the breakdown of the whole system. Corrosion can have many forms or specifically eight forms depending on the damage caused or the appearance of the metal after corrosion attack.

**Uniform Corrosion:** it is also known as general corrosion. Uniform corrosion

occurs to majority of metals and it is not really a big issue because it is predictable. Uniform corrosion is usually occurring in industrial environment due to the pollution or in salt water environment.

**Galvanic Corrosion:** this type of corrosion only occurs when two metals are in contact electrically, causing the flow of electrons from a metal to another but one of the two metals needs to have better corrosion resistance in terms of giving up electrons to the other metal. In this way the less anodic metal will be experiencing more corrosion. The reaction of the two metals will depend on the position of both metals in the galvanic series. If both selected metals are close to each other in the galvanic series, galvanic corrosion will be minimised.

**Pitting Corrosion:** this type of corrosion is very detrimental and it can cause holes on the metal which will lead to direct functional failure. Pitting happens in a lot of metals and it is common in engineering applications. It normally occurs in metals with protective films or coatings and it appears on the surface of the damaged area of the metal.

**Crevice Corrosion:** this type of corrosion is one of the attacking types caused at narrow opening or gaps between two different metals or between a metal to a non-metal edges and interfaces. The crevice corrosion is normally caused by either an accident or a crevice design such as rolled tube ends and threaded joints. This type of corrosion can affect passive metals and active metals.

**Erosion Corrosion:** this type of corrosion is caused when the rate of the attack to the metal is increased, because of the combination of the wear and corrosion. Erosion corrosion includes cavitation which is formed on the surface of the metal. This type of corrosion also includes fretting which is known as a relative motion between two different surfaces with a type of contacting called stick slip contact.

**Intergranular Corrosion:** this type of corrosion is also known as the grain boundaries corrosion, where the grains are not actually attacked. This is generally caused by the potential variances between both the grain boundaries regions and the precipitates, which then will cause impurities around grain boundaries. The Intergranular corrosion includes Exfoliation which happens in many industrial environments, and particularly aluminium alloys.

**Dealloying Corrosion:** in this type of corrosion active metal is removed from the alloy by selective corrosion. This type of corrosion can be avoided by alloy substitution.

**Enviromentally assisted cracking:** this type of corrosion can cause cracks due to the stress experienced and this is called Stress corrosion cracking (SCC). It

occurs frequently in engineering structures. This type can cause corrosion fatigue which can be best explained as the metal being under a cyclic stress. This type of corrosion also includes hydrogen damage which can deteriorate the mechanical properties of a metal. All these environmental situations can lead to accelerated crack formation and propagation of the metal.

## 2.7 Tribocorrosion

Tribocorrosion is the study of the combined effect of wear and corrosion [133]. Tribocorrosion includes the combination of chemical and mechanical interaction, where corrosion is caused by electrochemical reactions whilst wear is the mechanical part when there is sliding or rubbing on the surface. From the interactions of wear and corrosion it can be seen that there is a close relationship, meaning that the incensement of corrosion will increase wear, and wear will accelerate corrosion. The interactions depends on the load and the structure of the tribo-system [134]. Figure 2.13 below shows the process of surface degradation and how mechanical and chemical actions combined to become tribocorrosion.

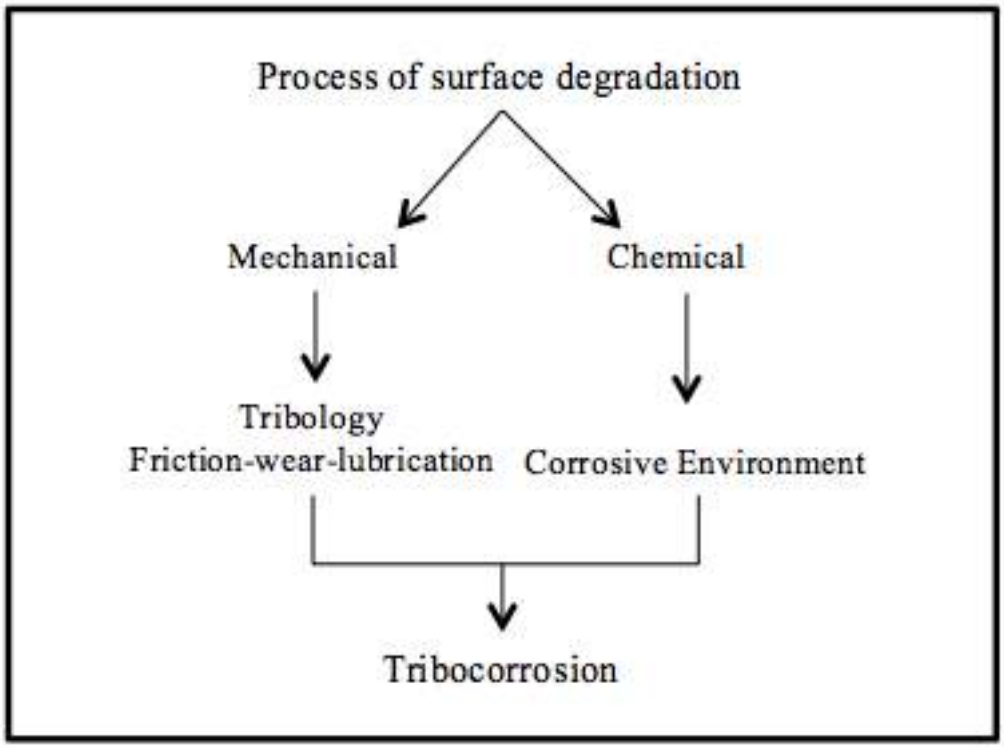


Figure 2.13: process of surface degradation

### 2.7.1 Tribocorrosion forms and Mechanisms

Tribocorrosion normally involves sliding contact in typical corrosive environments. This situation can be seen in many of today's applications such as hip and knee joints replacements, moving engine components, electromechanical machines and in plumbing. It can be noticed that cases such as hip and knee joints (artificial joints) and dental implants or in other words implantation in human body in general has been studied. Tribocorrosion have been listed under two different categories [133][135][136]:

- Tribocorrosion in living systems.
- Tribocorrosion in industrial systems.

Similar to corrosion, tribocorrosion can take different forms, depending on the contact mode such as sliding, fretting or rolling. Tribocorrosion forms are as followed:

- **Abrasion;** Rolling, grooving and sliding.
- **Erosion;** Cavitation erosion, liquid droplet and solid particle.
- **Fretting.**
- **Tribo-oxidation.**

Tribocorrosion can be caused by two body contacts or even three body contacts, and the relative motion can be in both direction or unidirectional such as in the case of pin sliding on a disk. On the other hand when fretting is involved, a special type of contact is defined as small magnitude motion. Rolling elements also experience tribocorrosion specifically in the case of ball bearings. One of the most important cases is erosion, which causes the attack by the combination of both mechanical and chemical actions, especially in plumbing pipes and pumps [137][138][139].

### 2.7.2 Tribocorrosion process affecting factors

Tribocorrosion process can be affected in many different ways [140][141]; there are many factors that play a role in influencing tribocorrosion and these factors are listed as follows:

- Electrochemical parameters: the electrochemical side of tribocorrosion is very important because corrosion occurs by the help of the basic electrochemistry. Many scientists have been working on this aspect, but the scientist are divided into two categories: tribologists and electrochemists. While tribologists are working on surface oxidation and mechanical wear, electrochemists are concentrating on the study of surface scratching on re-passivation kinetics. In this respect there are many parameters that can be considered such as corrosion resistance, the growth of passive films and active dissolution [142][143][144][145].

- Environment: environmental variables play a very important role in the science of tribocorrosion, because the electrolyte determines the surface state, passivity and activity of the surface which will change the mechanisms of corrosion and tribocorrosion.

- Material: the properties of materials play a very important role in tribocorrosion. Properties such as the yield strength, ductility, roughness and hardness are relevant. However the link between these properties and tribocorrosion is unclear. A lot of materials rely on a thin oxide passive film to resist corrosion, but this film can be removed by mechanical wear, which will cause a charge transfer at the interface and the film will be damaged depending on thickness of the film and the mechanical load [137][145][146][147].

- Operating parameters; the force applied and the type of contact whether its sliding, rolling or fretting, can affect the tribocorrosion of a metal for a given environment. However some other factors can affect the operating system such as the velocity of sliding and also the motion type such as circular motion. One important parameter is the size of the contacting bodies and vibrations, for example in fretting corrosion, there is small oscillations happening in the corrosive environment [137][146][148][149].

### 2.7.3 The Mathematical approach

Under conditions of tribocorrosion, the total material removal rate cannot be considered as the sum of mechanical wear and corrosion, because both wear and corrosion affect each other. The combination of such effect was termed corrosion-wear synergism, introduced by Watson [150], as represented in equation 2.11 [17].

$$V_t = V_w + V_c + V_s \tag{2.11}$$

Where $V_t$ is the total volume of removed material, $V_w$ and $V_c$ are the material's lost volume due to mechanical wear and corrosion respectively, whereas $V_s$ is the volume loss due to the combination effect of wear and corrosion. The testing of both properties of corrosion and pure wear of material cannot be monitored separately. However this calculation gives a small clue to the process of tribocorrosion mechanism and to define the wear caused from the combination of wear and corrosion.

On the other hand many researchers use another mechanistic approach in tribocorrosion study [133][143]. This approach considers that sliding is actually combined with corrosion to cause two types of mechanisms as shown in equ 2.12 [143].

$$V_{total} = V_{chemical} + V_{mechanical} \tag{2.12}$$

Where $V_{chemical}$ is chemical wear caused by accelerated corrosion due to the sliding action. $V_{mechanical}$ is the mechanical wear which may be affected by corrosion. This process can be best explained when the metal is exposed to a corrosive environment and experienced mechanical contact. By combining these two mechanisms, the total lost volume $V_{total}$ can be determined. Both mechanical wear and accelerated chemical wear affect each other, and the volume wear rate is affected by many variables such as speed and load.

## 2.8 Limitations of previous achievements

The current research of thermal oxidation (TO) and pack carburising (PC) of zirconium is limited due to many reasons:

- Previous achievements did not include optimising thermal oxidation or pack carburising processes. However, in this research an investigation of different effects has been done for both techniques such as temperature, time and roughness.

- In terms of exploring the feasibility of pack carburising, there is not many achievements to investigate the pack carburising of zirconium and its impact on tribological properties. In this research pack carburising has been investigated in depth and many effects has been processed including the effect of pack composition.

- The current research does not include deep characterisation of the structure and the properties of surface engineered zirconium. Therefore it is necessary

and timely to have a detailed study on process optimisation of thermal oxidation of Zr and on carburising of Zr, and further to study the structure and properties of surface engineered Zr for general engineering and biomedical application.

- Previous achievements did not include a comparison study between surface engineered zirconium and surface engineered titanium. In this research a deep investigation was done to compare surface engineered zirconium with titanium and to identify its application potentials in biomedical and general engineering sectors.

# Chapter 3

# Methodology and Experimental Procedures

## 3.1 Material and Sample Preparation

In this research all tests were done by using commercially pure zirconium grade 2 (99.2%) see table 3.1. Pure zirconium was used to avoid the complex effect of other alloying elements on thermal oxidation. Zirconium plates were received from Goodfellow Cambridge Limited and were cutted into specimens of 15mmx18mmx1mm sizes.

The samples were then ground using SiC grinding papers from P120 to P1200 grades. After grinding the samples were polished using $6\mu m$ and $1\mu m$ diamond polishing. Finally methanol was used to clean the samples ultrasonically for about 10 minutes.

In another series of experiments, different material surface finishes were prepared before thermal oxidation, by grinding the sample to P600, P1200 grades, and $1\mu$m polish; respectively. The initial surface finish was measured by a profilometer and the roughness parameter values are listed in Table 3.2.

Table 3.1: Chemical composition of CP-Zr samples

| Element | Total Percentage(%) |
|---|---|
| O | 0.16 |
| N | 0.025 |
| C | 0.05 |
| H | 0.005 |
| Fe | $\leq$0.2 |
| Hf | >0.2 |
| Zr | Rest |

Table 3.2: Initial surface finish after grinding/polish

| Preperation | $R_a(\mu m)$ | $R_q(\mu m)$ | $R_t(\mu m)$ |
|---|---|---|---|
| P600 | 0.26 | 0.34 | 2.4 |
| P1200 | 0.2 | 0.25 | 1.5 |
| Polished | 0.12 | 0.16 | 1.2 |

## 3.2 Thermal Oxidation

Thermal oxidation (TO) in this research was done in a CWF 110 thermal furnace manufactured by Carbolite and it was done at different temperatures of 550,600,625,650 and $700^oC$ and for a duration of 6 hours(360 minutes). After the process of thermal oxidation the samples were cooled down to normal room temperature in the furnace. This type of cooling is called furnace cooling (FC). Normally it takes from 6-7 hours to cool down from $700^oC$ to $100^oC$. Table 3.3 and Table 3.4 shows all the different conditions used during this project.

Two series of experiments were conducted. Firstly, the effect of oxidation temperature was studied by varying the TO temperature from $550^oC$ to $700^oC$ for a fixed TO time of 6 h, with the purpose to find the optimal TO temperature (Table 3.3). Secondly, the effect of TO time was investigated by varying the oxidation time from 1 h to 72 h at the optimal temperature of $650^oC$ (Table 3.4)

Table 3.3: Thermal oxidation conditions used for the first series of experiments

| Temperatures($^oC$) | Time (h) | Cooling Method |
|---|---|---|
| 550 | 6 | Furnace Cooling |
| 600 | 6 | Furnace Cooling |
| 625 | 6 | Furnace Cooling |
| 650 | 6 | Furnace Cooling |
| 700 | 6 | Furnace Cooling |

Table 3.4: Thermal oxidation conditions used for the second series of experiments

| Time(h) | Temperatures ($^oC$) | Cooling Method |
|---|---|---|
| 1 | 650 | Furnace Cooling |
| 6 | 650 | Furnace Cooling |
| 12 | 650 | Furnace Cooling |
| 24 | 650 | Furnace Cooling |
| 72 | 650 | Furnace Cooling |

## 3.3 Pack Carbuising

Pack carburising (PC) in this research was done in a CWF 110 thermal furnace manufactured by Carbolite and it was done at different temperatures of 825,880,925 and 980$^oC$ and for durations of 3, 10, 20 and 40h hours. After the process of pack carburising the samples were cooled down to normal room temperature in the furnace. This type of cooling is called furnace cooling (FC). Normally it takes from 10-12 hours to cool down from 980$^oC$ to 100$^oC$. Table 3.5 shows all the different conditions used during this period of the project.

Table 3.5: Pack carburising conditions used

| Temperatures($^oC$) | Time (h) | Cooling Method |
|---|---|---|
| 825 | 3,10,20,40 | Furnace Cooling |
| 880 | 3,10,20,40 | Furnace Cooling |
| 925 | 3,10,20,40 | Furnace Cooling |
| 980 | 3,10,20,40 | Furnace Cooling |

To effect pack carburising, some procedures must be followed strictly. These involve the use of carburising compounds (powders), packing the compounds in a container together with the samples to be treated, sealing the container to achieve air-tight, and heating the container to the carburising temperature, and holding at that temperature for the preset treatment time. Details of these procedures are given in Section 8.1.

## 3.4 Oxidised and carburised Sample Characterisation

After thermal oxidation the samples were characterised using several experimental and analytical techniques, as described below.

### 3.4.1 Weight gain measurement and calculation for oxidised samples

The measurement of weight gains helps to find the oxygen uptake by the samples and the thickness of oxidise layer in a theoretical way. This will be compared to the thickness measured through ball cratering technique and cross-sectional metallography. The measurements and calculations steps are as follow:

- First step is measuring the sizes of the samples to work out the total surface area exposed to thermal oxidation.
- Second step is measuring the weight of the sample before oxidation($w_o$) and the weight after oxidation($w_A$) in order to get the weight gain($\Delta w$) as expressed in equation 3.1.

$$\Delta w = w_A - w_o \tag{3.1}$$

- Third step is to find the Area ($A_o$) by using equation 3.2. This requires height(h) and width(w) and thickness of the sample(t) in centimetres(cm).

$$A_o = (h \times w \times 2) + 2(h + w) \times t \tag{3.2}$$

- Fourth step is finding the mass fraction of oxygen($O_w$) in $ZrO_2$ as shown in equation 3.3.

$$O_w = \frac{2 \times w_o}{w_{Zr} + 2 \times w_o} = \frac{2 \times 16}{91 + 2 \times 16} = 0.26 \tag{3.3}$$

  where $w_o$ and $w_{Zr}$ are the atomic weights of oxygen and zirconium, respectively.

- Finally to find the thickness of oxidise layer($h_{ol}$) by Equation 3.4. The equation requires the density of $ZrO_2(\rho)$ $5.68\frac{g}{cm^2}$, weight gain($\Delta w$) and the area($A_o$).

$$h_{ol} = \frac{\Delta w}{A_o \times \rho \times O_w} \tag{3.4}$$

The calculation in 3.4 is based on the assumption that all oxygen gained by the sample during thermal oxidation is used to form $ZrO_2$ layer. This deviates from reality since it is known that thermal oxidation produces two layer structure on zirconium: a $ZrO_2$ layer on the surface and an oxygen diffusion zone (ODZ) below the surface. Thus, not all oxygen gained is in the $ZrO_2$ layer, and some oxygen atoms diffuse inwards to form the ODZ. Therefore the calculated $ZrO_2$ layer thickness ($h_{ol}$) overestimate the actual oxide layer thickness. The degree of deviation depends on the amount of oxygen diffusing to ODZ and depends on thermal oxidation processing temperature.

### 3.4.2 Ball Cratering

Ball Cratering is a technique mainly used to measure the thickness of thin coatings [151][152]. This is done by using a large bearing steel ball with a diameter of 25.4mm. This ball rotates on the surface of the sample with the use of diamond paste ($1\mu m$). The rotation speed can be controlled between 10 and 120 rpm. As the ball rotates, it will gradually penetrate the coating on the surface producing a ball crater on the surface, revealing the coating and the substrate. An optical microscope is then used to measure the dimensions of the ball crater as shown in figure 3.1. This will make it easy to measure the thickness of the coating by using equation 3.5.

$$t = \frac{x \times y}{D} \tag{3.5}$$

where

t = the coating thickness, D = the diameter of the metal ball, x = the thickness of the visible part of the film, y = the diameter of the crater.

In the present work, a laboratory-made ball cratering machine was used. To produce a ball crater revealing the oxide or carbide layer, 10-20 minutes of ball rotation was required depending on the oxide layer thickness.

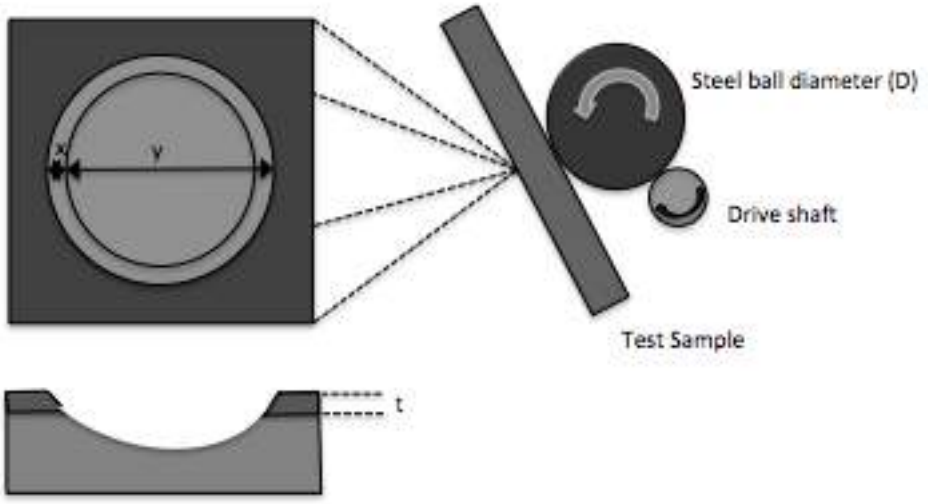


Figure 3.1: Ball crater technique for coating thickness measurements

### 3.4.3 Surface hardness measurement

In order to evaluate the hardening effect arising from thermal oxidation or pack carburising, microhardness testing was conducted on the oxidised or carburised surface under various indentation loads. ZHV microhardness tester was used in this work. This machine uses a Vickers indenter with a square based diamond pyramid. The loads applied were from 0.025kg to 0.5kg. The indentation sizes created on the surface were measured and hardness was calculated using equation 3.6, with reference to figure 3.2.

$$VHN = \frac{P \times 2Sin(\frac{136}{2})}{{d_{12}}^2} \tag{3.6}$$

Five measurements were performed under each load to obtain the average value. Hardness profiles below the surface in the cross-sections of the TO and PC samples were also measured using an indentation load of 0.025 kg. This allows for the assessment of the hardening effect in the subsurface across the diffusion zone.

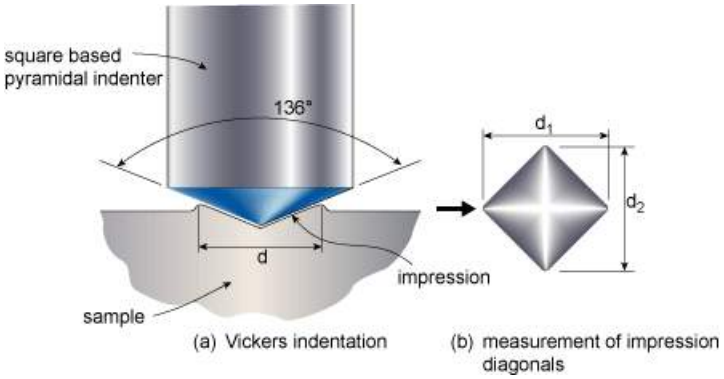


Figure 3.2: Process of Microhardness [9]

### 3.4.4 Surface roughness measurments

The surface profiles of the untreated and TO and PC treated surfaces were measured using a contact mode profilometer, Mitutoyo SJ-400 as shown in figure 3.3 [10].


Figure 3.3: Mitutoyo SJ-400 profilometer [10]

The surface roughness parameters were derived from the measurements repeated three times. The same technique was also used to measure the surface profile cross the wear tracks, which was then used to evaluate the wear volume, as detailed in section 3.6.

### 3.4.5 XRD Analysis

X-ray diffraction is known as non destructive testing tool to analyse the crystal structure of materials. This technique includes radiation diffraction by the material crystalline, which is dependant on Bragg's law [17][153][154]. The law of Bragg states that there is a relationship between the maximum diffraction position and the spacing of the atomic plane. This explains that x-rays reflects from the surface of the material will travel less distance than the x-rays that reflects from the atomic plane within the crystal, and the distance travelled is depending on the spaces between layers. Equation 3.7 expresses the law of Bragg[155].

$$\lambda = 2dsin(\theta) \tag{3.7}$$

where

$\lambda$=wave length of x-ray, $\theta$= half of the diffraction angle between the crystal plane and the x-ray, $d$= the spacing between the atomic planes.

Since De Montfort University initially did not have an x-ray diffraction machine till third year (2017), for oxidised samples the XRD was conducted by Dr.Bertram Mallia of the university of Malta, using Cu-$k_\alpha$ radiation. For carburised samples the XRD was conducted at De Montfort university. After XRD measurement, the diffraction spectra were compared with standard ones from pure Zr, $ZrO_2$ and $ZrC$ to identify the phase composition on the oxidised or carburised samples.

### 3.4.6 Cross sectional sample preparation

To facilitate microscopic examination of the subsurface structure and measurements of layer thickness, cross-sectional metallography samples were prepared following standard procedures. These include sectioning the TO and PC samples, mounting the cross-sectioned samples in Bakelite using the hot mounting machine, then grinding the mounted samples using SiC papers from P120 to P1200 grades, followed by diamond polishing down to the 1 micron finish. This produced a polished sample with a mirror-like surface to allow for the examination of the layer structure.

### 3.4.7 Optical microscopic examination

A standard optical microscope (Nikon) was used to examination the TO and PC surfaces, the cross-sections and the wear tracks. TO and PC layer thicknesses were

also measured from the cross-sectional samples using optical microscope. The magnifications used in examination are typically 40x to 1000x.

### 3.4.8 Scanning electron microscopic examination

The Leica S430 field emission scanning electron microscope was used to examined further details of the TO and PC samples and the wear track morphology and composition. The SEM is equipped with Energy dispersive X-ray microanalysis (EDX) facilities to allow for chemical composition analysis, including spot analysis, line analysis and area mapping.

### 3.4.9 Glow discharge optical spectrometry (GDOS)

Glow discharge optical spectrometer (GDOS) has found increasing use in chemical composition profiling analysis of surface coatings and surface treated materials [156]. It uses argon ions to sputter the sample surface, releasing atoms from the surface material. The sputtered material is then excited in plasma charge of low pressure. Light emissions from the excited plasma is then analysed with reference to standard spectra for individual elements. Continuous sputtering of the sample allows for the analysis layer by layer. In this work, the GDOS analysis was conducted at the University of Birmingham.

### 3.4.10 Scratch test

Scratch test has been widely used to measure the adhesion strength of coating systems [157][158][159]. It involves sliding a standard diamond tip over the coating surface under controlled load and speed conditions. The critical load at which the coating starts to debond from the substrate is used as a measure of the adhesion strength. In this work, a Rockwell diamond tip with a radius of 200 microns was used. The applied scratch load ranged from 1 N to 30 N. Under each load, the tip slide over the sample surface over a distance of 5 mm. After each test, the resultant scratch was examined microscopically to assess failure modes and the critical failure loads of the oxide layer. Only the TO samples were tested, while the PC samples were not tested due to the large thickness of the carburised layers.

## 3.5 Friction and Wear Testing

Friction and wear testing was mainly done in this study by a pin on disk (POD) tribometer, provided from Teer Coatings Ltd. This test involves unidirectional sliding of the sample (disk) against a stationary ball (pin) under controlled load and speed conditions. Some tests (in Chapter 7) were also conducted in a laboratory scale reciprocating wear test machine. These tests help in finding anti-wear performance of each sample and finding the wear rate by a sliding contact. In the POD configuration, the sample was placed on a rotating holder and the sample was rotating against an alumina ball(grade 5 $Al_2O_3$) produced by Trafalgar Bearings Ltd. This rotating motion resulted in a circular wear track on the surface of the sample. Figure 3.4 shows a schematic diagram of the machine used and how the wear track was generated.

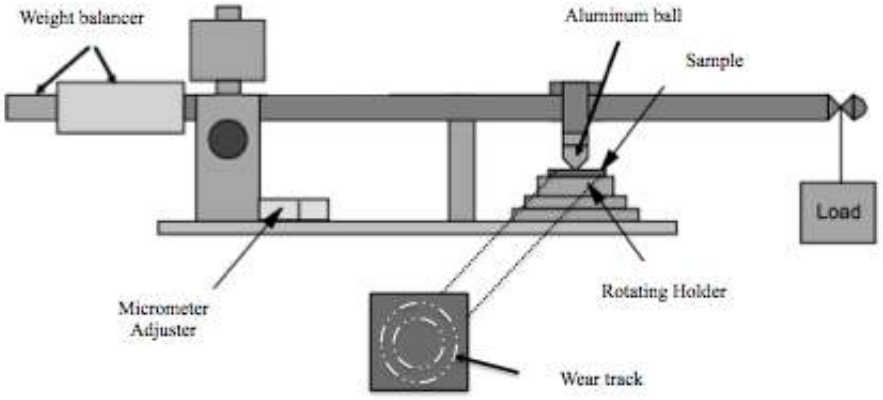


Figure 3.4: Friction and wear POD tribometer

There are many factors that can control friction and wear testing. These variable factors are:

- **Load**: The load was applied on the end of the beam opposite to the weight balancer and was controlled by weights on the shape of small disks. The loads used in this research are 1N, 2N, 5N and 10N for oxidised samples, and 5N, 10N, 20N and 40N for carburised samples.
- **Sliding speed**: controlling the sliding speed is very important, which is measured by revolutions per minute (rpm). The sliding speed in this research is 60rpm.

- **Distance**: The sliding distance($d$) is an important factor and it can be controlled by using both time($t$), frequency($f$) and the diameter of wear track($D_{wt}$). Equation 3.8 is used to find the distance.

$$d = fD_{wt}\pi t \tag{3.8}$$

- **Time**: The time of sliding started when the load was applied. The time was measured in seconds and the common time used in this research was 1 hour (3600s). Time will be changed for some experiments.

- **Contact pressure**: the contact pressure changes from situation to another depending on the two contacting materials in terms of the size and type of material and applied load. In this research the two contacting materials are grade 2 Zirconium and grade 5 Alumina ball($Al_2O_3$). Under various loads for this ball-on-flat contact, the contact pressures are calculated as follows, and the results are summarised in table 3.6.

To calculate the maximum pressure ($P_{max}$), two steps must be done:

- Finding $E_r$ by using equation 3.9 [8].

$$\frac{1}{E_r} = \frac{1-{v_1}^2}{E_1} + \frac{1-{v_2}^2}{E_2} \tag{3.9}$$

Therefore, by replacing poissons ratios ($v_1, v_2$) and youngs modulus ($E_1, E_2$) for Zr and $Al_2O_3$, respectively,

$$\frac{1}{E_r} = \frac{1-0.255^2}{375\times10^9} + \frac{1-0.26^2}{138\times10^9} = 9.25\times10^{-12}$$

$$E_r = \frac{1}{9.25\times10^{-12}} = 108.11GPa$$

- The next step is replacing the values of $E_r$, load applied(w) and radius of the ball(R) in equation 3.10 [17].

$$P_{max} = 0.5784\times\sqrt[3]{\frac{w{E_r}^2}{R^2}} \tag{3.10}$$

Therefore, for 1N.

$$P_{max} = 0.5784 \times \sqrt[3]{\frac{1 \times 108.11 \times 10^{9^2}}{(4 \times 10^{-3})^2}} = 520.91 MPa$$

Table 3.6: Initial contact pressure: 8mm diameter $Al_2O_3$ ball on Zr flat

| Applied load | $P_{max}$(MPa) |
|---|---|
| 1N | 520.91 |
| 2N | 656.31 |
| 5N | 890.75 |
| 10N | 1122.27 |

After friction and wear testing, the wear tracks were analysed using several techniques including:

1. Microscopic experimentation by optical and scanning electron techniques to examine wear track morphology and measure wear track dimensions.
2. Ball cratering on wear track to reveal the actual wear depth and examine deformation and cracking behaviour of the sample.
3. Wear track profile measurements by profilometer.

## 3.6 Wear Analysis

The wear rate can be measured and calculated using a few steps as follows:

- First step is by using a profilometer (model SJ-400 produced by Mitutoyo) to measure the cross-sectional profile of the wear track. The wear track profile was taken in four directions for each wear track.
- Second step is using the numerical integration method to calculate the area of the cross section(A) of each wear track, as shown in figure 3.5. The equation 3.11 numerically calculated the area of a small strip in the wear track profile. Equation 3.12 adds all areas together by integration to find the total area of the cross-section.

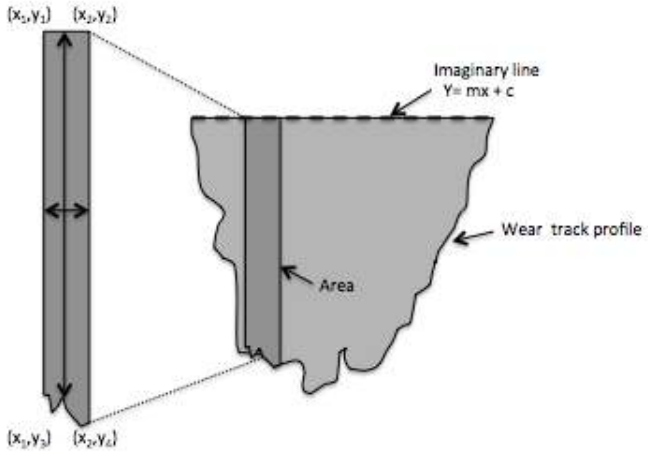


Figure 3.5: Finding the cross sectional area for the wear track

$$A' = (x_2 - x_1) \times (\frac{(y_1 - y_3) + (y_2 - y_4)}{2}) \tag{3.11}$$

$$A = \int A' dx \tag{3.12}$$

- Third step involves multiplying the cross sectional area (A) by the diameter of wear track($d_{wt}$) as showed in equation 3.13, in order to get the volume of wear track (V), i.e. the volume of removed material.

$$V = A \times d_{wt} \tag{3.13}$$

- Finally, the last step is using the wear track volume(V) to find the actual total material lost rate (TMLR) from the surface, by dividing V by the distance of sliding ($D_s$) as shown in equation 3.14.

$$TMLR = \frac{V}{D_s} \tag{3.14}$$

This provides a measure of material loss(wear rate) in terms of $mm^3$ per meter of sliding

# Chapter 4

# Effect of Oxidation Temperature and Initial Surface Roughness on Tribological Behaviour of Thermally Oxidized Pure Zirconium

Thermal oxidation (TO) is an effective surface engineering technique to harden the surfaces of zirconium (Zr) and its alloys for improvement in friction and wear performance. Unlike TO of titanium where the rutile oxide layer formed tends to be fragile and flake off easily when it is thicker than about 2 microns, TO of zirconium can produce a thick and adherent $ZrO_2$ layer without the danger of flaking off. However, an excessively thick ceramic $ZrO_2$ layer can lead to embrittlement of Zr surface and deteriorate its tribological properties. In the present investigation, the effect of TO temperature and surface roughness on the tribological properties of pure Zr was investigated. TO was carried out at temperatures between $550^oC$ and $700^oC$ to achieve $ZrO_2$ layer thickness ranging from 2 $\mu$m to 9 $\mu$m. Surface roughness before TO was varied between 0.12 $\mu$m ($R_a$) and 0.26 $\mu$m ($R_a$). Tribological tests under unlubricated sliding conditions demonstrated that TO was effective in reducing friction and wear rate of Zr and once the $ZrO_2$ layer maintained its integrity with the substrate, TO temperature had no significant effects on friction and wear. However, under high contact loads, the $ZrO_2$ layer tended to suffer from cracking in the wear track. The thinner layer produced at $550^oC$ suffered from cracking at a small load. Although increasing $ZrO_2$ layer thickness helped to increase load bearing capacity, cracking was unavoidable at high contact loads. It was also found that roughening the surface before oxidation helped to reduce the tendency of the oxide layer towards cracking during sliding.

## 4.1 Introduction

As mentioned in Chapter 1, thermal oxidation (TO) is an effective surface engineering technique to harden the surfaces of zirconium (Zr) and its alloys for improvement in friction and wear performance. Unlike TO of titanium where the rutile oxide layer formed tends to be fragile and flake off easily when it is thicker than about 2 $\mu$m [15], TO of zirconium can produce a thick and adherent $ZrO_2$ layer without the danger of flaking off, provided that the oxidation breakaway regime is avoided [25] [26].

Although oxidised zirconium (OxZr) has recently been introduced as an alternative bearing in total joint arthroplasty for artificial hip and knee joints [16][19][31][32], most of the published reports on clinic use of OxZr is based on the commercial process, OXINIUM (Smith and Nephew Inc.), which produces an $ZrO_2$ layer about 5 $\mu$m thick and an ODZ of 1.5 to 2 $\mu$m thick on Zr-2.5 wt%Nb alloy. The thicknesses of the oxide layer and ODZ, which can be controlled easily by TO temperature and time, are expected to have significant effects on the tribological and load bearing properties of OxZr. However, information in this respect is limited in open literature.

In the present investigation, the effect of TO temperature and initial surface roughness on the tribological properties of pure Zr was investigated by varying the initial TO temperature from $550^oC$ to $700^oC$ to produce $ZrO_2$ layer thickness ranging from 2 $\mu$m to 9 $\mu$m, and varying the surface roughness before TO from 0.12 $\mu$m ($R_a$) to 0.26 $\mu$m ($R_a$). The obtained results are presented and discussed in this chapter.

## 4.2 Material and Methods

The substrate material used is commercially pure zirconium (CP-Zr) grade 2 (99.2%) with the following composition (wt%): 0.16O, 0.025N, 0.05C, 0.005H, 0.2Fe, 0.2Hf and Zr (rest). The material (supplied by Goodfellow UK Ltd) was received in a sheet form of 1 mm thickness and was cut into sample of 20 mm x 15 mm dimensions. In the first series of experiments, the samples were manually ground using SiC grinding papers and finished by 1 $\mu$m diamond polishing. These samples were then thermally oxidized (TO) at various temperatures. In the second series of experiments, two different original surface finishes were prepared by grinding to P600 and P1200 SiC grinding paper, resulting in surface roughness ($R_a$) of 0.26 $\mu$m and 0.2 $\mu$m, respectively. These samples were then subjected to thermal oxidation treatment.

In the first series of experiments, thermal oxidation (TO) of polished samples was carried out in an air furnace (CWF 1100 produced by Carbolite) at temperatures of 550, 600, 625, 650 and $700^oC$, for duration of 6h. After TO, the samples were cooled down in the furnace to room temperature. In the second series of experiments, the samples with rougher surface finishes were subjected to thermal oxidation at $650^oC$ for 6 h.

The masses of the samples were measured before and after TO treatment using a balance accurate to 0.1 mg. The thickness of the oxide layer was then calculated theoretically assuming all gained oxygen atoms are consumed in forming a dense stoichiometric $ZrO_2$ layer, see section 3.4.1. The actual thicknesses of the oxide layer and oxygen diffusion zone (ODZ) were measured by the ball-cratering technique and from metallographic cross-sections, discussed in Section 3.4.2, 3.4.6 and 3.4.7.

X-ray diffraction (XRD) was conducted using Cu-$K_{\alpha 1}$ to identify the phases of thermal oxidized samples. Surface hardness was conducted using Indentec ZHV microhardness tester at various loads of 0.025-0.5kg. Optical and scanning electron microscopes were used to examine the morphological and structural features of the samples.

Scratch testing was conducted on the oxidised surfaces of the samples using a Rockwell C diamond stylus under various loads between 5-50N (steps of 5N). Optical microscope was used to examine the stages of scratch and show the characteristics of the samples after scratch testing.

Dry sliding friction and wear testing was conducted using a pin-on-disk tribometer (Teer Coatings Ltd). During the test, the sample was rotating against an alumina ball (Grade 25 $Al_2O_3$) with 8 mm diameter (produced by Trafalgar Bearings Ltd). The tests were conducted at room temperature ($22^oC$) without lubrication, using different contact loads of 1, 2, 5 and 10N, at a constant rotation speed of 60rpm for duration of 3600s. During the test, the coefficient of friction (COF) was recorded continuously using the computer data acquisition system. To measure the wear rate and wear volume, Stylus profilometer was used to measure the wear track profile at 4 different locations and the average value was taken. Wear volumes were then evaluated as detailed in Section 3.4.

After tribological testing, optical microscope and scanning electron microscope (SEM) was used to view the morphology of the worn surfaces. Efforts have been made by making a ball crater on the wear track to reveal the actual wear depth and any deformation and cracking behaviour below the wear surface.

## 4.3 Results and Discussion

### 4.3.1 Morphological characterization of thermally oxidized specimens

Fig. 4.1a shows a part of a ball crater made on the $650^oC$-oxidised surface, revealing clearly the oxide layer on the surface and the substrate beneath. The oxide layer has a black shinny appearance and adheres well with the substrate. The thickness of the oxide layer was measured from the ball crater for each oxidised sample. Although the oxygen diffusion zone (ODZ) can be faintly seen in the ball crater, its thickness could not be measured confidently. Thus cross-sections of the samples were prepared metallographically, as shown in Fig. 4.1b. Clearly, each oxidised sample comprises an oxide layer at the surface and an ODZ beneath. The thickness of the oxide layer measured in the cross-section is similar to that measured by the ball cratering technique. The ODZ is relatively thin, even thinner than the oxide layer in all cases.

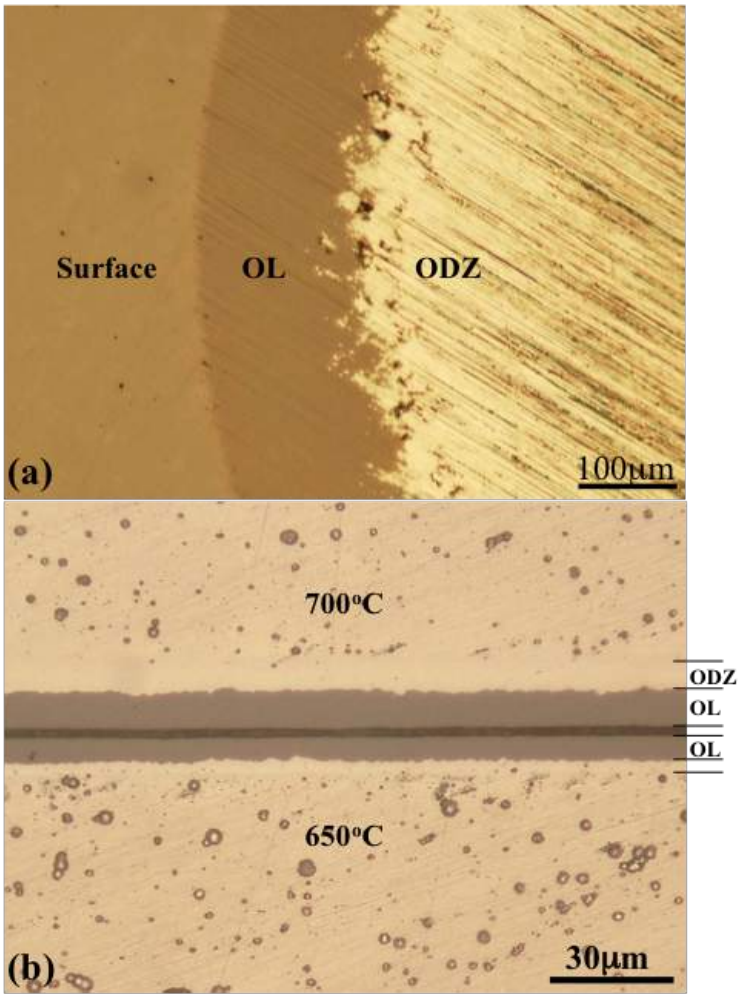


Figure 4.1: Microscopic images showing (a) part of a ball crater made on the $650^oC$ oxidised surface and (b) across sections of the $650^oC$ and $700^oC$ oxidised samples, revealing the oxide layer (OL) and the oxygen diffusion zone (ODZ) beneath. The metallographic sample in (b) was etched in 98% $H_2SO_4$.

The weight gain of the sample resulting from each TO treatment was measured by measuring the mass of the sample before and after the treatment. The thickness of the oxide layer was theoretically calculated from the weight gain based on the assumption that all the weight gain is due to oxygen uptake by the sample (ignoring possible uptake of nitrogen from air) and all the oxygen atoms are consumed in forming the oxide layer (ignoring the ODZ). The calculated results are plotted in Fig. 4.2 as a function of TO temperature, together with the measured oxide layer thickness. It can be seen that the measured oxide layer thickness increases smoothly with increasing temperature, which is expected for processes governed by thermal diffusion. The calculated oxide layer thickness slightly overestimates the actual

thickness at low temperatures (below $625^oC$) and deviates more significantly from the measured thickness at high temperatures. This is due to the formation of an ODZ which consumes some of the oxygen atoms gained by the sample. The higher the TO temperature, the larger the proportion of oxygen is consumed in forming the diffusion zone, as confirmed by the measured ODZ thickness. Below $625^oC$, the thickness of the ODZ is less than 2 microns. Similar values have also been reported by other investigators [14]. In order to achieve a reasonably thick ODZ, a higher TO temperature is required: at $700^oC$, the ODZ thickness is increased to 7 microns.

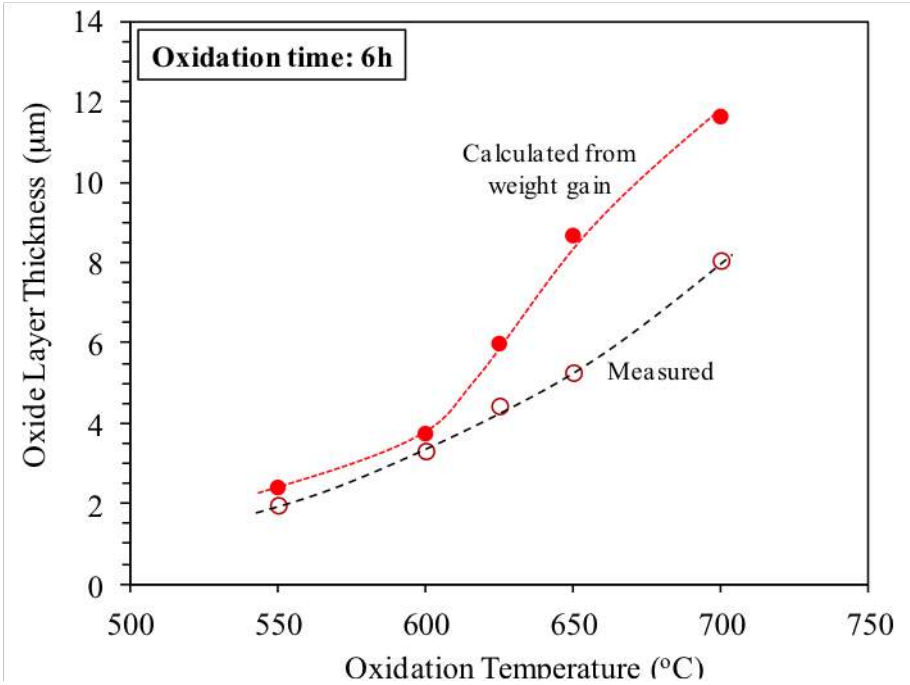


Figure 4.2: Comparison of calculated and measured oxide layer thickness as a function of oxidation temperature for 6 h treatment.

X-ray diffraction detects two phases, hexagonal close packed (hcp) $\alpha$-Zr and monoclinic dioxide $ZrO_2$, from the oxidised surfaces (Fig. 4.3). The intensity of the diffraction peaks from $\alpha$-Zr decreases and that from $ZrO_2$ increases with increasing TO temperature. This fact suggests that the surface layer is indeed a zirconium dioxide ($ZrO_2$) layer. As the oxide layer grows thicker at higher TO temperatures, X-ray becomes more difficult to penetrate to the underlying ODZ to produce high intensity diffraction peaks from $\alpha$-Zr.

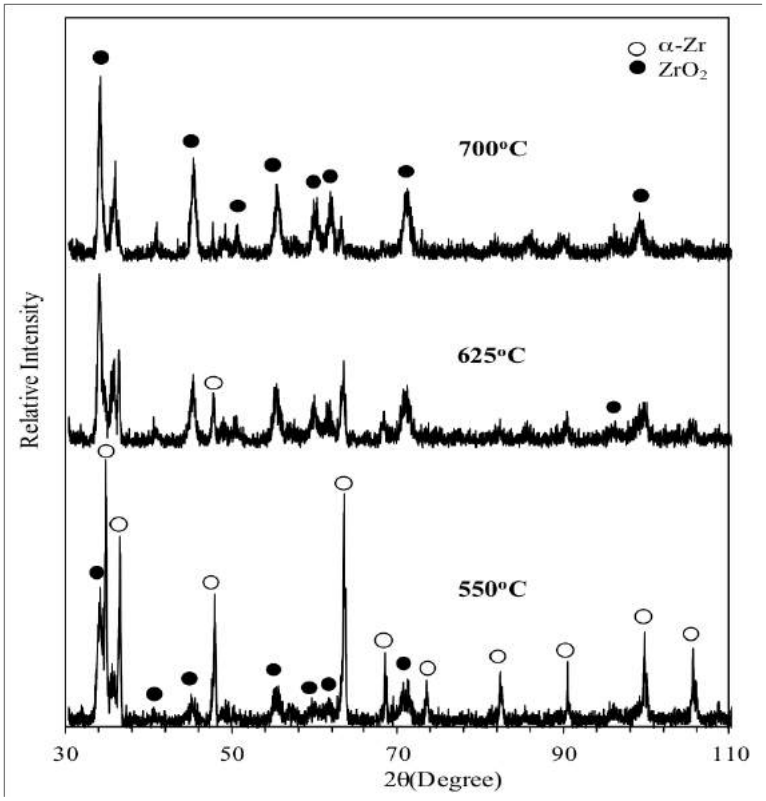


Figure 4.3: X-ray diffraction patterns generated from the oxidised samples, confirming the formation of monoclinic $ZrO_2$ layer on the surface. Cu-$K_\alpha$ radiation.

As a result of the formation of an oxide layer and ODZ, the surface hardness of CP-Zr is increased by several times (Fig. 4.4), from the base level about 200 HV for untreated CP-Zr to 750 HV-1300 HV for the oxidised samples. The measured surface hardness decreases with increasing indentation load, which can be accounted for by the increasing substrate effect as the indentation depth is increased. TO temperature has a significant effect on the hardening effect: the measured hardness at each load increases with increasing TO temperature. The enhanced load bearing capacity at higher TO temperatures is obviously derived from the increased oxide layer and ODZ thicknesses.

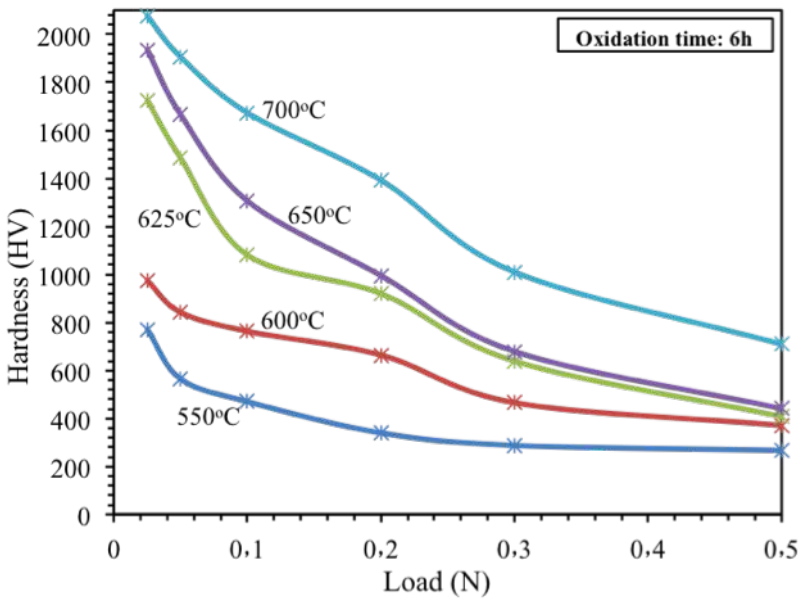


Figure 4.4: Surface microhardness as a function of indentation load for the oxidised samples.

In order to further characterise the oxidised samples, scratch tests are conducted on the oxidised surfaces using a Rockwell C diamond stylus under various loads. Fig. 4.5 shows typical scratch marks produced. On all oxidised samples, cracks are observed inside and outside the scratch mark at loads as low as 5 N. Cracking becomes more severe with increasing load. On the samples with thicker oxide layers, the chevron-type cracks tend to extend far beyond the scratch mark, indicating the high propagation rate of cracks in brittle $ZrO_2$. When a critical load is reached, failure of the oxide layer occurs in two different modes. The thinner oxide layers produced at $550^oC$ and $600^oC$ are failed first due to the penetration of the stylus through the oxide layer in the central region of the scratch mark, which then leads to the fracture of the oxide at the edges of the scratch mark (Fig. 4.5a). On the other hand, the thicker oxide layers always fail due to fracture at the edges of the scratch mark in association with the chevron-type cracks extended far beyond the scratch mark (Fig. 4.5b,c). The critical loads for the scratch failure of the oxide layers produced at various temperatures are summarised in Table 4.1. The critical load increases with increasing TO temperature, suggesting that a thicker oxide layer has better resistance to scratch failure. This agrees with the observations for many other ceramic coatings on soft substrates [157][160].

Table 4.1: Critical loads and signs appearance on scratch

| TO Temperature ($^oC$) | First crack | First sign of flaking |
|---|---|---|
| 550 | 3N (across) | 10N |
| 600 | 10N (across) | 15-20N |
| 625 | 5N (across) | 20N |
| 650 | 3N (outside track) | 20-25N |
| 700 | 5N (outside track) | 25N |

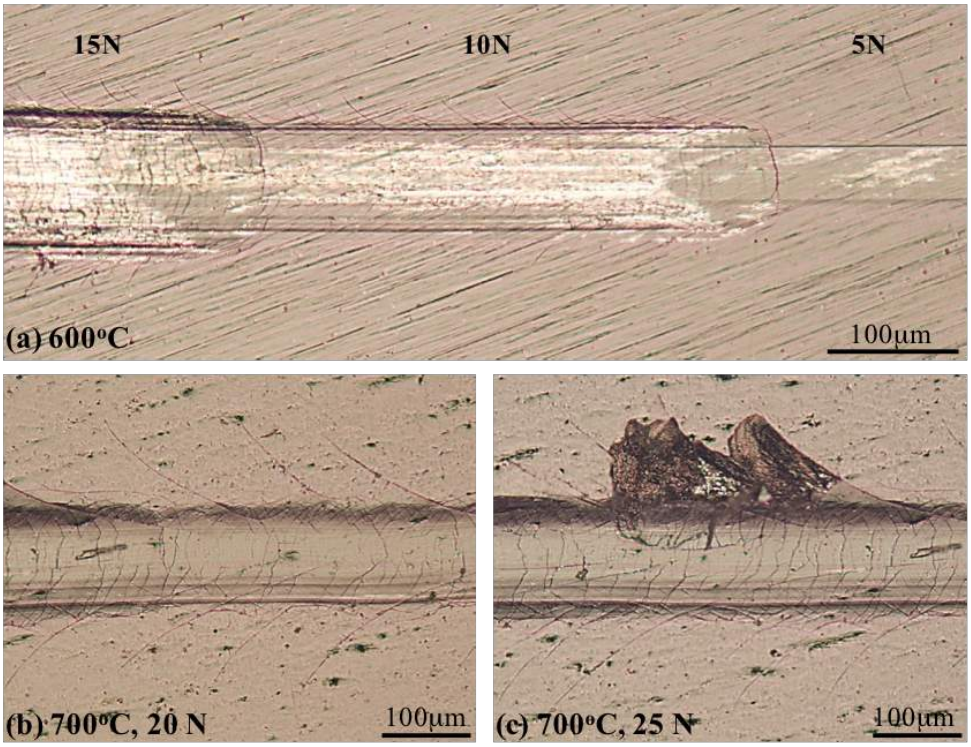


Figure 4.5: Microscopic images showing the scratch test scars on the $600^oC$ (a) and $700^oC$ (b and c) oxidised samples.

### 4.3.2 Effect of TO temperature on tribological behaviour

Fig. 4.6a shows the recorded friction curves at a contact load of 1 N for all test samples. The untreated sample shows very poor friction behaviour characterised by high and unstable friction with large frictional noises. TO is effective in improving the frictional behaviour of CP-Zr in that friction becomes smooth and the coefficient of friction (COF) is much reduced. The COF recorded varies with TO temperature and applied contact load. In Fig. 4.6b, the averaged COF values measured in three

repeated tests under each load are compared for all samples tested. The COF of the oxidised samples varies between 0.15 and 0.35 as compared to that between 0.5 and 0.6 for the untreated sample. Although no correlation is found between COF and TO temperature, a general pattern can be observed regarding the effect of load on COF. For each TO sample, the COF increases as the contact load is increased from 1 N to 5 N, and then decreases slightly at 10 N load. The increase in COF with load could be explained by the increased contact area between the slider and the oxidised surface, while the decrease in COF at 10 N could be related to the formation of cracks in the wear track, as discussed later. It should be pointed out that under the present test conditions, even under the highest load of 10 N, no failure and wearing-through of the oxide layer occurs. The results suggest that as long as the oxide layer maintains its integrity with the substrate, TO temperature has no significant effect on friction.

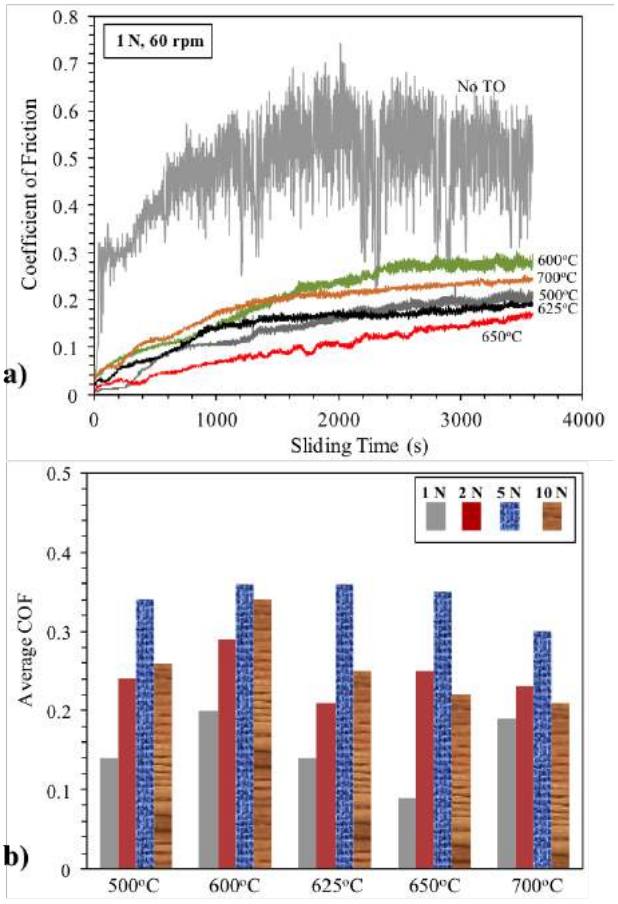


Figure 4.6: Recorded friction curves during dry sliding at 1 N load (a) and comparison of averaged coefficient of friction measured at various contact loads for the oxidised samples.

Microscopic examination shows that even under the smallest load of 1 N, the untreated sample suffers from severe metallic wear, characterised by plastic deformation, adhesion and delamination wear (Fig. 4.7). This explains the poor frictional behaviour experienced by the untreated sample (Fig. 4.6a). On the other hand, under light contact loads of 1 N and 2 N, only a few abrasion marks and asperity contact areas are observed in the wear tracks on the oxidised samples (Fig. 4.8a and b). The original fine polishing marks can still be clearly seen in the wear tracks. When the load is increased to 5 N, the wear track is widened and the contact area is increased with many abrasion marks (Fig. 4.8c). On the $550^oC$-oxidised sample, some fine cracks start to form at the edges of the wear track, but for the other oxidised samples no cracks were observed yet. However, when the contact load is increased to 10 N, cracks are observed in the wear tracks on all oxidised samples (Fig. 4.8d), mostly at the outside edge of the wear track which experiences higher sliding velocity than the inside edge under the unidirectional sliding condition.

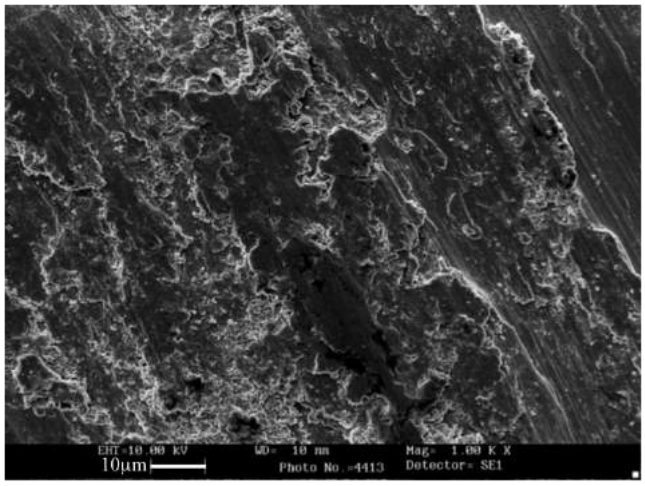


Figure 4.7: SEM image showing the morphology of the wear track produced on the un-oxidised sample at 1 N load.

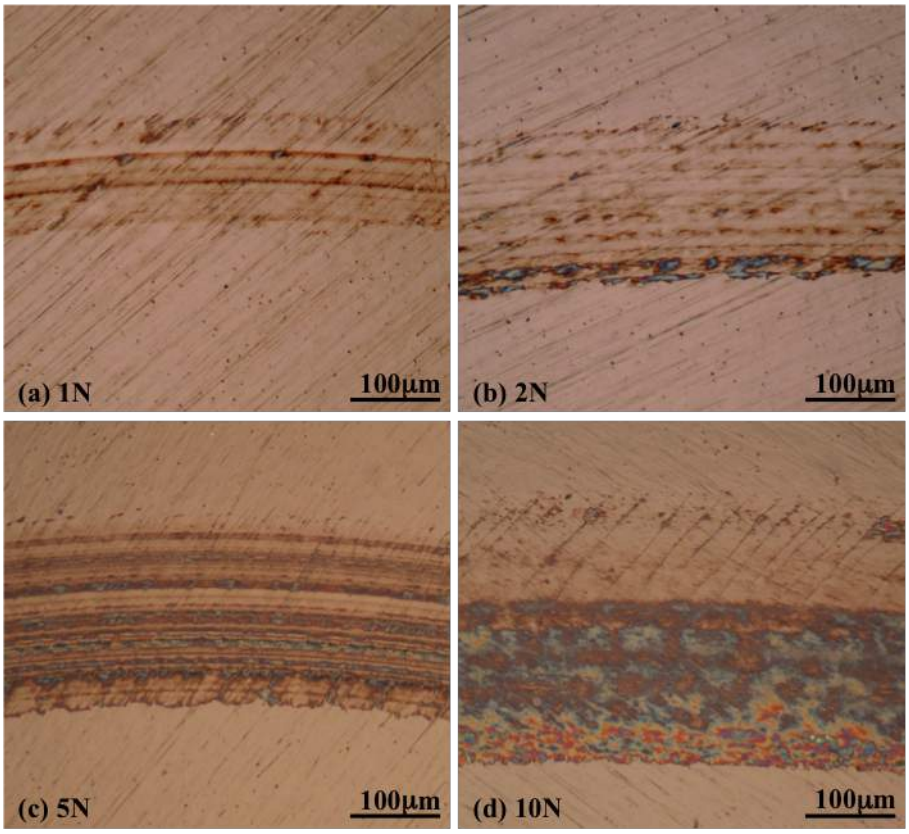


Figure 4.8: Microscopic images showing the wear tracks produced on the $600^oC$ oxidised sample at various contact loads.

Fig. 4.9 shows the cracks formed in the wear tracks during sliding under 10 N load. The cracks formed on the samples oxidised at temperatures below $650^oC$ are confined to one side of the wear track. However, cracks formed on the $700^oC$-oxidised sample travel across the wear track, taking the shape of an arc. It is also interesting to note that the inter-crack spacing increases with increasing TO temperature. Clearly, the thicker the oxide layer, the longer the cracks and the larger the space between the cracks. The formation of cracks under 10 N load helps to release the shear strain energy and this may explain the observed reduction in friction (Fig. 4.6b).

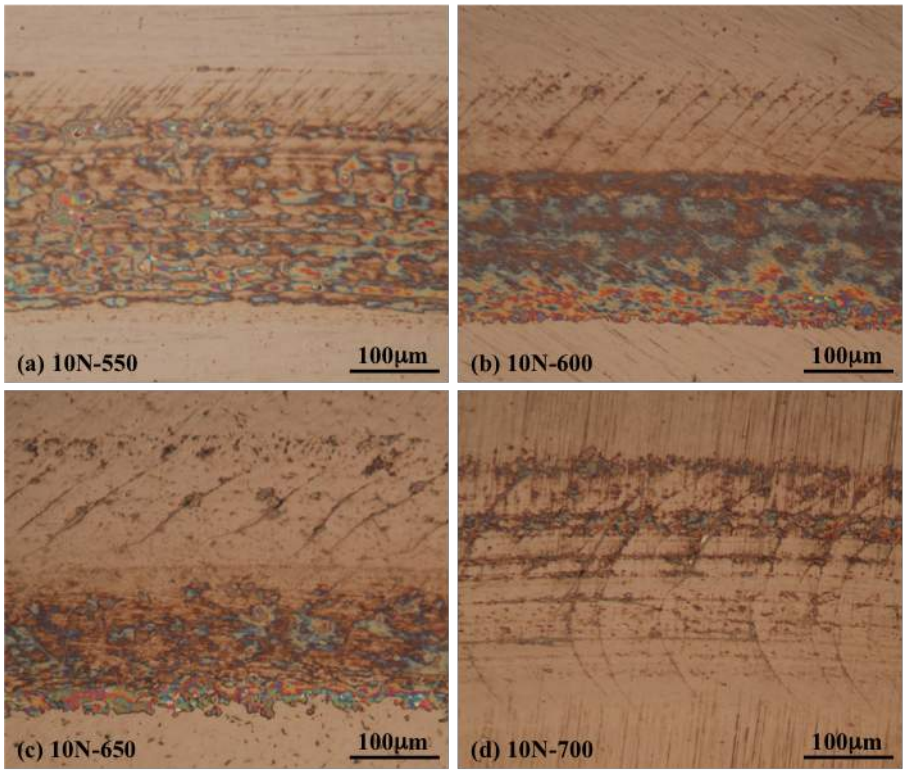


Figure 4.9: Microscopic images showing the wear tracks produced at a contact load of 10 N on the various oxidised samples. Note the existence of cracks in the wear tracks.

A natural question that could be raised is how deep would the cracks be and would the cracks penetrate to the substrate to cause interfacial failure. Ball craters are made on selected wear tracks produced under 10 N load, some of which are made on the cracked region and reveal not only the actual wear depth but also the penetration depth of the cracks, as shown in Fig. 4.10. All the cracks that are observed in this way are confined to the very superficial zone of the oxide layer and no cracks are found to have penetrated to the oxide layer-ODZ interface region. This suggests that the observed cracks on the wear track are initiated on the surface due to the large Hertzian stresses and the sliding traction.

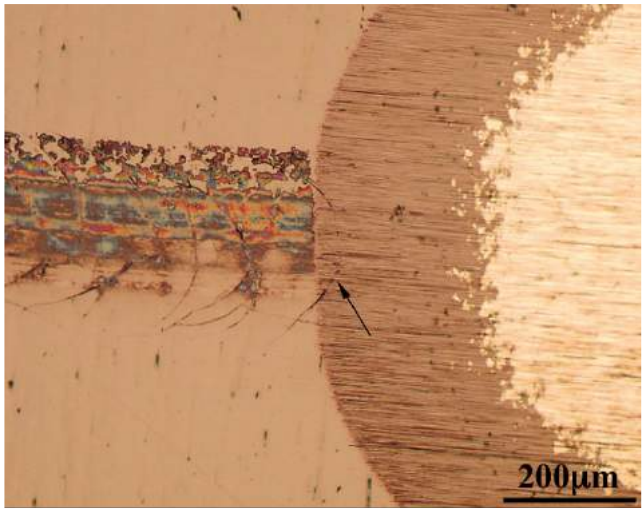


Figure 4.10: Microscopic image showing a ball crater made on the wear track produced on the $700^oC$ oxidised sample at 10 N load, revealing the penetration depth of the cracks in the wear track.

The wear volume resulting from the oxidised samples under the small loads of 1 N, 2 N and 5 N could not be measured confidently by measuring the wear track profiles using stylus profilometer. Only the wear rates resulting form 10 N sliding are measured and compared for the oxidised samples. On the other hand, the untreated sample suffers from excessively large amounts of wear even under small loads, thus no tests under 10 N load are considered necessary. Fig. 4.11a compares typical surface profiles measured across the wear tacks produced on the untreated sample under 1 N load and on selected oxidised samples under 10 N load. The benefit of thermal oxidation in improving dry sliding wear resistance of CP-Zr is obvious. In Fig. 4.11b, the measured wear rates are plotted against TO temperature. The measured wear rates for the untreated sample are not included in the figure because they are more than two orders of magnitude larger than those of the oxidised samples and thus do not fit in the figure. From Fig. 4.11b, it is clear that except for the $550^oC$-oxidised sample, all the other oxidised samples exhibit similar wear rates. As long as the oxide layer maintains its integrity with the substrate, the oxide layers produced at different temperatures have similar wear resistance. For the sliding time of 60 min tested in this work, no catastrophic failure of the cracked oxide coating happens. Longer sliding time is obviously required to further investigate the propagation of the cracks and their influence on material removal.

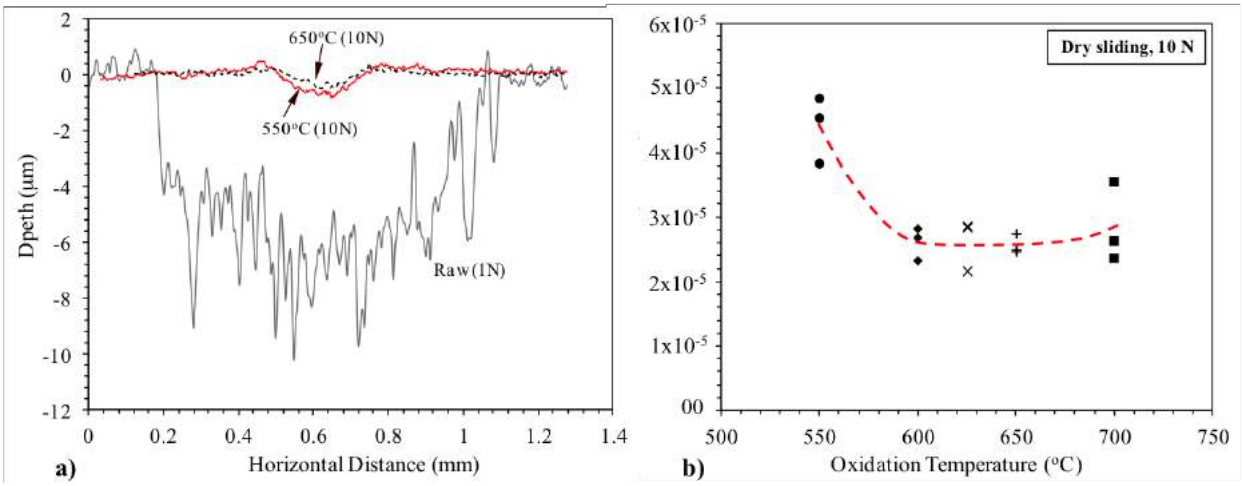


Figure 4.11: Typical surface profiles across the wear tracks (a) and wear rate as a function of oxidation temperature at the contact load of 10 N (b).

### 4.3.3 Effect of initial surface roughness on tribological behaviour

The observed crack formation during sliding at 10 N load on all oxidised samples and at a smaller load of 5 N on the $550^oC$-oxidsed sample imposes a concern regarding the sustainability of the oxide layer under high contact loads and even under small contact loads as the thickness of the oxide layer is gradual reduced due to wear. Further study is conducted on the effect of initial surface roughness on the tribological behaviour of the oxidised layers. Before TO, the surfaces of the samples are ground to P1200 and P600 SiC grade finishes to achieve rougher surfaces of 0.20 $\mu$m ($R_a$) and 0.26 $\mu$m ($R_a$), respectively. After TO at $650^oC$ for 6 h, the original surface finishes are almost retained and sliding wear tests are conducted on the as-oxidised surfaces.

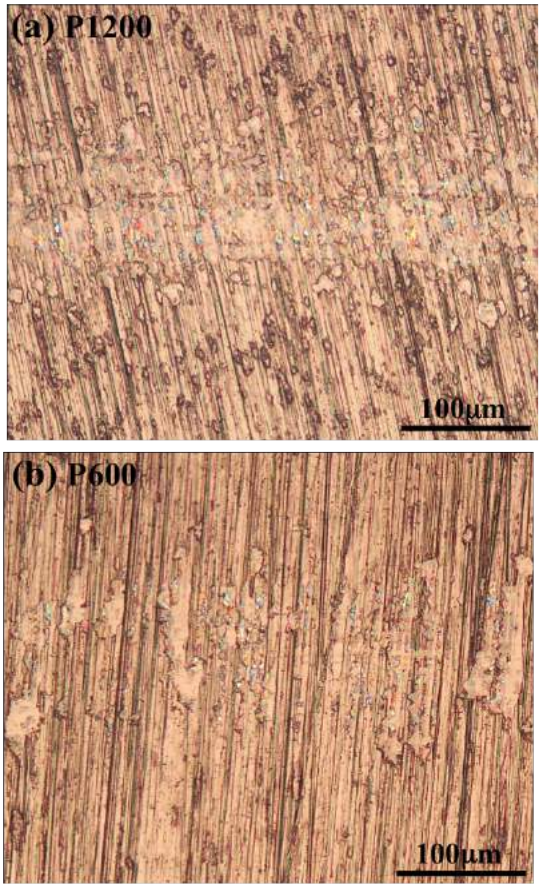


Figure 4.12: Microscopic images showing the wear tracks produced at a contact load of 1 N on the $650^oC$ oxidised sample with a rougher surface resulting from (a) P600 and (b) P1200 grade SiC paper grinding.

Fig. 4.12 shows the morphology of the wear tracks produced at a small load of 1 N on the as-oxidised samples with two different surface finishes. It can be seen that the contact between the slider and the oxidised surface is of the asperity level. The asperities are smoothened through fracture and plastic deformation as evident by the smearing of the asperity material to cover the surrounding valleys, which results in enlarged individual real contact areas. Such asperity contacts help to diversify the contact stress to the asperities, and reduce stresses in the bulk of the surface layer. When the load is increased, more asperities are brought into contact and the real contact area is increased. At 10 N load, a definite wear track can be clearly seen with the wear particles smeared into the valleys (Fig. 4.13a). Some of the original grinding marks can still be clearly seen in the 10 N wear track. However, the most striking feature after testing at 10 N load lies in that no cracks are observed in the wear tracks on the rough as-oxidised surfaces, as can be seen from Fig. 4.13a. It

thus seems that a roughened oxidised surface helps to reduce the tendency of the oxide layer towards cracking during sliding. This phenomenon is further confirmed in chapter 6.

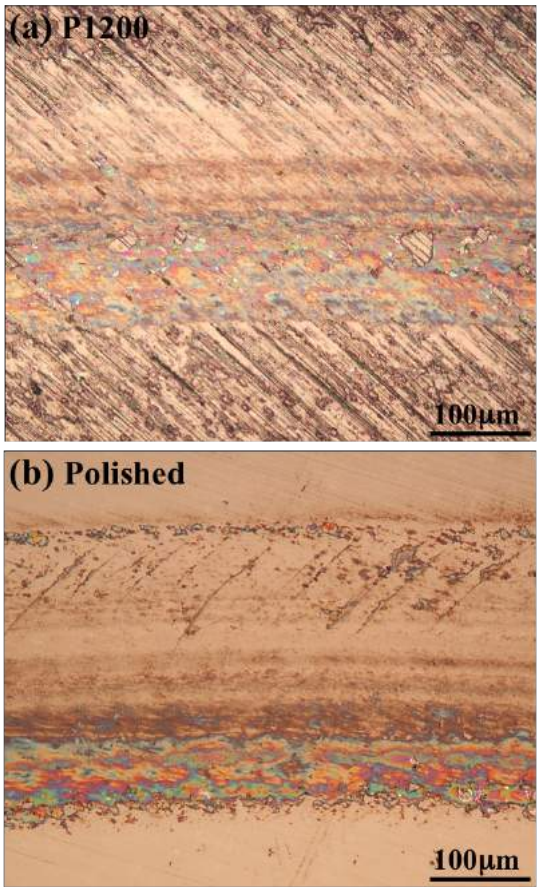


Figure 4.13: Microscopic images showing the wear tracks produced at a contact load of 10 N, (a) on the $650^oC$ oxidised sample with a rougher surface resulting from P1200 grade SiC paper grinding, and (b) on the same sample as (a) after the oxidised surface was polished.

Roughening the sample surface before oxidation could also result in a rougher interface between the oxide layer and the ODZ. In order to clarify whether the absence of cracks in Fig. 4.13a is not due to the existence of a rougher interface, the originally rough oxidised samples were further polished by 1 $\mu$m diamond paste to achieve a mirror-like surface finish, and then wear tests were conducted under the same conditions. Similar to the observations made in Section 4.3.2 (see Fig. 4.9), cracks are now observed in the wear track produced at 10 N load (Fig. 4.13b). Clearly, the elimination of crack formation at 10 N load is owing to the roughened oxidised surface, not due to the roughened interface. The wear track on the rough

oxide surface is covered with wear particles which are smeared into the valleys. The contact between the slider and the smeared particles seems to reduce the contact stresses in the bulk of the oxide layer, and thus reduces the tendency of the oxide layer towards cracking. The filling of the deep valleys with smeared wear particles also results in lower wear rates measured for the rough oxidised samples, as shown in Fig. 4.14. More detailed work on surface finish effect is discussed in Chapter 6.

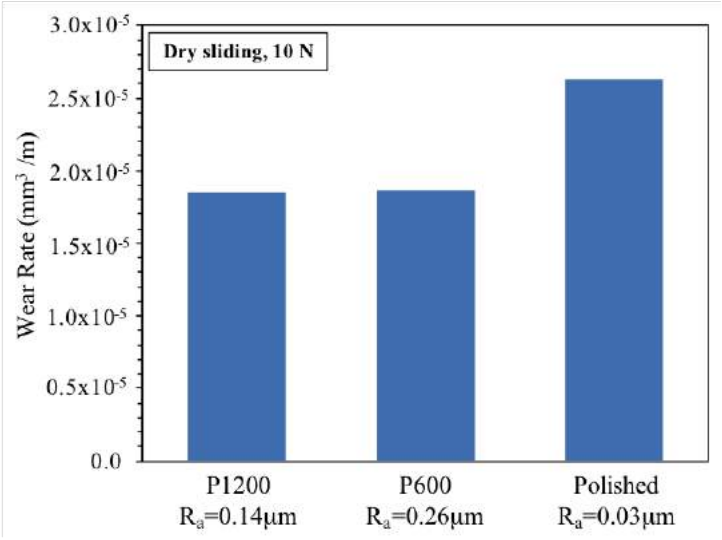


Figure 4.14: Comparison of wear rates of $650^oC$-oxidised sample with different surface roughness.

## 4.4 Conclusion

Based on the experimental results obtained in this work, several conclusions can be drawn, as follows:

- Thermal oxidation at temperatures between $550^oC$ and $700^oC$ results in the formation of a monoclinic $ZrO_2$ layer 2-9 $\mu$m thick and an oxygen diffusion zone of 1-7 $\mu$m thick on CP-Zr. The oxide layers are adherent and possess a hardness up to 1300 $HV_{0.025}$.

- TO was effective in reducing friction and wear rate of CP-Zr and once the $ZrO_2$ layer maintains its integrity with the substrate, TO temperature had no significant effects on friction and wear.

- Under high contact loads, the $ZrO_2$ layer tends to suffer from cracking in the wear track. The thinner layers suffer from cracking at small loads. Although

increasing $ZrO_2$ layer thickness helps to increase load bearing capacity, cracking is unavoidable at high contact loads.

- Roughening the surface before oxidation helps to reduce the tendency of the oxide layer towards cracking during sliding and to reduce wear rate.

# Chapter 5

# The effect of oxidation time on the tribological behaviour of thermally oxidised commercially pure zirconium

Thermal oxidation is an effective surface engineering technique to harden the surfaces of zirconium (Zr) and its alloys for improvement in friction and wear performance. In the present investigation, commercially pure zirconium (CP-Zr) is oxidized at $650^oC$ for a wide range of times from 1 h to 72 h with the aim to study the effect of oxidation time on the tribological performance of CP-Zr. It is found that a dense, pore-free and adherent zirconium dioxide ($ZrO_2$) layer can be produced at the surface for oxidation times less than 12 h. Further increasing oxidation time leads to the gradual development of pores in the inner part of the oxide layer and oxidation breakaway characterized by accelerated oxidation kinetics and crack formation. Oxidation time has a significant effect on the tribological behaviour of thermally oxidized CP-Zr under dry sliding conditions. The 6 $\mu$m thick oxide layer produced by 6 h treatment possesses the lowest friction, best wear resistance and the highest load bearing capacity. On the other hand, the thicker oxide layers produced by longer treatment times show deteriorated tribological behaviour. The results are discussed in terms of the morphology of the oxide layer and crack propagation in the oxide layer and the underlying diffusion zone.

## 5.1 Introduction

In Chapter 4, the effect of TO temperature on the oxidised layer structure of CP-Zr and tribological properties has been investigated for a fixed TO time of 6 h. It was found that a TO temperature of $625^oC$ and $650^oC$ produced the best oxide layer

integrity and tribological performance. Thus, $650^oC$ was chosen as the optimal temperature for a further study of TO time on structural evolution and tribological properties. In this chapter, commercially pure zirconium (CP-Zr) is oxidized at $650^oC$ for a wide range of times from 1 h to 72 h. The effects of oxidation time on the morphology and the tribological performance of the resultant oxide layers are investigated in this work.

## 5.2 Material and Methods

The substrate material, CP-Zr grade 2 (99.2%), and the test samples were the same as those described in Section 4.2. The specimens were manually ground using SiC grinding papers down to the P1200 grade to achieve a surface finish of 0.20 $\mu$m ($R_a$). After ultrasonically cleaning in methanol for 10 min, the specimens were then subjected to thermal oxidation treatment.

Thermal oxidation was carried out in an air furnace at a constant temperature of $650^oC$, for duration of 1 h, 6 h, 12 h, 24 h and 72 h. The heating rate of the furnace was $20^oC$ per minute. After thermal oxidation, the specimens were cooled down to room temperature slowly in the furnace. Furnace cooling took about 8 h from $650^oC$ to room temperature. The temperature of $650^oC$ was chosen based on the results reported in Chapter 4 experiments. At lower temperatures, it would take a significantly longer time to produce a sufficiently thick (e.g. 5 $\mu$m) oxide layer. At higher temperatures, the substrate material would suffer from grain growth with deteriorated properties.

X-ray diffraction (XRD) was conducted using Cu-$K_{\alpha 1}$ to identify the phases of thermally oxidized specimens. Surface hardness was measured using Indentec ZHV microhardness tester at various loads of 0.025-0.5 kg. Metallographic cross sections of oxidized specimens were prepared following standard procedures. In order to have an enlarged view of the oxide layer, a ball crater of about 1 mm diameter was made on the oxidized surface using a 25.4 mm diameter steel ball. Optical and scanning electron microscopes were then used to examine the morphological and structural features of the specimens in the cross section and the ball crater. Thermal oxidation for different times was expected to affect the surface roughness of the specimens. In order to eliminate the possible effect of surface roughness on tribological behaviour, before wear testing the oxidized surfaces were polished using diamond polishing compounds to achieve a mirror-like surface finish of 0.05 $\mu$m ($R_a$). This polishing operation removed about 0.5 $\mu$m thick material from the surface and thus slightly

reduced the thickness of each oxide layer.

Dry sliding friction and wear tests were conducted using a pin-on-disk tribometer (Teer Coatings Ltd). Although oxidized zirconium is currently mainly used in the bio-implant operating environments, dry sliding tests were conducted in this work to assess the response of the specimens to mechanical actions without interference from corrosion. Once the optimum oxidation time has been identified, further tests will be conducted in saline or bovine serum solution, which will introduce corrosion and tribocorrosion aspects to the overall degradation process. During the dry sliding wear process, the specimen was rotating against an alumina ball (Grade 25 $Al_2O_3$) of 8 mm diameter (produced by Trafalgar Bearings Ltd). The tests were conducted at room temperature ($22^oC$) without lubrication, at a constant rotation speed of 60 rpm for duration of 3600s. For the wear track diameter of 8 mm, these resulted in a sliding speed of 2.5 $cms^{-1}$ and a total sliding distance of 90.5 m. During the test, a computer data acquisition system was used to continuously record the coefficient of friction (COF). Initially, small contact loads of 1 N to 5 N were used in the tests. But these could not generate any measurable wear to the oxidized specimens. Thus, higher contact loads, 10 N and 20 N, were employed in this work. These generated an initial contact pressure of 1122 MPa and 1414 MPa, respectively, based on the contact between $Al_2O_3$ and untreated CP-Zr. These contact pressures were sufficiently high to cause plastic deformation of the untreated CP-Zr at the contact zone.

After sliding wear testing, stylus profilometer was used to measure the wear track profile at 4 different locations and the wear volume from each wear track was evaluated. All tests were repeated twice and the means results are presented. Optical microscope and scanning electron microscope (SEM) were used to examine the morphology of the worn surfaces. Efforts have been made by making a ball crater on the wear track to reveal the actual wear depth and any deformation and cracking behaviour below the wear surface.

## 5.3 Results and Discussion

### 5.3.1 Morphological characterization of thermally oxidized specimens

Fig. 5.1 shows typical cross sectional morphology of thermally oxidized specimens produced at $650^oC$ for various times. As expected, thermal oxidation produced

Table 5.1: Summary of oxide layer and oxygen diffusion zone thicknesses and surface hardness of oxidized specimens.(* OL thickness in thick region)

| TO time (h) | Oxide layer thickness ($\mu$m) | Diffusion layer thickness ($\mu$m) | Surface hardness | |
|---|---|---|---|---|
| | | | HV0.025 | HV0.05 |
| Untreated | 0 | 0 | 271 | 194 |
| 1 | 2.9 | 1.6 | 934 | 276 |
| 6 | 6.33 | 2.8 | 1039 | 353 |
| 12 | 8.09 | 4.6 | 1079 | 401 |
| 24 | 10.82 | 7.6 | 1173 | 564 |
| 72 | 15.45 (26*) | 12.3 | 1281 | 665 |

an oxide layer (OL) at the surface and an oxygen diffusion zone (ODZ) at the subsurface. The thickness values of OL and ODZ, together with surface hardness values measured at two indentation loads, are summarized in Table 5.1. The OL had a dark and shiny appearance and adhered well with the underlying diffusion zone, in agreement with the observation of other investigators [4][14][18][19].

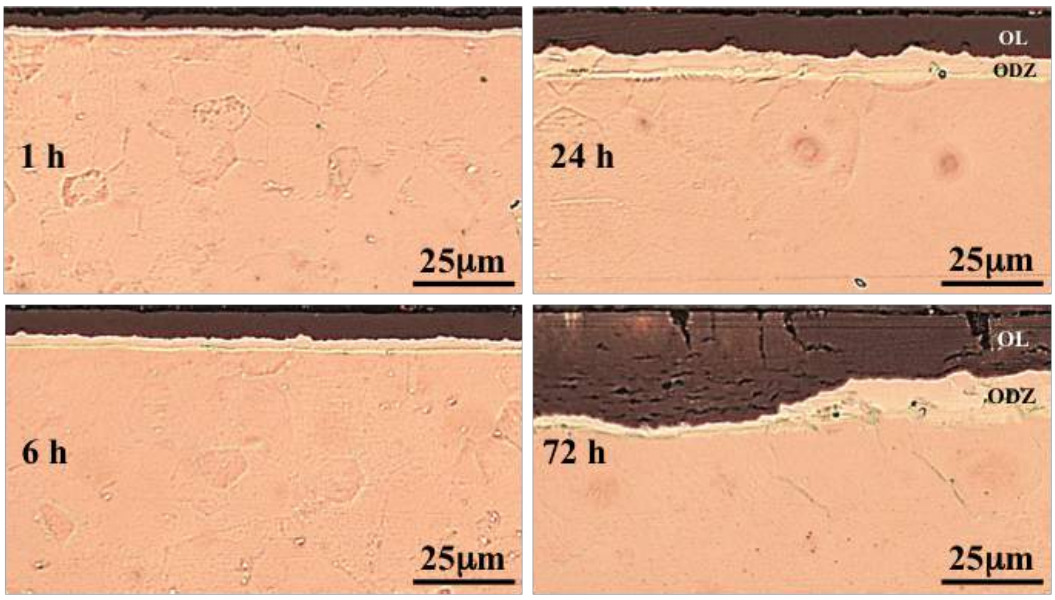


Figure 5.1: Microscopic images of the cross sections of selected oxidized specimens, showing the oxide layer (OL) and the oxygen diffusion zone (ODZ).

XRD analysis confirmed that the OL comprised monoclinic zirconium dioxide, $ZrO_2$. Fig. 5.2 is a typical XRD pattern generated from the oxidized surface, showing that only two phases were detected, i.e. $\alpha$-Zr from the substrate and monoclinic $ZrO_2$ from the surface OL. The thickness of the OL ranged from 3 $\mu$m to 15.5 $\mu$m and increased with oxidation time, as expected for processes governed by thermal

diffusion. The thickness of the ODZ ranged from 1.5 $\mu$m to 12 $\mu$m and also increased with oxidation time. It was noted that as compared to the OL, the ODZ was relatively thin, which can be explained by the slow transport of oxygen from the gas phase through the dense OL to the subsurface [14].

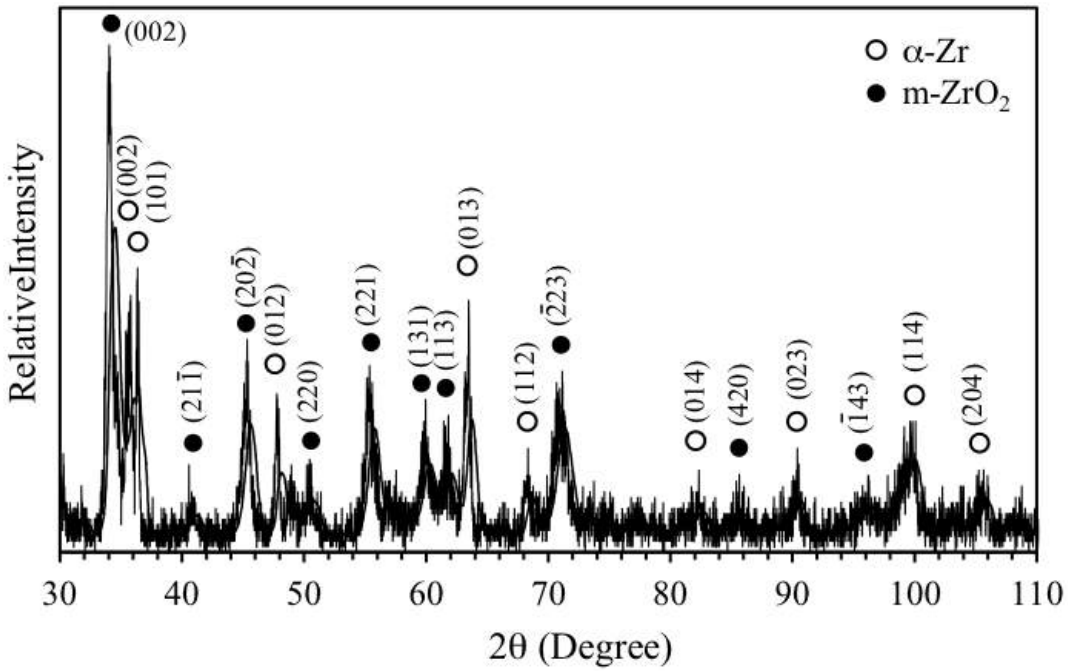


Figure 5.2: X-ray diffraction pattern generated from the thermally oxidized surface ($650^oC$/ 6 h). Cu-$K_{\alpha 1}$ radiation. The diffraction peaks were indexed according to the ICDD data files 99-101-0116 (for $\alpha$-Zr) and 99–100-6688 (for monoclinic $ZrO_2$).

As a result of the formation of the OL and the ODZ, the surface hardness of CP-Zr was significantly increased. At a small indentation load of 0.025 kg, the surface hardness was increased from the based level about 270 $HV_{0.025}$ to about 900 - 1300 $HV_{0.025}$ depending on oxidation time: the longer the oxidation time, the higher the surface hardness. At a higher indentation load of 0.5 kg, the surface hardness of the oxidized specimens decreased due to the substrate effect, but it was still much higher than that of the untreated specimen, demonstrating enhanced load bearing capacity by thermal oxidation treatment. The hardening effect induced by thermal oxidation was further confirmed by micro hardness profile measurements, shown in Fig. 5.3.

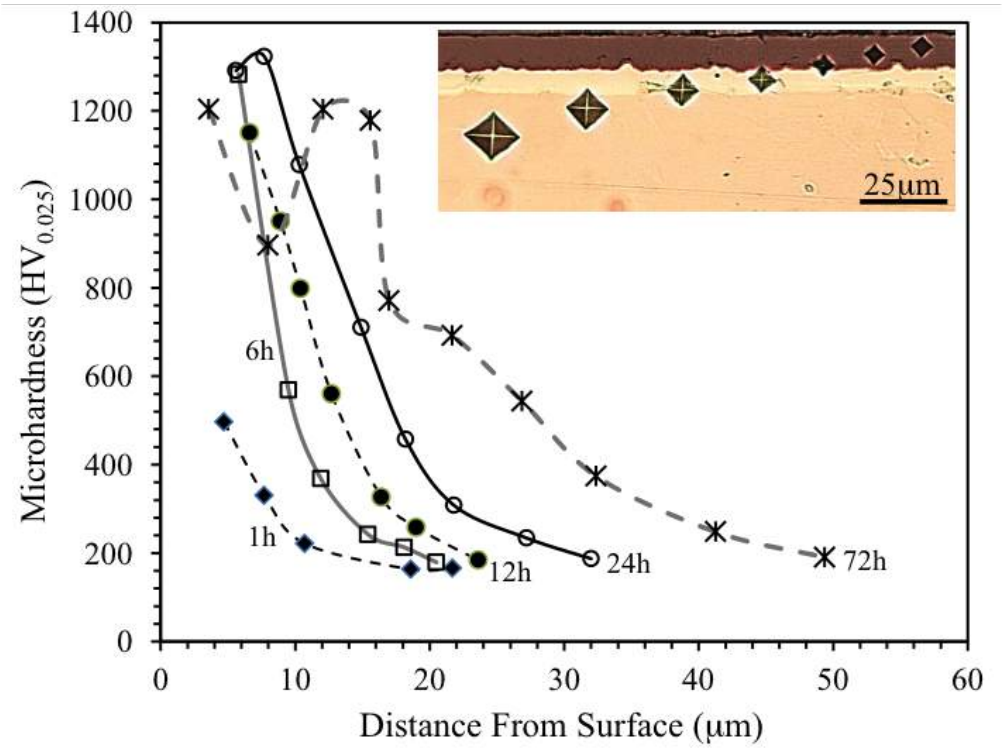


Figure 5.3: Microhardness profiles across the oxidized layers of the specimens treated for various times. The inset shows typical hardness indents made in the subsurface region for hardness profile acquisition.

Increasing oxidation time increased the hardening depth and the hardness across the OL and ODZ. It is interesting to note that the hardness of the 72 h treated specimen experienced a drop at a depth about 10 $\mu$m, which is in the inner part of the OL. This is due to the existence of pores in this region of the OL, shown in Fig. 4d. From Fig. 5.1, it can be seen that the OLs produced by relatively short time oxidation (1 h and 6 h) were dense, pore-free and uniform in thickness, while the OLs produced by long time oxidation (e.g. 72 h) were none uniform in thickness and contained pores in the inner part and cracks open to the surface. In order to have an enlarged view of the OLs, a ball crater was made on each oxidized surface and examined under microscope, as shown in Fig. 5.4. Clearly, the OL produced by 6 h oxidation was very dense and free from any pore formation (Fig. 5.4a). Increasing the oxidation time to 12 h led to the development of a small amount of pores in the inner part of the OL at the OL-ODZ interfacial region (Fig. 5.4b). Pore formation became more significant when the oxidation time was further increased to 24 h, as shown in Fig. 5.4c, where pores can be seen both in the inner part of the OL and in the ODZ. Finally, after 72 h oxidation, the inner part of the resultant OL became

extremely porous, with the porous zone extending towards the surface and the ODZ (Fig. 5.4d). Cracks can be seen in the OL of the 72 h oxidized specimen arising from the linkage of the pores.

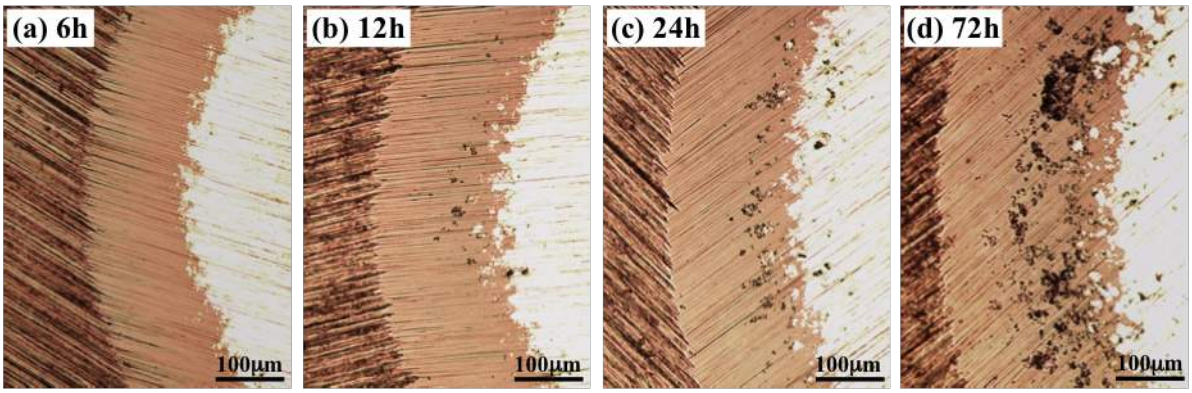


Figure 5.4: Microscopic images of ball craters made on the oxidized surfaces, showing the dense oxide layer produced by 6 h oxidation (a) and the development of pores in the inner part of the oxide layers produced by 12 h (b), 24 h (c) and 72 h (d) oxidation.

Oxidation of Zr and its alloys is governed by two distinctly different kinetics laws associated with the well-known phenomenon of oxidation breakaway [25][26][161]. Below a certain critical oxidation time, the OL grows following the parabolic or cubic rate law [161]. Above the critical oxidation time, oxidation breakaway occurs, where the oxide layer growth is accelerated, entering a nearly linear growth regime [25][161]. The resulting OL after breakaway becomes less protective because of the formation of cracks and pores. Under the present thermal oxidation condition at $650^oC$, breakaway occurred after 72 h treatment, resulting in a porous OL with cracks and none-uniform growth: some regions in the OL was as thick as 26 $\mu$m, as compared to 15.5 $\mu$m measured for the majority of the OL (Table 5.1). The present work also showed that oxidation breakaway was preceded by the gradual development of pores in the inner part of the OL (Fig. 5.4b and 5.4c). In order to have a better understanding of the oxidation kinetics under the present experimental conditions, the OL thickness data in Table 5.1 was plotted in Fig. 5.5 in the logarithm scale. Clearly, the growth of the OL followed a quasi-parabolic rate law with an exponent term of 0.41, just below 0.5 expected for solid diffusion, a phenomenon commonly observed for oxidation of Zr [161]. After 72 h oxidation, the thick regions of the OL suffered from breakaway and followed a linear growth law, as shown by the dotted line in Fig. 5.5.

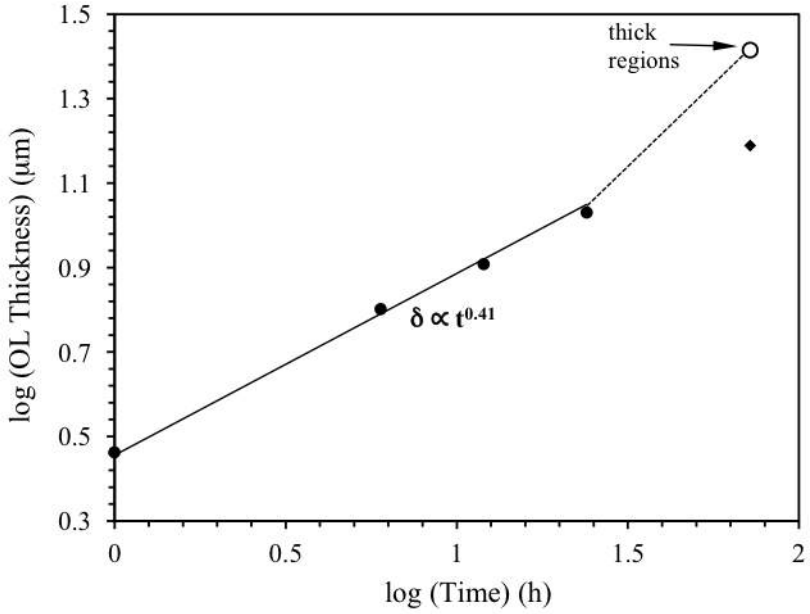


Figure 5.5: Oxide layer (OL) thickness as a function of thermal oxidation time at $650^oC$, plotted in the logarithm scale. Two data points are used for the 72 h oxidized specimen, one for the thick region and another for the overall of the OL.

### 5.3.2 Tribological behaviour

Fig. 5.6 shows typical friction curves recorded during dry sliding for selected specimens. After an initial running-in stage, the untreated specimen exhibited steady state friction with a coefficient of friction (COF) about 0.5 under both 10 N and 20 N loads. No large difference in friction was found at the two contact loads. On the other hand, contact load had a significant effect on the frictional behaviour of the oxidized specimens. At 10 N, the 1 h, 6 h and 12 h oxidized specimens exhibited similar friction behaviour, where after the running-in stage, the COF became stable around the value of 0.4. However, higher friction was found for the 24 h and 72 h oxidized specimens under the contact load of 10 N.

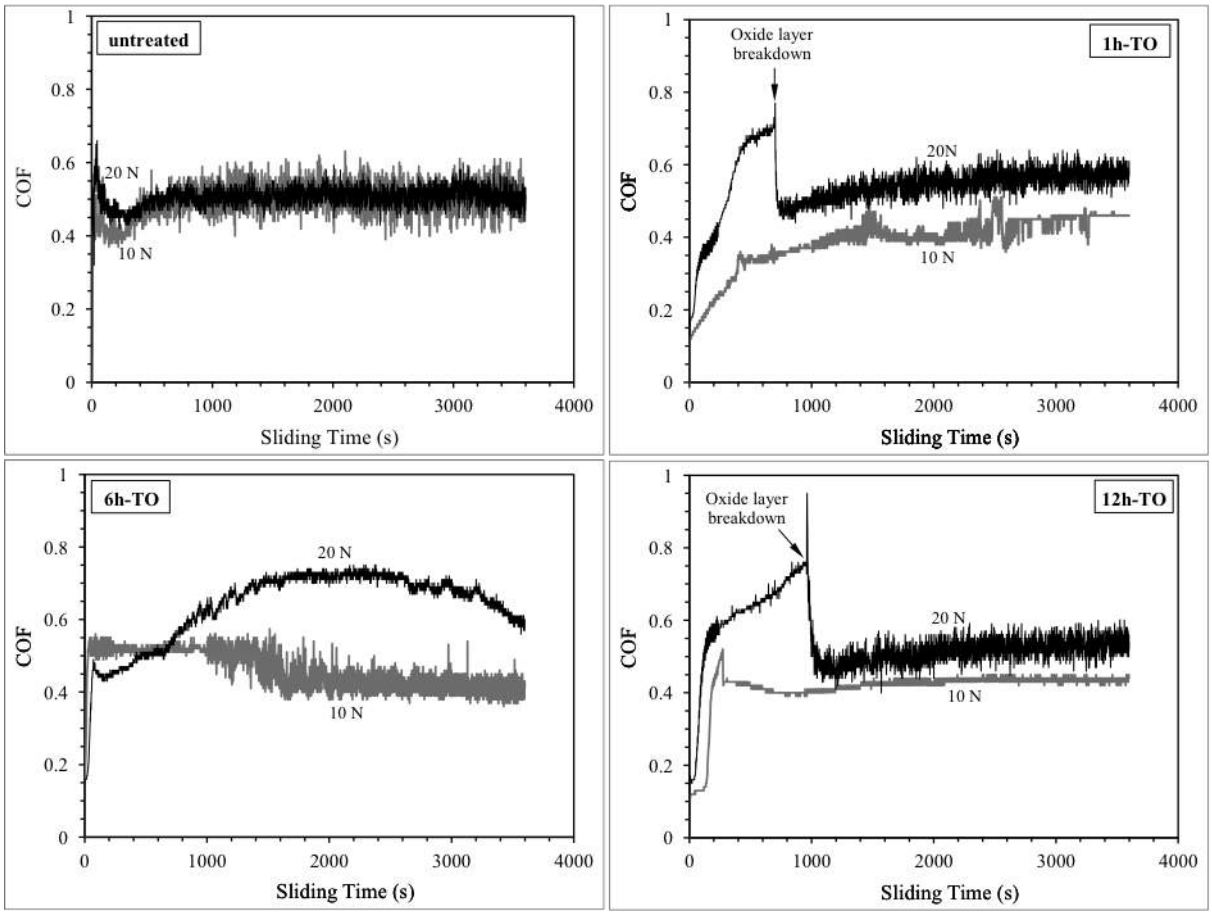


Figure 5.6: Recorded coefficient of friction (COF) curves for the untreated and thermally oxidized (TO) specimens.

In Fig. 5.7, the mean COF measured at 10 N was plotted against oxidation time. Clearly, COF showed a general trend of increasing with oxidation time and prolonged oxidation had a detrimental effect on friction. It thus seems that the development of pores in the OL had a negative effect on friction reduction.

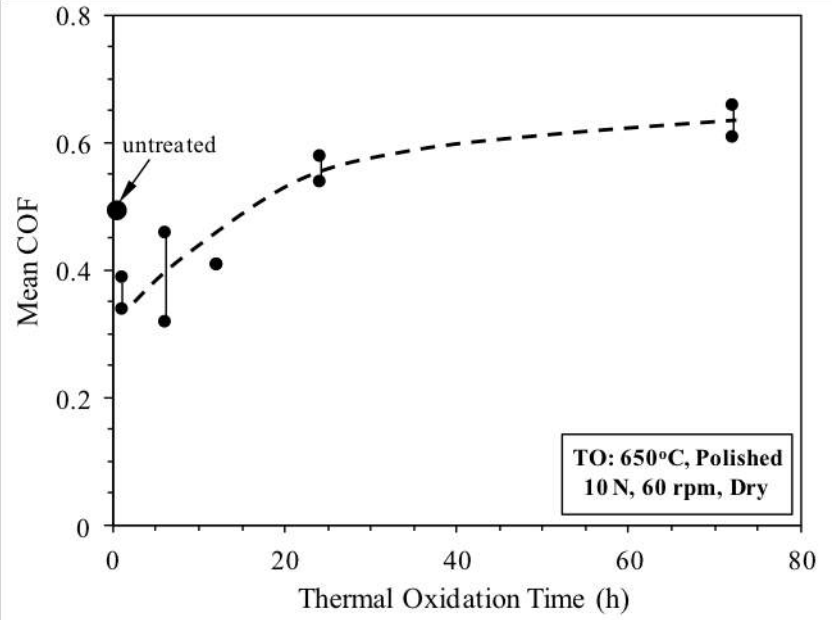


Figure 5.7: Mean coefficient of friction (COF) measured at 10 N load.

When the contact load was increased to 20 N, the oxidized specimens showed different frictional behaviour. Only the 6 h oxidized specimen exhibited a relatively smooth frictional behaviour with higher COF values than those at 10 N load (Fig. 5.6). The other oxidized specimens exhibited a clear transition in frictional behaviour after a certain period of sliding, characterized by the sudden increase in friction to result in a friction spike and then a sharp decrease in friction to reach COF values characteristic of the untreated specimen (see Fig. 5.6). This transition marked the sudden breakdown of the OL as confirmed by further tests ended before and after the transition point. Fig. 5.8 shows typical wear track cross sectional profiles measured by profilometer. The wear tracks produced on the 1 h and 12 h oxidized specimens at 10 N were narrow and shallow, without any sign of OL breakdown and removal (Fig. 5.8a). However, the wear tracks produced on the same specimens at 20 N load were wide, rough and as deep as 35 $\mu$m, with the OL and ODZ being completely removed (Fig. 5.8a). A similar behaviour was also observed for the 24 h and 72 h oxidized specimens. On the other hand, the 6 h oxidized specimen had the ability to resist the 20 N contact load without OL breakdown, as shown in Fig. 5.8b where the wear track profiles were narrow and shallow with wear depths confined within the OL. Clearly, the dense and pore-free OL on the 6 h oxidized specimen had the best load bearing capacity as compared to the OLs on other oxidized specimens. The OL on the 1 h oxidized specimen was obviously

too thin to resist high contact loads. Although the OLs on the 12 h, 24 h and 72 h oxidized specimens were much thicker than that on the 6 h oxidized specimen, the pores developed in these OLs obviously had a detrimental effect on the loading bearing capacity during the dry sliding wear process.

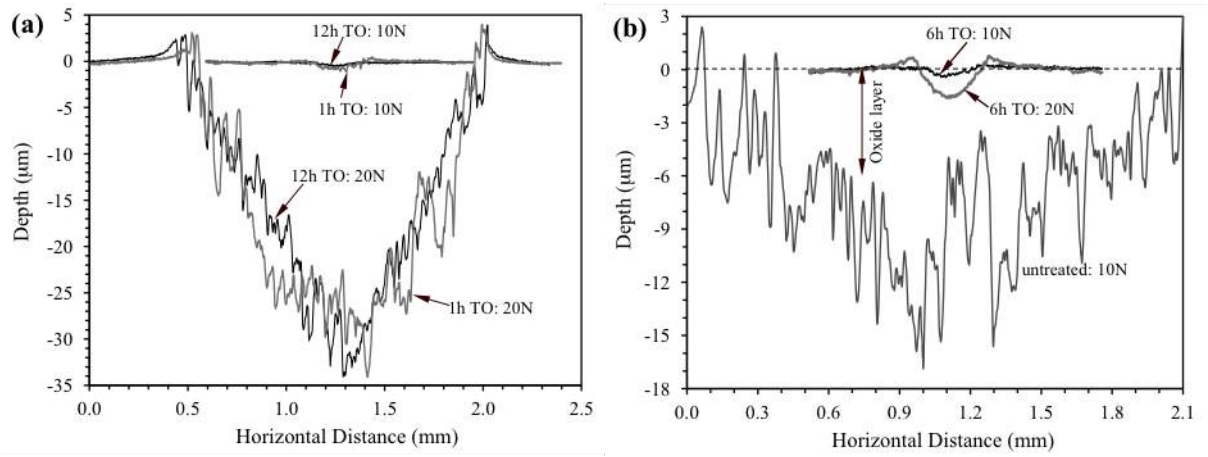


Figure 5.8: Typical wear track profiles measured for (a) 1 h and 12 h and (b) 6 h oxidized specimens, tested under 10 N and 20 N loads.

The total material loss (TML) from each wear track was measured from the wear track profiles. Fig. 5.9 compares the obtained results for different specimens at the two contact loads. At 10 N, except for the 72 h oxidized specimen, all other oxidized specimens were very effective in reducing TML of CP-Zr by two orders of magnitude. No breakdown of the OL was observed on these specimens at 10 N and wear occurred within the OL (Fig. 5.8). 6 h oxidation was the most effective in improving wear resistance of CP-Zr at 10 N load. Such an effectiveness of the 6 h oxidized specimen was maintained at the higher contact load of 20 N because the OL was not worn through (Fig. 5.9). However, for the other oxidized specimens, their effectiveness in reducing TML of CP-Zr at 20 N was much reduced because the OLs were worn through (Fig. 5.9). The breakdown of the OL at 20 N led to much accelerated TML by two orders of magnitude. Clearly, the 6 h oxidized specimen exhibited the best wear resistance under both contact loads.

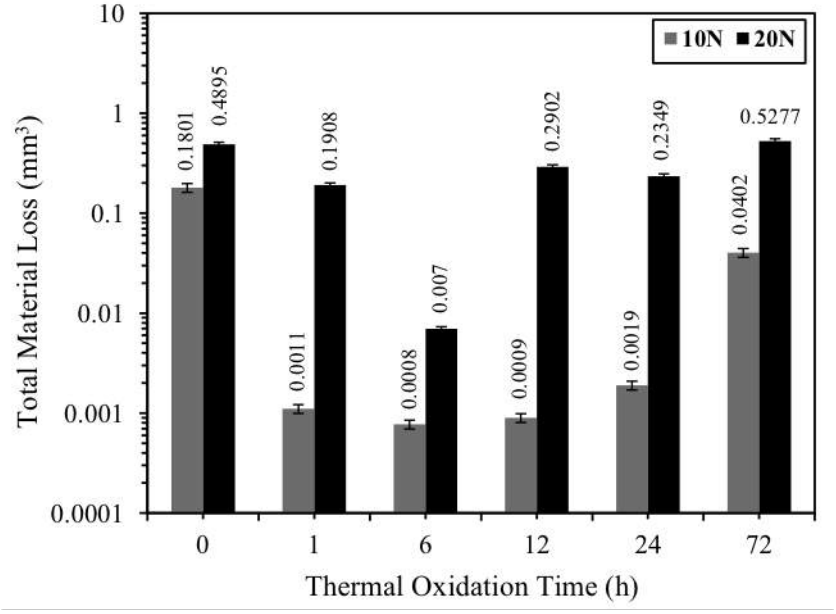


Figure 5.9: Wear volume measured for various specimens at 10 N and 20 N loads.

Typical surface morphology of the wear tracks produced on the oxidized specimens at the 10 N load is shown in Fig. 5.10. Many semi-circular shaped cracks were observed on the wear track surface. It is believed that these cracks were formed due to the tensile stress at the contact surface resulting from the sliding traction [162]. The tensile stress at the contact surface was sufficient to induce cracks in the brittle ceramic, $ZrO_2$. It is interesting to note that despite the formation of numerous cracks at the contact surface, the OL maintained its integrity with the substrate without flaking and delamination (Fig. 5.10a-c). However, for the 72 h oxidized specimen, local failure of the OL was observed, which was associated with the pre-existing cracks formed during the prolonged oxidation (see Fig. 5.10d). This seems to correlate with the measured high friction (Fig. 5.7) and large TML (Fig. 5.9) for this specimen. Obviously, the OL produced by 72 h oxidation was no longer protective under tribological conditions. As a result of the sliding motion, wear not only occurred to the test specimen but also to the alumina ball counterface. A flat wear scar was produced on the alumina ball. The size of the scar increased with sliding time. Fig. 5.11a shows the wear scar on the alumina ball after testing the 6 h oxidized specimen at 10 N for 3600 s. The mean diameter of the scar is about 140 $\mu$m. This means that the actual contact area increased as sliding proceeded, resulting in lowered contact pressure. Although the calculated initial maximum Hertz contact pressure (1122 MPa) was sufficient to cause plastic deformation in the untreated material, as sliding proceeded, the degree of plastic deformation should be

reduced due to the increased contact area and the reduced contact pressure.

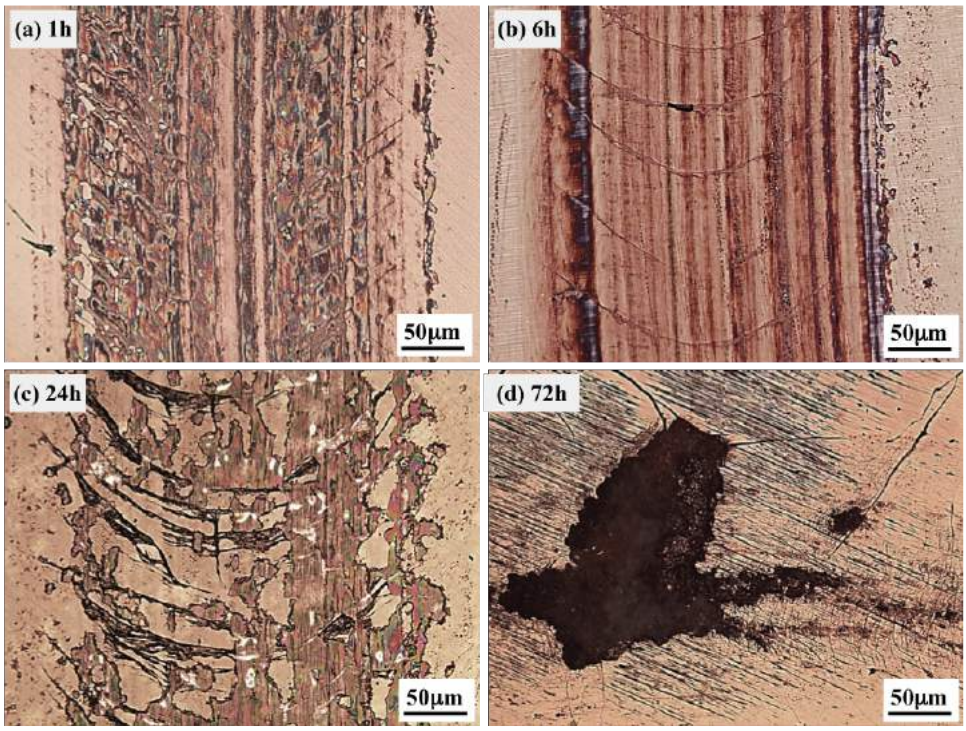


Figure 5.10: Microscopic images showing the wear tracks on the oxidized specimens tested under 10 N load.

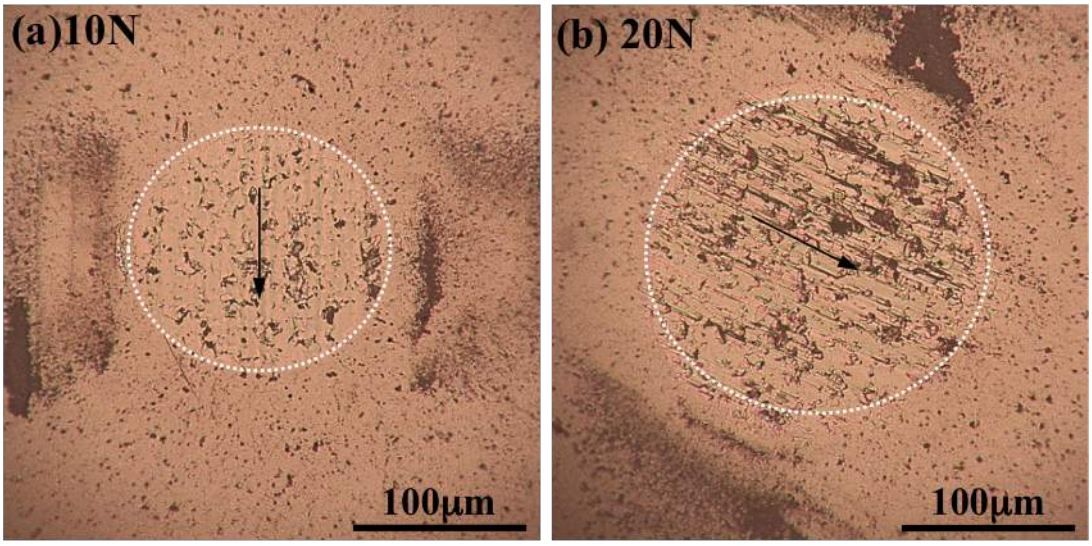


Figure 5.11: Microscopic images showing the wear scar on the alumina ball after sliding with the 6 h oxidized specimen under (a) 10 N and (b) 20 N load. The arrow indicates the sliding direction and the dotted line indicates the boundary of the contact area.

Fig. 5.12 shows the morphology of the wear tracks produced at the higher contact load of 20 N. Except for the 6 h oxidized specimen, the OL on all other specimens was worn through in the wear track, resulting a wide and deep wear track with a rough surface and many parallel scratch marks, a typical morphological feature of the worn surface of untreated CP-Zr. For the 6 h oxidized specimen, although the OL still maintained its integrity with the substrate, numerous closely-spaced semi-circular cracks formed in the wear track. It is anticipated that with further sliding for a longer time, this OL would be removed from the wear track, resulting a transition in friction and much accelerated TML. The wear scar on the alumina ball after testing the 6 h oxidized specimen at 20 N is shown in Fig. 5.11b. As compared to that produced at 10 N, the scar produced at 20 N was larger. It is also interesting to note that cracks were observed at the edge of the wear track (Fig. 5.12d), leading to chipping of the OL. These types of cracks were induced by bending of the ceramic layer due to substrate deformation in the wear track [163].

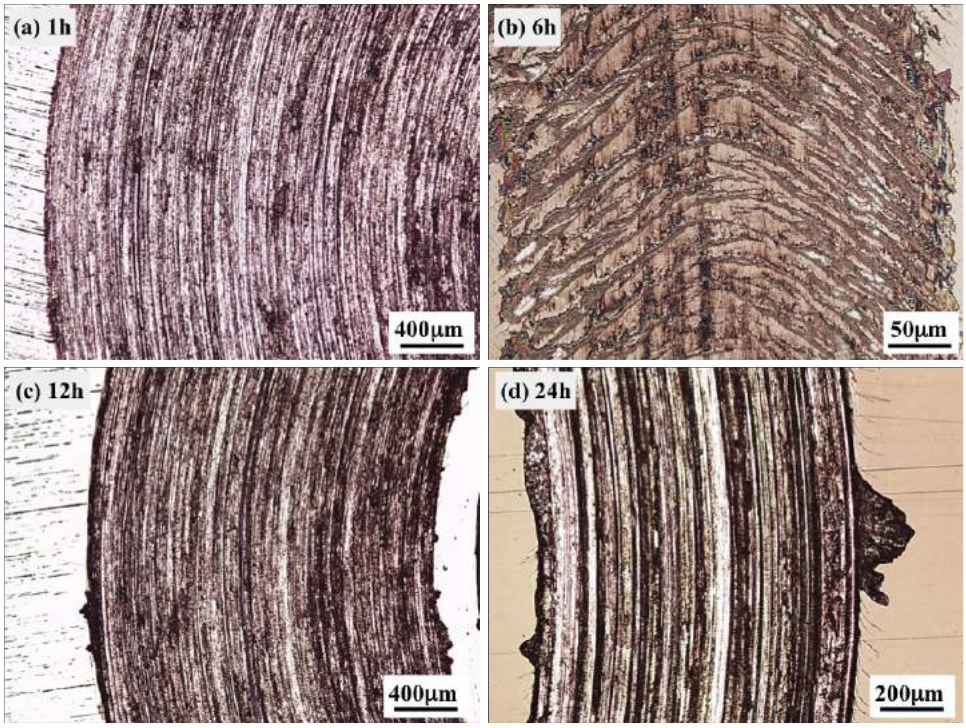


Figure 5.12: Microscopic images showing the wear tracks on the oxidized specimens tested under 20 N load.

Fig. 5.13 shows selected SEM images of the wear tracks produced at 10 N and 20 N loads. The semi-circular cracks can be clearly seen on the 10 N wear tracks, which show evidence of local fracture of the OL associated with the cracks (Fig.

5.13a), mild abrasion (Fig. 5.13a) and polishing (Fig. 5.13b). In the 20 N wear track on the 6 h oxidized specimen, the densely populated semi-circular cracks and local breakdown of the OL at the track edges can be clearly seen (Fig. 5.13c). It is also evident that the cracks were filled with wear debris from the tribo-system (Fig. 5.13d).

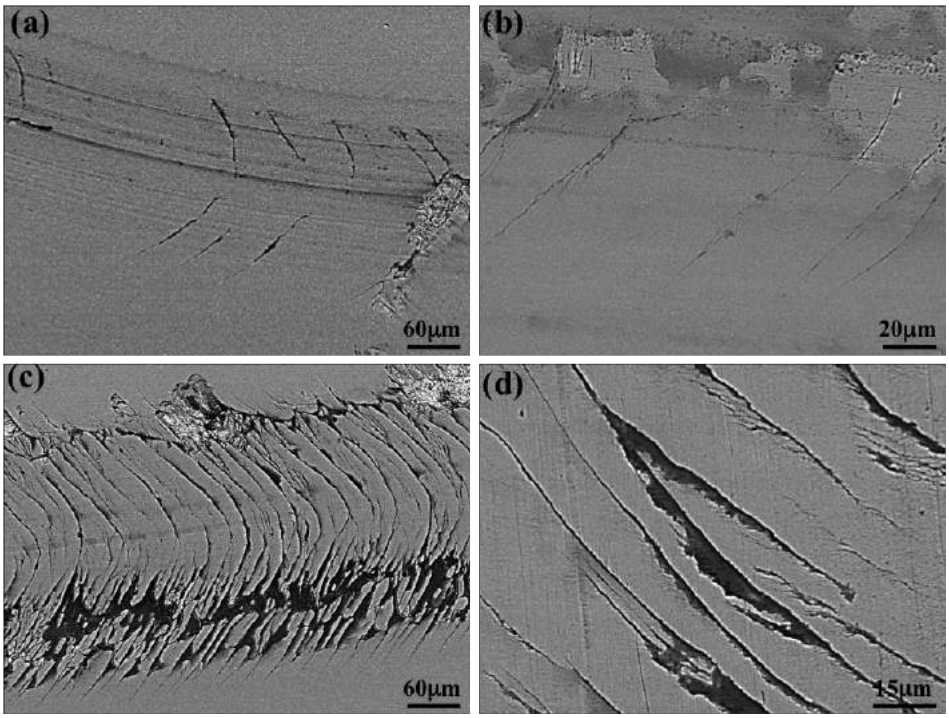


Figure 5.13: SEM images showing the morphology of the wear track on the 12 h oxidized specimen tested under 10 N load (a and b) and on the 6 h oxidized specimen tested under 20 N load (c and d).

From the results presented above, it is clear that the effect of thermal oxidation time on the tribological behaviour of CP-Zr was closely associated with the structural feature of the resultant oxide layer. The dense, pore-free and sufficiently thick (6 $\mu$m) OL on the 6 h oxidized specimen exhibited better wear resistance than the dense but thinner OL by 1 h oxidation and the thicker but porous OLs by 12h, 24 h and 72 h oxidation. From the results obtained, several interesting questions can also be raised here, regarding the sudden breakdown of the OL during sliding wear at 20 N load (Fig. 5.6), the integrity of the OL with the substrate despite the formation of numerous cracks in the wear track (Fig. 5.10), and the depth of penetration of the cracks. In order to have a visual view of the actual wear depth and the penetration of the surface cracks, a ball crater was made on the wear track

and then examined under a microscope. Fig. 5.14 shows two representative images. The cracks seen on the 10 N wear track surfaces (Fig. 5.10) were confined to the superficial zone of the OL and no cracks were found to have penetrated to the oxide layer-ODZ interface region (Fig. 5.14a). At 20 N, only the wear track on the 6 h oxidized specimen was available for such examination (Fig. 5.14b). In this case, the cracks have penetrated through the OL and across the OL-ODZ interface into the ODZ (Fig. 5.14b). Deformation of the OL towards the substrate at 20 N load was also evident from Fig. 5.14b, which could be responsible for the bending type cracks seen at the edge of the wear tracks (Fig. 5.12d and Fig. 5.14b). The fact that the OL on the 6 h oxidized specimen still maintained its integrity with the substrate after sliding at 20 N load suggests that penetration of the surface cracks through the OL to the ODZ was not sufficient to cause the sudden breakdown of the OL. It is anticipated that once the cracks propagate further into the substrate, the OL would be broken down, leading to the observed transition in friction (Fig. 5.6) and the accelerated TML (Fig. 5.9). This also suggests that a thick ODZ would help to delay the breakdown of the OL and enhance the load bearing capacity of the oxidized specimen. Thus, an ideal thermally oxidized system for Zr should comprise a dense, pore-free and sufficiently thick OL at the surface and a thick ODZ at the subsurface [14].

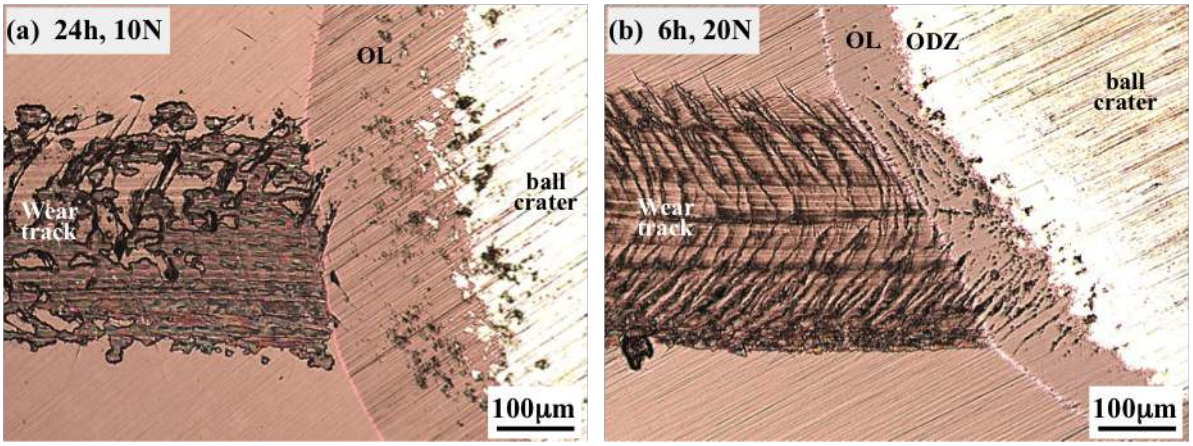


Figure 5.14: Microscopic images showing the wear track and a ball crater made on the wear track on the (a) 24 h oxidized specimen after testing under10 N load and (b) 6 h oxidized specimen after testing under 20 N load.

## 5.4 Conclusion

From the results obtained in this work, it can be concluded that thermal oxidation at $650^oC$ for duration less than 12 h produces a relatively thick, dense, pore free and adherent oxide layer at the surface and a thin oxygen diffusion zone at the subsurface. Such a combination of the oxide layer and the oxygen diffusion zone possesses the lowest friction, best wear resistance and highest load bearing capacity. Although prolonged oxidation can increase the thicknesses of the oxide layer and the oxygen diffusion zone, it leads to the gradual development of pores in the inner part of the oxide layer and finally the breakaway of oxidation characterized by accelerated oxide growth and crack formation in the oxide layer. The formation of pores in the oxide layer has detrimental effects on friction reduction, wear resistance and load bearing capacity. The oxide layer surface tends to suffer from cracking under the present dry sliding process, and the oxide layer suffers from sudden breakdown after a certain period of sliding contact motion. This can be associated with the propagation of the surface cracks through the oxide layer and then the oxygen diffusion zone to reach the oxygen diffusion zone-substrate interface.

# Chapter 6

# Surface finish effect on dry sliding wear behaviour of thermally oxidized commercially pure zirconium

The aim of this chapter was to further investigate the effect of surface polishing on the wear behaviour of thermally oxidized commercial pure zirconium (CP-Zr) under dry sliding conditions. Surface ground CP-Zr with a roughness of 0.21 $\mu$m ($R_a$) was thermally oxidized (TO) at $650^oC$ for 6 h. After TO, some samples were polished to smoothen the surface with a finish of 0.04 $\mu$m ($R_a$). The response of the polished and unpolished TO samples to dry sliding wear was investigated under unidirectional sliding conditions. The results show that surface polishing after TO affects the dry sliding wear behaviour of TO CP-Zr in several aspects, including coefficient of friction, wear rate, crack formation and oxide layer breakdown. In particular, it is found that smoothening the TO surface favors the formation of semi-circular cracks in the wear track and accelerates oxide layer breakdown during dry sliding. A slightly rough TO surface helps to reduce the tendency of the oxide layer towards cracking and to increase the wear resistance at high contact loads. The mechanisms involved are discussed in terms of asperity contacts, crack formation, propagation and final fracture.

## 6.1 Introduction

Thermally oxidized zirconium (TO-Zr), as an alternative to the most commonly used Co-Cr alloys, has been used in artificial hip and knee joints [31][32][33]. One of the benefits of oxidized Zr in arthroplasty is its extremely good resistance to surface scratching which may be caused by trapped hard particles [33][35][36][37], which is

crucial for reducing wear of the counter articulating part made of polyethylene (PE). In such an application, a very smooth and polished TO surface is necessary. However, TO-Zr also has potential uses in other fields involving sliding contact motions [4], where a polished surface may not be necessary. In manufacturing engineering components, smoothening by polishing is quite time consuming and costly. Therefore, polishing operations should be avoided whenever possible [164].

Surface finish is known to affect the tribological performance of engineering components and the counter bodies [165][166]. The friction and wear properties could be affected by surface roughness by altering the contact conditions, the stress distribution, the ploughing actions and the adhesion behaviour [167][168][169]. The majority of published investigations have found that a rougher surface results in a higher wear rate from both the component and the counter body [170][171]. When frictional behaviour is concerned, the effect of surface roughness is more complicated, because friction is affected by many factors, such as the adhesion junctions formed at the real contact areas, the ploughing actions of the asperities, the trapped wear particles and the mechanical interlocking of asperities. Depending on sliding contact conditions and contacting materials involved, rougher surfaces may result in higher friction [164][168][172][173] or lower friction [167][171], or have no effect on friction [169]. Most of the investigations concerning surface roughness effect on tribology have been focused on friction and wear rate, very few work have been reported on the effect of surface finish on the formation of cracks and their propagation in coating systems during dry sliding wear. In Chapter 4, the effect of original surface finish on the tribological behaviour of TO CP-Zr was investigated. It was found that a slightly roughened original surface before TO is beneficial in enhancing the load bearing capacity of the TO sample. However, an interesting question still remains, i.e. how does surface finish after TO affect the tribological properties?

Thus, in this Chapter, surface ground commercially pure zirconium (CP-Zr) with a surface finish of 0.21 $\mu$m ($R_a$) was thermally oxidized (TO) at $650^oC$ for 6 h. After TO, some samples were polished to generate a smooth surface finish of 0.04 $\mu$m ($R_a$). Some were unpolished in the as-oxidized state. The effect of these two different surface finishes on the dry sliding wear behaviour was investigated. Particular attention was paid to the effect of surface finish on the formation and propagation of surface cracks and the integrity of the oxide layer during dry sliding.

## 6.2 Material and Methods

Commercially pure (CP) zirconium, grade 2, was used as the substrate material. The CP-Zr was supplied by Goofellow UK Ltd in the form of 1 mm thick sheets with the following nominal composition: 0.16 wt% O, 0.025 wt% N, 0.05 wt% C, 0.005 wt% H, 0.2 wt% Fe, 0.2 wt% Hf and Zr (rest). Before TO, the samples (20 mm x 15 mm) were ground using P1200 grade metallographic grinding paper, which produced a surface finish of 0.21 $\mu$m ($R_a$). The samples were then cleaned in methanol and dried in a stream of hot air.

Thermal oxidation (TO) of the samples was implemented in an air furnace at $650^oC$ for 6 h, which is the optimum condition determined previously [174]. The TO process conditions and the structural features of the resultant oxidized layers have been reported elsewhere [174]. The cross-sectional view of the TO sample and the microhardness profile measured in the cross section are shown in Fig. 6.1. TO produced a dark and uniform oxide layer (OL) of 6.3 $\mu$m thick at the surface and a 2.8 $\mu$m thick oxygen diffusion zone (ODZ) in the subsurface. Although increasing TO time could increase OL and ODZ thicknesses, this could lead to pore formation in the oxide layer due to oxidation breakaway of zirconium [26][174]. The hardness of the oxide layer was about 1300 $HV_{0.025}$, a typical value reported for bulk $ZrO_2$ [4]. The hardness decreased gradually across the ODZ to reach the substrate base level of about 200 $HV_{0.025}$.

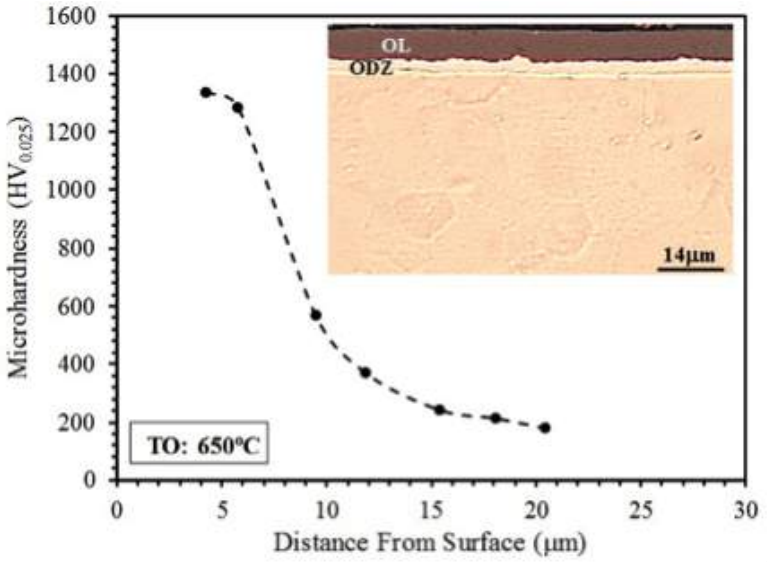


Figure 6.1: Microhardness profile measured across the oxide layer (OL) and the oxygen diffusion zone (ODZ) in the cross section and microscopic image showing the cross-sectional morphology (inset) of the oxidized sample.

After TO for 6 h, the surface roughness ($R_a$) value was slightly increased from 0.21 $\mu$m to 0.23 $\mu$m. Some of the TO samples were polished to achieve a smoothened surface with a finish of 0.04 $\mu$m ($R_a$). These polished samples are designated as "TO-polished", and the TO samples in the as-oxidized state without further polishing are designated as "TO-unpolished" in this paper. Fig. 6.2 compares the surface roughness profiles measured from the untreated, the TO-unpolished and TO-polished samples. It can be seen that polishing considerably smoothened the TO surface and this polishing operation removed some material (0.3 - 0.4 $\mu$m thick) from the TO surface. This resulted in a slightly reduced oxide layer thickness.

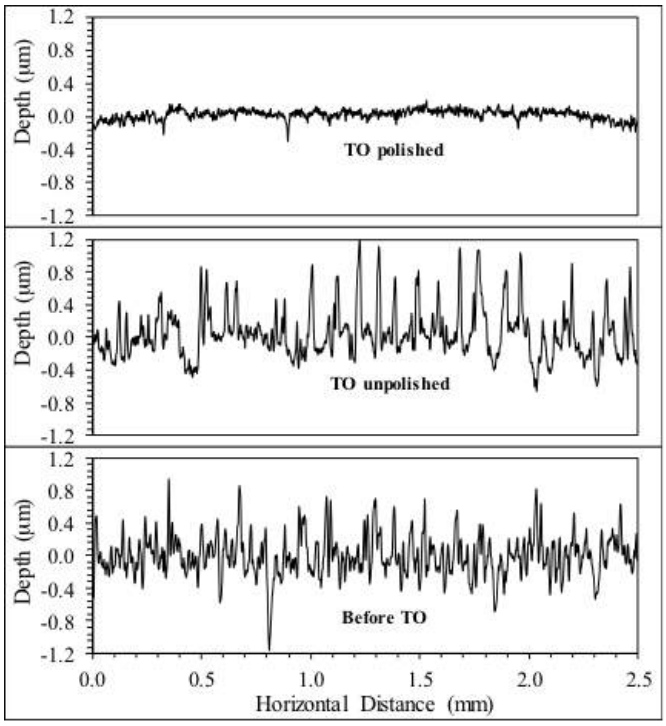


Figure 6.2: Surface roughness profiles measured before TO, after TO and after polishing.

Oxidized Zr is used as bearing components in artificial implants which are subjected to tribocorrosion involving combined mechanical wear and corrosion actions [33], but it also has potential uses in other fields involving dry sliding wear [4][18]. The main focus of this work was on the dry sliding wear behaviour of the TO samples with two different surface finishes. For this purpose, tribological tests were done using the pin-on-disk configuration under dry unlubricated conditions. A 7.9 mm diameter alumina ball (Grade 25 $Al_2O_3$) served as the counterface slider which was kept stationary during the test. The test sample was rotating against the slider

at 60 rpm for 3600 s, producing a circular wear track of 8 mm diameter. During the test, the coefficient of friction (COF) was measured continuously by the use of an integrated strain gauge and a computer data acquisition system. Two normal contact loads, 10 N and 20 N, were employed, which corresponded to initial contact pressures of about 1100 MPa and 1400 MPa, respectively, according to Hertz contact analysis based on the alumina ball contacting the untreated CP-Zr.

The wear volume was evaluated by using a stylus profilometer to measure the wear track profiles. From each profile, the cross-sectional area of the wear track was calculated and the wear volume was obtained by multiplying the cross-sectional area by the wear track circumference length. All tests were repeated twice and the average results are presented. After wear testing, an optical microscope and a scanning electron microscope (SEM) (equipped with EDX facilities for elemental composition analysis) were used to examine the worn surfaces in order to derive the wear mechanisms involved. To provide an inclined and enlarged view of the actual wear depth and the subsurface beneath the wear track, a ball crater was made on the wear track using a rotating bearing steel ball of 25.4 mm diameter. Such a ball-cratering technique has been widely used for measuring the thickness of thin coatings. It has recently been employed to aid in the examination of coating deformation beneath a wear track [175].

## 6.3 Results

Fig. 6.3a shows the COF curves recorded for the samples at 10 N load. Due to the dominance of plastic deformation in the untreated sample, the polished and unpolished untreated samples showed similar frictional behaviour. Thus only the COF curve for the unpolished sample is included for clarity purpose. From Fig. 6.3a, it can be seen that in the steady state after about 1000 s sliding, the TO-unpolished sample showed higher friction than the TO-polished sample. However, at the beginning up to 800 s, the TO-unpolished sample experienced lower friction than the TO-polished sample, which could be explained by the smaller contact area in the unpolished sample due to the initial asperity contact. It is also noted that in the steady state, the TO-unpolished sample showed higher friction than the untreated sample, while polishing after TO treatment was beneficial in lowering friction. As discussed later, under small contact loads (10 N), the OL did not suffer from any serious damage and was not worn through. Thus, the COF curves shown in Fig. 6.3a are characteristic of the OLs and the respective surface finish conditions.

Under high contact loads (20 N), the beneficial effect of polishing on reducing friction of the TO samples diminished, instead the TO-polished sample showed higher COF than the TO-unpolished sample during the entire sliding process (Fig. 6.3b). The COF of the TO-unpolished sample increased continuously during sliding, which could be related to the fact that the contact area also increased with time. The TO-polished sample initially followed the same trend, but after about 2000 s sliding, its COF started to decline, which may suggest a change in wear mechanism.

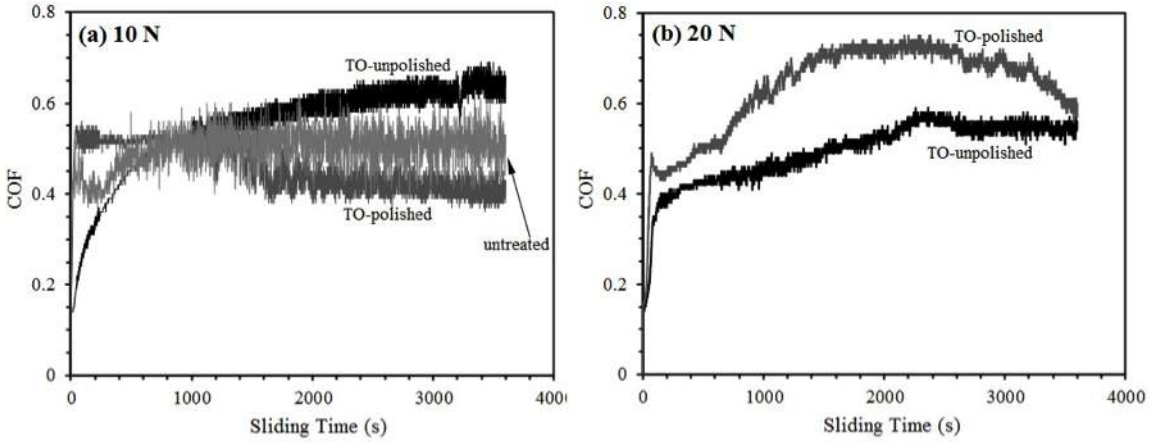


Figure 6.3: Coefficient of friction (COF) curves for the tested samples recorded during dry sliding under (a) 10 N and (b) 20 N contact loads.

The measured wear volumes from the wear tracks are summarized in Fig. 6.4. Surface finish did not have a significant effect on wear behaviour of the untreated sample, most likely due to the dominance of plastic deformation. At the smaller load of 10 N, the wear volume of CP-Zr was reduced by up to 100 times by the thermal oxidation treatment. Polishing after TO further reduced the wear volume of the TO sample. Polishing reduced the wear volume by 137%, as compared to the corresponding TO-unpolished sample. However, as the contact load was increased to 20 N, polishing after TO had an opposite effect on wear volume of the TO sample: polishing resulted in an increase in wear volume by 41%.

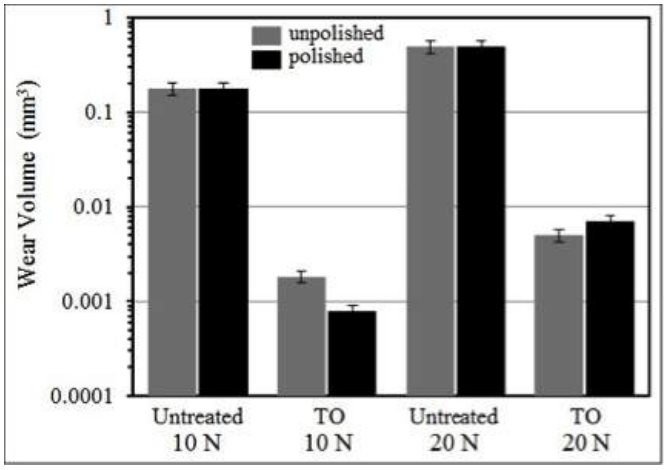


Figure 6.4: Measured wear volume for the tested samples after dry sliding for 3600 s under 10 N and 20 N contact loads.

Clearly, the effect of surface finish was load dependent. At low contact loads (10 N), smoothening the TO surface was beneficial in further reducing friction and wear, while at high contact loads (20 N), a slightly rough TO surface seemed more beneficial. To have a better understanding of the wear mechanisms and material deformation behaviour involved during sliding, the worn surfaces and subsurfaces were examined microscopically, as presented in the following paragraphs.

Fig. 6.5 presents SEM micrographs taken from the wear tracks on the TO samples produced under 10 N contact load. After 3600 s sliding, the TO-unpolished sample suffered from mild abrasive wear as some abrasion marks, together with some original grinding marks can be seen in the wear track (Fig. 6.5a). No cracks were observed in the wear track on the TO-unpolished sample. Interestingly, for the TO-polished sample, in addition to the parallel abrasion marks, many cracks, which ran across the sliding track and had a nearly semi-circular shape, were observed in the wear track (Fig. 6.5c and 6.5d). Clearly, a polished TO surface favoured the formation of cracks during dry sliding. Further examination revealed that the contact between the TO-unpolished surface and the alumina ball was at the asperity level, i.e. the sliding contact was made at the surface roughness peaks such that the roughness peaks were fragmented and fractured to generate wear debris, some of which filled the surrounding roughness valleys (Fig. 6.5a). Fig. 6.5b is a high magnification view of the real contact areas in Fig. 6.5a, revealing that many micro cracks were formed at the real contact areas and wear debris were generated. EDX elemental analysis revealed that the real contact areas contained a significant amount of aluminium, while in the non-contact areas, no aluminium was found (Fig. 6.6).

This suggests that material transfer occurred from the alumina ball to the TO-unpolished surface during sliding contact. On the contrary, the contact between the TO-polished surface and the alumina ball was more uniform with the majority of the wear track area making contact with the slider (Fig. 6.5c). Under higher magnifications, it was found that the real contact areas on the TO-polished surface were covered with a tribofilm (Fig. 6.5d). EDX analysis confirmed that the real contact areas were rich in aluminium, similar to the situation shown in Fig. 6.6. Thus material transfer also occurred from the alumina ball to the TO-polished surface.

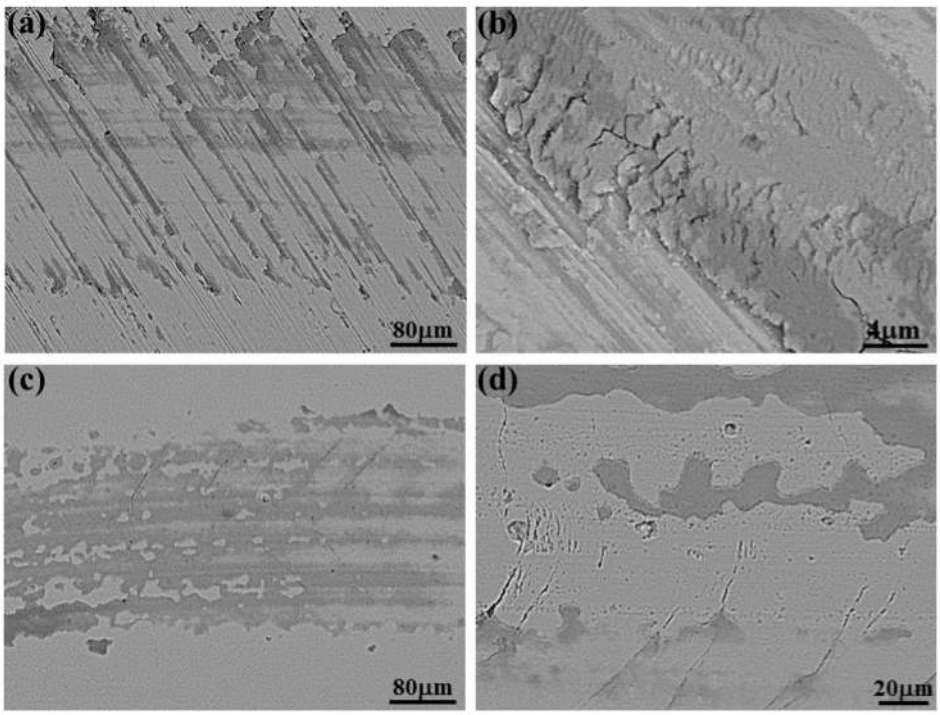


Figure 6.5: SEM images showing the morphology of the wear tracks produced under 10 N contact load on the TO-unpolished sample ((a) and (b)) and on the TO-polished sample ((c) and (d)). Note the formation of cracks on the TO polished sample in (c) and (d).

Fig. 6.7a shows a ball crater created by rotating a 25.4 mm steel ball on the wear track produced on the TO-polished sample at 10 N load. This made the subsurface region beneath the wear track visible in an inclined view. The enlarged view of the highlighted area in Fig. 6.7a is given in Fig. 6.7b. The wear depth was just a small fraction of the OL thickness. The semi-circular cracks at the wear track surface were found to have penetrated through the OL into the ODZ and the substrate, to a depth of more than 10 microns (arrowed, Fig. 6.7b). No obvious plastic deformation of

the oxide layer into the substrate can be observed at 10 N load, as evidenced by the maintenance of the circular contour of the interface between the OL and the ODZ in Fig. 6.7a. Thus it is safe to state that under the contact load of 10 N, the 6 $\mu$m thick OL, together with the underlying 3 $\mu$m thick ODZ, was effective in preventing the subsurface from plastic deformation. This may also explain why the OL could maintain its integrity with the substrate without breakdown despite the formation of many cracks which penetrated to the substrate.

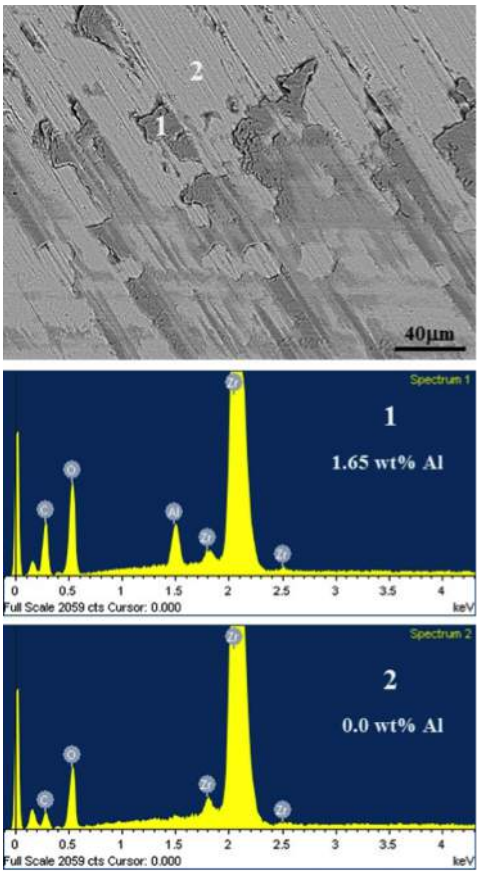


Figure 6.6: SEM image and EDX elemental spot analysis in area 1 and 2 of the wear track produced under 10 N contact load on the TO-unpolished sample.

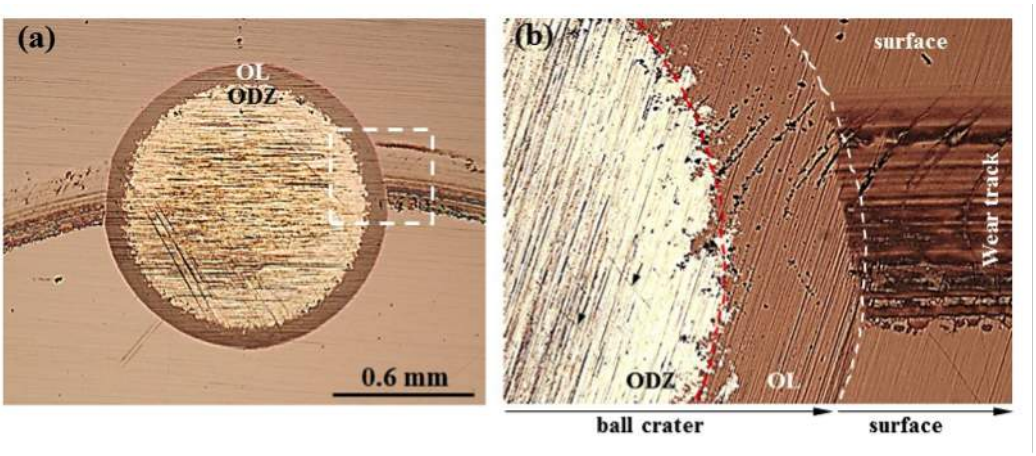


Figure 6.7: (a) Microscopic image showing the ball crater made on the wear track on the TO-polished sample after dry sliding under 10 N contact load, and (b) an enlarge view of the highlighted rectangle to show crack propagation beneath the wear track. Note the circular contour of the interface between the OL and ODZ in (a) and the penetration of cracks to the substrate (arrowed) in (b).

However, at a higher contact load (20 N), the situation became quite different. Fig. 6.8 shows the wear tracks produced at 20 N on the TO-unpolished and TO-polished samples. The original grinding marks, together with some cracks, can be visible in the wear track on the TO-unpolished sample (Fig. 6.8a). Cracking and failure of the OL were much more severe on the TO-polished sample (Fig. 6.8b). The OL on the TO-polished sample suffered from local breakdown and severe cracking with densely populated semi-circular cracks in the wear track (Fig. 6.8b). A comparison with the corresponding unpolished sample confirmed again that polishing after TO indeed favoured crack formation during dry sliding. The ball crater created on the wear track on the TO-polished sample (Fig. 6.9a) revealed that the OL was deformed or pushed into the substrate under the 20 N load. The surface cracks also penetrated through the OL into the ODZ and the substrate (Fig. 6.9b). Local failure of the OL can be seen in the wear track on the TO-polished sample.

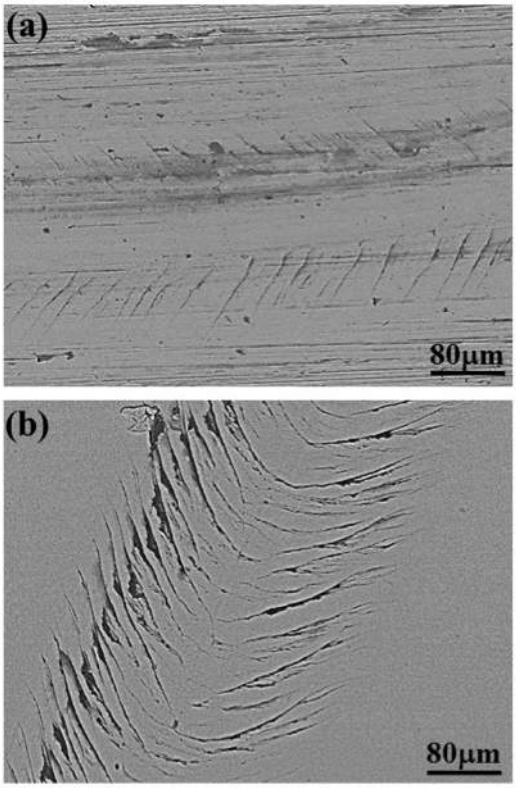


Figure 6.8: SEM images showing the wear tracks produced on the (a) unpolished and (b) polished TO sample under 20 N contact load.

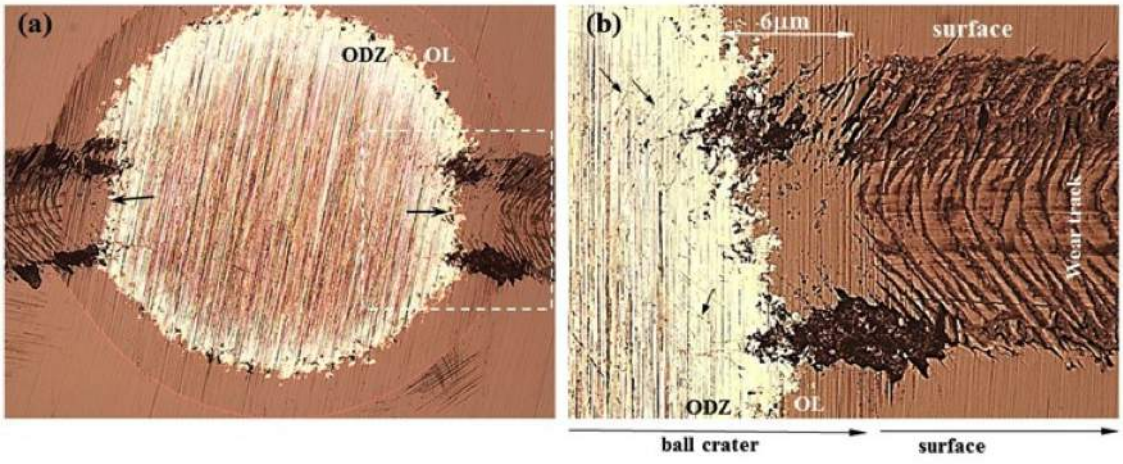


Figure 6.9: (a) Microscopic image showing the ball crater made on the wear track on the TO-polished sample after dry sliding under 20 N contact load, and (b) an enlarge view of the highlighted rectangle to show crack propagation beneath the wear track. Note the deformation of the OL into the substrate in (a) (arrowed) and propagation of cracks to the substrate (arrowed) in (b).

SEM examination (Fig. 6.10) showed that the cracks on the TO-polished specimen were filled with wear debris. EDX analysis, shown in Fig. 6.10, revealed that there was much more aluminium in the cracks filled with wear particles than in the real contact areas outside the cracks. This demonstrates that wear of the alumina ball contributed to wear debris formation in the tribosystem.

To gain a further insight into the contact behaviour and the development of cracks with sliding time, a series of experiments were conducted involving sliding for various times, followed by microscopic examination of the wear track and the wear scar on the counterface. Fig. 6.11 compares the wear tracks on the TO-polished sample after sliding at 10 N and 20 N for various times. At 10 N, the contact between the TO-polished surface and the alumina ball was confined to a narrow width during the first 300 s sliding. No cracks were observed at this stage (Fig. 6.11a). As sliding proceeded, the wear track width and the wear scar size on the counterface ($Al_2O_3$ ball) were increased. After sliding for 1800 s at 10 N, semi-circular cracks started to appear (Fig. 6.11b). With continuous sliding to 3600 s, semi-circular cracks were fully developed on the polished sample (Fig. 6.5c). The development of cracks on the polished sample was load dependent. Under the higher load of 20 N, semi-circular cracks were developed after sliding for just 300 s (Fig. 6.11c). With continuous sliding to 900 s, the cracks were further developed with new cracks formation within the widened wear track (Fig. 6.11d). After sliding for 3600 s, densely populated cracks were developed, leading to the onset of OL breakdown (Fig. 6.9b).

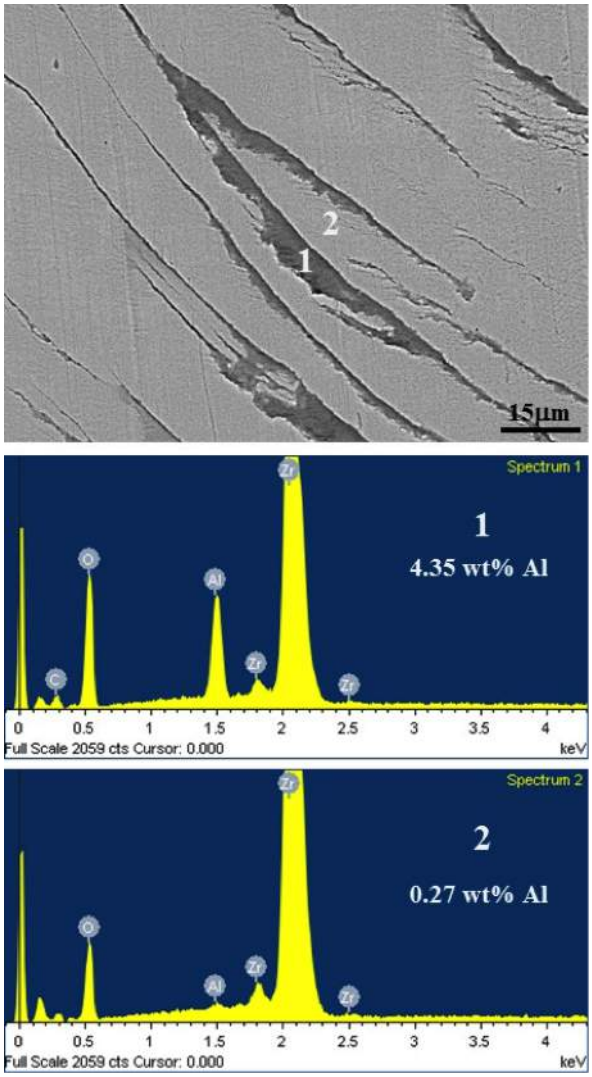


Figure 6.10: SEM image and EDX elemental spot analysis of area 1 and 2 of the wear track produced under 20 N contact load on the TO-polished sample.

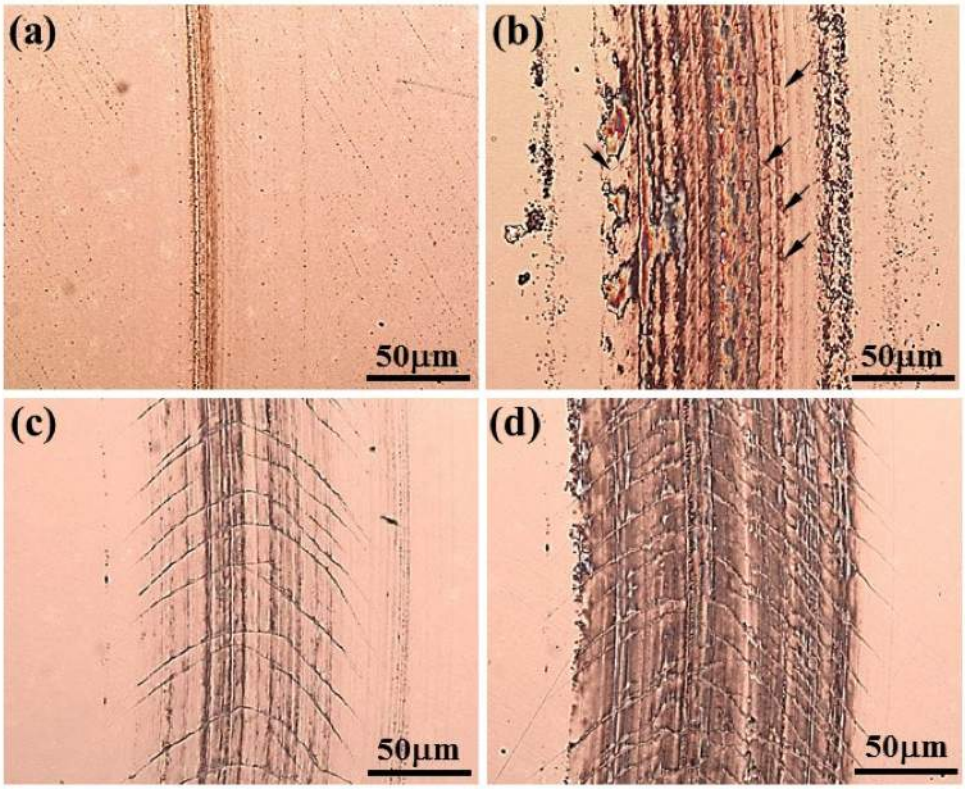


Figure 6.11: Microscopic images showing the morphology of the wear tracks after dry sliding testing the TO-polished sample at 10 N for (a) 300 s and (b) 1800 s, and at 20 N for (c) 300 s and (d) 900 s. Note the formation of semi-circular cracks after sliding for 1800 s in (b) (arrowed).

In Fig. 6.12, the measured mean diameter of the wear scar on the counterface is plotted against sliding time at 10 N. The wear scar was larger when sliding against the TO-unpolished surface. Thus, as compared to the TO-polished surface, the TO-unpolished surface caused more wear of the counterface alumina ball, which is expected from the general principle of tribology of rough surfaces [166][170].

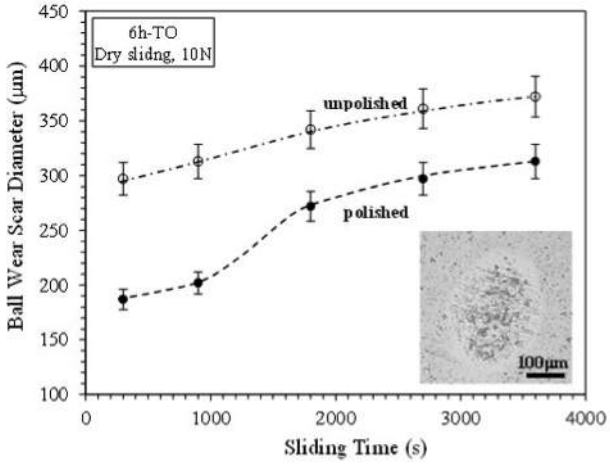


Figure 6.12: Mean diameter of the wear scar on the alumina ball counterface as a function of sliding time on the TO-polished and unpolished samples.

## 6.4 Discussion

The experimental results demonstrated that surface finish affected the tribological behaviour of thermally oxidized CP-Zr in several aspects, including COF, wear volume, crack formation and breakdown of the OL. At relatively small contact loads (e.g. 10 N), smoothening the TO surface by polishing was beneficial in reducing friction (Fig. 6.3a) and wear volume (Fig. 6.4). This agrees with general observations made by other investigators for both bulk and coating materials that a rougher surface results in higher friction and higher wear rates of both the test specimen and the counterface. The higher friction and wear rates resulting from rough surfaces have several origins, including the ploughing action of the surface peaks, the deformation and fracture of the asperities, the change in real contact areas, the filling of the surface roughness valleys with wear debris and the mechanical interlocking provided by the asperities. It is also generally observed that after a certain period of sliding, the surface asperities become gradually flattened and the original surface finish is destroyed, thus the initial surface finish effect on friction and wear will diminish [169][170][171][173].

The most striking observation made in this work is that smoothening the surface by polishing after TO favoured the formation of cracks running across the wear tracks (Fig. 6.5 and Fig. 6.8). Although at 10 N contact load, the hardened surface was effective in preventing plastic deformation in the substrate (Fig. 6.7a), many semi-circular cracks were developed in the wear track on the TO-polished sample,

but no such cracks were found on the corresponding unpolished sample (Fig. 6.5). There seemed an incubation time for the formation of semi-circular cracks on the TO-polished sample, as shown in Fig. 6.11. Such an incubation time was load dependent: it took about 1800 s for the cracks to form at 10 N, while at 20 N, cracks formed at the very early stage of sliding (300 s). These cracks on the TO-polished sample propagated through the surface layers down to the substrate (Fig. 6.7 and Fig. 6.9). The fact that the OL did not detach or flake from the substrate indicates that the crack length was not sufficient to cause final fracture of the OL under 10 N load. According to the principle of fracture mechanics, a material fractures when a critical crack length is reached. Such a critical crack length decreases with increasing stress level. Under the present contact condition at 10 N load, the contact stress level and the crack prorogation depth were not sufficient to cause OL breakdown. Increasing the contact load to 20 N was sufficient to cause the fracture and even the local breakdown of the OL (Fig. 6.8b and Fig. 6.9b). The existence of an incubation time for the formation of cracks (Fig. 6.11) suggests that the fracture of the OL was a fatigue process. Thus, it can be predicted that with prolonged sliding, the OL would breakdown at 10 N load once the cracks propagate to reach critical lengths.

In the wear tracks on the TO-unpolished sample, semi-circular cracks were not observed at 10 N and were only observed at 20 N, but to a lesser extent than those on the TO-polished sample. The beneficial effect of surface roughness in delaying semi-circular crack formation and propagation can be explained as follows. Under the present testing conditions, the contact between the TO-unpolished surface and the smooth alumina ball was at the asperity level (Fig. 6.5). The hard $ZrO_2$ asperities not only had a ploughing action on the alumina ball to result in a large wear scar on the ball (Fig. 6.12), but also suffered from extremely high contact pressures, as predicted by the contact models developed for rough surfaces [169][176][177]. Thus the contact stresses were concentrated at the highest asperities and the stresses in the non-contacting areas and in the bulk of the OL must be much reduced. The high stresses at the asperities resulted in the flattening of the contacting asperities through fragmentation and fracture. Although semi-circular cracks were not observed at 10 N load, many micro cracks were found at the real contact areas, which led to wear debris formation through fracture (Fig. 6.5b). Thus the micro cracks at the contacting asperities did not have the opportunity to develop into larger cracks in the bulk of the OL at 10 N load. With increasing sliding time, more asperities were brought into contact and the ball wear scar size increased (Fig. 6.12). The increased apparent and real contact areas helped to reduce contact stresses at the

asperities. Semi-circular cracks were only able to form in the smoothened areas at 20 N (Fig. 6.8a), where asperity deformation and fracture became less dominant.

## 6.5 Conclusion

The dry sliding wear behaviour of TO-unpolished and TO-polished CP-Zr samples were investigated. The main findings are summarized as follows:

- Smoothening the oxidized surface by polishing is beneficial in reducing friction and wear volume of the TO sample if the contact load is relatively small (10 N).
- Under high contact loads (20 N), smoothening the oxidized surface deteriorates the wear resistance of the TO sample and accelerates the breakdown of the oxide layer.
- Smoothening the oxidized surface by polishing favours the formation of large semi-circular cracks in the wear tracks during dry sliding under both contact loads.
- The semi-circular cracks developed at the TO-polished surface propagate through the surface layers to reach the substrate. This leads to the local breakdown of the oxide layer after sliding for a certain period of time under sufficiently large contact loads (e.g. 20 N), because at higher loads there is more contact between the alumina ball and surface of the sample.
- A slightly rough TO surface (unpolished) is beneficial in reducing the tendency of the oxide layer towards cracking during dry sliding, owing to the dominance of asperity contacts which lead to micro crack formation at the real contact areas and fracture of the contacting asperities.

# Chapter 7

# A comparative study of the mechanical behaviour of thermally oxidized commercially pure titanium and zirconium

The objective of this study is to compare the mechanical behaviour of thermally oxidised commercially pure titanium (CP-Ti) and commercially pure zirconium (CP-Zr). For this purpose, these two bio-metals were thermally oxidised under the same condition ($650^oC$ for 6 h) and the oxidised specimens were characterised using various analytical and experimental techniques, including oxygen uptake analysis, layer thickness and hardness measurements, scratch tests, dry sliding friction and wear tests and tribocorrosion tests in Ringer's solution. The results show that under the present thermal oxidation condition, 4 times more oxygen is introduced into CP-Zr than into CP-Ti and the oxide layer produced on CP-Zr is nearly 6 times thicker than that on CP-Ti. Thermally oxidised CP-Zr possesses a higher hardness, a deeper hardening depth and better scratch resistance than thermally oxidised CP-Ti. Under dry sliding and tribocorrosion conditions, thermally oxidised CP-Zr also possesses much better resistance to material removal and a higher load bearing capacity than thermally oxidised CP-Ti. Thus, thermally oxidised Zr possesses much better mechanical behaviour than thermally oxidised Ti.

## 7.1 Introduction

Titanium (Ti) and zirconium (Zr) are bio-metals that are used in the biomedical sector to make medical devices and implants [3][178][179]. They possess a good combination of strength, corrosion resistance and biocompatibility, which are desirable as biomaterials [180]. Both metals have a hexagonal close packed (HCP) crystal

structure at room temperature and derive their corrosion resistance and passivity by the naturally occurring oxide film at the surface. Both Ti and Zr are also known to possess poor tribological properties. When in contact motion with themselves or other materials, they suffer from severe metallic wear with the tendency towards galling and seizure [4][178][181]. Thus, the uses of Ti and Zr have been restricted to mostly non-tribological applications. However, with proper surface modification to alter the surface chemical, physical and mechanical properties, Ti and Zr and their alloys can be used to make bearing components such as in artificial hip and knee joints [19][182].

Thermal oxidation offers a simple and cost-effective way to modify the surfaces of Ti and Zr and their alloys to achieve much enhanced tribological and bio-tribological properties [4][14][18][181][183][184]. Indeed, thermally oxidised Ti alloys have been reported to have the potential use in artificial hip joints [185][186][187], and thermally oxidized Zr has recently been introduced as an alternative bearing in total joint arthroplasty for artificial knee and hip joints [31][32][33][37]. Thermally oxidised Ti and Zr possess the desirable combination of a ceramic bearing surface to resist wear and a tough metallic core to resist fracture [182][14][174].

Both Ti and Zr are reactive metals with a high affinity with oxygen to form an oxide film easily. They can also dissolve a large amount of oxygen in the HCP lattice to form a solid solution with a significant hardening effect. Thermal oxidation is normally carried out at temperatures between $500^oC$ and $700^oC$ in ambient atmosphere or in controlled atmospheres. During thermal oxidation, oxygen diffuses into the CP materials to form an oxygen diffusion zone (ODZ) with interstitial solid solution hardening, and once the surface is saturated with oxygen, an oxide layer (OL) develops at the surface. Thus thermally oxidised CP-Ti and CP-Zr comprise an OL at the surface and a hardened ODZ in the subsurface [15][18][174][188]. The OL can improve frictional characteristics and offer wear resistance, while the ODZ can offer load bearing capacity. However, the quality of the OL depends on thermal oxidation conditions, such as temperature and time. High temperature and/or long time oxidation would produce a none-adherent, fragile and crumbly OL on Ti, which has a tendency to delaminate from the substrate [15][189][190]. Similarly, oxidation breakaway would occur to Zr during high temperature or long time oxidation, characterised by the formation of pore and cracks in the OL [25][26][161]. It has been observed that an oxidation temperature between $600^oC$ and $700^oC$ offers the best compromise between generating a sufficiently thick oxide layer and maintaining good adhesion between the OL and the substrate for both Ti and Zr [14][191][192].

Despite the extensive research in recent years on thermal oxidation of Ti and Zr for enhanced tribological properties and biomedical applications, no studies have been reported to directly compare their oxidation behaviour and their mechanical performances after thermal oxidation. Due to the importance of these two bio-metals and their ability to be hardened by oxidation, it is necessary to compare the thermal oxidation behaviour of these two bio-metals and their response to mechanical and combined mechanical and chemical actions. In this investigation, commercially pure Ti and Zr were thermally oxidised under the same condition. Using the same oxidation condition provides a direct comparison of the oxidation behaviour and the resultant mechanical properties of the two biometals. The oxidised specimens were compared in terms of layer thickness, hardness, scratch resistance, and tribological behaviour under dry unlubricated conditions and tribocorrosion behaviour under simulated physiological conditions.

## 7.2 Material and Methods

### 7.2.1 Materials and thermal oxidation

Commercially pure titanium (CP-Ti) grade 2 (99.4% purity) and commercially pure zirconium (CP-Zr) grade 2 (99.2% purity) were used in this work. The original metallurgical structure of these CP materials comprised HCP $\alpha$-phase. Specimens of 20 mm x 15 mm x 1 mm were prepared by machining the as-received plates. The specimens were wet ground using metallographic SiC grinding papers down to the P1200 grade, then polished in 6 micron diamond suspensions for 5 min, and finally finished by polishing in silica suspensions for 40 min to achieve a mirror-like surface finish of 0.03 $\mu$m ($R_a$).

Before thermal oxidation (TO), the specimens were ultrasonically cleaned in methanol for 10 min, thoroughly dried in a stream of hot air, and weighed using an analytical balance accurate to 0.1 mg. After TO, the specimens were weighed again to obtain the total mass gain by each type of specimens. The total mass gain was divided by the total surface area of the specimens to obtain the mass gain per unit surface area ($mgcm^{-2}$). This provides information regarding oxygen uptake by the CP-Ti and CP-Zr specimens during the TO process.

Thermal oxidation was conducted in an air furnace at a constant temperature of $650^oC$ for a constant time of 6 h. After 6 h at $650^oC$, the specimens were allowed to cool slowly in the furnace down to room temperature. This TO condition was chosen

based on many preliminary experiments and previous work, which can produce an adherent oxide layer at the surface and an oxygen diffusion zone in the subsurface of CP-Ti and Ti alloys [15][190][193] and in CP-Zr and Zr alloys [14][174]. This condition also ensured that no phase transformation took place in the core of the CP materials because the oxidation temperature was below the $\alpha$-$\beta$ transformation temperatures.

### 7.2.2 Characterisation of TO specimens

After TO, the specimens were characterised by (1) surface roughness measurements using a contact mode profilometer (Mitutoyo SJ-400); (2) surface hardness measurements using a micro Vickers hardness tester (Indentc ZHV) at various loads from 0.025 to 1.0 kg; (3) X-ray diffraction (XRD) analysis using Cu-$K_\alpha$ radiation to identify the phases of thermally oxidised specimens; (4) microscopic examination of the cross sectional morphology and measurement of the thicknesses of the oxidised layers; (5) micro Vickers hardness profile measurements across the oxidised layers in the cross section using an indentation load of 0.025 kg; and (6) scratch testing of the oxidised surface using a Rockwell diamond tip with a radius of 200 $\mu$m under various constant loads from 1 N to 30 N. After scratch testing, the width of each resultant scratch mark was measured and the morphology of the scratch was examined microscopically to assess the failure modes and the critical failure load of the oxide layer. A ball crater of about 1 mm diameter was also made on the scratch by rotating a bearing steel ball of 25.4 mm diameter at the same spot at a speed of 60 revolutions per minute to provide an inclined and enlarged view of the deformation behavior beneath the scratch. Fig. 7.1 shows a typical scratch on the TO-Zr surface and a ball crater made on the scratch which provides a clear view of the scratch depth and the deformation of the OL towards the substrate. By zooming in the highlighted rectangular zone, the deformation and crack penetration behaviour could be more clearly observed.

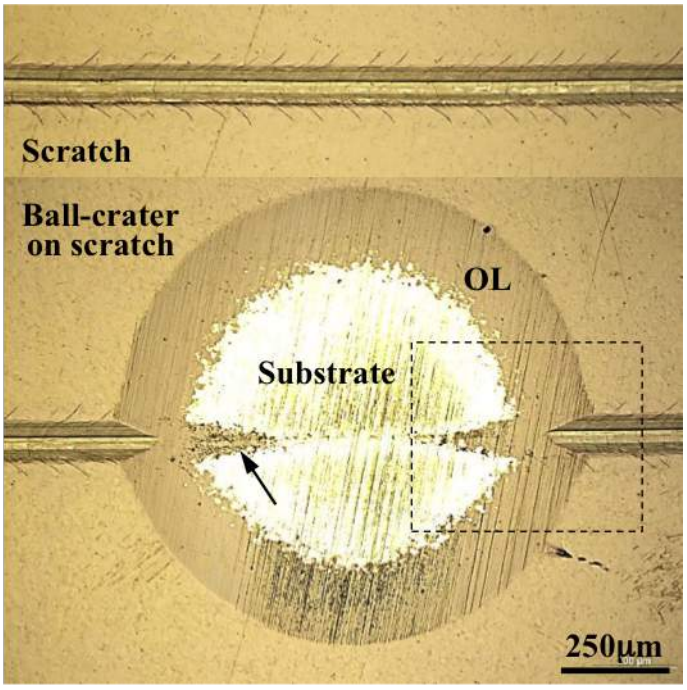


Figure 7.1: A typical scratch on the TO-Zr surface and a ball crater made on the scratch to provide an enlarged view of the OL and the material deformation behavior beneath the scratch (arrowed).

### 7.2.3 Dry sliding wear and tribocorrosion tests

Dry sliding friction and wear tests were conducted using a laboratory-scale reciprocating wear tester. During the test, the specimen reciprocated linearly at a frequency of 1 Hz and amplitude of 8 mm. The contacting counterface was an 8 mm diameter alumina ball (Grade 25 $Al_2O_3$ supplied by Trafalgar Bearings Ltd) due to its inertness and high hardness. The tests were carried out at room temperature ($22^oC$), in ambient environment for duration of 3600 s. During the test, the coefficient of friction (COF) was recorded by a computer data acquisition system. The contact loads ranged from 1 N to 20 N. Hertzian contact stress calculation showed that these contact loads resulted in initial maximum contact pressures ranging from 468 MPa to 1272 MPa for the Ti specimens and from 412 MPa to 1119 MPa for the Zr specimens. All tests were duplicated and the mean results are presented.

Tribocorrosion tests were conducted using the same reciprocating wear tester at a reciprocating frequency of 1 Hz and amplitude of 8 mm. The tests were carried out by immersing the test specimen in 1 M Ringer's solution maintained at $37^oC$, contained in a tribo-electrochemical cell made of an insulating material, nylon. An alumina ball of 8 mm diameter was used as the slider and the applied contact loads

ranged from 1 N to 20 N. All tests were conducted at open circuit without externally applied potential. Before each test, the specimen was stabilised at open circuit for 300 s without contact with the slider. After sliding for 3600 s, the specimen was left in the solution for further 300 s without contact with the slider. The open circuit potential (OCP) was recorded continuously before, during and after sliding. An ACM Gill AC potentiostat was used to measure the OCP of the specimen using a saturated calomel electrode (SEC) as the reference electrode.

Every dry sliding wear and tribocorrosion test was duplicated and the results from two tests were consistent. After the tests, the wear and corrosion-wear tracks were examined under optical and scanning electron microscopes. The cross-sectional profiles of the wear tracks were measured by a stylus profilometer (Mitutoyo SJ-400) to assess the actual depth and width of the tracks and the amount of material removal. The measured total material removal (TMR) in volume was then divided by the total sliding distance and the applied contact load to obtain the specific total material removal rate in $mm^3N^{-1}m^{-1}$. A ball crater about 1 mm diameter was then made on the wear track by rotating a 25.4 mm diameter bearing steel ball to reveal the actual wear depth and the deformation and cracking behaviour beneath the wear surface, as highlighted in Fig. 7.1 for the scratch on the oxidised surface.

## 7.3 Results and Discussion

### 7.3.1 Structural characteristics

Fig. 7.2 shows the cross-sections of the thermally oxidised (TO) Ti and Zr specimens and Table 7.1 summarises the characteristics of the untreated and TO specimens. In consistency with the observations of other investigators [193][194], TO produced a dark oxide layer (OL) at the surface and an oxygen diffusion zone (ODZ) at the subsurface of both materials (Fig. 7.2). After the TO treatment, the originally polished surface was slightly roughened, with the $R_a$ value increased from about 0.03 $\mu$m to about 0.05 $\mu$m for both TO specimens (Table 7.1). This could be due to the anisotropic growth of the oxide layer in different grain orientations. Another observation lies in that the mass gain during TO by Zr was 4 times larger than that by Ti, see Table 7.1. This suggests that under the present TO conditions, 4 times more oxygen was incorporated into the surface region of Zr than into Ti. The greater oxygen uptake by Zr was confirmed by microscopic examination of the cross-sections of the TO specimens, shown in Fig. 7.2. A much thicker OL was

Table 7.1: Surface and layer characteristics of raw and TO Ti and Zr. Note: Each value in the table is the average of 6 measurements. The deviations are rounded to respective decimal places.

| Specimen | Surface finish $R_a$ ($\mu$m) | Mass gain after TO ($mgcm^{-2}$) | Surface hardness $HV_0.025$ | OL thickness ($\mu$m) | ODZ thickness ($\mu$m) |
|---|---|---|---|---|---|
| Raw Ti | 0.032±0.005 | - | 186±9 | - | - |
| TO Ti | 0.055±0.005 | 0.26±0.02 | 1115±56 | 1.1±0.2 | 4.5±0.3 |
| Raw Zr | 0.032±0.005 | - | 198±9 | - | - |
| TO Zr | 0.048±0.005 | 1.04±0.02 | 1383±57 | 6.3±0.2 | 2.9±0.3 |

formed on Zr than on Ti under the same TO condition. The OL formed on Zr was 6.3 $\mu$m thick, while that on Ti was only 1.1 $\mu$m thick. However, the oxygen diffusion (ODZ) measured from Fig. 7.2 was thicker in Ti (4.5 $\mu$m, see Table 7.1) than in Zr (2.9 $\mu$m). XRD analysis (Fig. 7.3) confirmed that the thin OL formed on Ti was rutile titanium dioxide (R-$TiO_2$), while the thick OL formed on Zr was monoclinic zirconium dioxide (m-$ZrO_2$). The diffraction peaks from the substrate ($\alpha$-Ti and $\alpha$-Zr) were shifted to lower angles as compared to standard peaks due to the dissolution of oxygen in the diffusion zone, which caused expansion of the hexagonal close packed (hcp) lattices. For example, the $\alpha$-Ti (101) and (012) peaks were shifted from $40.20^o$ and $53.03^o$ to $40.03^o$ and $52.51^o$, respectively. The $\alpha$-Zr (101) and (012) peaks were shifted from $36.54^o$ and $48.03^o$ to $36.32^o$ and $47.74^o$, respectively.

Based on the atomic weight of the involved elements (Ti, Zr and O), the molar mass of $ZrO_2$ (123.22 $gmol^{-1}$) and $TiO_2$ (79.87 $gmol^{-1}$), and the theoretical density of m-$ZrO_2$ (5.68 $gcm^{-3}$) and R-$TiO_2$ (4.23 $gcm^{-3}$), using equation (3.4), it can be estimated that it would require 0.93 $mgcm^{-2}$ oxygen uptake to form a dense m-$ZrO_2$ layer of 6.3 $\mu$m thick on Zr and 0.19 $mgcm^{-2}$ oxygen uptake to form a dense R-$TiO_2$ layer of 1.1 $\mu$m thick on Ti. Subtracting these values from the measured mass gain in Table 7.1 led to that in the TO-Ti specimen, 0.07 $mgcm^{-2}$ oxygen uptake during TO diffused into the subsurface to form the diffusion zone, as compared to 0.11 $mgcm^{-2}$ in the TO-Zr specimen. Thus more oxygen diffused to the subsurface of TO-Zr than to that of TO-Ti. The above analysis was based on the assumption that the weight gain was caused by oxygen only. Nitrogen uptake was not considered because nitrogen is more inert than oxygen and XRD could not detect any nitride formation in the oxidised specimens.

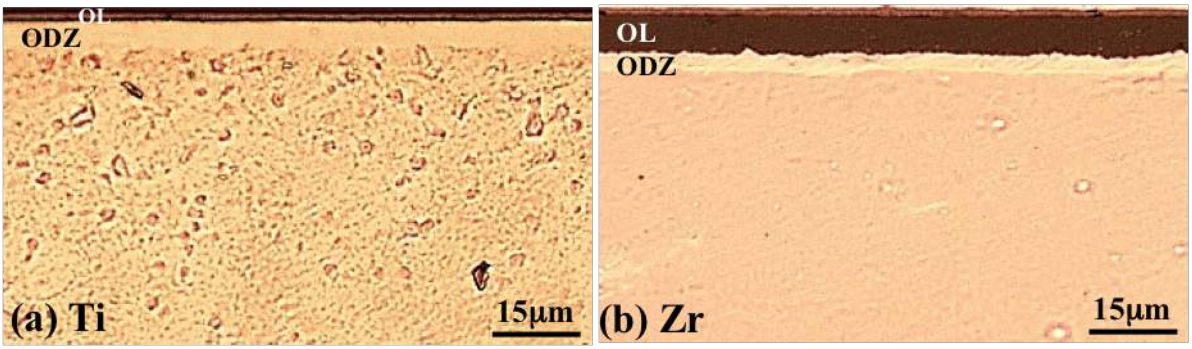


Figure 7.2: Microscopic images showing the cross-sectional morphology of the (a) TO-Ti and (b) TO-Zr specimens produced at $650^oC$ for 6 h.

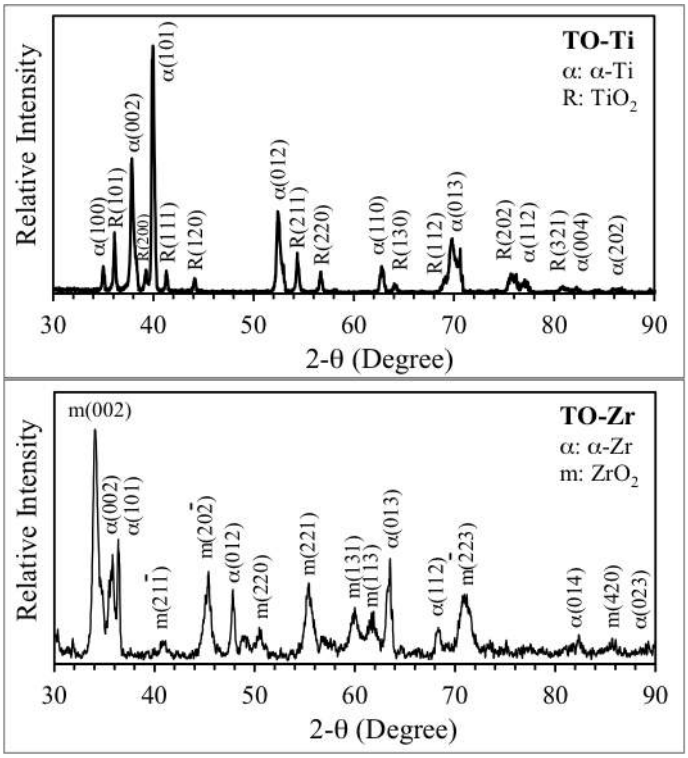


Figure 7.3: X-ray diffraction patterns generated from the TO-Ti and TO-Zr specimens.

### 7.3.2 Surface hardness and hardness profiles

As the result of oxygen incorporation in the surface and subsurface regions to form an OL and an ODZ, the surface and subsurface hardness of CP-Ti and CP-Zr were significantly increased. Fig. 7.4(a) shows the surface hardness as a function of indentation load and Fig. 7.4(b) shows the hardness profiles measured across the

OL and ODZ in the cross section. The measured surface hardness decreased with increasing indentation load (Fig. 7.4a) due to the increased substrate effect. At the small indentation load of 0.025 kg, the TO-Zr surface exhibited a hardness close to 1400 $HV_{0.025}$, which was higher than the surface hardness of TO-Ti (about 1100 $HV_{0.025}$). Under all indentation loads, the TO-Zr specimen possessed higher surface hardness and thus better load bearing capacity than the TO-Ti specimen. From the insets in Fig. 7.4(a), it can also be seen that indentation under high loads (higher than 0.02 kg) led to the formation of cracks surrounding the indent, without flaking of the OL. This suggests that both OLs were relatively brittle but had good adhesion with the underlying ODZ. Hardness profile measurements in the cross sections revealed that the TO-Zr specimen possessed higher hardness than the TO-Ti specimen at all measurement depths, see Fig. 7.4(b). The better hardening effect in TO-Zr can be explained by the greater oxygen uptake and the resultant thicker OL.

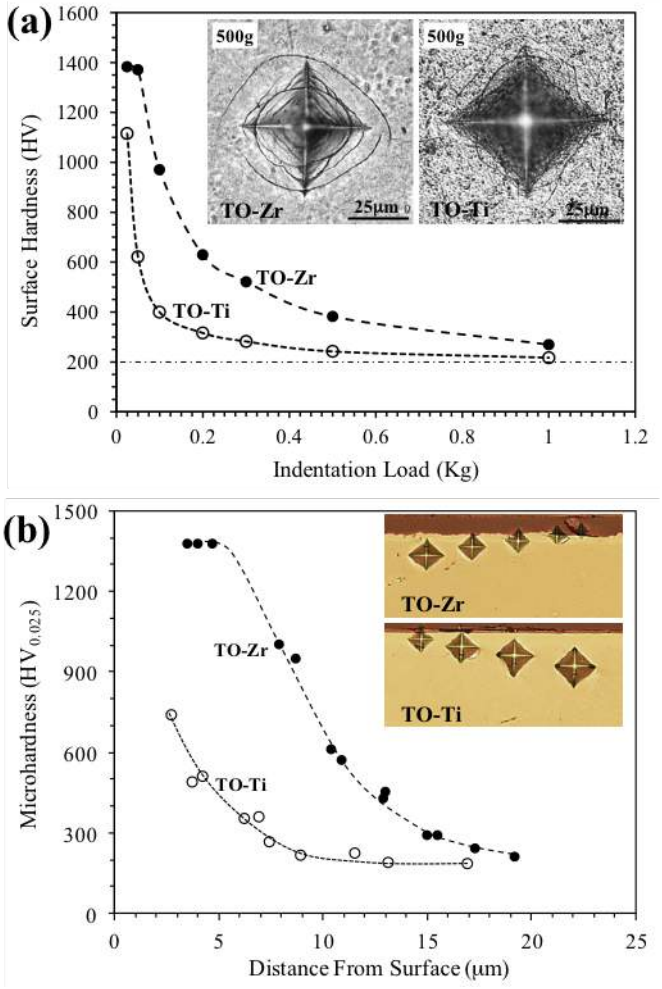


Figure 7.4: Surface hardness of the TO-Ti and TO-Zr specimens as a function of indentation load (a) and microhardness profiles measured across the oxidised layers (b). The insets show the hardness indents made on the surface (a) and in the subsurface (b). The hardness indents shown in (b) are for illustration only. In actual measurements, the distance between two indents was more than three times of the indent size.

### 7.3.3 Scratch resistance

Fig. 7.5 shows the variation of scratch width with applied scratch load for TO-Ti and TO-Zr. At all scratch loads, the scratch width on TO-Zr was smaller than that on TO-Ti. Thus TO-Zr had better scratch resistance than TO-Ti.

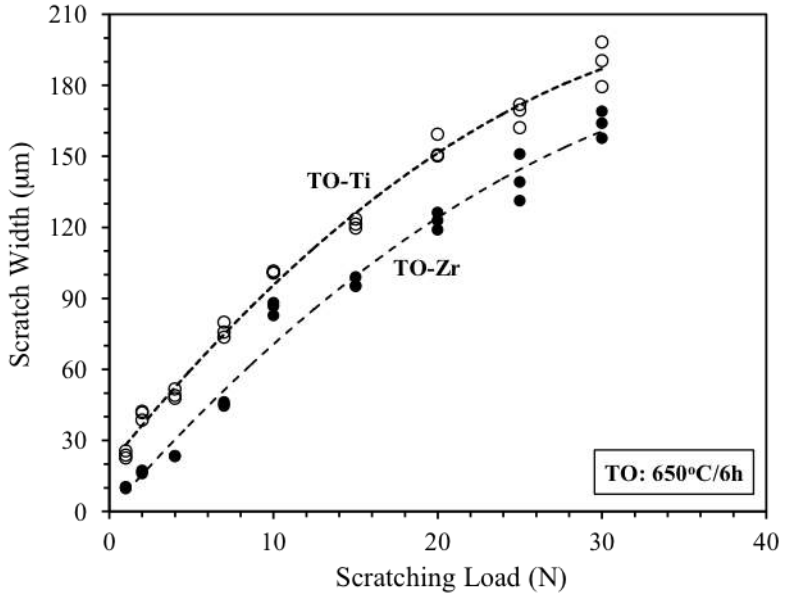


Figure 7.5: Scratch width as a function of scratch load for the TO-Ti and TO-Zr specimens.

Typical microscopic images of the scratches on TO-Ti are given in Fig. 7.6, from which it can be seen that cracks started to form both inside and outside the scratch at a scratch load as low as 4 N. The cracks inside the scratch were nearly perpendicular to the scratch direction and were the result of the tensile stresses caused by the tangential traction of the stylus [162], while the cracks outside the scratch had a chevron shape and were most likely caused by the bending of the OL due to plastic deformation inside the scratch [163]. When the scratch load was increased to 7 N, cracking of the OL inside the scratch became more serious and spallation or flaking of the OL occurred at the edges of the scratch. Cracking and edge spallation of the OL became more severe when the scratch load was further increased to 10 N and above. Thus, the critical load for the $TiO_2$ layer failure was 7 N.

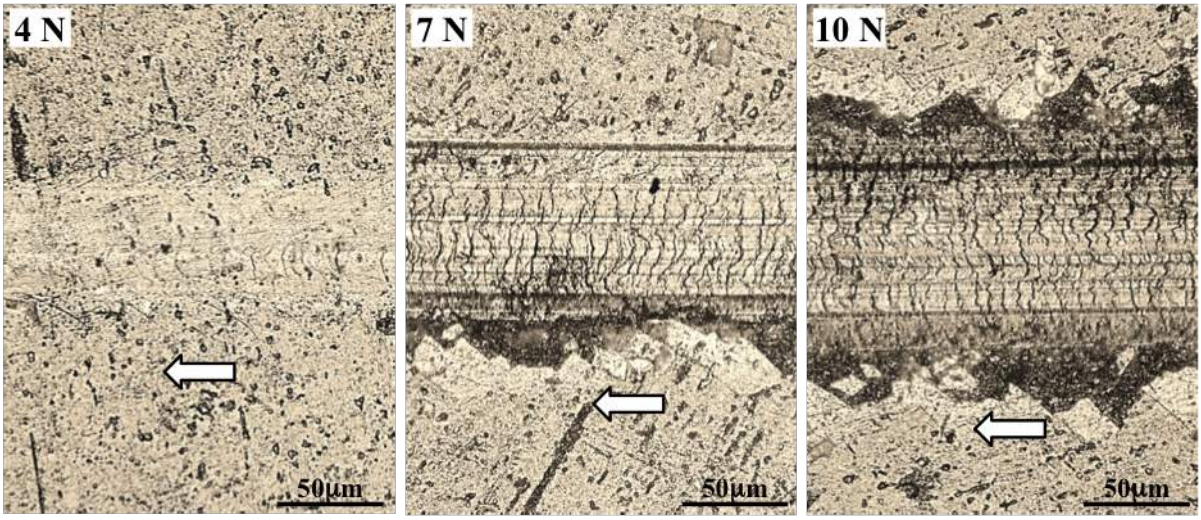


Figure 7.6: Microscopic images showing the scratches made on the TO-Ti surface at various scratch loads. Arrow indicates the scratch direction.

Fig. 7.7 shows the scratches on the TO-Zr specimen, together with zoom-in view of the ball craters made on the scratches to reveal the OL and the substrate beneath each scratch. It can be clearly seen that at 10 N scratch load (Fig. 7.7a), the OL in the scratch was plastically deformed into the substrate. Despite such a significant plastic deformation, no adhesive failure such as debonding and flaking of the OL was observed. The plastic deformation of the OL inside the scratch caused the bending of the OL at the edges of the scratch and thus the formation of the chevron type cracks. When the scratch load was increased to 15 N and 20 N (Fig. 7.7b), the OL inside the scratch was deformed further into the substrate without layer detachment. However, at the edges of the scratch, in association with the chevron type cracks, chipping of the OL layer was observed. The depth of such chippings was approximately at the OL-ODZ interfacial region, thus demonstrating the adhesive failure nature. At further higher scratch loads, 25 N and 30 N (Fig. 7.7c), chipping at the edges became more significant, and at the same time the OL inside the scratch was removed completely. Thus, the critical load for adhesive failure of the $ZrO_2$ layer was 15 N, which was much larger than 7 N measured for the $TiO_2$ layer. More importantly, the results shown in Fig. 7.7 demonstrate that the $ZrO_2$ layer had the ability to accommodate severe plastic deformation without adhesive failure (Fig. 7.7a). The good integrity of the $ZrO_2$ layer with the underlying ODZ can be explained by the variation of stoichiometry and oxygen vacancies with depth from the surface in the $ZrO_2$ layer. It has been found that in the OL produced on Zr-2.5%Nb alloy by the commercial $Oxinium^{TM}$ process, there existed an interfacial

region about 1 $\mu$m thick between the OL and ODZ where a peculiar stoichiometric balance was achieved with a diffuse-type oxygen concentration [194]. This would help to relieve the residual stresses arising from the thermal expansion mismatch between the surface ceramic OL and the metallic ODZ, and thus would contribute to enhanced integrity of the OL.

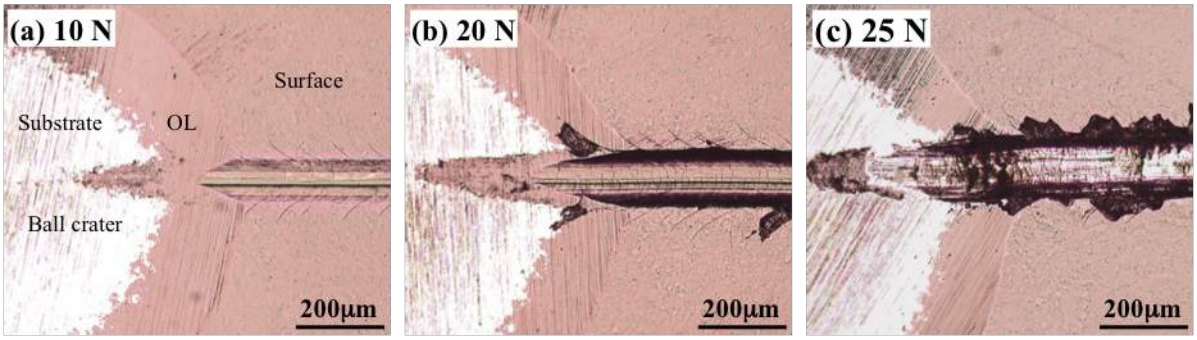


Figure 7.7: Microscopic images showing the zoom-in view of ball craters on scratches made on the TO-Zr surface at various scratch loads.

### 7.3.4 Dry sliding wear behaviour

During dry sliding, a transition in friction and wear behaviour was observed above certain critical loads for the TO-Ti and TO-Zr specimens. Fig. 7.8 shows the recorded coefficient of friction (COF) curves for the two specimens at various contact loads. At a small contact load of 1 N, both specimens behaved similarly and exhibited a smooth frictional behaviour. The COF value gradually increased with sliding time and then reached a stable value between 0.5 and 0.6. Increasing the contact load to 2 N led to an increase in COF values but did not change the generally smooth frictional behaviour of both specimens. Such a smooth frictional behaviour was maintained in the TO-Zr specimen up to the contact load of 10 N (Fig. 7.8b). However, for the TO-Ti specimen, when the contact load was increased to 4 N (Fig. 7.8a), the frictional behaviour was changed significantly, characterised by the initial smooth regime for the first 600 s sliding and the sudden change to a fluctuating regime characteristic of the untreated CP-Ti specimen (not shown for clarity purpose). Such a sudden change in friction marked the breakdown of the OL and led to much accelerated wear of the TO-Ti specimen.

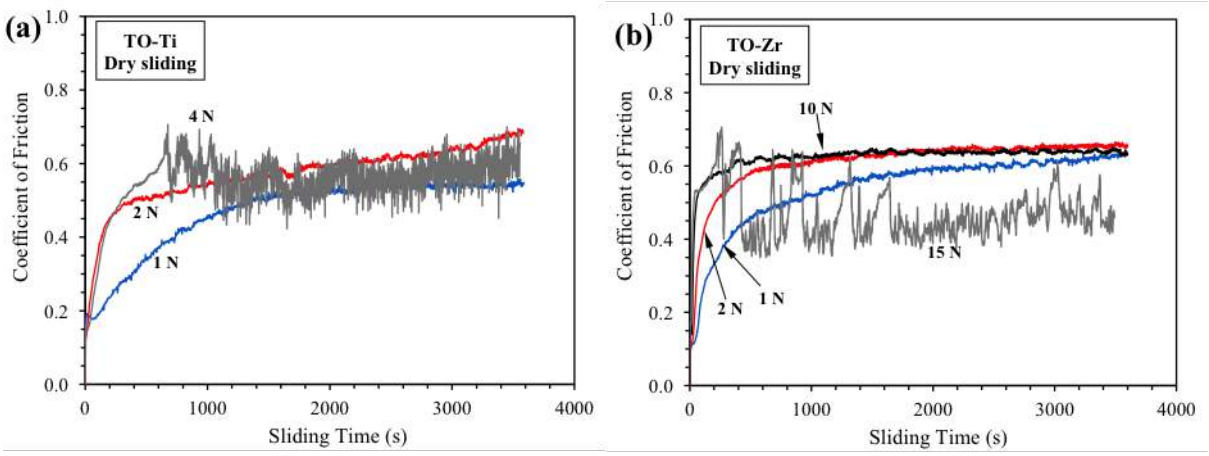


Figure 7.8: COF curves recorded during dry sliding of the TO-Ti (a) and TO-Zr (b) specimens under various contact loads.

Fig. 7.9 shows the morphology and the surface profiles measured across the wear tracks produced on the TO-Ti specimen at 2 N and 4 N loads. It can be seen that after dry sliding at 2 N for 3600 s, the wear depth in the wear track was mostly within the OL thickness and only in some local areas was the OL worn through (Fig. 7.9a). However, after sliding at the higher contact load of 4 N, the OL and the ODZ were removed completely from the wear track (Fig. 7.9b). Thus under the present dry sliding conditions, the TO-Ti specimen can only resist up to a contact load of 2 N without serious OL and ODZ breakdown.

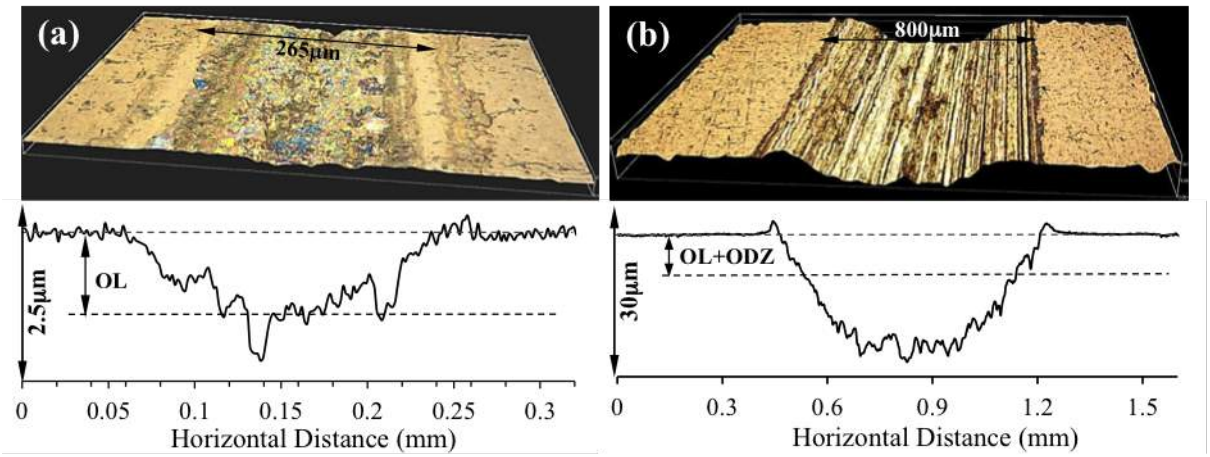


Figure 7.9: Three dimensional view of the wear tracks and the measured surface profiles across the tracks produced by dry sliding of the TO-Ti at (a) 2N and (b) 4 N.

On the other hand, the TO-Zr specimen can resist a much higher contact load without OL and ODZ breakdown, as shown in Fig. 7.8(b) and Fig. 7.10(a). For the

TO-Zr specimen, a sudden change in frictional behaviour occurred during sliding at 15 N load, as compared to 4 N for the TO-Ti specimen (Fig. 7.8). As shown in Fig. 7.10(b), such a sudden change in frictional behaviour was also related to the breakdown of the OL and ODZ, leading to much accelerated wear of the TO-Zr specimen. Clearly, under the present dry sliding conditions, the TO-Zr specimen possessed a load bearing capacity that was at least 5 times larger than that of the TO-Ti specimen.

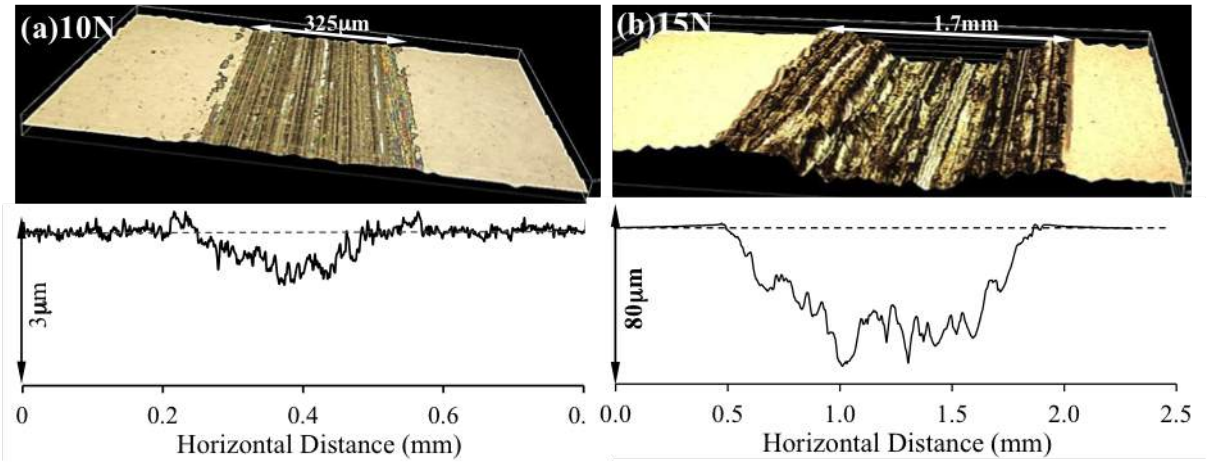


Figure 7.10: Three dimensional view of the wear tracks and the measured surface profiles across the tracks produced by dry sliding of the TO-Zr at (a) 10N and (b) 15 N.

The measured total material removal (TMR) rate from the wear track as a function of contact load is given in Fig. 7.11(a). Since a nearly circular wear scar was produced on the counterface alumina ball, the mean diameter of the wear scar was measured and presented in Fig. 7.11(b) as a function of contact load. For comparison purpose, untreated raw Ti and Zr specimens were also tested at low contact loads and the results are also shown in Fig. 7.11. It can be seen that wear from the specimen and from the alumina ball followed the same trend as contact load was increased. A larger TMR rate from the wear track corresponded to a larger wear scar on the ball due to the increased contact area. As compared to the untreated specimens, TO effectively reduced the TMR rate at the small contact load of 1 N by more than two orders of magnitude (Fig. 7.11a). As long as the OL maintained its integrity with the substrate, TO-Ti and TO-Zr behaved similarly in terms of wear resistance. However, with increasing load from 1 N to 4 N, the TMR rate from the TO-Ti specimen increased steeply due to the wearing through and breakdown of the OL and the ODZ. At further higher contact loads, the substrate dominated the

wear process because the OL and ODZ were worn through during the early stage of sliding. On the other hand, the TO-Zr specimen maintained a very small TMR rate up to the contact load 10 N, above which the TMR rate increased abruptly due to the breakdown of the OL and ODZ. Thus, TO-Zr possessed much better wear resistance at high contact loads than TO-Ti.

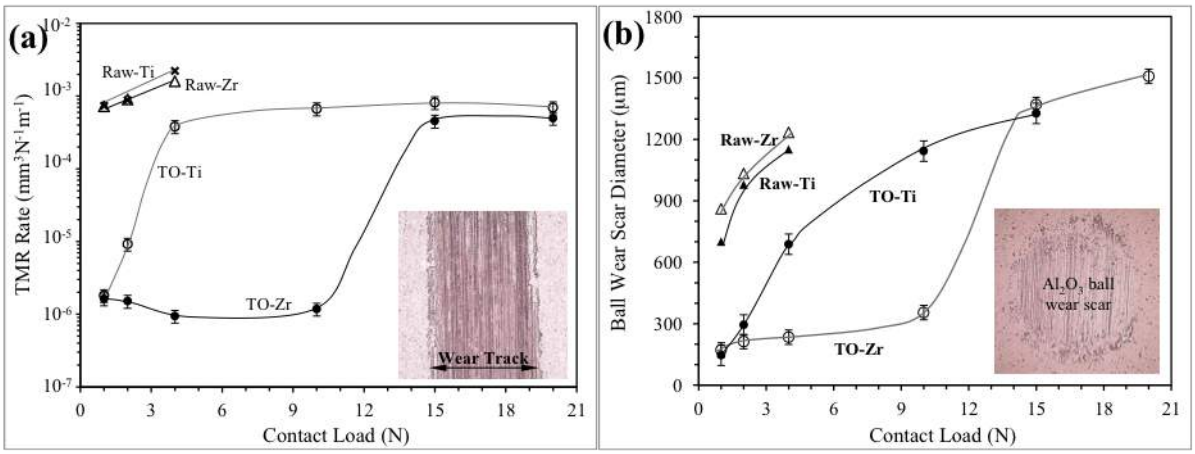


Figure 7.11: Measured total material removal (TMR) rate from the wear track (a) and ball wear scar diameter (b) for the TO-Ti and TO-Zr specimens under various contact loads.

Fig. 7.12 shows typical SEM images taken from the wear tracks on TO-Ti ((a) and (b)) and TO-Zr ((c) and (d)). Fig. 7.12(a) shows that at 2 N, the OL on the TO-Ti specimen was worn smoothly and the ODZ was exposed at the centre of the wear track, in agreement with the observation and measurement in Fig. 7.9. At 4 N, the OL on TO-Ti suffered from severe flaking at the edges of the wear track and wear mainly occurred in the substrate (Fig. 7.12b). Flaking of the OL led to the observed sudden change in friction shown in Fig. 7.8(a). As mentioned earlier, no OL breakdown occurred in the TO-Zr specimen at contact loads below 15 N. Fig. 7.12(c) and (d) show that at contact loads below this critical load, wear of the OL was caused by micro abrasion, microcracking and delamination within the thick OL. The wear track surface was populated with microcracks (Fig. 7.12d). The linkage of these microcracks led to the formation of wear debris, leaving behind some shallow craters on the worn surface. The depths of these craters, shown in Fig 7.12(c) and (d), were very small, within the OL. Fig. 7.13 shows a wear crater caused by the cohesive failure of the OL and the results of EDS spot elemental analysis inside and outside the crater. The results showed that inside the crater, the chemical composition was near stoichiometric $ZrO_2$, thus confirming that the crater

depth was shallower than the OL thickness and the failure was cohesive. Outside the crater, some Al and C were detected, indicating material transfer from the alumina ball and contamination of the real contact areas from the environment.

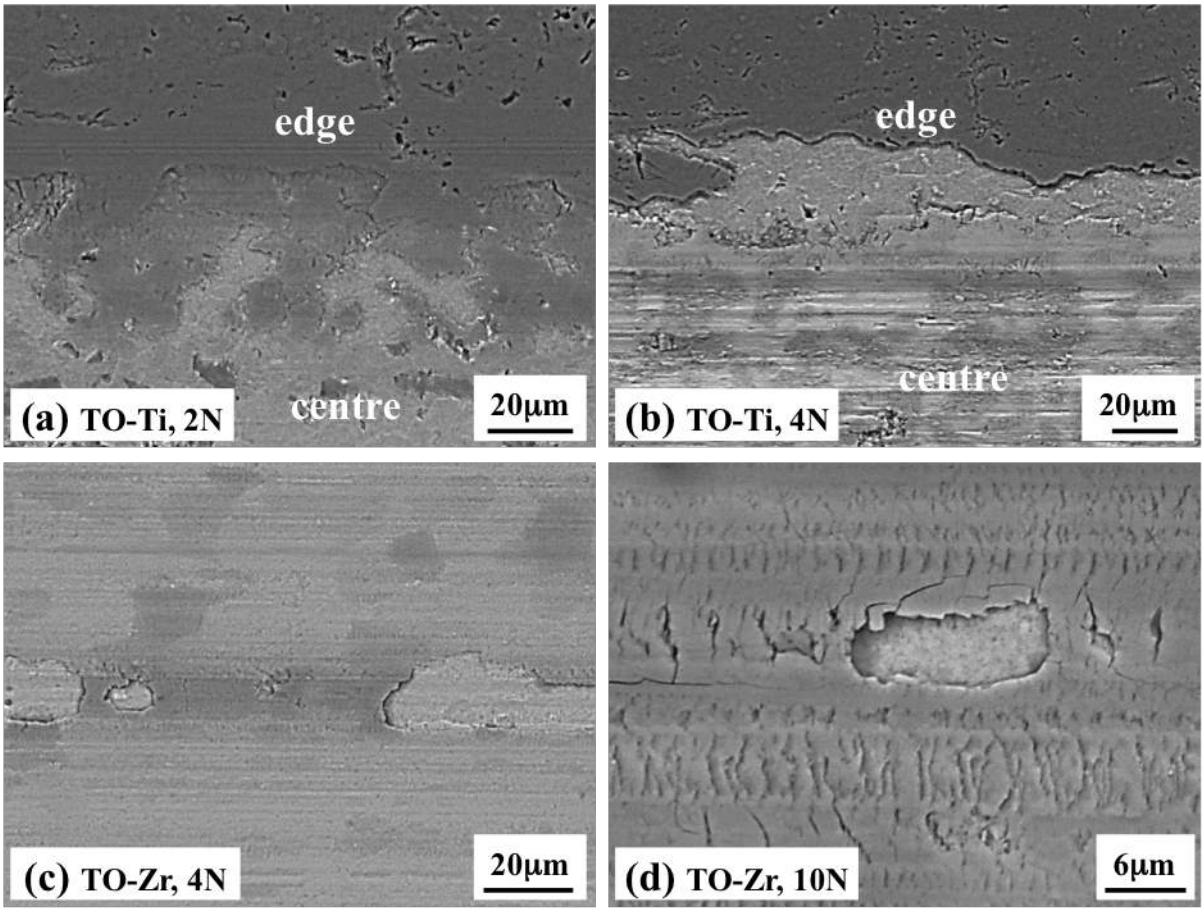


Figure 7.12: SEM images showing the morphology of the wear tracks produced on the TO-Ti (a and b) and TO-Zr (c and d) specimens during dry sliding under various contact loads.

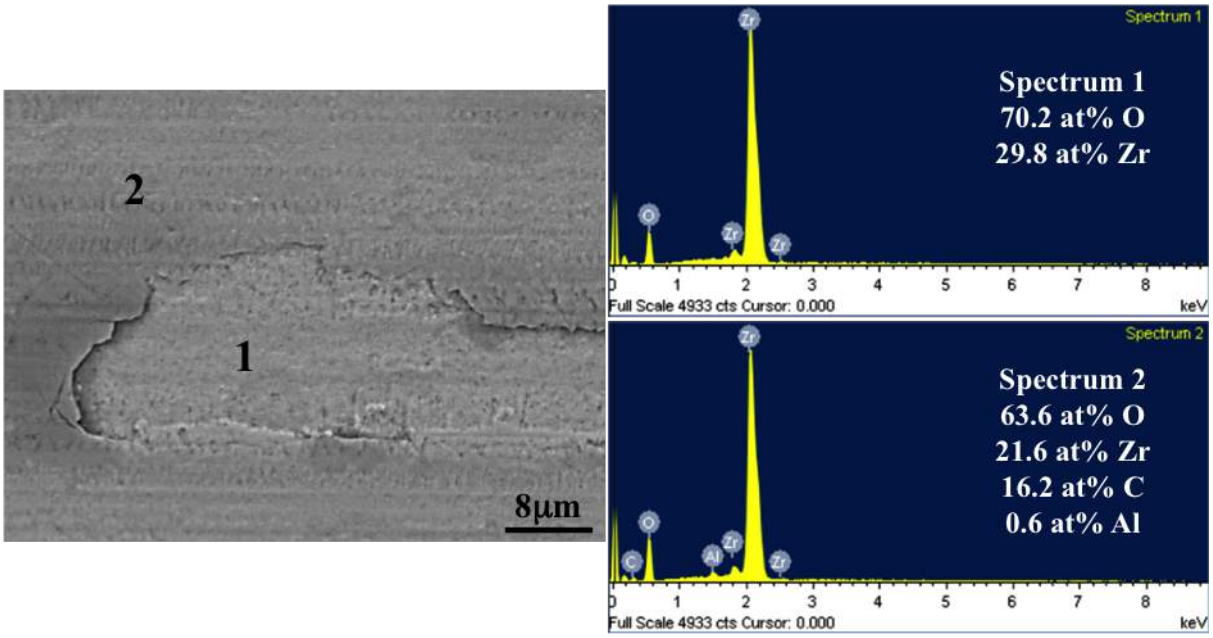


Figure 7.13: SEM image and EDS elemental spot analysis in area 1 and 2 of the wear track produced on the TO-Zr specimen during dry sliding under 4 N load.

### 7.3.5 Tribocorrosion behaviour

During tribocorrosion testing in Ringer's solution at $37^oC$ at open circuit without externally applied potential, attempts were made to measure and record the evolution of open circuit potential (OCP) continuously. Fig. 7.14(a) shows the recorded OCP curves for the untreated (raw) Ti and TO-Ti specimens. Since R-$TiO_2$ is a semiconductor and the OL on TO-Ti was thin, OCP could be measured before, during and after sliding. However, difficulties were encountered in measuring the OCP of the TO-Zr specimen due to the poor conductivity of the dense and thick m-$ZrO_2$ layer which is a barrier layer. The measured OCP of the TO-Zr specimen varied largely between 0 mV(SCE) and 2000 mV(SCE) without a stable value, as can be seen from the large spike in Fig. 7.14(b) for the first 300 s measurement without sliding.

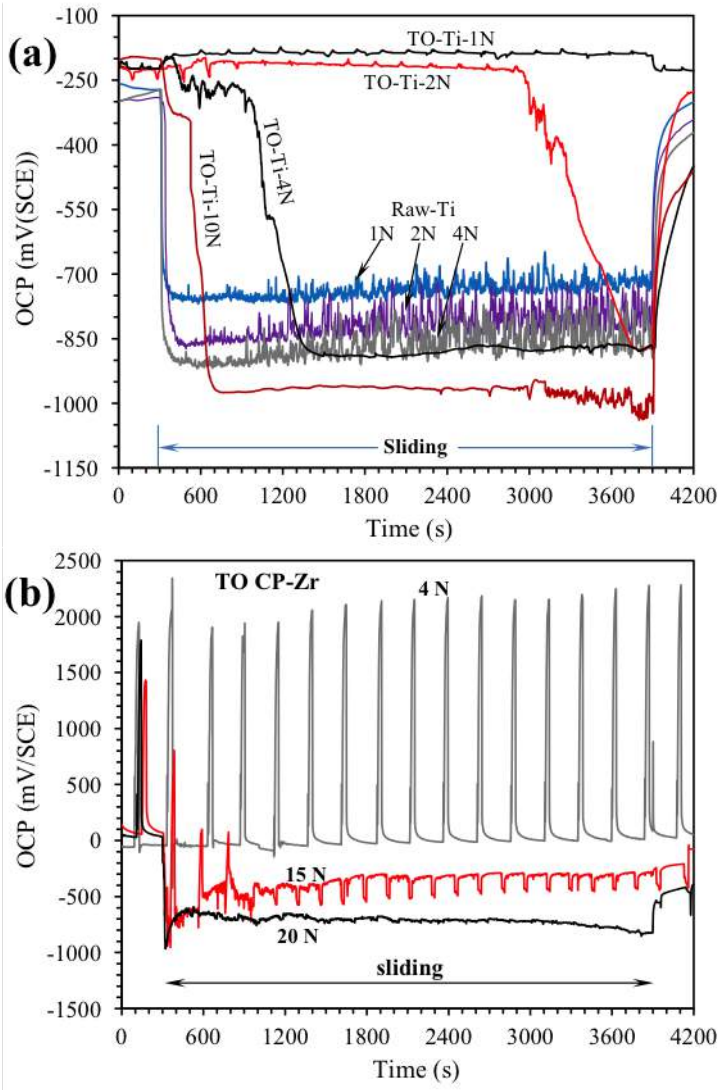


Figure 7.14: Open circuit potential (OCP) recorded before, during and after sliding of the untreated Ti and TO-Ti (a) and TO-Zr (b) specimens, in Ringer's solution at $37^oC$.

From Fig. 7.14(a), it can be seen that for the untreated Ti specimen, sliding led to a significant drop in OCP due to the destruction or removal of the passive film by the mechanical sliding action. This is a common phenomenon observed for passive metals by many investigators [140][195][196][197]. The drop in OCP during sliding increased with increasing contact load, presumably due to the increased mechanical damage and the increased wear track area [133][143]. Sliding of the TO-Ti specimen at a small contact load 1N did not lead a significant change in OCP, Fig. 7.14(a). Thus the wear track was in a passive state during sliding at 1 N load. This is because the OL maintained its integrity with the substrate, as confirmed by wear track profile

measurements and microscopic examination. It is interesting to note that during sliding of TO-Ti at 2 N load, the OCP initially followed a similar trend to that at 1N load, but experienced a significant drop after about 3000 s to gradually reach OCP values characteristic of the untreated Ti in the activated state. Such a significant drop in OCP was also observed at higher contact loads of 4 N and 10 N, Fig. 7.14(a). The time at which OCP started to drop decreased with increasing contact load. Fig. 7.15(a) shows the cross-sectional profiles of the wear tracks on TO-Ti. The OL in the 2 N wear track was just worn through in the central region, leading to the exposure of the ODZ. Microscopic examination showed that in the central region of the 2 N wear track, only patches of the OL remained and in many areas the ODZ was exposed. Sliding at the higher contact load of 4 N led to the complete removal of the OL, but the wear depth was confined within the ODZ (Fig. 7.15(a)). At the further higher contact load of 10 N, the OL and ODZ were removed completely from the wear track, leading to the exposure of the substrate (Fig. 7.15(a)). It is thus clear that the significant drop in OCP of the TO-Ti specimen during sliding at contact loads 2 N and above (Fig. 7.14(a)) was caused by the wearing through of the OL (at 2 N and 4 N) and then wearing through of the ODZ (at 10 N).

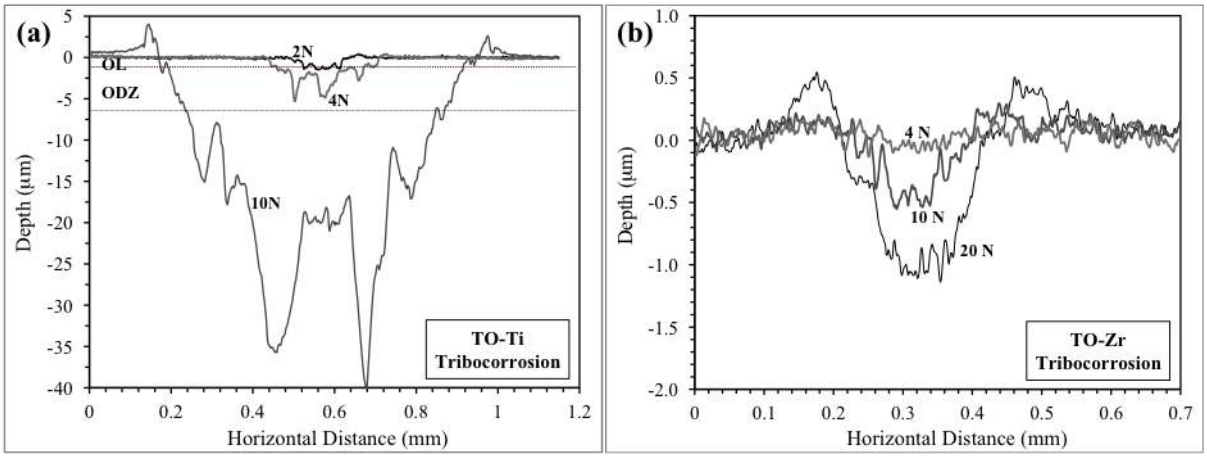


Figure 7.15: Typical cross-sectional profiles of the wear tracks produced on the TO-Ti (a) and TO-Zr (b) specimens during tribocorrosion under various contact loads.

Fig. 7.14(b) shows OCP curves recorded during tribocorrosion of the TO-Zr specimen. For clarity purpose, the OCP curves of the untreated Zr specimen are not included, which are similar to those of the untreated Ti specimen shown in Fig. 7.14(a). As mentioned earlier, due to the poor conductivity of the thick $ZrO_2$ layer, it was unrealistic to measure the OCP of the TO-Zr specimen. Indeed, at contact

loads of 10 N and below, the recorded OCP values before, during and after sliding were unstable with large potential spikes. However, when the contact load was increased to 15 N, OCP became measurable after about 600 s sliding. This suggests that the specimen became conductive after a certain period of sliding. At the further higher contact load of 20 N, the OCP became measurable after a short period of sliding. Fig. 7.15(b) shows the cross-sectional profiles of the wear tracks on the TO-Zr specimen. The wear tracks were narrow and shallow. At the highest contact load of 20 N applied, the wear depth was about 1.3 $\mu$m, which was much smaller than the OL thickness. Clearly, the improved conductivity of the TO-Zr specimen at 15 N and 20 N loads was not due to the wearing-through or removal of the non-conducting OL in the wear track. In fact, the OL maintained its integrity with the substrate, as shown in Fig. 7.16. The wear track produced at 10 N comprised of many abrasion marks and corrosion products. No cracks were evident in the 10 N wear track (Fig. 7.16a). However, in the wear track produced at 15 N, many cracks were observed on the worn surface. Some of these cracks can be seen penetrating through the OL and propagating to the substrate (Fig. 7.16b). Cracking of the OL and propagation of the cracks to the substrate were more obvious at the higher contact load of 20 N (Fig. 7.16c). Fig. 7.16(d) is an SEM image showing more clearly the propagation of cracks from the OL to the substrate. It is thus clear that the improved conductivity of the TO-Zr specimen at high contact loads was due to crack formation in the wear track and the propagation of the cracks to reach the conductive substrate.

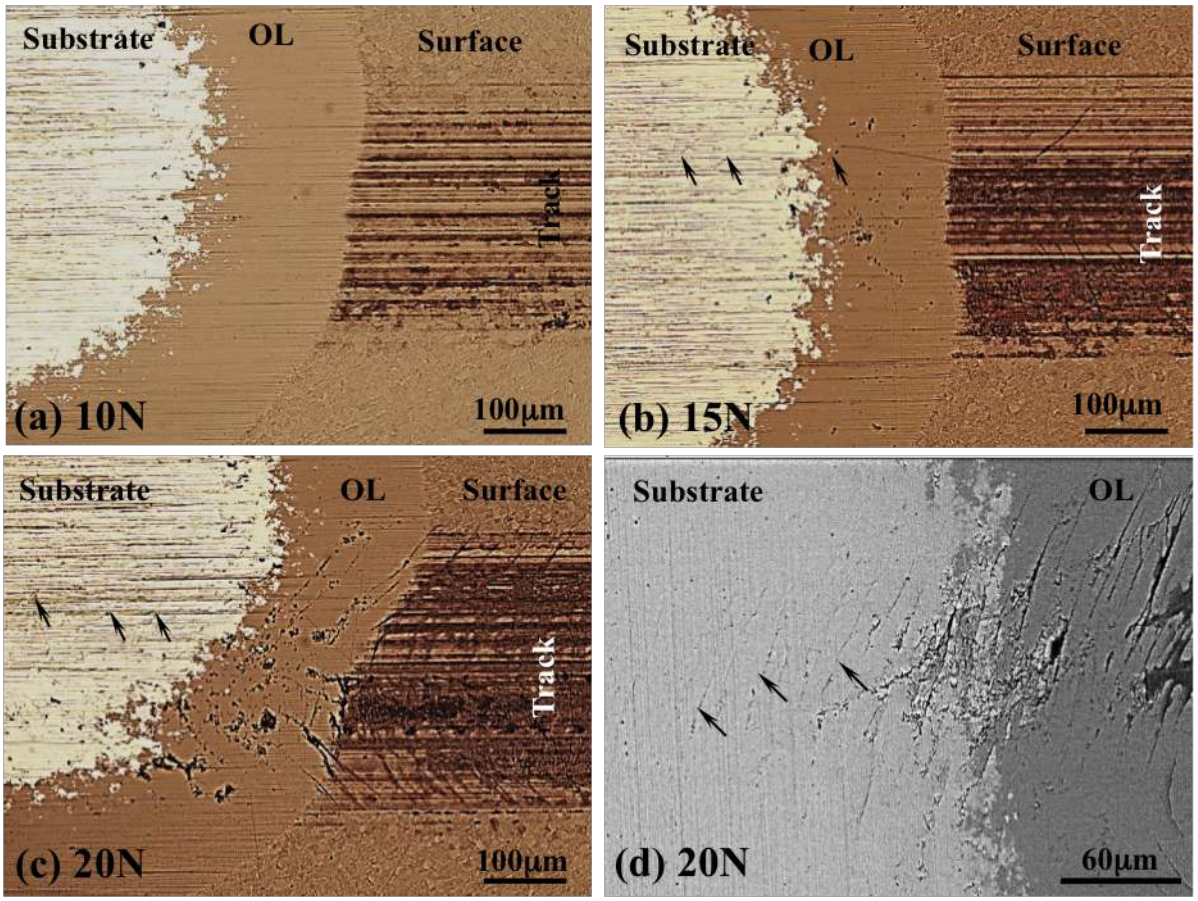


Figure 7.16: Microscopic images of the zoom-in view of ball craters made on the wear tracks produced on the TO-Zr specimen during tribocorrosion in Ringer's solution at $37^oC$ under (a) 10 N, (b) 15 N, (c) and (d) 20 N contact loads, showing the wear tracks, the OL and substrate beneath each wear track. Arrows show the penetration of cracks in the substrate.

Fig. 7.17 shows the average COF measured during tribocorrosion for the test specimens. Sliding in the Ringer's solution resulted in lower COF than dry sliding due to the lubricating effect of the solution. At low contact loads, TO-Ti exhibited much lower COF than the untreated Ti, demonstrating the friction-reducing effect of the OL. At high contact loads, the breakdown of the OL lead to much increased friction. On the other hand, the TO-Zr specimen maintained relatively low COF at all contact loads because the OL was not removed during sliding. The increase in COF at high contact loads could be related to the formation of cracks in the corrosion-wear track, which can change the real contact area and stress distribution in the contact zone.

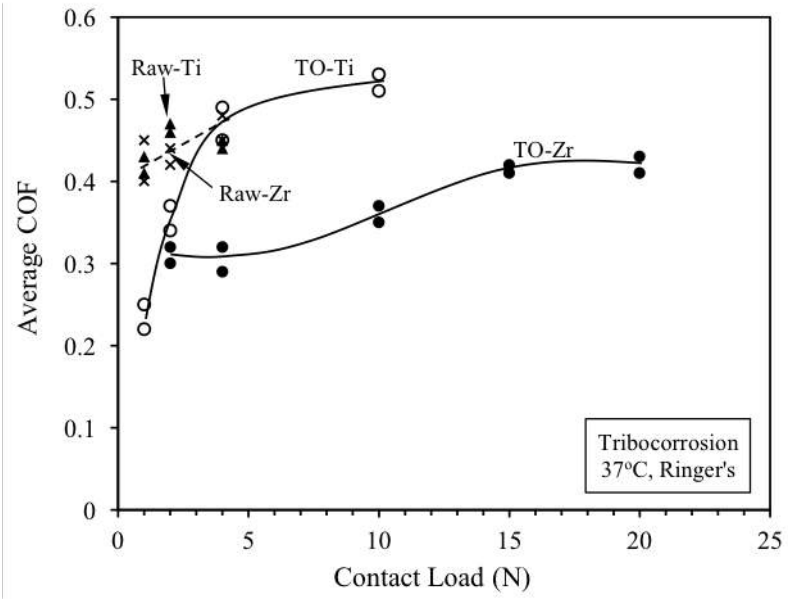


Figure 7.17: Measured average coefficient of friction for the test specimens under tribocorrosion conditions.

The measured TMR rate from the corrosion-wear track and the mean diameter of the wear scar on the alumina ball are given in Fig. 7.18. As compared to the untreated specimens, TO effectively reduced the TMR rate by 2 to 3 orders of magnitude at small contact loads of 1 N and 2 N (Fig. 7.18(a)). Wear of the counterface alumina ball was also reduced by TO treatment of the specimens (Fig. 7.18(b)). At higher contact loads, the effectiveness of TO-Ti in reducing TMR rate of Ti was reduced due to the breakdown of the OL and the ODZ. On the other hand, TO-Zr possessed very good resistance to TMR at high contact loads because the OL maintained its integrity with the substrate despite the formation and propagation of cracks. At contact loads above 2 N, the resistance of TO-Zr to TMR caused by tribocorrosion in the Ringer's solution was two orders of magnitude better than that of TO-Ti (Fig. 7.18(a)).

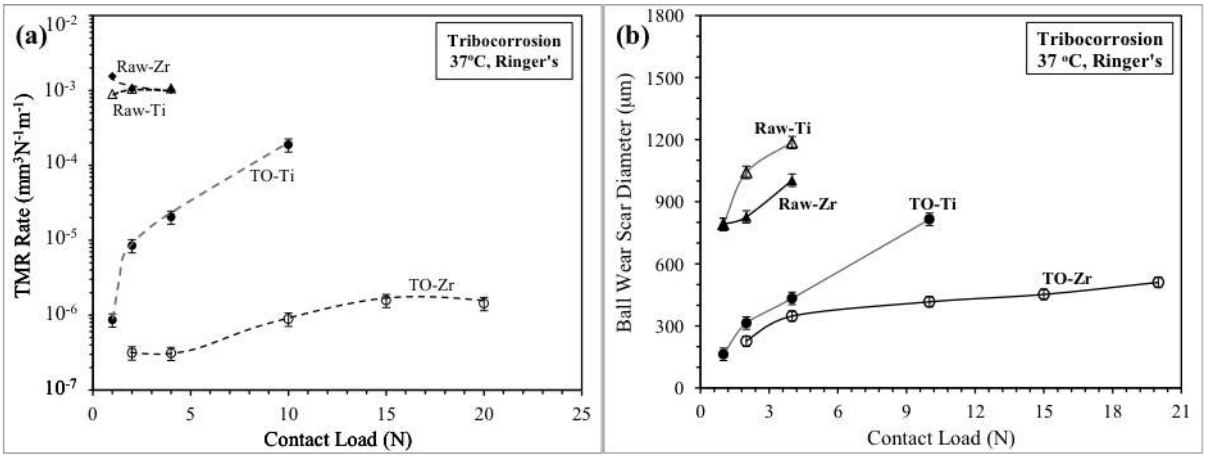


Figure 7.18: Measured total material removal (TMR) rate from the corrosion wear track (a) and ball wear scar diameter (b) for the TO-Ti and TO-Zr specimens under tribocorrosion conditions.

## 7.4 Conclusion

The comparative study in this work has unveiled the difference in mechanical behaviour between thermally oxidised Ti and Zr. The conclusions are as follows:

- Under the present thermal oxidation condition, 4 times more oxygen is introduced into CP-Zr than into CP-Ti. As a result, the oxide layer produced on CP-Zr is nearly 6 times thicker than that on CP-Ti.
- The TO-Zr possesses higher hardness, a deeper hardening depth (about 10$\mu$m) and a greater load bearing capacity than the TO-Ti.
- The TO-Zr exhibits better scratch resistance than the TO-Ti. During the scratch test, the oxide layer on TO-Ti suffers from edge spallation at a load as small as 7 N, while the oxide layer on TO-Zr can resist a scratch load up to 15 N without adhesive failure. The oxide layer on TO-Zr can accommodate severe plastic deformation and maintains good integrity with the substrate at high scratch loads.
- Under the present dry sliding conditions, as long as the oxide layer maintains integrity with the substrate, such as at small contact loads, both TO-Ti and TO-Zr specimens show similar wear resistance. However, at high contact loads, the oxide layer on TO-Ti is removed easily, leading to accelerated wear of the TO specimen. On the other hand, the oxide layer on TO-Zr can resist much

higher contact loads without breakdown and thus possesses a much higher load bearing capacity and better wear resistance than TO-Ti.

- Under tribocorrosion conditions in Ringer's solution, the oxide layer on TO-Ti is removed from the corrosion-wear track at contact load as small as 2 N and thus loses its barrier nature in the corrosive environment. On the other hand, the oxide layer on TO-Zr maintains its integrity and barrier nature up to a contact load of 10 N without crack formation and layer breakdown. Although at higher contact loads of 15 N and above, the oxide layer on TO-Zr still maintains its integrity with the substrate during tribocorrosion, cracks form in the oxide layer and penetrate through the oxide layer to reach the substrate, thus losing the barrier nature of the oxide layer against corrosion.

# Chapter 8

# Pack Carburising

## 8.1 Pack Carburisatioin of CP-Zr with oxygen diffusion for improved tribological performance

Zirconium Carbide (ZrC) is a very good and important non-oxide ceramic and it is widely used due to its low density, high hardness (2600-3200HV), high melting point and wear resistance. Carburising has been used to produce TiC on titanium and its alloys in order to improve the tribological properties [39]. Carburisation has a lot of benefits when it comes to improving the tribological properties. However one of the main issues linked with zirconium carburisation is the high affinity between Zirconium and oxygen. This will result in the formation of zirconium dioxide ($ZrO_2$) at certain temperatures (around $825^oC$). Therefore pack carburising ideally should be undertaken in a vacuum or oxygen isolated environment in order to allow carbon absorption instead of oxygen. This way carburising process will be done instead of oxidation.

After the investigation of the behaviour of thermal oxidation on zirconium in Chapters 4-7, another technique, i.e. pack carburising, was investigated in this chapter. The goal of this method is to produce a carbide layer on top of a carbon and/or oxygen diffusion zone ($\alpha$-Zr(O)). In this work, three main effects were investigated:

- The effect of carburising temperature.
- The effect of carburising time.
- The effect of Pack composition.

In the current study the concentration of both oxygen and carbon on the carburised was studied, and more focus was placed on tribological behaviour and wear resistance. The used carburising pack composition was chosen because it was the optimal composition using for titanium carburising [17][39]. Zirconium and titanium have a similar crystal structure and similar mechanical and tribological properties; therefore this composition was used to create ZrC samples. However, some tests were done using different compositions to study the effect of pack composition on carburising.

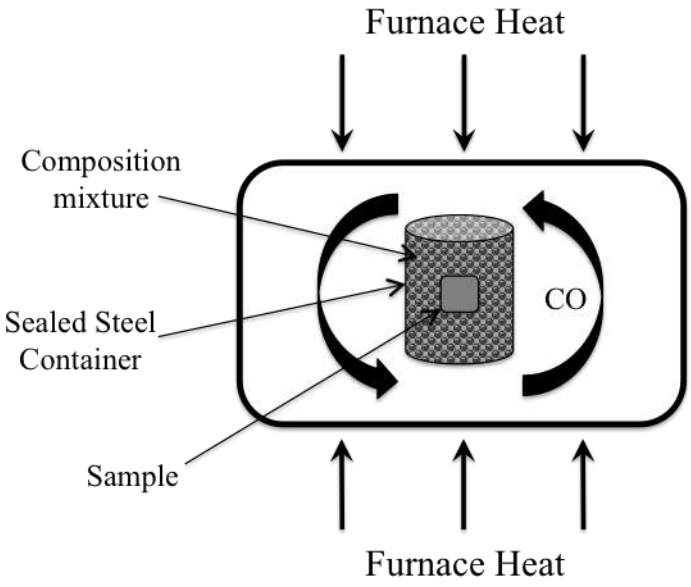


Figure 8.1: Schematic diagram of experimental setup.

Figure 8.1 presents a schematic diagram to show the used experiment setup. Samples are placed in the mixture of pack compounds inside the container. It is very important to seal the steel container using heat resistant sealants after placing the samples in the container. The container is then placed in the heating furnace and treatment is initiated under controlled temperature and time conditions. The composition of carburising powders is a very important factor to get a good carbide film. The composition of the powders can affect the size and strength of the carbide film. Four agents or powders were used to make the mixture and they have different roles during carburising:

- **Charcoal**: It is used as the source of carbon during carburising reactions.
- **Barium carbonate** ($BaCO_3$): It is widely used in ceramic industry as glazing ingredient; it plays the role of energiser to activate the carbon.

- **Sodium carbonate ($Na_2CO_3$)**: Common compound in ceramic industry, it is used as bonding agent and an activator as it allows active carbon to form and then adhere into the sample.
- **Calcium carbonate ($CaCO_3$)**: This compound is used as the main energiser and activator to generate active carbon species inside the container.

## 8.2 The effect of temperature on carburisation process

### 8.2.1 Process

The initial pack composition used in the mixture was the same composition used for typical titanium carburisation. Therefore the composition used for the pack was 70% carbon and 30% energiser. The energiser was created using Barium carbonate ($BaCO_3$), sodium carbonate ($Na_2CO_3$) and calcium carbonate ($CaCO_3$) in ratio of 3:2:1. This pack of carbon and energiser was used to determine the optimal temperature for Zirconium carburisation. Carburisation treatment took place at various temperatures ($825^oC$, $880^oC$, $925^oC$ and $980^oC$) for duration of 20h and then cooled down using furnace cooling (FC). After carburisation the samples were then tested tribologically to determine the effect of temperature and also to determine the best temperature to produce a very good wear resistance structure.

### 8.2.2 Layer Morphology

Because of the existence of oxygen in the steel container during pack carburising, it is predicted that oxygen will diffuse into the zirconium samples for certain temperatures. The reason behind this is that there is a very high attraction between zirconium and oxygen [17][198]. To prove this idea, every sample was cut into half to provide cross-sectional images. The samples were then nickel plated and mounted in green resin followed by polishing. The reason nickel plate was used is that it's very hard to see the edges of the films and this method helps to show the dark surface films against the resin mount. After polishing all samples, samples were then cleaned using ethanol. Microscopic images were taken to show the structure produced by carburising treatment (Figure 8.2). From Fig.8.2, it can be seen that a thin dark grey film was formed on the surface, followed by a thick diffusion zone

beneath. The surface film is presumably a ZrC film or an oxide film.

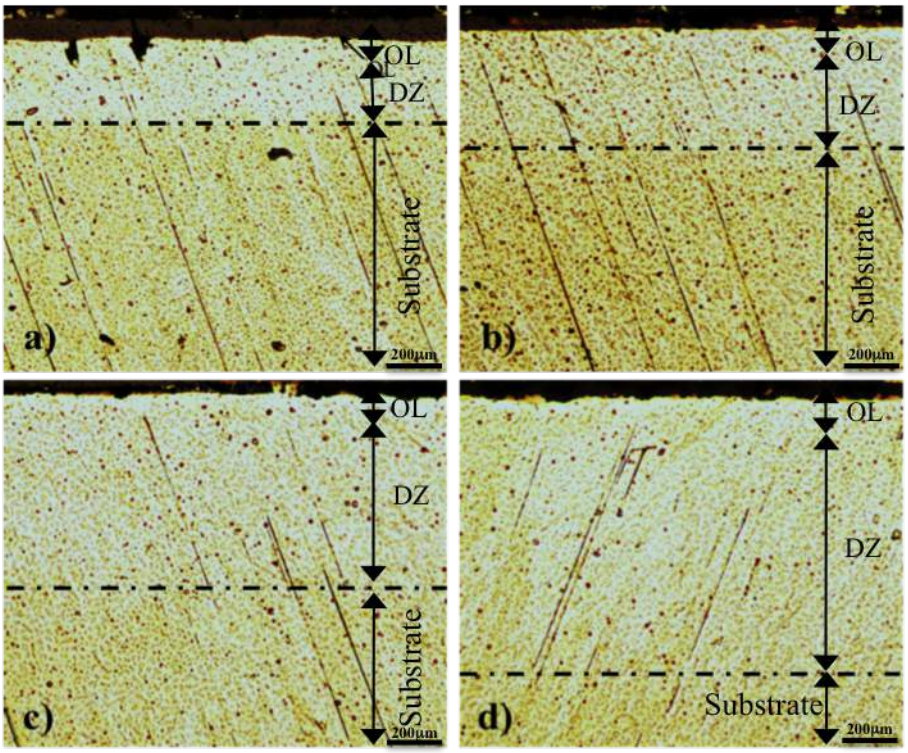


Figure 8.2: Cross-sectional images showing structure after pack carburising for 20h at temperatures of: (a) $825^oC$, (b) $880^oC$, (c) $925^oC$ and (d) $980^oC$

Figure 8.3 shows SEM images that was taken for the cross section of all samples. As it can be seen $825^oC$ and $880^oC$ sample are similar in the appearance. As shown in all samples there is a thick pack residue at the surface and some cracks at the surface followed by ununiformed subsurface as shown clearly in $880^oC$ sample (Figure 8.3a).

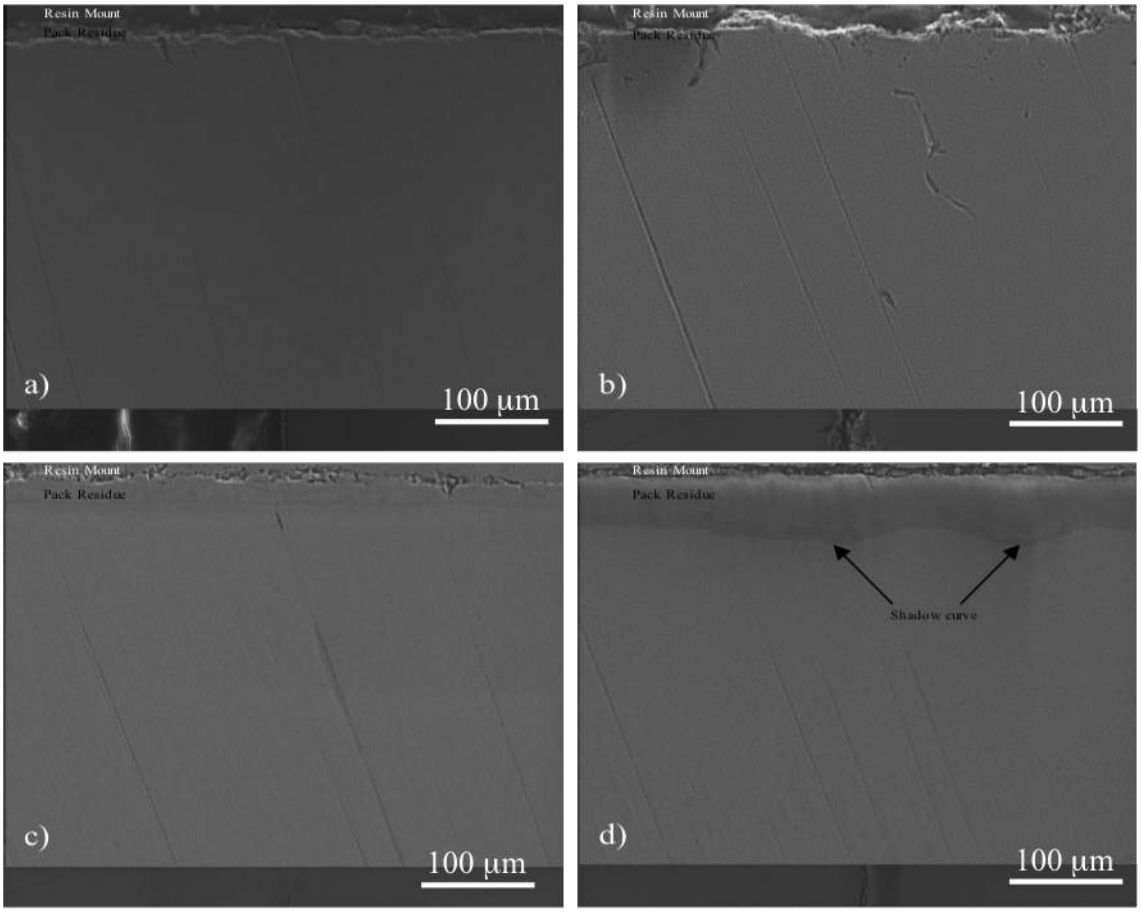


Figure 8.3: SEM images showing cross-sectional structure after pack carburising for 20h at temperatures of: (a) $825^oC$, (b) $880^oC$, (c) $925^oC$ and (d) $980^oC$

When the sample is carburised at $925^oC$ (Figure 8.3c), it can be seen that it shows a better and uniformed pack residue layer compared to all other samples. The $925^oC$ sample shows no delamination on the structure suggesting good adhesion to the substrate. However when the sample is carburised at $980^oC$, there is a new structural feature. This feature is named as the shadow curve so it can be labelled as shown in (Figure 8.3d) which explains that there is another darker layer below the pack residue. This feature is only about 1-2$\mu$m thick below the residue pack and it created a curvy shape. This can be explained by treating the sample with high temperature ($980^oC$) that created an extra layer due to the acceleration of carburising treatment.

After carburising the sample at $825^oC$, the surface layer was about 5.8$\mu$m thick (Figure 8.3a), which was increased to about 6.5 and 7.1 $\mu$m after increasing the temperature of the treatment to $880^oC$ and $925^oC$ (Figure 8.3b and c). After increasing the treatment temperature to $980^oC$, the thickness of carburised layer produced was

Table 8.1: Layer thickness developed after pack carburising

| Temperature of carburising ($^oC$) | Carbide layer Thickness ($\mu$m) | Oxygen diffusion depth ($\mu$m) |
|---|---|---|
| 825 | 5.8 | 153 |
| 880 | 6.5 | 162 |
| 925 | 7.1 | 175 |
| 980 | 9.6 | 206 |

about 9.6 $\mu$m (Figure 8.3c). It can be seen that carburising needs a high temperature to produce a good layer or in other words undamaged layer.

Table 8.1 lists the thicknesses of the surface layer and the oxygen diffusion depth for all treated samples. It can be seen that as the temperature of carburising increases both carbide layer thickness and oxygen diffusion depth are increased. This is due to the increased diffusion at high temperatures of carburising treatment, which helps in providing thicker layer. Figure 8.4 shows the film thicknesses of the ZrC and ODZ with regard to the temperature of carburising.

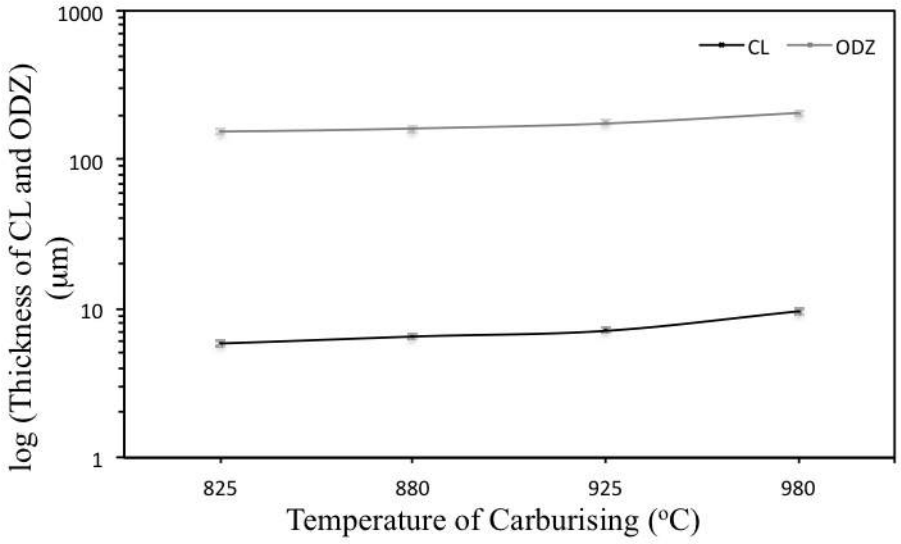


Figure 8.4: Film thickness of CL and ODZ with regard to temperature of carburising, for samples carburised for 20h at temperatures of $825^oC$, $880^oC$, $925^oC$ and $980^oC$

It can be seen that as the temperature of carburising increases, the thickness of carbide layer increases and the depth of oxygen diffusion zone increases too. Figure 8.4 states that temperature of carburising has a huge effect on the formation of carbide layer and oxygen diffusion zone.

### 8.2.3 Glow discharge optical spectroscopy GDOS

The combination of both carbon and oxygen into the surface of treated zirconium was investigated using GDOS in order to find the composition profile along the depth below the surface. Figure 8.5a shows both carbon and oxygen profiles. It can be clearly seen that the diffusion of carbon was effective at temperatures $925^oC$ and $980^oC$. However, when the temperature is lower than $925^oC$ the carbon diffusion is limited and carbon content decreases. The penetration of carbon is just around 1-4$\mu$m at temperature of $825^oC$ compared with about 15-20$\mu$m for $980^oC$ sample.

When investigating the oxygen diffusion within the treated samples (figure 8.5b), the amount of oxygen is constant throughout the depths for $925^oC$ and $980^oC$. But for $825^oC$ and $880^oC$ it can be seen that the amount of oxygen is increasing and penetrating about 2-4$\mu$m. This indicates that when the content of carbon is low, the content of oxygen is high for all treated samples. When carburising is undertaken at $980^oC$, the oxygen concentration start to drop sooner than any of the other treated samples and the oxygen concentration is settling at about 2%. The drop of the oxygen concentration is decreased whenever the temperature is lower and at $825^oC$ the oxygen concentration is settling at about 30%.

From the GDOS results, it can be concluded that carburising is effective only at temperatures higher than $900^oC$. While at lower temperatures, oxidation becomes dominant. This is because the dissociation of the carburising compounds in the steel container is a thermally activated process, requiring sufficiently high temperatures to produce active carbon species [17][39][199]. Thus pack carburising should be conducted at $925^oC$ and above. This is confirmed by XRD phase composition analysis, discussed in Section 8.2.5.

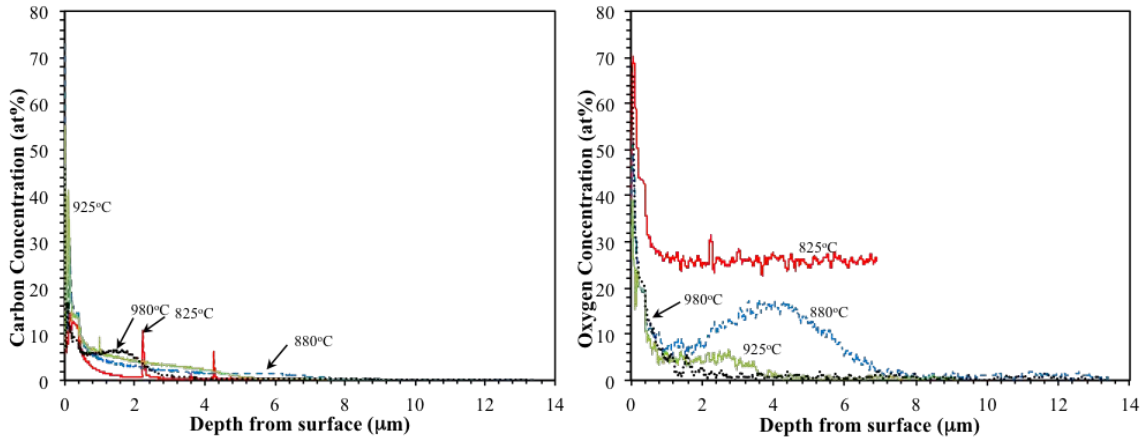


Figure 8.5: Carbon (a) and oxygen (b) concentration profiles measured by GDOS produced by carburisation at temperatures of: (a) $825^oC$, (b) $880^oC$, (c) $925^oC$ and (d) $980^oC$

### 8.2.4 Micro-Hardness profile

Micro-hardness testing was conducted on cross-sections on all samples ($825^oC$, $880^oC$, $925^oC$ and $980^oC$) and it was compared with untreated samples as shown in figure 8.6. Carburised samples have a very harder surface compared to thermal oxidised samples, with hardness of about 1200HV which is expected for zirconium carbide [200].

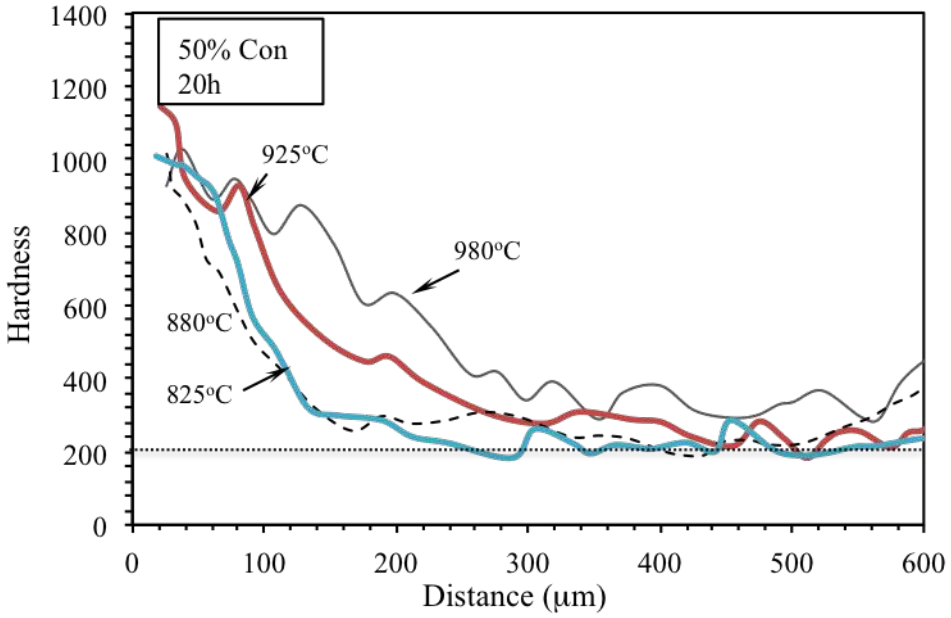


Figure 8.6: Cross-sectional hardness curves for the carburised samples treated for 20h at temperatures of $825^oC$ ,$880^oC$ ,$925^oC$ and $980^oC$.

As shown in figure 8.6, surface hardness depends on the thickness of the carburised layer built on the surface. There is definite correlation between carburisation temperature and layer thickness. This means when the temperature is higher, the hardness will be higher too until it reaches a certain depth (600$\mu$m). When hardness is measured between 400 and 600$\mu$m which is the centre of the cross-section of all samples, this will be the meeting point of the surface substrate and it is similar to the hardness of the untreated sample.

The $825^oC$ sample is the only sample that went out of the 400-600 $\mu$m ranges more than one time, exceeding the range to 600$\mu$m. This can be explained by the low temperature of the carburising treatment which leads to oxidation rather than carburisation. The low temperature prevents carburising effect, encouraging the oxygen to form an oxide layer.

This oxide layer is then covered by a carbide layer during the carburising treatment (20h). From figure 8.6 it can be seen that the hardness remains high until it reaches a depth of about 25-35$\mu$m. There is a sharp reduction in hardness from 1100Hv to 900HV across the carbide layer; this can be explained by the reduced amount of ZrC phase with depth. The sharp reduction is followed by gradual decline in hardness across the oxygen diffusion zone (ODZ) from 900HV to that of untreated zirconium 200HV.

Increasing the carburisation temperature helps the oxygen to diffuse deeper into the zirconium substrate creating larger ODZ. When the ODZ is larger, this will help in increased load bearing capacity. This also states that the structure of all samples is a multi-layered structure consisting of ZrC (carbide layer) or a $ZrO_2$ layer and $\alpha$-Zr(O) (oxygen diffusion zone). In general it can be stated that increasing the temperature of carburising increases both oxygen diffusion zone and the carbide layer thickness.

### 8.2.5 X-Ray Diffraction XRD

X-Ray diffraction results were analysed (figure 8.7). It can be seen that the samples treated with high temperatures such as $925^oC$ and $980^oC$ show that ZrC was formed on the surface. ZrC was the main content on the surface. At $980^oC$ the content of ZrC is higher than $925^oC$, confirming that higher temperatures favour the formation of carbide film. It also states that the carbon diffusion happens faster at higher temperatures. XRD also helps in demonstrating the presence of oxygen within zirconium subsurface. The $\alpha$-Zr peaks of the untreated sample are shifted to a smaller $2\theta$ angle, meaning that the lattice expansion happened as a result of oxygen dissolution. This was also investigated and observed by other authors [17].

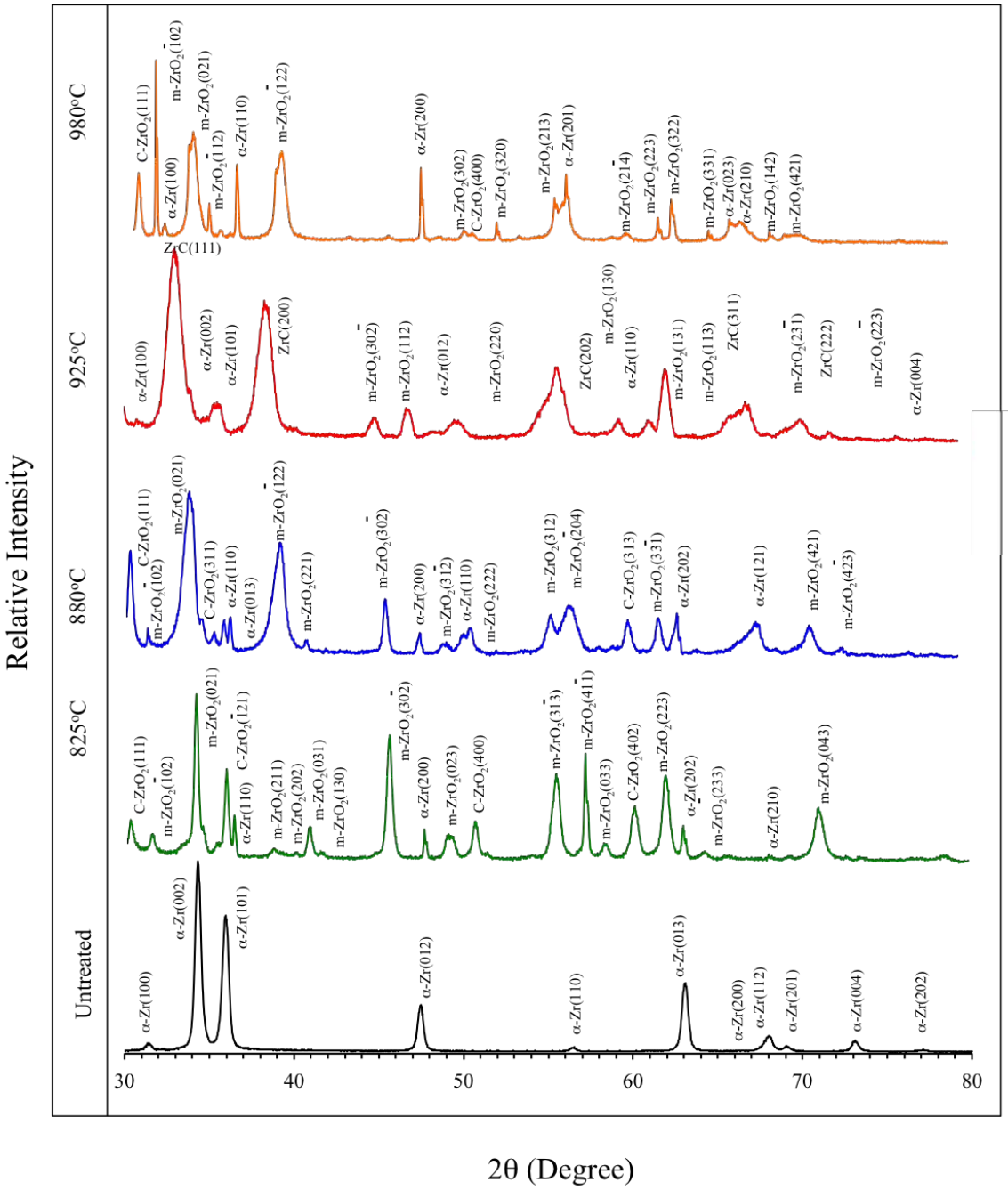


Figure 8.7: X-Ray diffraction patterns generated from samples carburised at temperatures of $825^oC$ and $925^oC$ for 20h against untreated zirconium

Table 8.2 summarises the phase composition for each treated and untreated samples, resulted from XRD analysis in Fig.8.7. It can be seen that at higher temperatures ($980^oC$ and $925^oC$) ZrC phase is very strong. However, when the temperature is lower than $925^oC$ $\alpha$-Zr and m-$ZrO_2$ are more dominant.

As mentioned previously at $825^oC$ the sample was oxidised rather than car-

Table 8.2: Summary of XRD results

| Temperature ($^oC$) | Phase composition |
|---|---|
| Untreated | $\alpha$-Zr |
| $825^oC$ | $C-ZrO_2$(mediate),m-$ZrO_2$ (strong), $\alpha$-Zr (mediate) |
| $880^oC$ | $C-ZrO_2$(mediate),m-$ZrO_2$ (mediate), $\alpha$-Zr (mediate) |
| $925^oC$ | ZrC (strong), $C-ZrO_2$(weak),m-$ZrO_2$,(strong), $\alpha$-Zr (weak) |
| $980^oC$ | ZrC (strong), $C-ZrO_2$(weak),m-$ZrO_2$ (strong), $\alpha$-Zr (weak) |

burised. From table 8.2 it can be seen that the m-$ZrO_2$ phase is strong at $825^oC$. This can confirm that at low temperature of about $825^oC$, the oxide layer is formed at the beginning of carburising treatment. When the temperature is increased to $880^oC$, the only difference is that the m-$ZrO_2$ phase is weaker due to the fact that there was no formation of oxide layer compared with $825^oC$ sample. However at high temperatures ($925^oC$ and $980^oC$) it can be seen that ZrC phase is stronger, this states that at higher temperatures the formation of carbide layer is generated with more carbon concentration. It is also noted that at $925^oC$ and $980^oC$, a high temperature oxide phase, i.e. cubin c-$ZrO_2$, is also formed, together with monoclinic $ZrO_2$ and ZrC. Thus, the carbide layer contains a mixture of carbide, and oxides. This is expected because the carburising container comprised both carbon and oxygen.

### 8.2.6 Tribological response

One of the most important aims of this research is to improve the tribological response of zirconium. Therefore, it is very important to characterise the treated samples in order to evaluate their tribological performance. All carburised samples were used for tribological testing (friction and wear testing). Testing was operated until film failure under load of 10N. The coefficient of friction (COF) was recorded and wear rates were measured. Figure 8.8 shows the response of friction for different temperatures (825,880,925 and $980^oC$).

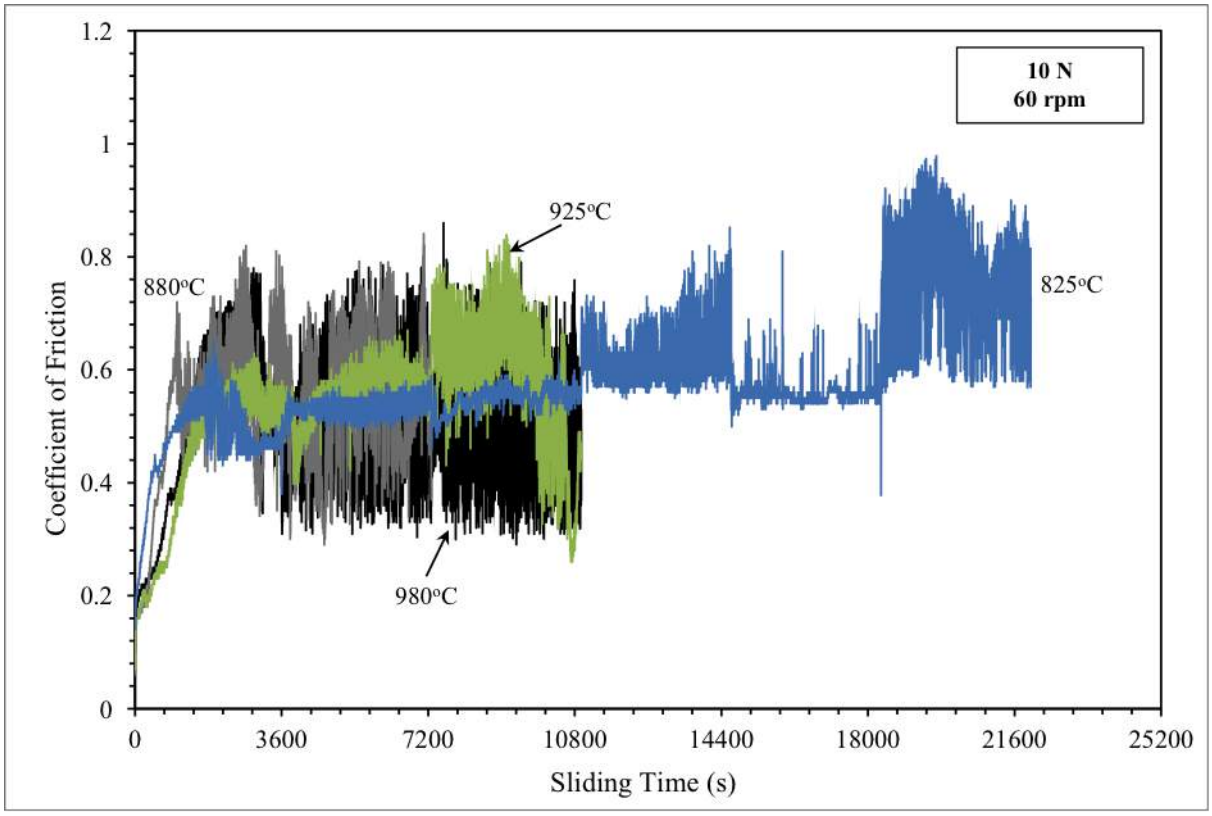


Figure 8.8: Coefficient of friction (COF) curves recorded for samples pack carburised at 825$^oC$, 880$^oC$, 925$^oC$ and 980$^oC$for 20h under load of 10N

Figure 8.8 shows that under dry sliding conditions, the COF of all samples always start with low values. This is due to the fact that the wear track takes about 720s to be generated. This means that the removal of carbide layer does not always occur at the start of friction and wear testing, depending on many factors such as the applied load and speed of rotation. Figure 8.8 also shows that zirconium treated at 825$^oC$ was able to stand a load of 10N for about 4h (14354s), longer than any other samples. The COF observed is higher than 0.6. The reason that 825$^oC$ sample survived for that long time is that the sample is rich in $ZrO_2$ and more in-line with that of oxygen rich zirconium and less carbon [17][201]. Further details will be explained in the diffusion section. Zirconium sample treated at 880$^oC$ as able to withstand a load of 10N for about 1000s with lower COF ($\mu$ ≈0.5). After breaking through the film the COF is then increased until it reached about 0.8, so another hour was added to the test to see the reaction of COF. Again similar to the previous sample the COF is consistent with that of oxygen rich zirconium. When the temperature was increased to 925$^oC$ the sample was able to withstand load of 10N for duration of 7120s with low COF of about 0.5, but then the film started to breakdown and

this lead in increasing the COF until about 0.8. Zirconium treated at $980^oC$ was able to withstand a load of 10N for about 2700s with COF of about 0.7. After the film removal the sample suffered from high friction and like every sample another hour was added to the test after breakdown of the film, the COF after film removal was about 0.75.

However the samples treated at low temperature ($825^oC$ and $880^oC$) had expected COF, but that they perform better. The reason behind this is that at $825^oC$ there is a mixture of oxidised and carburised features and this explains the longer survival. The $880^oC$ sample did show low COF in the beginning but only survived for 1000s and after the breakdown the COF increased up to 0.8. Both $880^oC$ and $925^oC$ samples have similar starting COF, but the $925^oC$ sample has a longer low friction region. It is clear that the $925^oC$ sample is better than the $980^oC$ sample; thus, increasing the temperature does not always give lower COF. When the temperature is increased to $980^oC$ the diffusion of carbon into the deeper substrate leading to a thinner carbide layer on the surface. This explains the sudden rise in friction. Oxygen diffusion within the zirconium substrate also plays a role here. In theoretical sense there is limited amount of oxygen inside the carburising container. Therefore the rate of oxygen diffusion will increase with increasing the carburising temperature, leading in the distribution of oxygen in the substrate with reduced oxygen content in the surface region.

The low COF observed can be linked with the amount of carbon within zirconium as shown in figure 8.8. It can be clearly seen that the samples with more carbon diffusion will last longer period in tribological testing. It has been noticed that sample carburised at $925^oC$ has a favourable structure leading to low COF which lasts longer period of sliding time (see figure 8.3).

### 8.2.7 Wear rates

Wear rate was compared between all treated samples every hour till failure as shown in table 8.3. It can be seen that when the test is initiated for the first hour, the wear rate is always low until certain time. The $825^oC$ sample was carburised at low temperature, but it shows a very low wear rate ($0.000229mm^3/m$) in the first hour. This can confirm the idea of having mixture of oxide and carbide layers. The $880^oC$ sample suffered from high friction which lead to having high wear rate ($0.004493mm^3/m$) in the first hour. Both $925^oC$ and $980^oC$ samples have low wear rates ($0.000148mm^3/m$ and $0.000401mm^3/m$) in the first hour.

Table 8.3: Wear rate of carburised zirconium till failure in steps of 1h under load of 10N

| Carburising Temperature | Hour of testing | | | | | |
|---|---|---|---|---|---|---|
| | $1^{st}$ hour | $2^{nd}$ hour | $3^{rd}$ hour | $4^{th}$ hour | $5^{th}$ hour | $6^{th}$ hour |
| 825 | 0.000046 | 0.000229 | 0.000275 | 0.000323 | 0.000398 | 0.000585 |
| 880 | 0.004993 | 0.019789 | - | - | - | - |
| 925 | 0.000148 | 0.000697 | 0.003405 | - | - | - |
| 980 | 0.000401 | 0.008011 | 0.016922 | - | - | - |

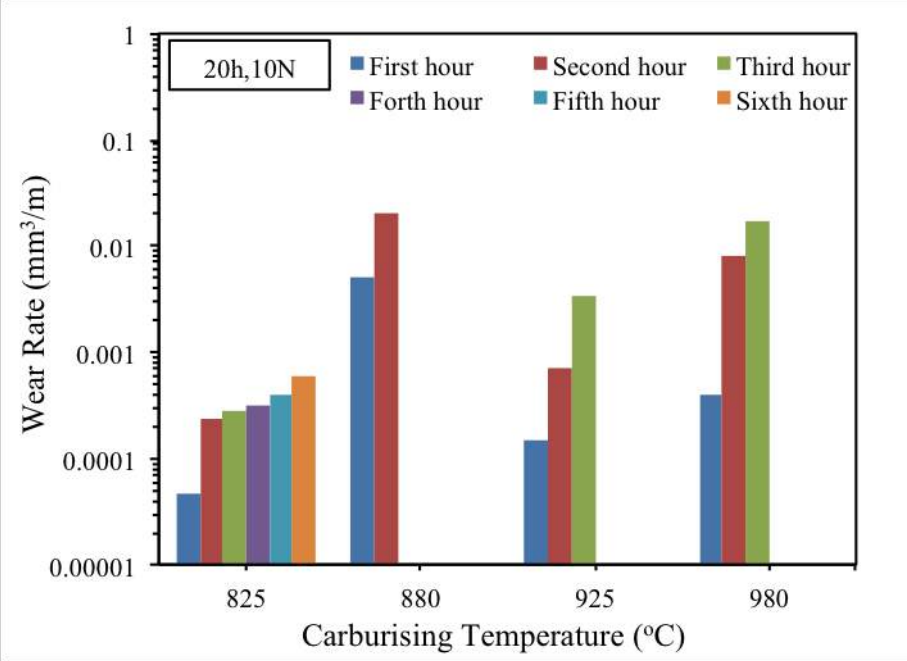


Figure 8.9: Wear rate of carburised zirconium till failure in steps of 1h under load of 10N

During the second hour of testing, again the $825^oC$ sample showed the lowest wear rate ($0.000229mm^3/m$). The $880^oC$ showed no improvement and wear rate increased to ($0.0019789mm^3/m$) and film broke through. The $925^oC$ sample showed lower wear rate ($0.000697mm^3/m$) during the second hour compared with $880^oC$ sample. While the $980^oC$ sample shows a high wear rate ($0.008010mm^3/m$) during the second hour and this is the second highest wear rate compared with other samples. In the third hour, the $825^oC$ sample shows the lowest wear rate ($0.000275mm^3/m$). The $925^oC$ sample showed the second lowest wear rate (0.0003405 $mm^3/m$) during the third hour and then film broke through. The film broke through for the $980^oC$ sample and it showed a very high wear rate ($0.016922mm^3/m$) com-

pared with both $825^oC$ and $925^oC$. It was noticed that the $825^oC$ sample was the only sample to last 6h before failure in friction and wear testing. In the fourth and fifth hours, the $825^oC$ sample managed to survive with low wear rate ($0.000323mm^3/m$ and $0.000398mm^3/m$). In the sixth hour the $825^oC$ sample managed to survive, this confirms that the sample has mixture of oxide and carbide layers performs the best.

### 8.2.8 wear track morphology

Wear track morphology was investigated after every hour of friction and wear testing as shown in figures 8.10,8.11,8.12 and 8.13. Figure 8.10 shows the first stage of wear tracks for all samples in the first hour of the wear and friction testing. It can be seen that the wear tracks demonstrate the effect of carburising temperature during the process.

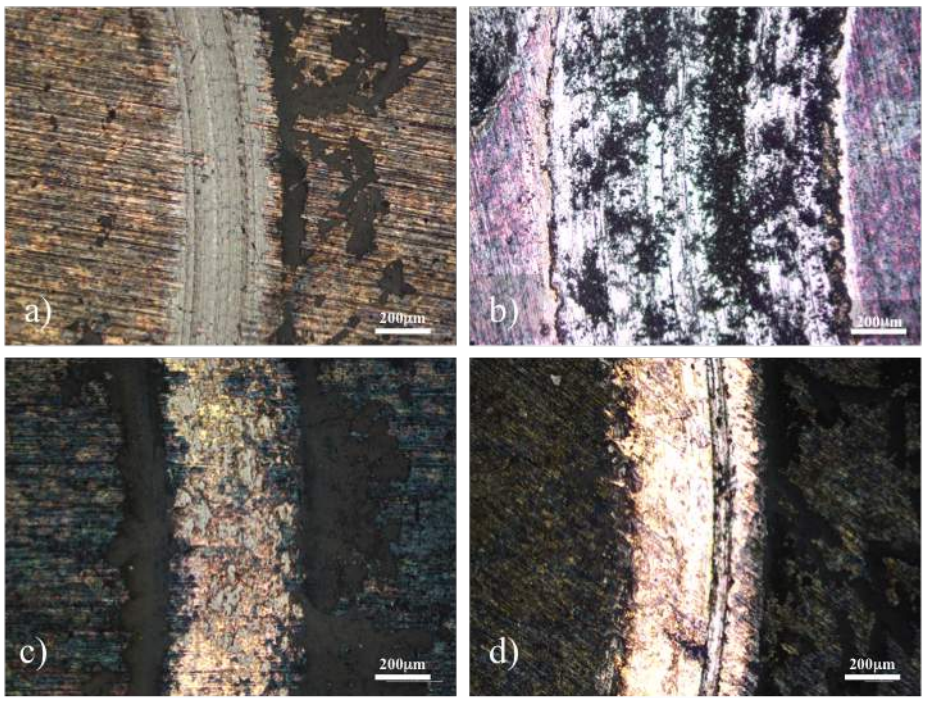


Figure 8.10: Optical microscopic images showing wear track morphology of zirconium carburised for 20h at temperatures of (a) $825^oC$, (b) $880^oC$, (c) $925^oC$ and (d) $880^oC$ tested under load of 10N for 3600s after initiating the wear and friction testing

After the first hour the $825^oC$ sample shows light material removal on the wear track (figure8.10a). In fact the $825^oC$ sample shows the best wear resistance after

1h of friction and wear testing. This can be linked to the fact that there is a mixture of carbide and oxide layer. The $880^oC$ sample shows severe wear compared to the other samples with dominating mechanisms of adhesion, abrasion and delamination. However as stated in Section 8.2.7, the $880^oC$ sample (figure8.10b) shows more material removal compared to the other samples (figure8.10a,c and d). For the $880^oC$ sample the breakdown of the ZrC structure within the wear track allows the exposure of the oxygen diffusion zone (ODZ) to become the dominating factor in defining both coefficient of friction and wear rate. It can be seen that delamination exists after removing the ZrC layer as well as abrasive wear on the exposed oxygen diffusion zone (ODZ). It is noticeable that the $825^oC$ sample shows micro-polishing of the surface layer. On the other hand the $925^oC$ sample shows a very good wear resistance and light material removal. The $925^oC$ and $980^oC$ samples are carburised at high temperatures, but it can be seen that the $980^oC$ sample shows a wider wear track during the first hour (figure8.10d). Both $925^oC$ and $980^oC$ samples show some abrasion marks in the inner side of wear track (figure8.10c and d).

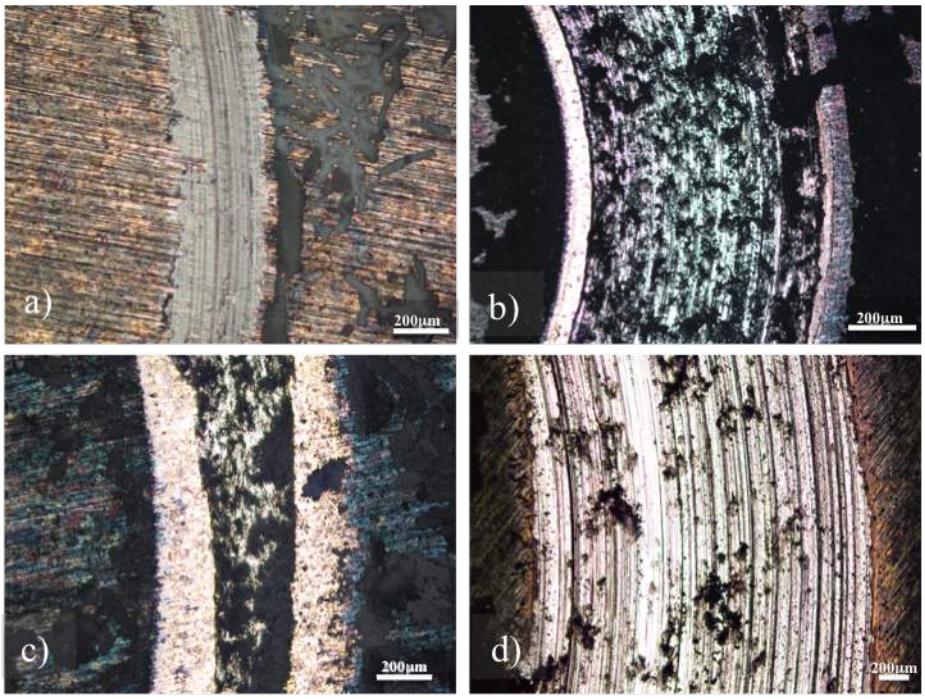


Figure 8.11: Optical microscopic images showing wear track morphology of zirconium carburised for 20h at temperatures of (a) $825^oC$, (b) $880^oC$, (c) $925^oC$ and (d) $980^oC$ tested under load of 10N for 3600s after second hour of the wear and friction testing.

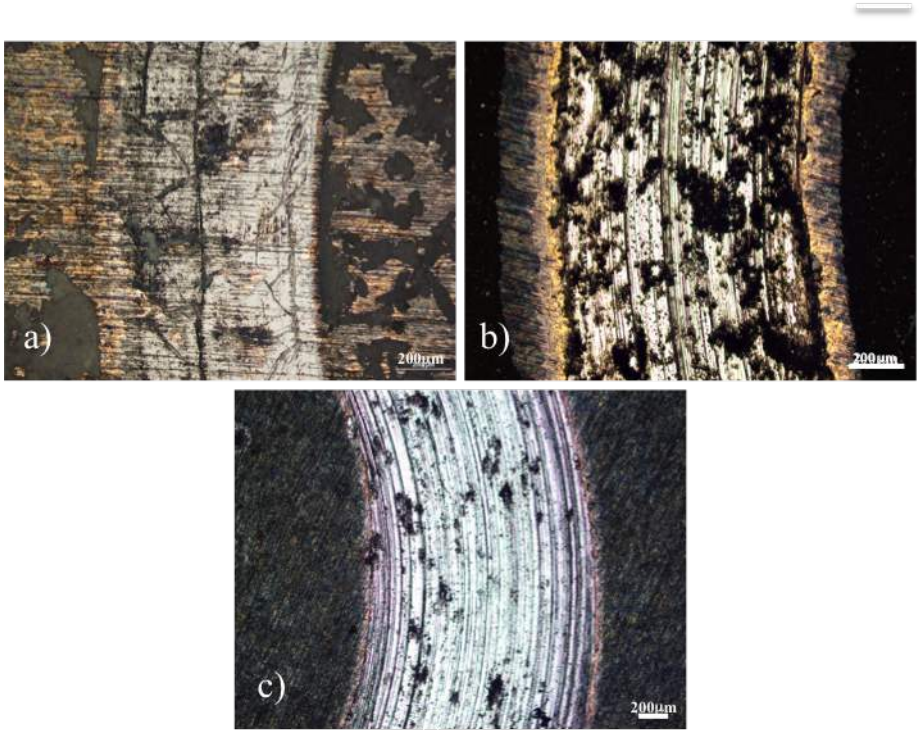


Figure 8.12: Optical microscopic images showing wear track morphology of zirconium carburised for 20h at temperatures of (a) $825^oC$, (b) $925^oC$ and (c) $980^oC$ tested under load of 10N for 3600s after third hour of the wear and friction testing.

Figure 8.11 shows the wear track morphology after the second hour of testing. It is clearly shown that all samples survived friction and wear testing after the second hour apart from the $880^oC$ sample. The $825^oC$ sample suffered from higher material removal (figure 8.11a) compared to the first hour (figure 8.10a), but the principal wear mechanism is still micro abrasion and polishing. For the $880^oC$ it can be seen that the film was removed completely (figure 8.11b), resulting in severe wear.

The $925^oC$ sample showed better wear resistance (figure 8.11c), but the sample suffered from more material removal especially in the center of wear track. However, the inner side of the wear track suffered from less material removal. After the second hour, the $925^oC$ sample started to have abrasion marks on outer side of wear track. The $980^oC$ sample (figure 8.11d) shows a very wide wear track and many abrasion marks throughout the wear track (figure 8.11d).

Figure 8.12 shows the wear track morphology after the third hour of testing. It is clearly shown that $925^oC$ and $980^oC$ samples did not survived friction and wear testing after the third hour (figure 8.12b and c). On the other hand the $825^oC$ was the only sample to survive after third hour of friction and wear testing (figure 8.12a).

The $825^oC$ sample did survive, but there is a lot of large cracking everywhere on the wear track. Similar to the second hour of testing (figure 8.11a), the $880^oC$ sample shows delamination of the surface layer with abrasion in the center of wear track.

The $925^oC$ sample showed poor wear resistance (figure 8.12b) when compared to the second hour of friction and wear testing (figure 8.11c). Again it can be seen that the sample suffered from more material removal especially in the center and inner sides of wear track. After the third hour, the $925^oC$ sample showed more abrasion marks everywhere on the wear track followed by delamination. The $980^oC$ sample (figure 8.12c) also showed very poor wear resistance. This is because the sample suffered from high friction during the third hour of testing. After third hour of friction and wear testing the $980^oC$ sample showed more abrasion marks mostly in the center and inner side of wear track (figure 8.12c).

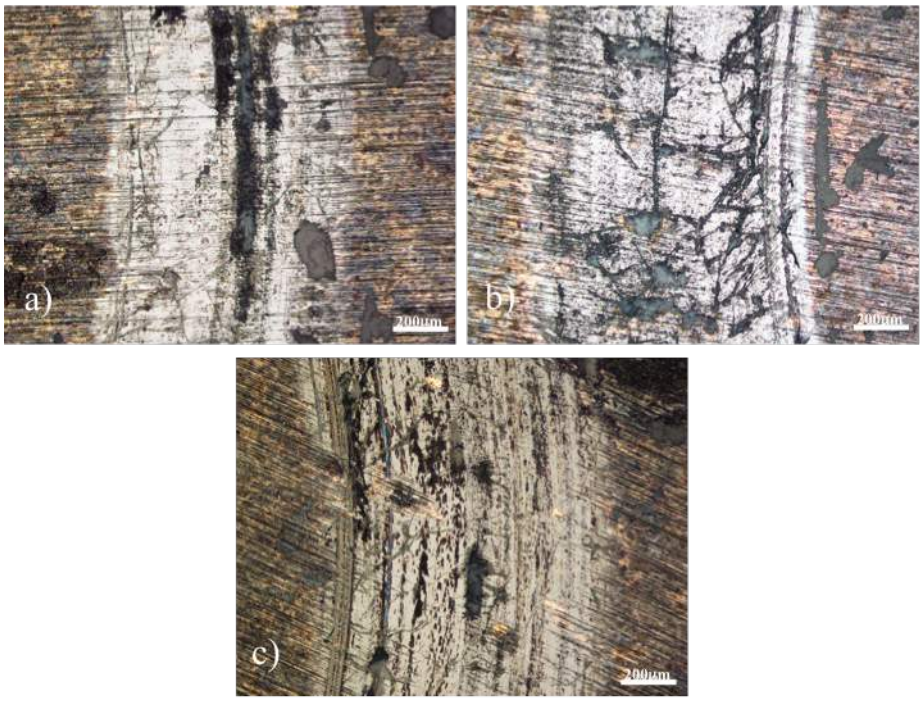


Figure 8.13: Optical microscopic images showing wear track morphology of zirconium carburised for 20h at temperature of $825^oC$ tested under load of 10N for 3600s after (a) 4h, (b) 5h and (c) 6h of wear and friction testing.

Since all testing were done until failure, the $825^oC$ sample was the only sample to survive after 3h of friction and wear testing. Figure 8.13 shows the wear track of the $825^oC$ sample after the fourth, fifth and sixth hours of friction and wear testing. After the fourth hour of testing it can be seen that the sample suffered from high friction and cracks started to form on the wear track. These cracks were mainly

formed on the inner side of wear track (figure 8.13a). However, after the fifth hour of testing the cracks increased in number and size (figure 8.13b). After the sixth hour it can be seen that the $825^oC$ sample has a lot of cracks, mostly in the inner side of wear track (figure 8.13c), and abrasion marks are spreading mainly in the center and inner side of wear track.

$825^oC$ is the lowest temperature used during the investigation of effect of temperature on carburizing process. The survival of the $825^oC$ sample longer than any other sample could be explained by the strong combination of oxide and carbide layers. This happens because $825^oC$ is not sufficient high to generate active carbon species in the container, thus oxidation becomes more dominant.

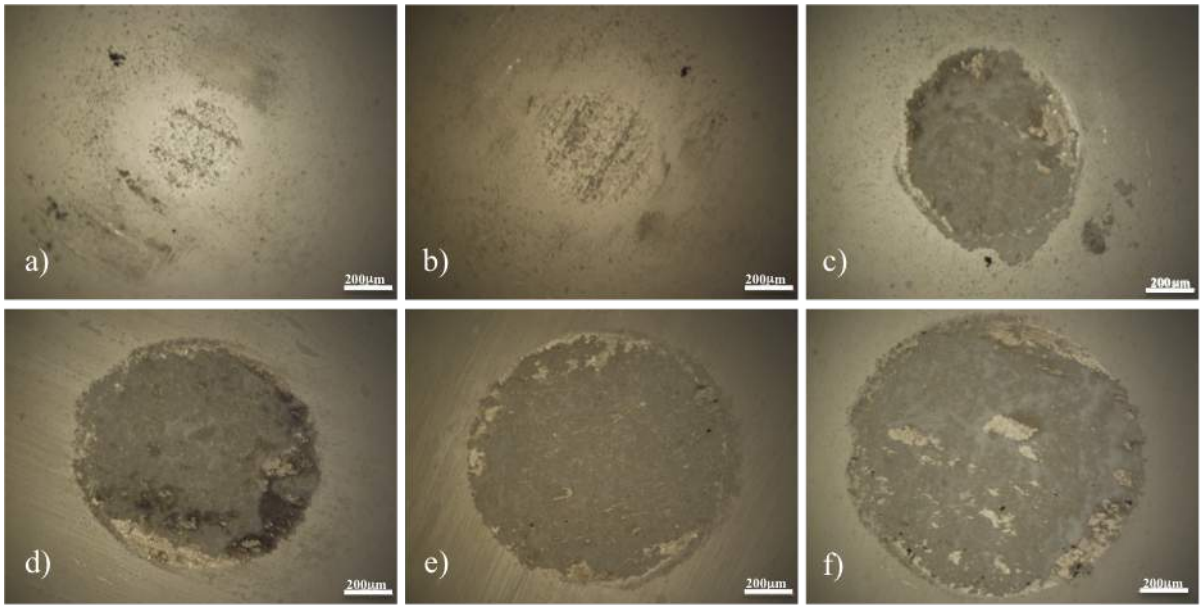


Figure 8.14: Microscopic images of the wear scar on the alumina ball after sliding with zirconium carburised for 20h at temperature of $825^oC$ under 10N load after (a) 1h, (b) 2h, (c) 3h, (d) 4h, (e) 5h and (f) 6h of friction and wear testing.

Figure 8.14 shows the wear scar on alumina ball used during friction and wear testing on the $825^oC$ sample. It can be seen that in the first and second hour (8.14a and b), the scar is small and the diameters are 399$\mu$m and then 474$\mu$m. But after the third and fourth hours of testing (8.14c and d), due to the high friction there is a lot of removed material sticking on the alumina ball and the diameters of the scar has increased to 735$\mu$m and then 929$\mu$m. This transfer of material is occurring due to the high stress on the sample, forcing the softer surface to stick on the harder surface. Finally after the fifth and sixth hours of testing (8.14e and f), the size of the scars have increased further. The scar increased to 1004$\mu$m after the fifth hour

and then to 1152$\mu$m after the final hour.

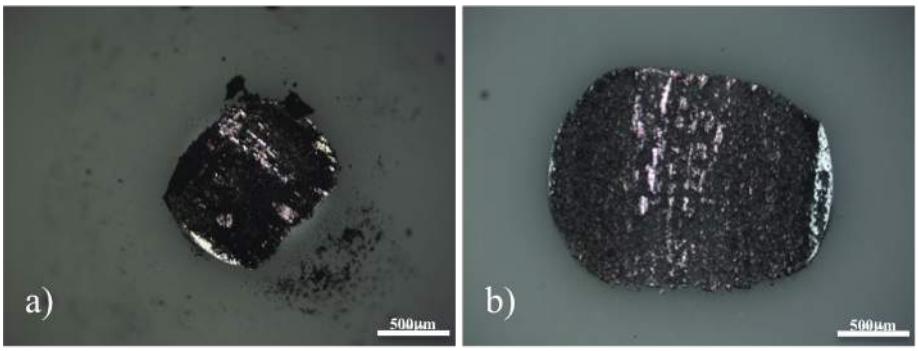


Figure 8.15: Microscopic images showing the wear scar on the alumina ball after sliding with zirconium carburised for 20h at temperature of 880$^oC$ under 10N load after (a) 1h and (b) 2h of friction and wear testing.

Figure 8.15 shows the scar on the alumina ball used during friction and wear testing on the 880$^oC$ sample. It can be seen that after the first hour (8.15a), a lot of material from the sample is sticking on the alumina ball. The diameter of wear scar after the first hour of friction and wear testing is 629$\mu$m. After the second hour of testing (8.15b) the diameter size increased to 961$\mu$m, and it can be seen that the ball suffered from massive material loss. This can be linked to figure (8.11b), which shows that the carbide layer was removed completely.


Figure 8.16: Microscopic images showing the wear scar on the alumina ball after sliding with zirconium carburised for 20h at temperature of 925$^oC$ under 10N load after (a) 1h, (b) 2h and (c) 3h of friction and wear testing.


Figure 8.17: Microscopic images showing the wear scar on the alumina ball after sliding with zirconium carburised for 20h at temperature of $980^oC$ under 10N load after (a) 1h, (b) 2h and (c) 3h of friction and wear testing.

Figure 8.16 shows the scar on the alumina ball used during friction and wear testing on the $925^oC$ sample. It can be seen that after the first hour (8.16a), the scar is small and there is no material sticking on the ball. The diameter of wear scar after the first hour of friction and wear testing is 470$\mu$m. After the second hour of testing (8.16b) the diameter size increased to 733$\mu$m, and it can be seen that the ball suffered from high material loss compared with after the first hour. However, after the third hour of testing, the scar has increased in size to about 1183$\mu$m.

On the other hand, Figure 8.17 shows the wear scar on alumina ball used during friction and wear testing on the $980^oC$ sample. It can be seen that after the first hour (8.17a), a lot of material from the sample is sticking on the ball, and the wear scar is quite large, about 613$\mu$m in diameter. After the second hour of testing the scar increased in size and there is some material transferred from the sample (8.17b). The scar diameter has increased to 1552$\mu$m after the second hour of testing. But when the sample was tested for the third hour (8.17c), the scar has changed in shape and size. The diameter of the scar increased to 1719$\mu$m after the carbide layer failure. Figure 8.18 shows a clear comparison between all the scars.

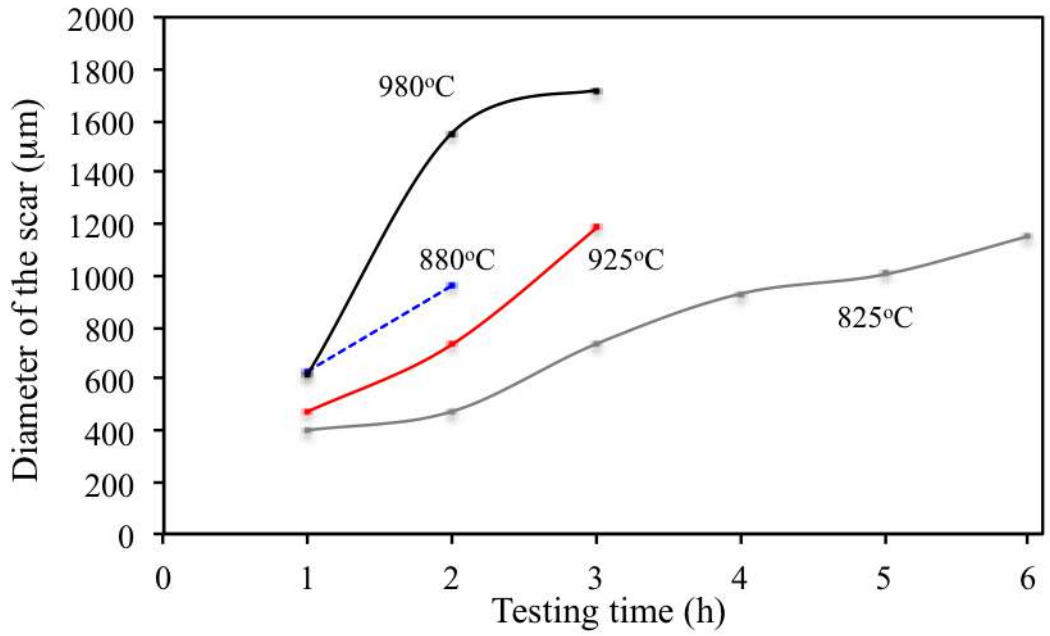


Figure 8.18: Scar diameter comparison between 825, 880, 925 and 980$^oC$

## 8.3 The effect of time on carburisation process

From Section 8.2, it has been demonstrated that carburising at 925$^oC$ was more effective than any other temperatures. This temperature was chosen because it was effective at generating the diffusion of both oxygen and carbon. All the tests that were conducted until this point were done using the duration of 20h. In this section the effect of carburising time is investigated at a fixed temperature of 925$^oC$.

### 8.3.1 Process

The initial composition used in the pack compound mixture was the same composition used in Section 8.2. Therefore the composition used for the pack was 70% carbon and 30% energiser. The energiser was created using Barium carbonate ($BaCO_3$), sodium carbonate ($Na_2CO_3$) and calcium carbonate ($CaCO_3$) in ratio of 3:2:1. This pack of carbon and energiser was then used to determine the optimal time for Zirconium carburisation. Carburisation treatment took place at temperature of 925$^oC$ for various durations of 3h, 10h, 20h and 40h. Then cooled down using furnace cooling (FC). After carburisation the samples were then tested tribologically to determine the effect of treatment time and also to determine the best

carburising time to produce a very good wear resistance structure.

### 8.3.2 Layer Morphology

#### Ball Crater

The surface features have been observed in this work. Typical ball craters made on the carburised surfaces are shown in Fig. 8.19. The ball craters has a grey colour appearance. The carbide layer thicknesses were measured from the ball crater. However it's very hard to distinguish the diffusion zone for carburised samples. Therefore diffusion zone thicknesses were measured using the cross section technique.

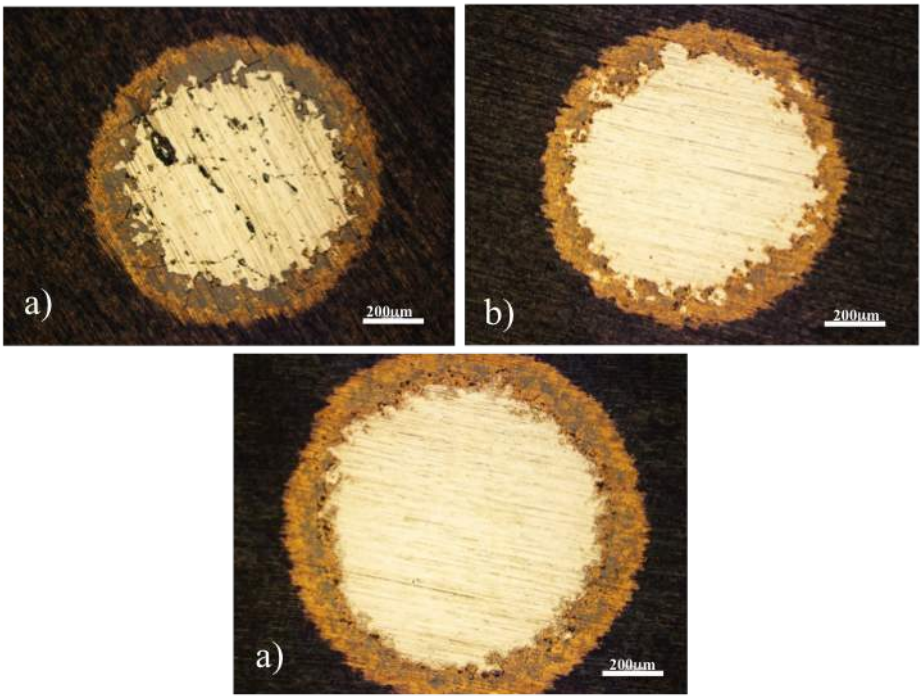


Figure 8.19: Ball crater made on the surface of carburised sample at $925^oC$ for duration of: a) 3h, b) 20h and c) 40h. Showing carburised layer on the surface.

#### Cross-section

Similar to what was done previously in Section 8.2, cross-sections were also produced as shown in figure 8.20 for 3h (a), 20h (c) and 40h (e) samples. Also SEM images of the cross-sections were also taken for 3h (b), 20h (d) and 40h (f) samples. From ball crater (Figure 8.19) and cross-sectional results (figure 8.20), it can be seen that the duration of carburising has a large effect on the thickness of carbide layer.

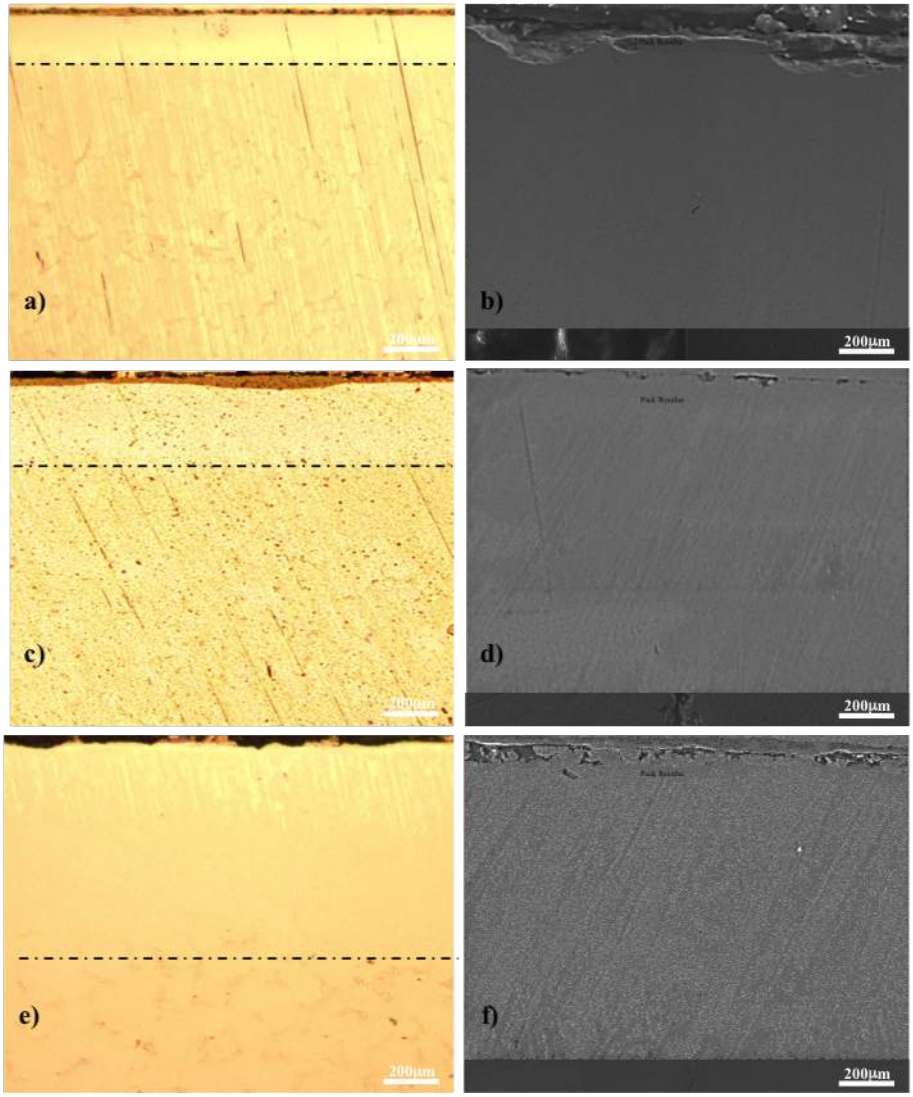


Figure 8.20: Optical and SEM micrographs showing cross-sectional morphology of pack carburised zirconium carburised at $925^oC$ for durations of 3h (a and b), 20h (c and d) and 40h (e and f). Optical images were taking using magnification of 200X and SEM images were taking using magnification of 1000X

After carburising the sample for 3h, the carbide layer was about 3.5$\mu$m thick (Figure 8.19a), which was increased to about 5.7 and 7.1$\mu$m after increasing the duration of the treatment to 10 and 20h (Figure 8.19b). After increasing the treatment duration to 40h, the thickness of carburised layer produced was about 9.9$\mu$m (Figure 8.19c). It can be seen that carburising needs a high temperature and long time to produce a thick carbide layer. This can be proved by seeing the poor adhesion, spalling and cracks on the ball crater of the 3h sample (Figure 8.19a). On the other hand both 20h and 40h samples (Figure 8.19b and c) show uniformed ball

Table 8.4: Layer thickness developed after pack carburising

| Duration of carburising (h) | Carbide layer Thickness ($\mu$m) | Oxygen diffusion depth ($\mu$m) |
|---|---|---|
| 3 | 3.5 | 130 |
| 10 | 5.7 | 155 |
| 20 | 7.1 | 175 |
| 40 | 9.6 | 215 |

crater with hardly seen cracks.

Table 8.4 lists the thicknesses of the carbide layer and oxygen diffusion depth for all treated samples. It can be seen that as the time of carburising increases both carbide layer thickness and oxygen diffusion depth are increased. This is due to the longer duration of carburising treatment, which helps in providing thicker layer. Figure 8.21 shows the film thicknesses of the ZrC and ODZ regard to the duration of carburising, plotted in the logarithm scale for thickness. A nearly linear relationship is found for both the carbide layer and the diffusion zone. This is expected from the solid diffusion law.

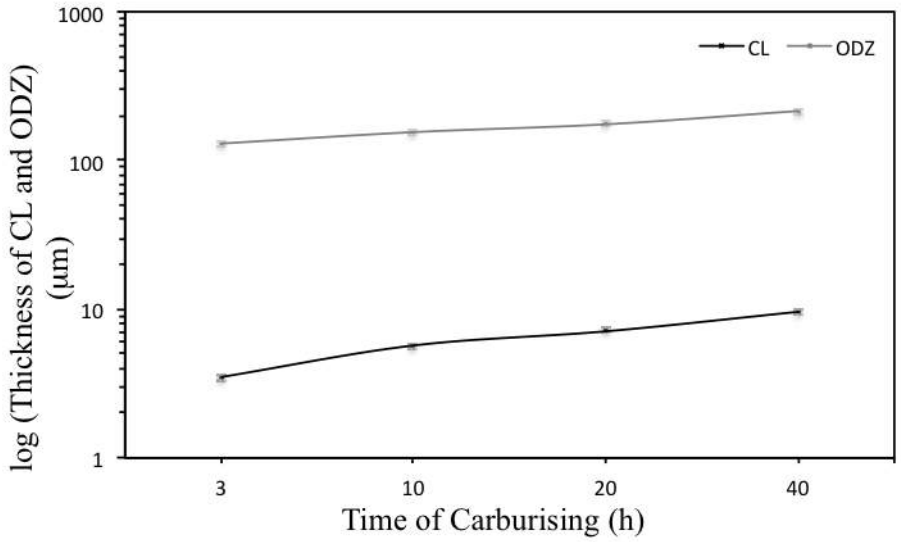


Figure 8.21: Film thickness of CL and ODZ with regard to time of carburising, for samples carburised at $925^oC$ for durations of 3h, 10h, 20h and 40h

It can be seen that as the time of carburising increases, the thickness of the carbide layer increases and the depth of oxygen diffusion zone increases too. Figure 8.21 states that duration of carburising has a huge effect on the formation of carbide layer and oxygen diffusion zone. According to the law of diffusion, under a constant

surface concentration and temperature, the diffusion depth is governed by:

$$d = Ct^{1/2}, i.e. log(d) = C + 1/2t \tag{8.1}$$

Thus a linear relationship between log(d) and t is expected, as shown in Fig. 8.21.

### 8.3.3 Glow discharge optical spectroscopy GDOS

The combination of both carbon and oxygen into the surface of treated zirconium was also investigated using GDOS to see if the duration of carburisation can affect the results and also in order to find the composition profile measurements. Figure 8.22 shows both carbon and oxygen profiles. It can be clearly seen that the diffusion of carbon was more effective for duration of 20h and 40h. However, when the duration is lower than 20h the carbon diffusion decreases. From GDOS profile it can be seen clearly that carbon is penetrating about 4$\mu$m for the 3h sample and compared with 14$\mu$m for the 40h sample. On the other hand, the oxygen diffusion was also investigated for all treated samples as shown in figure 8.22b. The amount of oxygen is not constant through the depths of 10h, 20h and 40h samples. But for the 3h sample it can be seen that the oxygen concentration is high and goes up to 40% and the amount of oxygen penetrating is about 14$\mu$m. This indicates that the carbon content is low when the oxygen content is high for all carburised samples. Figure 8.22b shows that when carburising is undertaken for duration of 40h, the oxygen concentration starts to drop faster than any of the other carburised samples. In fact the oxygen concentration for the 40h sample is settled less than 1%. However the dropping of oxygen concentration is decreased for the 3h sample and the oxygen concentration settled about 2-4%.

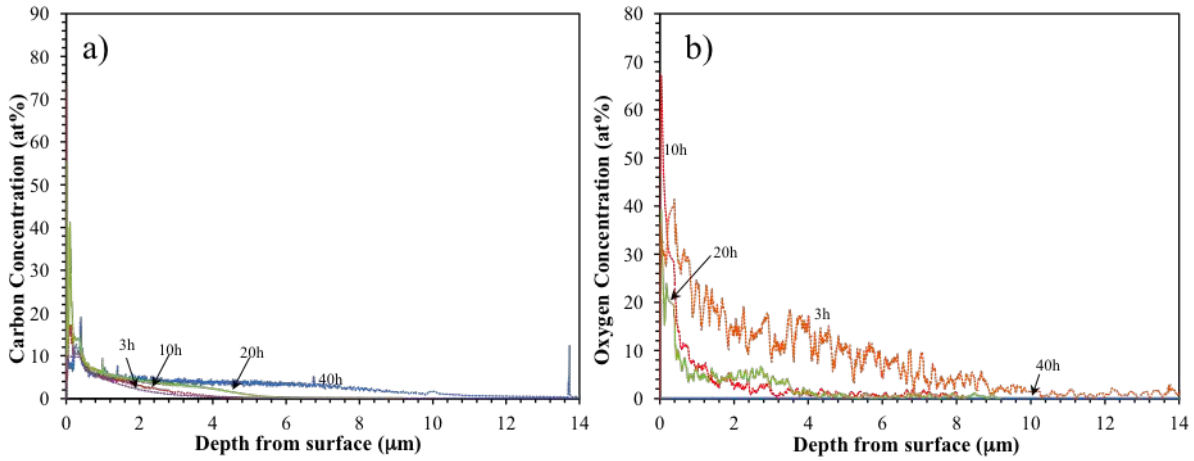


Figure 8.22: Carbon (a) and oxygen (b) concentration profiles measured by GDOS produced by carburisation at temperature of $925^oC$ for 3h, 10h, 20h and 40h.

### 8.3.4 Micro-Hardness profile

Micro-hardness testing was conducted on cross-sectional samples (3h, 10h 20h and 40h) and it was compared with untreated samples as shown in figure 8.23. Carburised samples have a very harder surface compared to thermal oxidised samples, with hardness up to 1200HV which is similar to that of carburised titanium [200].

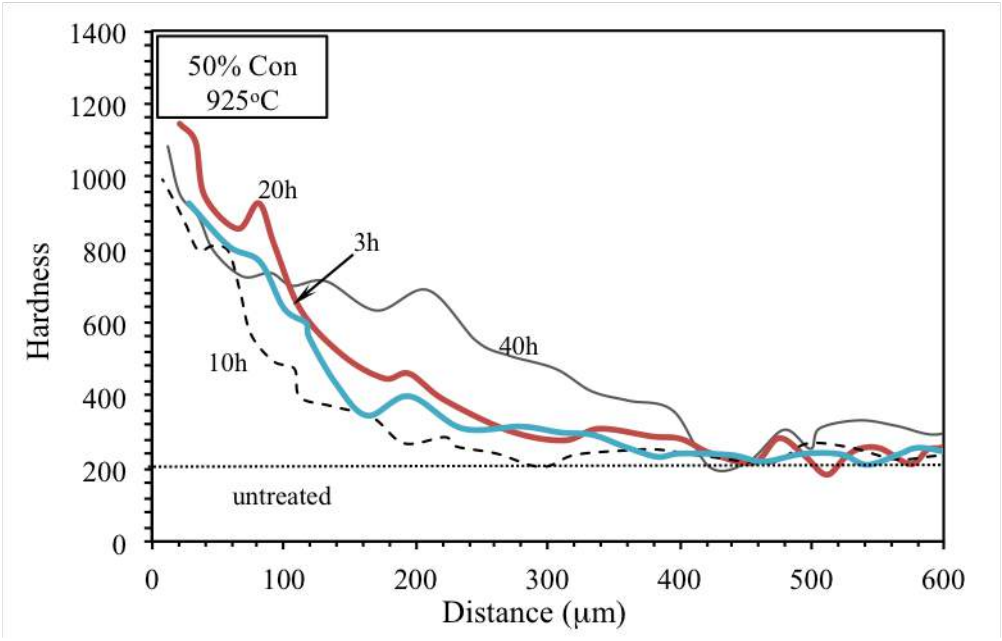


Figure 8.23: Cross-sectional hardness curves for the carburised samples treated at $925^oC$ for 3h, 10h, 20h and 40h

As shown in figure 8.23, surface hardness depends on the thickness of the carburised layer built on the surface. It can be seen clearly that there is definite correlation between the duration of the carburisation and layer thickness. This means when the duration is longer, the hardness will be higher too until it reaches a certain depth (400-600$\mu$m). When hardness is measured between 400 and 600$\mu$m which is the centre of the cross-section of all samples, this will be the meeting point of the substrate and it is similar to the hardness of the untreated sample. The 3h sample is the only sample that went out of the 400-600$\mu$m ranges, but only by few microns. This can be explained by the smaller diffusion depth for the short duration

From figure 8.23 it can be seen that the hardness remains high until it reaches a depth of about 20-30$\mu$m. There is a sharp reduction in hardness from 1200Hv to 800HV across the carbide layer, this can be explained by the reduced amount of ZrC phase with depth. The sharp reduction is followed by gradual decline in hardness across the oxygen diffusion zone (ODZ) from 800HV to that of untreated zirconium 200HV.

Increasing the carburisation duration helped the oxygen to diffuse deeper into the zirconium substrate creating larger ODZ. When the ODZ is larger, this will help in increased load bearing capacity. This also states that the structure of all samples is a multi-layered structure consisting of ZrC (carbide layer) and $\alpha$-Zr(O) (oxygen diffusion zone).In general it can be stated that increasing the duration of carburising increases the thicknesses of both oxygen diffusion zone and the carbide layer.

### 8.3.5 X-Ray Diffraction XRD

Similar to the previous section, x-ray diffraction (XRD) was undertaken using Cu-K radiation. This helps in finding the existing phases that are present in the carburised sample. Figure 8.24 shows the X-ray diffraction results for untreated sample as well as the samples carburised for different durations (3h, 20h and 40h). The diffraction pattern shows that the surface layer consists zirconium carbide (ZrC). Theoretically it is expected to see the peaks of $\alpha$-Zr shifting down with increasing the duration of carburising. The XRD graph is also showing clearly that with increasing the duration of the carburisation, the thickness of the carbide layer increases. The X-ray radiation couldn't penetrate the 3h sample to an appropriate depth to detect the ODZ. This could also explain why the $\alpha$-Zr peaks are reduced from 10h sample to the 20h sample and even lower in the 40h sample.

From the XRD results, it can be deduced that during the early stage of car-

burising, oxidation of the CP-Zr surface is dominant, leading to the formation of an oxide layer on the surface. With increasing curburising time, carbirisation becomes more dominant and a ZrC layer is formed. Clearly, carburisation is preceded by oxidation. A sufficiently long time is required (more than 20 h) for the carburising effect to happen to form a ZrC layer.

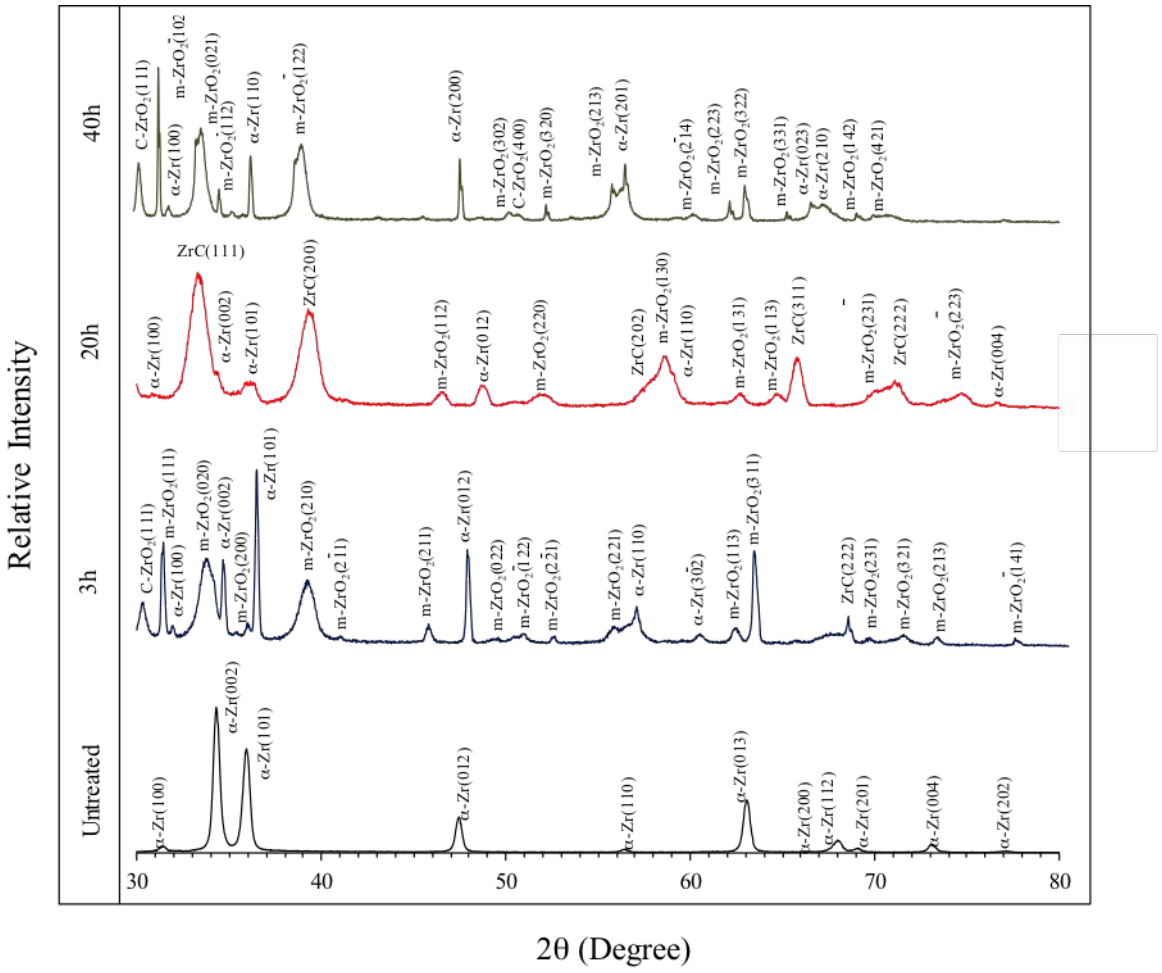


Figure 8.24: X-Ray diffraction patterns generated from samples carburised at temperature $925^oC$ for durations of 3h, 20h and 40h against untreated zirconium

Table 8.5 shows the phase composition for each treated and untreated samples. It can be seen that for longer duration (20h and 40h) ZrC phase is very strong. However, when the carburizing time is lower than 20h $\alpha$-Zr and m-$ZrO_2$ are more dominant.

From table 8.5 it can be seen that the $\alpha$-Zr and m-$ZrO_2$ phases are strong in the 3h sample. This indicates that short carburizing time would only form a thin carbide layer on surface of the sample. It can be stated that the strong m-$ZrO_2$

Table 8.5: Summary of XRD results

| Time (h) | Phase composition |
|---|---|
| Untreated | $\alpha$-Zr |
| 3 | ZrC (weak),$C-ZrO_2$(mediate),m-$ZrO_2$ (strong), $\alpha$-Zr (strong) |
| 10 | ZrC (weak),$C-ZrO_2$(weak),m-$ZrO_2$ (mediate), $\alpha$-Zr (mediate) |
| 20 | ZrC (strong), $C-ZrO_2$(weak),m-$ZrO_2$,(mediate), $\alpha$-Zr (weak) |
| 40 | ZrC (strong), $C-ZrO_2$(mediate),m-$ZrO_2$ (strong), $\alpha$-Zr (weak) |

phase exist because oxidation initiated before carburizing. For carbide layer to be formed perfectly, the duration of carburizing should be longer. When the duration is increased to 10h, the only difference is that the m-$ZrO_2$ phase is weaker due to the fact that there are less chances for the formation of oxide layer compared with 3h sample. However at longer durations (20h and 40h), the ZrC phase is stronger, this states that at longer durations the formation of carbide layer is generated with more carbon concentration.

### 8.3.6 Tribological response

The samples were tested tribologically under dry conditions against an alumina ball ($Al_2O_3$). 20h and 40h samples lasted at least for three hours under load of 10N, but both 3h and 10h samples were unable to last up to three hour as shown in figure 8.25.

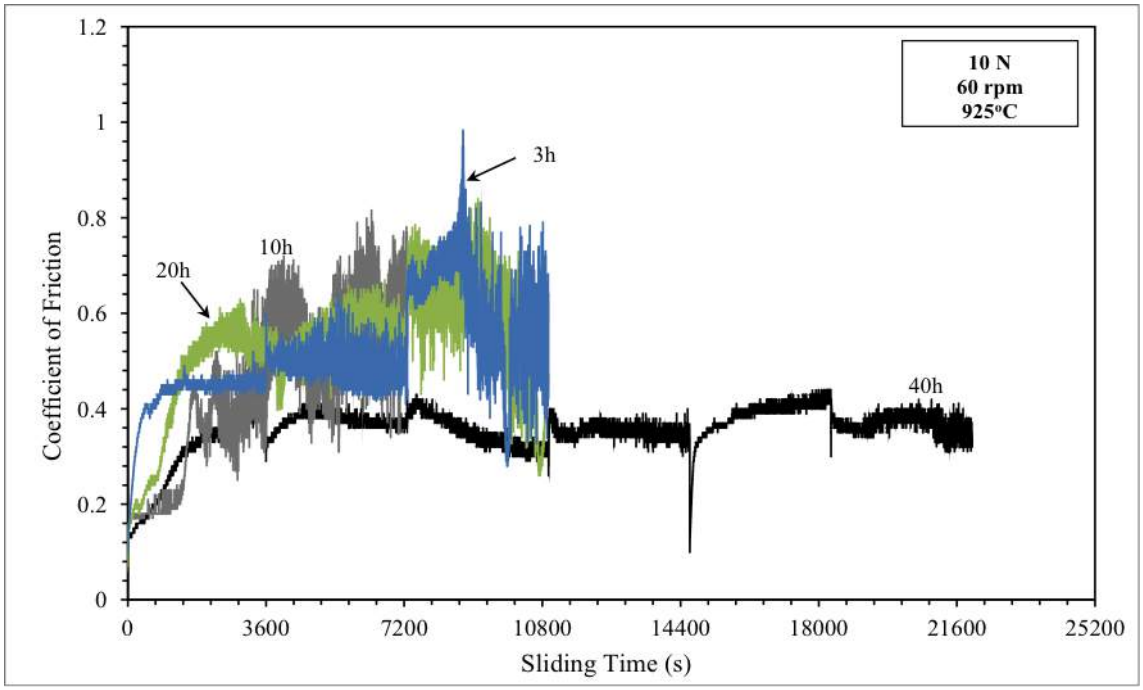


Figure 8.25: Coefficient of friction (COF) curves recorded for samples pack carburised at $925^oC$ for duration of 3h, 10h, 20h and 40h under load of 10N

Figure 8.25 shows the coefficient of friction (COF) curves recorded under load of 10N. The results show that carburising treatment creates a low friction and stable COF. The duration of carburisation has a noticeable effect on the initial frictional response of all treated samples. The 3h sample lasted nearly about 7200s with COF of about 0.5. However when the carburising duration was increased to 10h the COF increased to about 0.6 and the ZrC layer couldn't last for two hours. This is interesting and unexpected because the 3h sample lasted longer. The reason behind this could be because of the mixture of both oxide and carbide layers that gave the 3h sample better friction resistance. On the other hand, the 20h sample lasted much longer, about 10800s, because there is no obvious breakdown of the ZrC layer. Finally the 40h sample is an interesting sample, because there was a lot of cracks on the ZrC layer but which did not breakdown fully compared with other samples. The 40h sample lasted more than 14400s with no cracks, but the ZrC layer started having cracks and removal signs after 15120s. When comparing both tribological response and the characterisation of all treated samples, then it can be clearly seen that there is a strong correlation between the thickness of ZrC layer and the low friction regime gained from friction and wear testing.

### 8.3.7 Wear rates

Wear rate was compared in two stages (first hour and last hour) as shown in figure 8.26. It can be seen that when the test is initiated for the first hour, the wear rate is always low. The 3h sample shows lowest wear rate ($0.00009mm^3/m$) in the first hour confirming the idea of having mixture of oxide and carbide layers. The 10h sample suffered from high friction which lead to having high wear rate ($0.00069mm^3/m$) in the first hour. Both 20h and 40h samples have low wear rates ($0.00015mm^3/m$) demonstrating that samples carburised for longer durations have better and thicker ZrC layers. However in the last hour, the 3h sample lost the advantage of having the lowest wear rate and it went high to $0.01099mm^3/m$ and the film broke through. The 10h sample showed no improvement and wear rate increased to ($0.0.01769mm^3/m$) and film broke through.

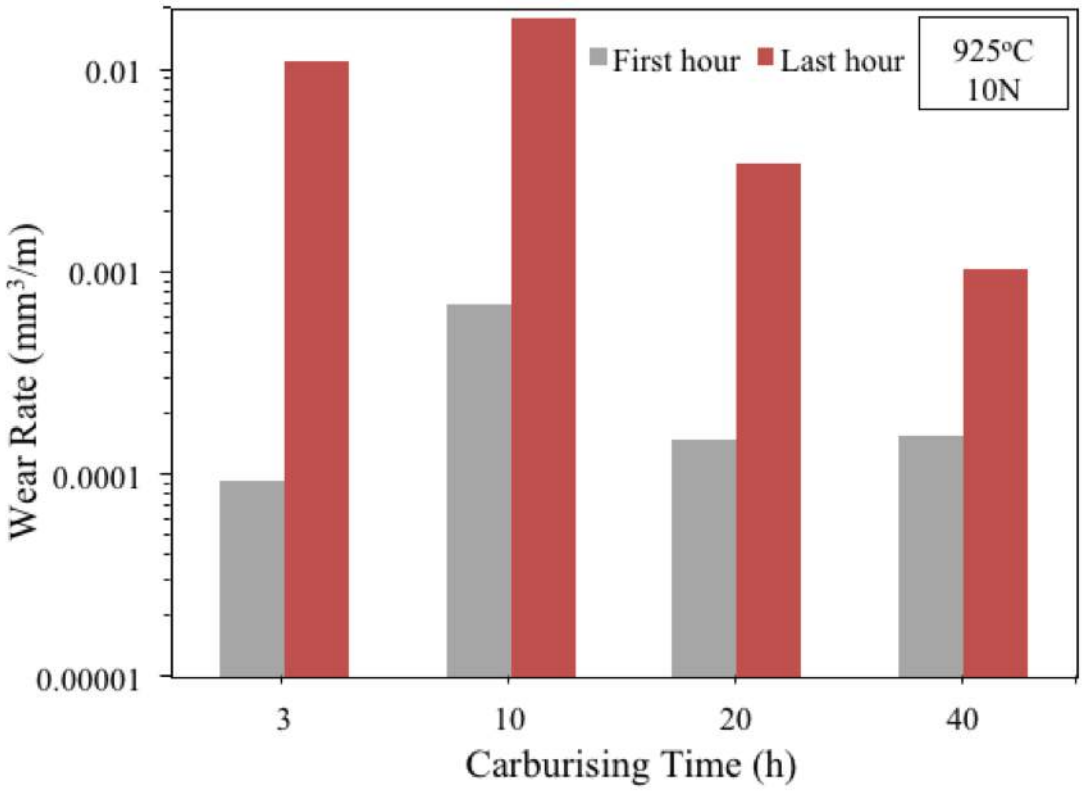


Figure 8.26: Wear rate comparison for carburised samples produced at $925^oC$ for durations of 3h, 10h, 20h and 40h under load of 10N in stages of first hour and last hour.

The 20h sample showed lower wear rate ($0.00340mm^3/m$) compared to both 3h and 10h samples and film broke through in most parts of the wear track. While the

40h sample shows the lowest wear rate ($0.00102mm^3/m$) in the last hour, confirming that carburising for longer duration has a large effect on wear behaviour.

### 8.3.8 wear track morphology

Wear track morphology was investigated every hour till failure as shown in figures 8.27, 8.28, 8.29 and 8.30. Figure 8.27 shows the wear tracks after the first hour of wear and friction testing. It can be seen that all samples managed to survive without film failure. All samples were worn mildly by micro-abrasion and polishing and show low wear rates.

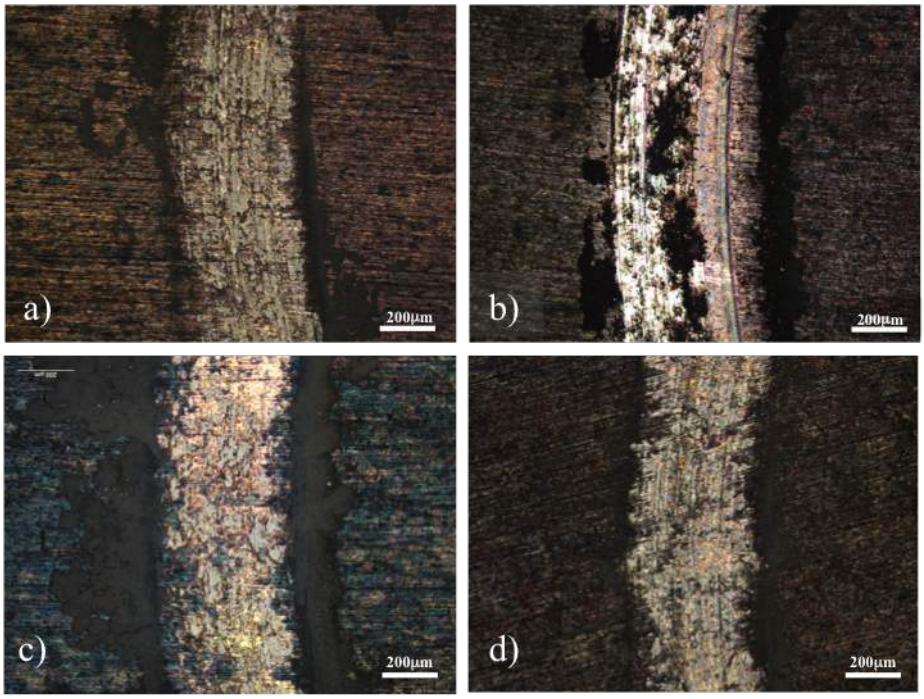


Figure 8.27: Optical microscopic images showing wear track morphology of zirconium carburised at $925^oC$ for durations of (a) 3h, (b) 10h, (c) 20h and (d) 40h tested under load of 10N for 3600s after first hour of friction and wear testing.

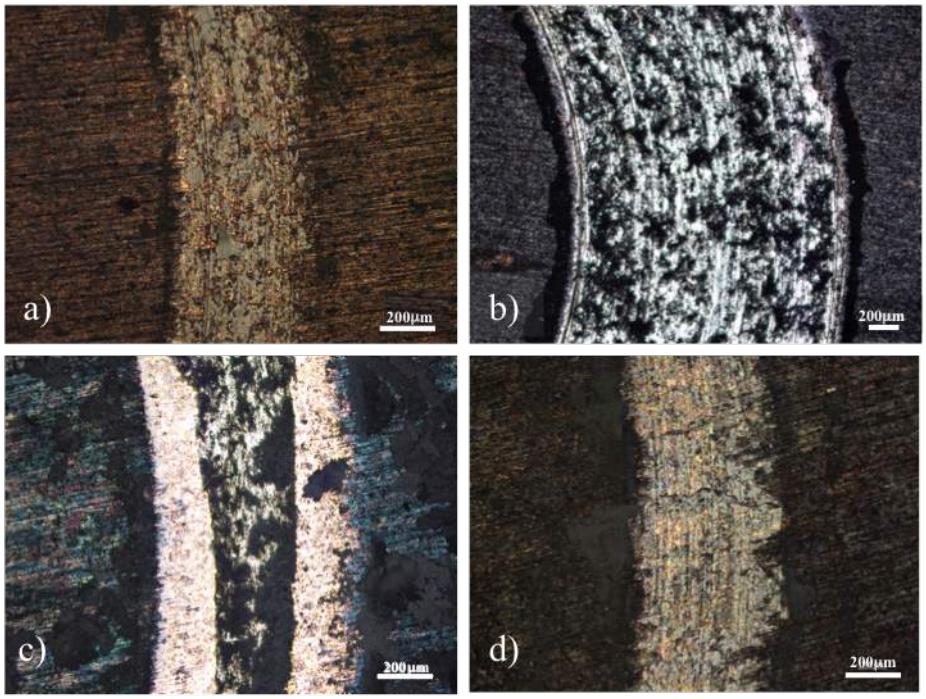


Figure 8.28: Optical microscopic images showing wear track morphology of zirconium carburised at $925^oC$ for durations of (a) 3h, (b) 10h, (c) 20h and (d) 40h tested under load of 10N for 3600s after second hour of friction and wear testing.

After the second hour of friction and wear testing, all samples managed to survive without film failure apart from the 10h sample (figure 8.28). The 3h sample still show good wear resistance after the second hour of testing, dominating by micro-abrasion and polishing. However, figure 8.28b shows that the 10h sample suffered from breakdown of the carbide layer after the second hour of testing, resulting in a wide and deep wear track. The carbide film is removed completely followed by cracks everywhere on the wear track and around it.

The 20h sample showed better wear resistance (figure 8.28c), but the sample suffered from more material removal especially in the center of wear track. However, the inner side of the wear track suffered from less material removal. After the second hour, the 20h sample started to have abrasion marks on the outer side of the wear track. The 40h sample (figure 8.28d) showed better wear resistance compared with other samples, this is due to the long duration of carburisation which built a thick ZrC layer. But the 40h sample started to show abrasion marks across the wear track.

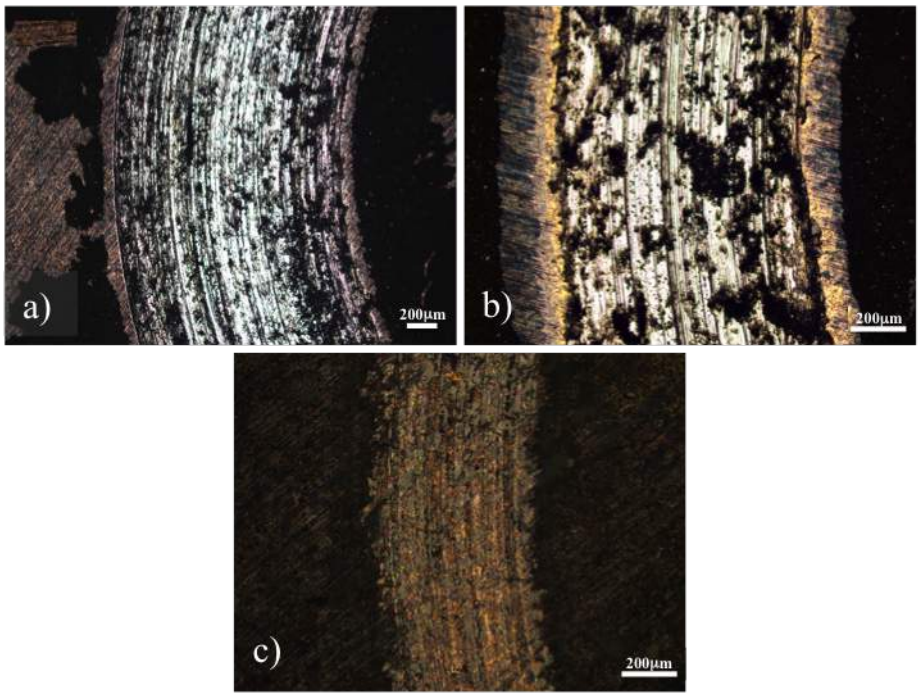


Figure 8.29: Optical microscopic images showing wear track morphology of zirconium carburised at $925^oC$ for durations of (a) 3h, (b) 20h and (c) 40h tested under load of 10N for 3600s after third hour of friction and wear testing.

Figure 8.29 shows the breakdown of ZrC layer of 3h and 20h samples, but the 40h sample managed to survive. It can be seen that for durations of 3h and 20h (8.29a and b) the film was removed completely. Both samples suffered from severe wear and high friction followed by abrasion across the wear track. The 40h sample (figure 8.29c) showed better wear resistance without ZrC layer breakdown. However, there are a lot of abrasion marks and small cracks started to form after the third hour of testing.

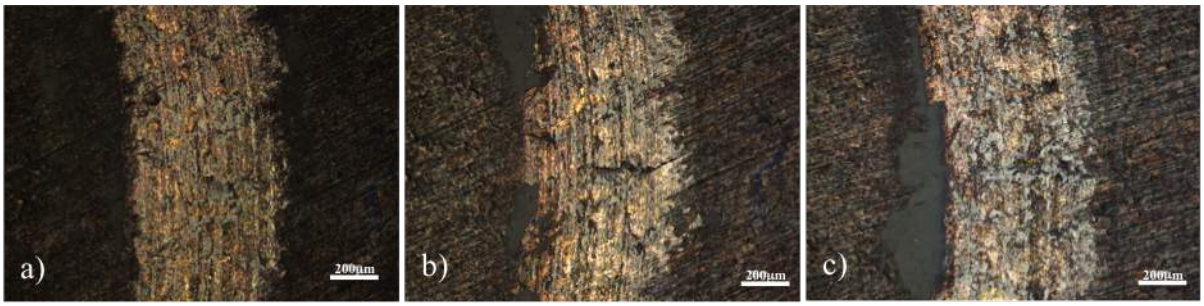


Figure 8.30: Optical microscopic images showing wear track morphology of zirconium carburised at $925^oC$ for duration of 40h tested under load of 10N for 3600s after (a) 4h, (b) 5h and (c) 6h of friction and wear testing.

The 40h sample was the only sample to survive for more than 3h of friction and wear testing. Figure 8.30 shows the wear tracks of the 40h sample after fourth, fifth and sixth hours of testing. It can be seen that after the fourth hour (8.30a), the 40h sample suffered from more material loss compared to the wear track after the third hour of friction and wear testing (8.29c). It is clearly seen that cracks started to increase in size and number and abrasion marks are spreading everywhere on wear track. After the fifth hour, it can be seen that abrasion is taking over the center of wear track. There is also more delamination around the wear track (8.30b). Finally after the six hour of friction and wear testing (8.30c), the 40h sample managed to survive. However, the sample suffered form a lot of material loss due to abrasive wear and delamination.

Overall, it is confirmed that increasing carburising time produces a thicker ZrC layer and diffusion zone. The thicker the layer, the longer the film lasts on the surface of zirconium sample during sliding wear. Figures 8.27,8.28, 8.29 and 8.30also confirms what was showed in figure 8.25, that the longer the film remains with contact zone the lower is the friction observed from the tests. It is also noticed that increasing the carburising duration will allow more carbon diffusion into the zirconium subsurface as demonstrated by GDOS (figure 8.22). Increasing carbon diffusion into zirconium surface creates a thicker layer of ZrC to form. This was confirmed by the cross-sectional images (figure 8.20). In conclusion the ZrC layer formed because of increasing the duration of carburising is responsible in observing lower friction during friction and wear testing.


Figure 8.31: Microscopic images showing the wear scar on the alumina ball after sliding with zirconium carburised for 3h at temperature of $925^oC$ under 10N load after (a) 1h, (b) 2h and (c) 3h of friction and wear testing.

Figure 8.31 shows the wear scar on the alumina ball used during friction and wear testing on the 3h sample. It can be seen that as the in the first and second hour (8.31a and b), the scar is small and the diameters are 455$\mu$m and then 617$\mu$m. But

after the third hour of wear and friction testing (8.14c), there is a lot of removed material sticking on the alumina ball and the diameters of scar has increased to 1653$\mu$m. This is due to the failure of carbide layer of the 3h sample.

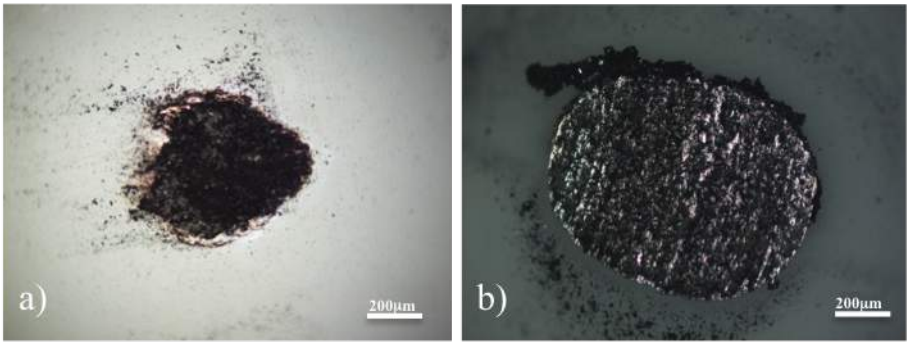


Figure 8.32: Microscopic images showing the wear scar on the alumina ball after sliding with zirconium carburised for 10h at temperature of 925$^oC$ under 10N load after (a) 1h and (b) 2h of friction and wear testing.

Figure 8.32 shows the wear scar on alumina ball used during friction and wear testing on the 10h sample. It can be seen that after the first hour (8.32a), a lot of material from the sample is sticking on the alumina ball. The diameter of the alumina ball scar after the first hour of friction and wear testing is 649$\mu$m. After the second hour of testing (8.32b) the diameter increased to 1892$\mu$m, and it can be seen that the ball suffered from massive material loss. This can be linked to figure (8.28b), which shows that the carbide layer was removed completely from the sample.


Figure 8.33: Microscopic images showing the wear scar on the alumina ball after sliding with zirconium carburised for 20h at temperature of 925$^oC$ under 10N load after (a) 1h, (b) 2h and (c) 3h of friction and wear testing.

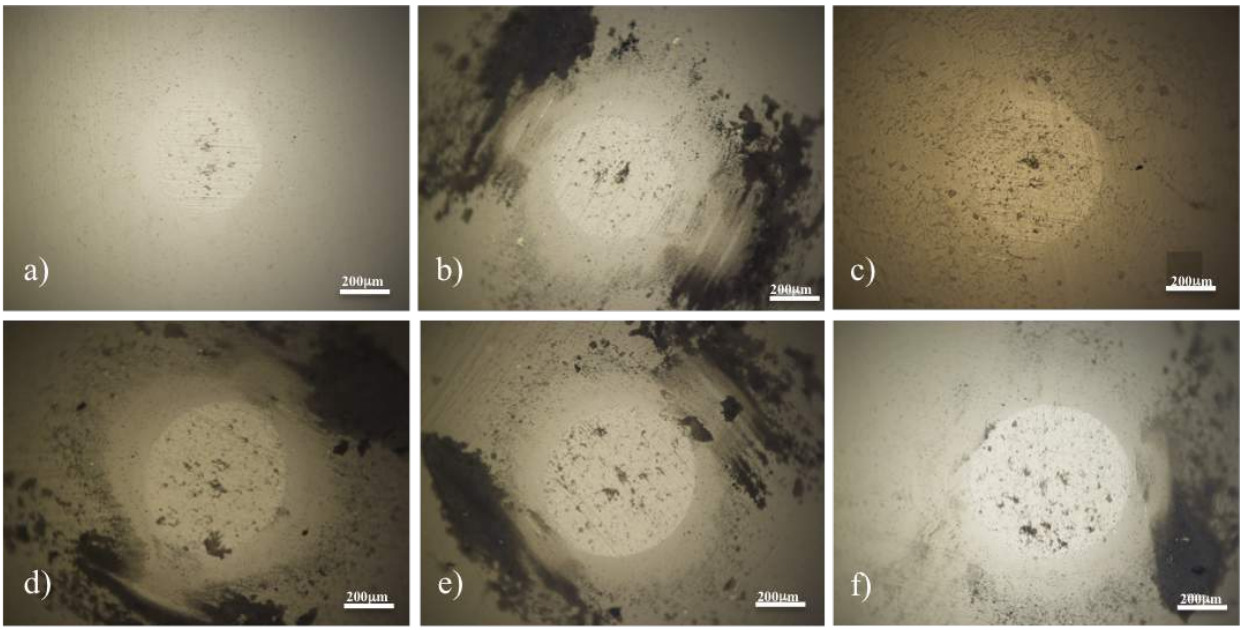


Figure 8.34: Microscopic images showing the wear scar on the alumina ball after sliding with zirconium carburised for 40h at temperature of $925^oC$ under 10N load after (a) 1h, (b) 2h, (c) 3h, (d) 4h, (e) 5h and (f) 6h of friction and wear testing.

Figure 8.33 shows the wear scar on the alumina ball used during friction and wear testing on the 20h sample. It can be seen that after the first hour (8.33a), the scar is small and there is no material sticking on the alumina ball. The diameter of the ball scar after the first hour of friction and wear testing is 470$\mu$m. After the second hour of testing (8.33b) the diameter size increased to 733$\mu$m, and the ball suffered from high material loss compared with after the first hour. However, after the third hour of testing, the wear scar has increased in size to about 1183$\mu$m (8.33c). This is because the ZrC layer broke down during the sliding process.

On the other hand, Figure 8.34 shows the wear scar on the alumina ball used during friction and wear testing on the 40h sample. It can be seen that after the first hour the scar diameter was about 498$\mu$m (8.34a), and there is no material sticking on the alumina ball. After the second hour of testing the scar increased in size and there is some material removed from the ball (8.34b). The scar diameter has increased to 508$\mu$m after the second hour of testing. But when the sample was tested for the third hour (8.34c), the scar has not changed in shape, but the diameter of the scar increased to 572$\mu$m. After the fourth and fifth hours of testing (8.14d and e), there is a lot of removed material sticking on the ball and the diameters of the scar has increased to 601$\mu$m and then 627$\mu$m. After sixth hour of testing (8.34f), the size of the scar has increased considerably compared with first hour. The scar

Table 8.6: Carbon and energiser percentage used within the pack

| Carbon (wt%) | Energiser (wt%) | Ratio (C:$BaCO_3$:$Na_2CO_3$:$CaCO_3$) |
|---|---|---|
| 80 | 20 | 24:3:2:1 |
| 70 | 30 | 14:3:2:1 |
| 50 | 50 | 6:3:2:1 |

increased to 655$\mu$m after the final hour, but the shape of the scar hasn't changed and this is because the 40h sample managed to survive friction and wear testing without ZrC layer breakdown.

## 8.4 The effect of pack composition on carburisation process

### 8.4.1 Process

The initial composition used in the pack mixture was the same composition used for typical titanium carburization [17]. The energiser was created using Barium carbonate ($BaCO_3$), sodium carbonate ($Na_2CO_3$) and calcium carbonate ($CaCO_3$) in ratio of 3:2:1 (70% carbon concentration). This pack of carbon and energiser was used at the start to determine the optimal temperature and time for Zirconium carburisation (Section 8.2 and 8.3). The mixtures used in this section have different energizer concentration (20%, 30% and 50%) as listed in table 8.6. Carburisation treatment took place at the temperature of $925^oC$ with duration of 20h and then cooled down using furnace cooling (FC). After carburisation the samples were then tested tribologically to determine the effect of pack composition and also to see the best composition to produce a very good wear resistance structure.

### 8.4.2 Layer Morphology

#### Ball Crater

The surface features have been observed to see the effect of composition on carbide layer. Figure 8.35 shows a typical ball craters made on the carburised surface. Unlike the ball crater on oxidised surface, which has a grey colour appearance, the ball crater on carburised surface shows a dark yellowish appearance. However it is very hard to distinguish the diffusion zone for carburised samples.

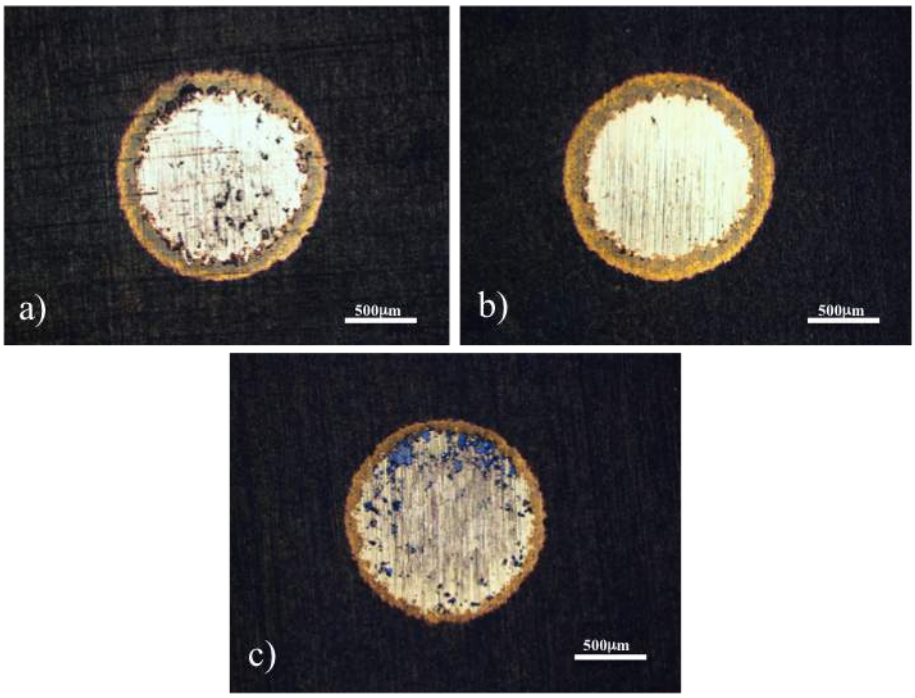


Figure 8.35: Ball crater made on the surface of carburised samples at $925^oC$ for duration of 20h using various composition: a) 20%, b) 30% and c) 50%.

The 20% (energiser) sample shows a lot of carcks and pittings, this is due to the lower content of energizer, resulting in insufficient active carbon in the container and thus less carbide formation. On the other hand the 30% (energiser) sample shows the best carbide layer appearance. Clearly, pack carburising composition has affected the formation of carbide layer. But increasing the energiser composition in the pack does not always produce a good carbide layer. As shown in figure 8.35b, the 30% sample showed better carbide layer compared with the 50% sample (8.35c). This is due to the reduction of carbon content in the 50% sample as shown in table 8.6. The carbide layer of the 50% sample is thick, but the surface is not uniformed and there are small cracks in some areas. This indicates that the carbide layer is no longer protective.

### Cross-section

Similar to what was done previously in both temperature and time effect on carburising, cross-sections were also produced as shown in figure 8.36 for 20% (a), 30% (c) and 50% (e) samples. Also SEM images of the cross-sections were also taken for 20% , 30% and 50% samples (figure 8.36b, d and f). From ball crater (Figure 8.35) and cross-sectional results (figure 8.36), it can be seen that pack composition has a

significant effect on the thickness of carbide layer and the diffusion zone.

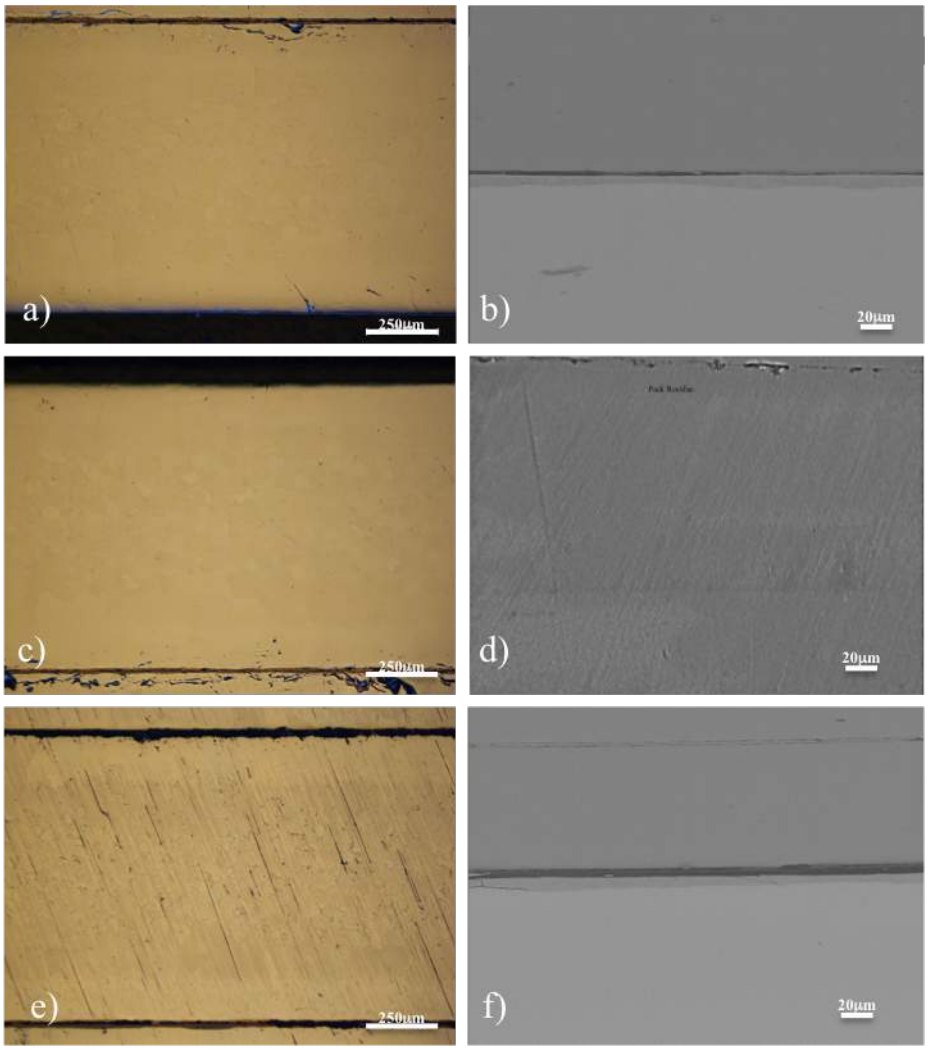


Figure 8.36: Optical and SEM micrographs showing cross-sectional morphology of pack carburised zirconium carburised at $925^oC$ for durations of 20h using composition of 20% (a and b), 30% (c and d) and 50% (e and f).

After carburising the sample using composition of 20% energiser, the carbide layer was about 5.5$\mu$m thick (Figure 8.36a), which was increased to about 7.1 and 10.1 $\mu$m after increasing the energiser composition to 30% and 50% (Figure 8.36b and c). Clearly, carburising needs a sufficient amount of energiser in the pack to produce sufficient active carbon for the formation of a thick carbide layer.

Table 8.7 lists the thicknesses of the carbide layer and the oxygen diffusion zone for all treated samples. It can be seen that as the energiser content increases both carbide layer thickness and oxygen diffusion depth are increased.

Table 8.7: Layer thickness developed after pack carburising

| Composition of carburising (%) | Carbide layer Thickness ($\mu$m) | Oxygen diffusion depth ($\mu$m) |
|---|---|---|
| 20 | 5.5 | 164 |
| 30 | 7.1 | 175 |
| 50 | 10.1 | 220 |

### 8.4.3 Micro-Hardness profile

Micro-hardness testing was conducted on cross-sections on all samples (20%, 30% and 50%) and it was compared with untreated samples as shown in figure 8.37. Carburised samples have a very harder surface compared to thermal oxidised samples, with hardness up to 1200HV which is similar to that of carburised titanium [17].

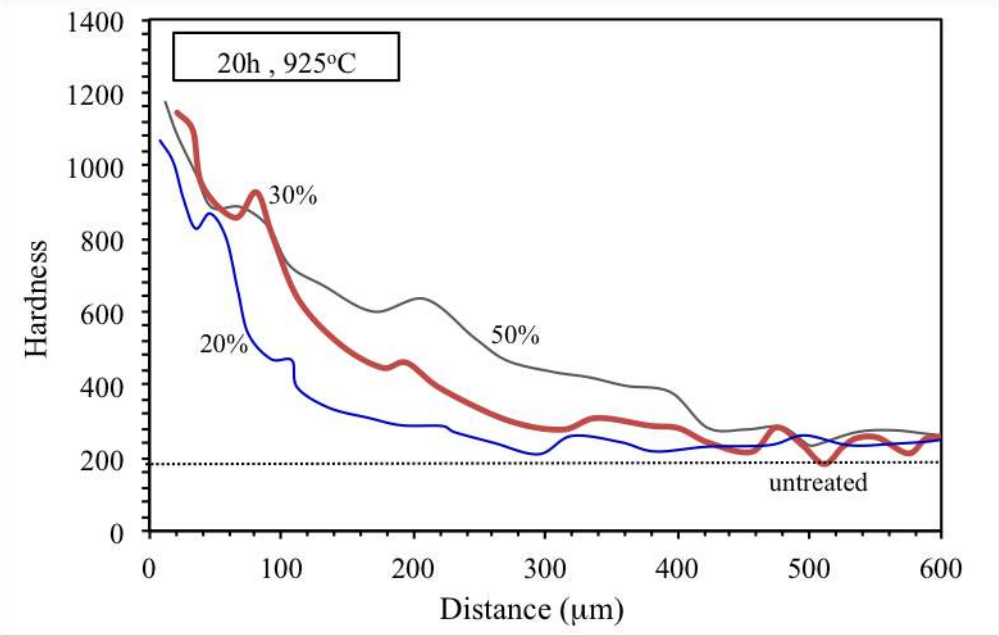


Figure 8.37: Cross-sectional hardness curves for the carburised samples treated at $925^oC$ for 20h using composition of 20%, 30% and 50%.

As shown in figure 8.37, surface hardness depends on the thickness of the carburised layer built on the surface. It can be seen clearly that there is definite correlation between the pack composition of the carburisation and layer thickness. This means when the energiser composition percentage is high, the hardness will be higher too until it reaches a certain depth (500-600$\mu$m). When hardness is measured between 400 and 600$\mu$m which is the centre of the cross-section of all samples, this will be the meeting point of the substrate and it is similar to the hardness of the

untreated sample. The 20% sample is the only sample that went out of the 400-600$\mu$m ranges. This can be explained by the low content of energiser in the mixture which leads to building a thin carbide layer on the surface of zirconium.

From figure 8.37 it can be seen that the hardness remains high until it reaches a depth of about 30-40$\mu$m. There is a sharp reduction in hardness from 1180Hv to 850HV across the carbide layer; this can be explained by the reduced amount of ZrC phase with depth. The sharp reduction is followed by gradual decline in hardness across the oxygen diffusion zone (ODZ) from 850HV to that of untreated zirconium 200HV.

Increasing the energiser content in the mixture of carburisation helped the oxygen to diffuse deeper into the zirconium substrate creating larger ODZ. However, it can be seen that the 30% sample is actually harder in the first 100$\mu$m distance compared with other samples (figure 8.37). After the depth of 100$\mu$m, the 50% sample show higher hardness all the way to substrate (200HV).

### 8.4.4 X-Ray Diffraction XRD

X-ray diffraction (XRD) was undertaken using Cu-K radiation. This helps in finding the excising phases that are present in the carburised sample. Figure 8.38 shows the X-ray diffraction results for untreated sample as well as the samples carburised using different pack compositions (20%, 30% and 50%). The diffraction pattern shows the existence of zirconium carbide (ZrC) and monoclinic ($ZrO_2$). The XRD graphs show clearly that with increasing the energiser content in the carburising pack, the thickness of the carbide layer increases, because the X-ray radiation could not penetrate the sample to an appropriate depth to detect the ODZ. This could also explain why the $\alpha$-Zr peaks are reduced as the concentration of energiser is increased.

Table 8.8: My caption

| Composition (%) | Phase composition |
|---|---|
| Untreated | $\alpha$-Zr |
| 20 | ZrC (weak),$C-ZrO_2$(weak),m-$ZrO_2$ (mediate), $\alpha$-Zr (mediate) |
| 30 | ZrC (strong), $C-ZrO_2$(weak),m-$ZrO_2$,(mediate), $\alpha$-Zr (weak) |
| 50 | ZrC (strong), $C-ZrO_2$(mediate),m-$ZrO_2$ (strong), $\alpha$-Zr (weak) |

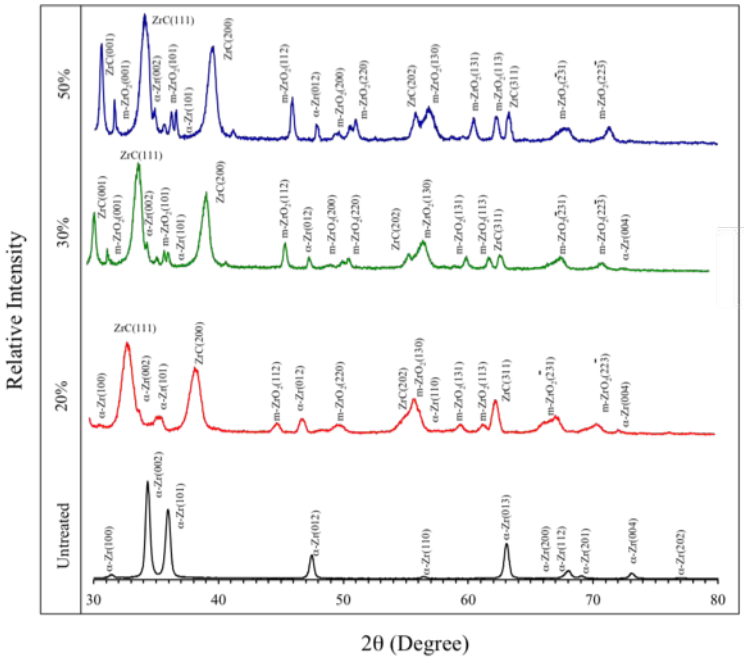


Figure 8.38: X-Ray diffraction patterns generated from samples carburised at temperature $925^oC$ for duration of 20h using composition of 20%, 30% and 50% against untreated sample

Table 8.8 shows the phase composition for each treated and untreated samples. It can be seen that using more energizer concentration (30% and 50%) ZrC phase is very strong. However, when the energizer concentration is lower than 50% $\alpha$-Zr and m-$ZrO_2$ are more dominant.

From table 8.8 it can be seen that the $\alpha$-Zr and m-$ZrO_2$ phases are strong in the 20% sample. This indicates that carburizing using less energizer concentration would only form a thin carbide layer on surface of the sample. It can be stated that the strong m-$ZrO_2$ phase exist because oxidation initiated before carburizing. For carbide layer to be formed perfectly, the concentration of energiser should be increased. When the concentration is increased to 30%, the only difference is that the m-$ZrO_2$ phase is weaker due to the fact that there are less chances for the formation

of oxide layer compared with 20% sample. However, by using more concentration of energizer(30% and 50%), ZrC phase is stronger, which states that choosing the mixture of charcoal and energizer is an important factor for the formation of carbide layer.

### 8.4.5 Tribological response

The samples were tested tribologically under dry conditions against an alumina ball ($Al_2O_3$). The 20% sample lasted at least for six hours under load of 10N, but both 30% and 50% samples were able to last up to three hour as shown in figure 8.39.

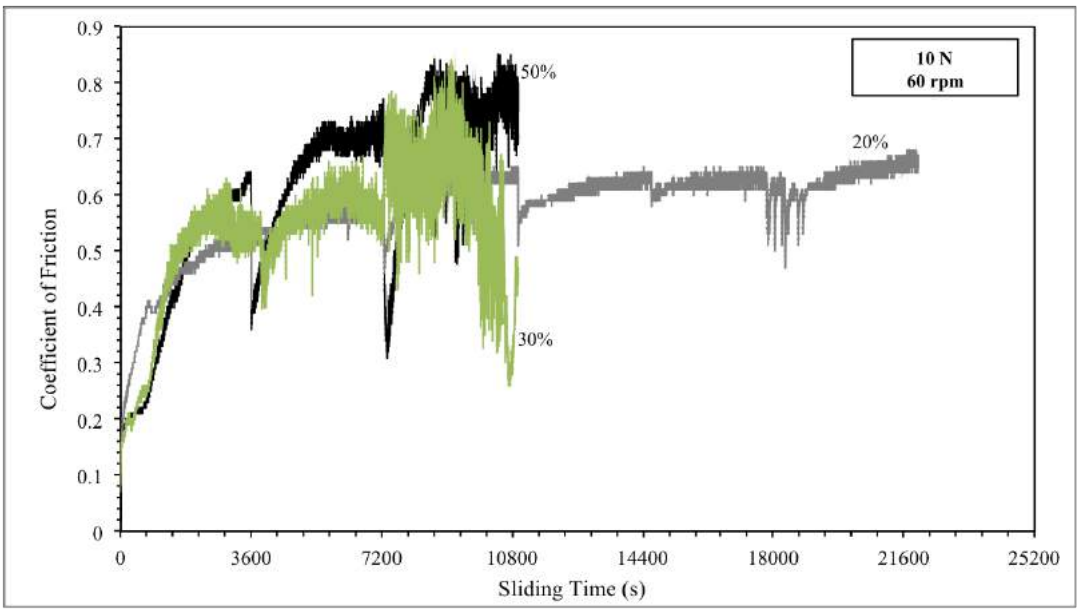


Figure 8.39: Coefficient of friction (COF) curves recorded for samples pack carburised at $925^oC$ for duration of 20h using composition of 20%, 30% and 50% under load of 10N

Figure 8.39 shows the coefficient of friction (COF) curves recorded under load of 10N. The results show that energiser composition of carburisation has a noticeable effect on the initial frictional response of all treated samples. The samples show lower COF, this can be linked to the thick ZrC layer that helped in friction reduction.

It can be seen that the 20% sample survived for 21600s with COF of about 0.6. However when the energiser composition was increased to 30% the COF settled on 0.55. But the ZrC layer couldn't last more than 10800s, and COF increased to 0.65 after the carbide layer was removed. When the energiser composition was increased to 50%, the COF increased to about 0.7. Similar to the 30% sample, the 50%sample

couldn't last more than 10800s. However at the end of friction and wear testing, the carbide layer was removed and the COF increased to about 0.8.

Clearly, there is a strong correlation between the thickness of or ZrC layer and the low friction results gained from friction and wear testing. This can state that the composition of both energizer and carbon have a significant effect as shown from (8.39).

### 8.4.6 Wear rates

Wear rate was compared between all treated samples every hour till failure as shown in figure 8.40. It can be seen that when the test is initiated for the first hour, the wear rate is always low. The 20% sample was carburised with very high carbon concentration and it shows a very low wear rate ($0.000044 mm^3/m$) in the first hour. The 30% sample suffered from slightly higher wear compared with the 20% sample ($0.000148 mm^3/m$) in the first hour. It can be seen that the 50% sample showed similar wear rate to the 30% sample after the first hour of testing ($0.000117 mm^3/m$).

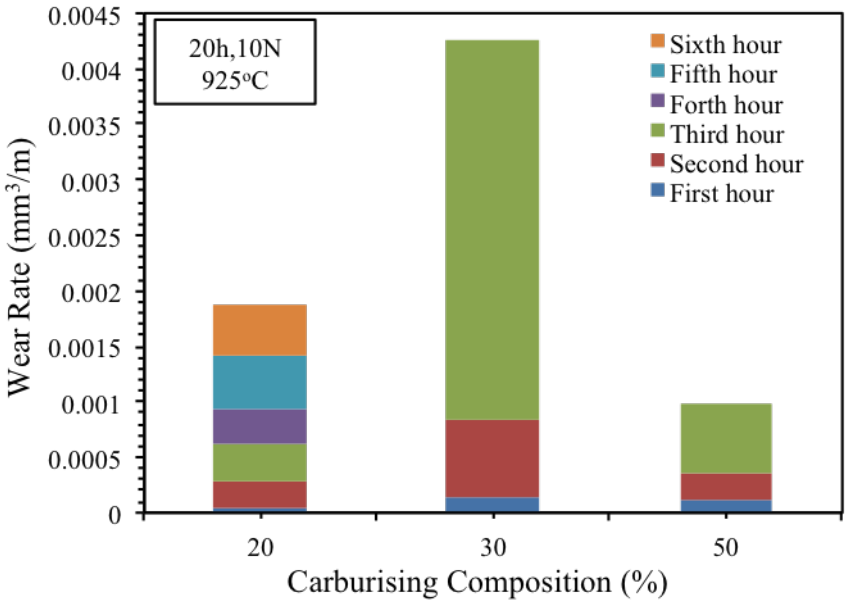


Figure 8.40: Wear rate comparison for carburised samples produced at $925^oC$ for durations of 20h using compositions of 20%, 30% and 50% under load of 10N in stages of 1h till failure

During the second hour of testing, again the 20% sample showed the lowest wear rate ($0.000241 mm^3/m$). The 30% sample suffered from high wear during the second hour of friction and wear testing and wear rate increased to ($0.000697\ mm^3/m$).

The 50% sample showed lower wear rate (0.000246 $mm^3/m$) during the second hour compared with 30% sample.

In the third hour, the 20% sample shows the lowest wear rate (0.000325 $mm^3/m$) compared to the 30% and 50% sample (0.003404 and 0.000615$mm^3/m$). It can be seen that the 30% sample suffered from high severe wear during the third hour. Wear track morphology will be investigated to confirm the removal of the carbide layer. The 50% sample showed the second lowest wear rate (0.000615$mm^3/m$) during the third hour and then film broke through.

It was noticed that the 20% sample was the only sample to last 6h before failure in friction and wear testing. In the fourth and fifth hours, the 20% sample managed to survive with low wear rate (0.000325 and 0.000471 $mm^3/m$). In the sixth hour the 20% sample managed to survive, this can be linked to the rich carbon concentration in the mixture.

### 8.4.7 wear track morphology

Wear track morphology was investigated every hour till failure as shown in figures 8.41, 8.42, 8.43 and 8.44. Figure 8.41 shows the wear tracks after the first hour of wear and friction testing . It can be seen that the wear tracks demonstrate the effect of carburising composition on wear.

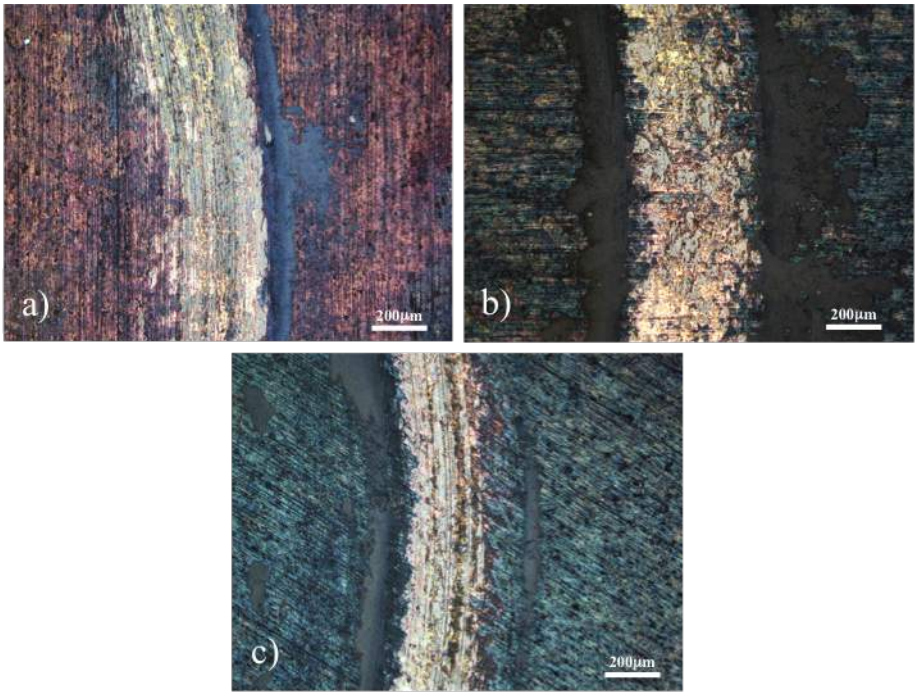


Figure 8.41: Optical microscopic images showing wear track morphology of zirconium carburised at $925^oC$ for durations of 20h tested under load of 10N for 3600s after first hour of friction and wear testing using composition of (a) 20%, (b) 30% and (c) 50%.

After the first hour of friction and wear testing (Figure 8.41), all samples managed to survive without film failure. The 20% and 30% samples show heavier wear compared with the 50% sample with dominating mechanism due to the fine polishing abrasion. But it is also clearly seen that the 30% sample suffered from higher wear compared with other samples although the carbide layer has not been removed.

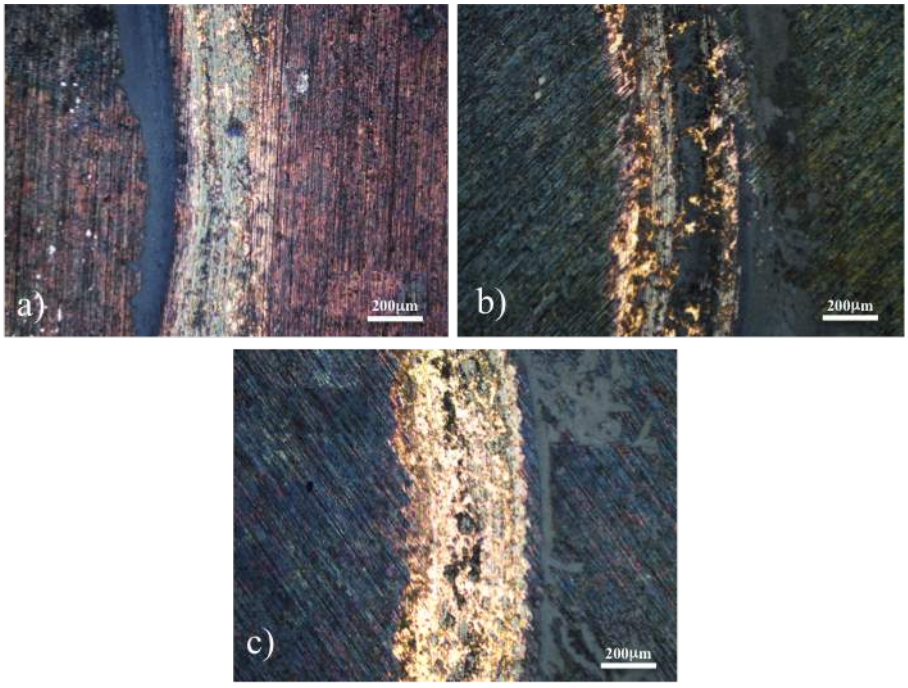


Figure 8.42: Optical microscopic images showing wear track morphology of zirconium carburised at $925^oC$ for durations of 20h tested under load of 10N for 3600s after second hour of friction and wear testing using composition of (a) 20%, (b) 30% and (c) 50%.

After the second hour of friction and wear testing, all samples managed to survive without film failure (figure 8.42). Its clearly seen that the 20% sample show good wear resistance after the second hour of testing compared with both 30% and 50% samples (figure 8.42b and c). However, the 20% sample (figure 8.42a) suffered from slightly more material removal compared to wear track after the first hour (figure 8.41a). Figure 8.42b shows that the 30% sample is about to fail to resist friction and wear testing after the second hour. The carbide film is nearly removed from the center and outer side of wear track. There are a lot of small cracks and abrasion marks on the outer side of wear track; this indicates that the sample is suffering from severe wear.

The 50% sample suffered from more material removal especially in the center of wear track. After the second hour, the 50% sample started to have abrasion marks on the center of wear track without carbide layer breakdown.

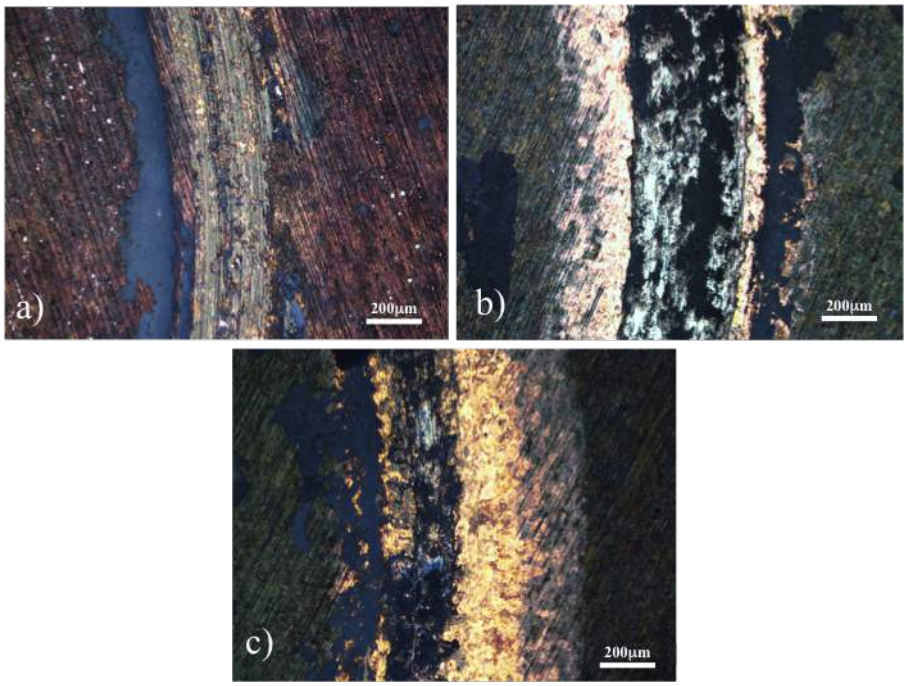


Figure 8.43: Optical microscopic images showing wear track morphology of zirconium carburised at $925^oC$ for durations of 20h tested under load of 10N for 3600s after third hour of friction and wear testing using composition of (a) 20%, (b) 30% and (c) 50%.

Figure 8.43 shows the breakdown of ZrC layer of 30% and 50% samples, but the 20% sample managed to survive. Although the 20% sample survived, there is more material removal followed by minor delamination after the third hour of testing. There are also abrasion marks in the center of wear track (8.43a).

It can be seen that for energiser composition of 30% (8.43b) the carbide layer was removed. Some parts managed to survive, but the carbide layer is no longer protecting the surface of zirconium after the third hour. Similar to the 30%, the 50% sample failed to resist friction and wear testing after the third hour.

The 30% and 50% samples suffered from severe wear and high friction followed by abrasion across the wear track. Although the 50% sample failed to survive (figure 8.43c) and the film was removed, but still some parts of the film survived. The breakdown of the ZrC structure within the wear track allows the exposure of the oxygen diffusion zone (ODZ) to become the dominating factor in defining both coefficient of friction and wear rate. Delamination exists after removing the ZrC layer as well as abrasive wear on the exposed oxygen diffusion zone (ODZ).


Figure 8.44: Optical microscopic images showing wear track morphology of zirconium carburised at $925^oC$ for 20h using composition of 20% tested under load of 10N for 3600s after (a) 4h, (b) 5h and (c) 6h of friction and wear testing.

The 20% sample was the only sample to survive for more than 3h of friction and wear testing. Figure 8.44 shows the wear tracks of the 20% sample after fourth, fifth and sixth hours of testing. It can be seen that after 4 to 6 hours (8.44), the 20% sample suffered from more material loss compared to the wears track after the first three hours of friction and wear testing (8.41c, 8.42c and 8.43c). It is clearly seen that cracks started to get larger and abrasion marks are spreading everywhere on wear track.

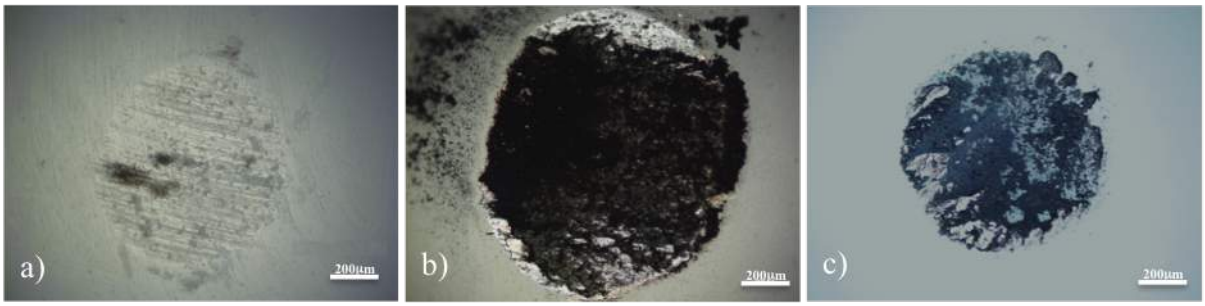


Figure 8.45: Microscopic images showing the wear scar on the alumina ball after sliding with zirconium carburised for 20h at temperature of $925^oC$ under 10N load using composition of (a) 20%, (b) 30% and (c) 50%.

Figure 8.45 shows the wear scars on alumina ball used during friction and wear testing on the carburised samples with different energiser compositions (20%, 30% and 50%). It can be seen that for the 20% sample (8.45a), the scar is very rounded and smooth with diameter of 869$\mu$m. This can be explained by the low wear rate of the 20% sample as shown in figure 8.40. After increasing the energiser composition to 30% (8.45b), the wear scar on the ball is larger and the diameters of the scar is 1183$\mu$m. This is due to the break through of the carbide layer of the 30% sample, which leads the removed material to stick on the ball. For the 50% sample (8.45c),

it can be seen that the scar is smaller compared with 30% sample (8.45b). The scar on the ball sliding against 50% sample has a diameter of 857$\mu$m, and the scar is covered with material removed from the sample.

## 8.5 Conclusion

Due to time constraints, the pack carburisation work reported in this chapter is rather preliminary, focusing on three processing parameters, i.e. temperature, time and pack composition. The conclusions that can be drawn are as follows:

- Pack carburising is only effective at sufficient high temperatures above $900^oC$, for sufficiently long treatment duration more than 10 h and in carburising packs with sufficient energiser concentration.
- Successfully carburised CP-Zr comprises a thin ZrC carbide layer of a few microns thick at the surface and an oxygen and carbon diffusion zone up to 400 microns thick in the subsurface. The residual oxygen in the sealed container facilitates oxygen diffusion to the substrate during high temperature cauburising.
- The combination of the carbide layer and the diffusion zone offers improved frictional characteristics and wear resistance to CP-Zr under dry sliding conditions.
- The optimum carburising conditions to achieve the best tribological properties are as follows: $925^oC$, 20 h, 50% energiser in the carburising pack.
- At temperatures below $900^oC$ and treatment duration shorter than 20 h, oxidation becomes more dominant. At the surface an oxide layer is formed with traces of carbides inside. Such a mixed surface layer is found to possess better friction and wear resistant characteristics than the carburised layers produced at high temperatures and for long duration.
- Further optimisation of the pack carburising process should involve fine-tune the process parameters and pack compositions to achieve a relatively thick surface layer comprising a good mixture of carbides and oxides.

# Chapter 9

# Conclusions and Future Work

## 9.1 Conclusion

This work focuses on two surface engineering techniques for CP-Zr, i.e. thermal oxidation and pack carburising. The conclusions that can be drawn from this work are summaried in each chapter from chapter 4 to chapter 8. For clarity purpose, these conclusions are list below.

### 9.1.1 Effect of TO temperature and initial surface finish

- Thermal oxidation at temperatures between $550^oC$ and $700^oC$ results in the formation of a monoclinic $ZrO_2$ layer 2-9 $\mu$m thick and an oxygen diffusion zone of 1-7 $\mu$m thick on CP-Zr. The oxide layers are adherent and possess a hardness up to 1300 $HV_{0.025}$.

- TO was effective in reducing friction and wear rate of CP-Zr and once the $ZrO_2$ layer maintains its integrity with the substrate, TO temperature had no significant effects on friction and wear.

- Under high contact loads, the $ZrO_2$ layer tends to suffer from cracking in the wear track. The thinner layers suffer from cracking at small loads. Although increasing $ZrO_2$ layer thickness helps to increase load bearing capacity, cracking is unavoidable at high contact loads.

- Roughening the surface before oxidation helps to reduce the tendency of the oxide layer towards cracking during sliding and to reduce wear rate.

### 9.1.2 Effect of TO time

- Thermal oxidation at $650^oC$ for duration less than 12 h produces a relatively thick, dense, pore free and adherent oxide layer at the surface and a thin oxygen diffusion zone at the subsurface.
- Such a combination of the oxide layer and the oxygen diffusion zone possesses the lowest friction, best wear resistance and highest load bearing capacity.
- Although prolonged oxidation can increase the thicknesses of the oxide layer and the oxygen diffusion zone, it leads to the gradual development of pores in the inner part of the oxide layer and finally the breakaway of oxidation characterized by accelerated oxide growth and crack formation in the oxide layer.
- The formation of pores in the oxide layer has detrimental effects on friction reduction, wear resistance and load bearing capacity.
- The oxide layer surface tends to suffer from cracking under the present dry sliding process, and the oxide layer suffers from sudden breakdown after a certain period of sliding contact motion. This can be associated with the propagation of the surface cracks through the oxide layer and then the oxygen diffusion zone to reach the oxygen diffusion zone substrate interface.

### 9.1.3 Effect of surface finish

- Smoothening the oxidized surface by polishing is beneficial in reducing friction and wear volume of the TO sample if the contact load is relatively small (10 N).
- Under high contact loads (20 N), smoothening the oxidized surface deteriorates the wear resistance of the TO sample and accelerates the breakdown of the oxide layer.
- Smoothening the oxidized surface by polishing favours the formation of large semi-circular cracks in the wear tracks during dry sliding under both contact loads.
- The semi-circular cracks developed at the TO-polished surface propagate through the surface layers to reach the substrate. This leads to the local breakdown

of the oxide layer after sliding for a certain period of time under sufficiently large contact loads (e.g. 20 N).

- A slightly rough TO surface (unpolished) is beneficial in reducing the tendency of the oxide layer towards cracking during dry sliding, owing to the dominance of asperity contacts which lead to micro crack formation at the real contact areas and fracture of the contacting asperities.

### 9.1.4 Comparison between TO Zr and TO Ti

- Under the present thermal oxidation condition, 4 times more oxygen is introduced into CP-Zr than into CP-Ti. As a result, the oxide layer produced on CP-Zr is nearly 6 times thicker than that on CP-Ti.

- The TO-Zr possesses higher hardness, a deeper hardening depth and a greater load bearing capacity than the TO-Ti.

- The TO-Zr exhibits better scratch resistance than the TO-Ti. During the scratch test, the oxide layer on TO-Ti suffers from edge spallation at a load as small as 7 N, while the oxide layer on TO-Zr can resist a scratch load up to 15 N without adhesive failure. The oxide layer on TO-Zr can accommodate severe plastic deformation and maintains good integrity with the substrate at high scratch loads.

- Under the present dry sliding conditions, as long as the oxide layer maintains integrity with the substrate, such as at small contact loads, both TO-Ti and TO-Zr specimens show similar wear resistance. However, at high contact loads, the oxide layer on TO-Ti is removed easily, leading to accelerated wear of the TO specimen. On the other hand, the oxide layer on TO-Zr can resist much.

- Under tribocorrosion conditions in Ringer's solution, the oxide layer on TO-Ti is removed from the corrosion-wear track at contact load as small as 2 N and thus loses its barrier nature in the corrosive environment. On the other hand, the oxide layer on TO-Zr maintains its integrity and barrier nature up to a contact load of 10 N without crack formation and layer breakdown. Although at higher contact loads of 15 N and above, the oxide layer on TO-Zr still maintains its integrity with the substrate during tribocorrosion, cracks form in the oxide layer and penetrate through the oxide layer to reach the substrate, thus losing the barrier nature of the oxide layer against corrosion.

### 9.1.5 Pack carburising of CP-Zr

- Pack carburising is only effective at sufficient high temperatures above $900^oC$, for sufficiently long treatment duration more than 10 h and in carburising packs with sufficient energiser concentration.
- Successfully carburised CP-Zr comprises a thin ZrC carbide layer of a few microns thick at the surface and an oxygen and carbon diffusion zone up to 400 microns thick in the subsurface. The residual oxygen in the sealed container facilitates oxygen diffusion to the substrate during high temperature cauburising.
- The combination of the carbide layer and the diffusion zone offers improved frictional characteristics and wear resistance to CP-Zr under dry sliding conditions.
- The optimum carburising conditions to achieve the best tribological properties are as follows: $925^oC$, 20 h, 50% energiser in the carburising pack.
- At temperatures below $900^oC$ and treatment duration shorter than 20 h, oxidation becomes more dominant. At the surface an oxide layer is formed with traces of carbides inside. Such a mixed surface layer is found to possess better friction and wear resistant characteristics than the carburised layers produced at high temperatures and for long duration.
- Further optimisation of the pack carburising process should involve fine-tune the process parameters and pack compositions to achieve a relatively thick surface layer comprising a good mixture of carbides and oxides.

## 9.2 Future Work

- Characterisation of oxide layer can be deeply investigated using photoelectron spectroscopy (XPS), surface ion mass spectroscopy (SIMS) and atomic force microscope (AFM). This will help to focus more on the response of thermally oxidised zirconium.
- Modelling of the growing thermal oxide layer on Zirconium needs to be investigated. This will help to identify the related mechanical parameters; which leads in gaining accurate mechanical characteristics parameters. A method

using CFD (computational fluid dynamics) software Flow-3D, Oxide Film Entrainment Model (OFEM), needs to be investigated to allow the assessment of entraining events and the marking and tracking of entrained oxidised films.

- In the current research, thermal oxidation method was applied to improve the tribological properties of CP-Zr. It was noticed that the cooling of oxidised samples is not controlled. Future work should focus investigating the effect of cooling down after oxidation. This can help to improve the formation of thicker zirconium oxide ($ZrO_2$) layers with increased adhesion. Slow cooling would help to reduce the thermal contractions between the oxide layer and substrate.

- Future work should focus on investigating the tribocorrosive response of both oxidised ($ZrO_2$) and carburised zirconium (ZrC) when charged cathodically. This will help to detect zirconium hydride formation. The results can be achieved using photoelectron spectroscopy (XPS), surface ion mass spectroscopy (SIMS).

- For practical and industrial applications it would be benifecial to investigate the fatigue properties of PC-Zr. Therefore, fatigue testing should be done on carburised zirconium with oxygen diffusion.

- In this research only one carburising method was used (pack carburising), this is because this was the available method during research period. Further investigation should be done to develop more carburising techniques such as gas carburising, plasma carburising and vacuum furnace carburising. This will help to control the stages of carburising treatment. The outcome of this study can help to create a strong film containing a mixture of both $ZrO_2$ and $ZrC$.

- Characterisation using transmission electron microscope (TEM) would be very helpful to identify the ZrC networks crystal structure of the film.

- It is very important to investigate the relationship between oxygen and carbon in depth. This can help to understand the process of carburising treatment. This can also help in controlling the content of carbon and oxygen in the film rather than predicting it.

- In this research CP-Zr and CP-Ti were compared, but it would be interesting to create a Zr film on the surface of titanium followed by thermal oxidation.

The outcome of this method can help the samples to gain good tribological and tribo-corrosion properties. It can also proved better characterisation in terms of hardness and oxide layer thicknesses.

# References


[1] B Cox, VG Kritsky, C Lemaignan, V Polley, IG Ritchie, H Ruhmann, VN Shishov, Yu K Bibilashvili, and AV Nikulina. Waterside corrosion of zirconium alloys in nuclear power plants. *IAEA TECDOC*, 996:124, 1998.

[2] R Webster. Zirconium for chemical processing applications. *Met. Prog.;(United States)*, 113(2), 1978.

[3] J Chevalier. What future for zirconia as a biomaterial? *Biomaterials*, 27(4):535–543, 2006.

[4] J Haygarth and L Fenwick. Improved wear resistance of zirconium by enhanced oxide films. *Thin Solid Films*, 118(3):351–362, 1984.

[5] T Jun, D Armstrong, and T Britton. A nanoindentation investigation of local strain rate sensitivity in dual-phase ti alloys. *Journal of Alloys and Compounds*, 672:282–291, 2016.

[6] H El Kadiri, Z Utegulov, M Khafizov, M Zaeem, M Mamivand, A Oppedal, K Enakoutsa, M Cherkaoui, R Graham, and A Arockiasamy. Transformations and cracks in zirconia films leading to breakaway oxidation of zircaloy. *Acta Materialia*, 61(11):3923–3935, 2013.

[7] C Aparecido, D Lago, and F Maria da Consola. *Maintenance of Reducers with an Unbalanced Load Through Vibration and Oil Analysis Predictive Techniques*. INTECH Open Access Publisher, 2011.

[8] I Hutchings. *Tribology: friction and wear of engineering materials*. Butterworth-Heinemann Ltd, 1992.

[9] G Mathers. Hardness testing part 1, technical knowledge, job knowledge. *The Welding Institute global*, 2008.

[10] T Yanagitani, N Mishima, M Matsukawa, and Y Watanabe. Electromechanical coupling coefficient k15 of polycrystalline zno films with the c-axes lie in the substrate plane. *IEEE transactions on ultrasonics, ferroelectrics, and frequency control*, 54(4):701–704, 2007.

[11] A Motta, A Yilmazbayhan, M Da Silva, R Comstock, G Was, J Busby, E Gartner, Q Peng, Y Jeong, and J Park. Zirconium alloys for supercritical water reactor applications: Challenges and possibilities. *Journal of Nuclear Materials*, 371(1):61–75, 2007.

[12] T Maeder, P Muralt, L Sagalowicz, I Reaney, M Kohli, A Kholkin, and N Setter. Pb (zr, ti) o3 thin films on zirconium membranes for micromechanical applications. *Applied physics letters*, 68(6):776–778, 1996.

[13] S Tkachenko, O Datskevich, L Kulak, S Jacobson, H Engqvist, and C Persson. Wear and friction properties of experimental ti–si–zr alloys for biomedical applications. *Journal of the mechanical behavior of biomedical materials*, 39:61–72, 2014.

[14] V Pawar, C Weaver, and S Jani. Physical characterization of a new composition of oxidized zirconium–2.5 wt% niobium produced using a two step process for biomedical applications. *Applied Surface Science*, 257(14):6118–6124, 2011.

[15] R Bailey and Y Sun. Unlubricated sliding friction and wear characteristics of thermally oxidized commercially pure titanium. *Wear*, 308(1):61–70, 2013.

[16] M Ries. Oxidized zirconium in total joint arthroplasty. In *Seminars in Arthroplasty*, volume 17, pages 161–164. Elsevier, 2006.

[17] R Bailey. *Surface Engineering Titanium for Improved Tribological, Electrochemical and Tribo-electrochemical Performance.* PhD thesis, De Montfort University, 2015.

[18] R Ji, XY Li, and H Dong. Ceramic conversion treatment of zirconium alloys to combat corrosion wear. *Surface Engineering*, 26(1-2):30–36, 2010.

[19] G Hunter, CM Asgian, and GI Hines. Methods of surface hardening zirconium alloys and resulting products. 2002.

[20] J Wu, L Chen, Y Qu, L Dong, J Guo, D Li, and W Xue. In-situ high temperature electrochemical investigation of zro2/crn ceramic composite film on zirconium alloy. *Surface and Coatings Technology*, 359:366–373, 2019.

[21] M Sandhyarani, M Ashfaq, T Arunnellaiappan, M Selvan, S Subramanian, and N Rameshbabu. Effect of electrical parameters on morphology and in-vitro corrosion resistance of plasma electrolytic oxidized films formed on zirconium. *Surface and Coatings Technology*, 269:286–294, 2015.

[22] L Wang, X Hu, and X Nie. Deposition and properties of zirconia coatings on a zirconium alloy produced by pulsed dc plasma electrolytic oxidation. *Surface and Coatings Technology*, 221:150–157, 2013.

[23] E Matykina, R Arrabal, P Skeldon, GE Thompson, P Wang, and P Wood. Plasma electrolytic oxidation of a zirconium alloy under ac conditions. *Surface and Coatings Technology*, 204(14):2142–2151, 2010.

[24] H Dong and T Bell. Enhanced wear resistance of titanium surfaces by a new thermal oxidation treatment. *Wear*, 238(2):131–137, 2000.

[25] G Wallwork, C Rosa, and W Smeltzer. Breakaway phenomena in the oxidation of zirconium at 850 and 950c. *Corrosion Science*, 5(2):113–120, 1965.

[26] R Ploc. An electron microscope study of breakaway oxidation of zirconium at 623 k. *Journal of Nuclear Materials*, 91(2-3):322–328, 1980.

[27] B Cox and Y-M Wong. Simulating porous oxide films on zirconium alloys. *Journal of nuclear materials*, 218(3):324–334, 1995.

[28] B Cox. Oxidation of zirconium and its alloys. In *Advances in corrosion science and technology*, pages 173–391. Springer, 1976.

[29] R Ploc. Breakaway oxidation of zirconium at 573 k. *Journal of Nuclear Materials*, 82(2):411–418, 1979.

[30] DL Douglass. Oxide plasticity in the oxidation mechanism of zirconium and its alloys. *Corrosion Science*, 5(4):255–268, 1965.

[31] A Patel and M Spector. Tribological evaluation of oxidized zirconium using an articular cartilage counterface: a novel material for potential use in hemiarthroplasty. *Biomaterials*, 18(5):441–447, 1997.

[32] V Good, K Widding, G Hunter, and D Heuer. Oxidized zirconium: a potentially longer lasting hip implant. *Materials & design*, 26(7):618–622, 2005.

[33] M Galetz, E Fleischmann, C Konrad, A Schuetz, and U Glatzel. Abrasion resistance of oxidized zirconium in comparison with cocrmo and titanium nitride coatings for artificial knee joints. *Journal of Biomedical Materials Research Part B: Applied Biomaterials: An Official Journal of The Society for Biomaterials, The Japanese Society for Biomaterials, and The Australian Society for Biomaterials and the Korean Society for Biomaterials*, 93(1):244–251, 2010.

[34] R Laskin. An oxidized zr ceramic surfaced femoral component for total knee arthroplasty. *Clinical orthopaedics and related research*, 416:191–196, 2003.

[35] J DesJardins, B Burnikel, and M LaBerge. Uhmwpe wear against roughened oxidized zirconium and cocr femoral knee components during force-controlled simulation. *Wear*, 264(3-4):245–256, 2008.

[36] K Ezzet, J Hermida, N Steklov, D Darryl, et al. Wear of polyethylene against oxidized zirconium femoral components: effect of aggressive kinematic conditions and malalignment in total knee arthroplasty. *The Journal of arthroplasty*, 27(1):116–121, 2012.

[37] M Innocenti, F Matassi, C Carulli, L Nistri, and R Civinini. Oxidized zirconium femoral component for tka: a follow-up note of a previous report at a minimum of 10 years. *The Knee*, 21(4):858–861, 2014.

[38] J Hofer and K Ezzet. A minimum 5-year follow-up of an oxidized zirconium femoral prosthesis used for total knee arthroplasty. *The Knee*, 21(1):168–171, 2014.

[39] R Bailey and Y Sun. Pack carburisation of commercially pure titanium with limited oxygen diffusion for improved tribological properties. *Surface and Coatings Technology*, 261:28–34, 2015.

[40] R Bailey and Y Sun. Corrosion and tribocorrosion performance of thermally oxidized commercially pure titanium in a 0.9% nacl solution. *Journal of Materials Engineering and Performance*, 24(4):1669–1678, 2015.

[41] T Rose, C Chalk, and J Nicholls. Microscopy of damage mechanisms in diesel engine pre-combustion chambers in a cyclic oxidising–carburising environment. *Materials at High Temperatures*, 26(3):223–232, 2009.

[42] J Fernandes, P Amaral, L Rosa, D Martinez, J Rodriguez, and N Shohoji. X-ray diffraction characterisation of carbide and carbonitride of ti and zr prepared through reaction between metal powders and carbon powders (graphitic or amorphous) in a solar furnace. *International Journal of Refractory Metals and Hard Materials*, 17(6):437–443, 1999.

[43] G Tkecza, R Zapala, and M Kawalec. The role of ti, zr and ce in shaping of the cr-ni-nb cast steel resistance to carburising. *Archives of Foundry Engineering*, 8(3s):144–148, 2008.

[44] D Lide. Crc handbook of chemistry and physics, (crc handbook of chemistry and physics). *CRC, June*, 2007.

[45] R Krebs. *The history and use of our earth's chemical elements: a reference guide*. Greenwood Publishing Group, 2006.

[46] M Klaproth. the chemical investigation of uranite, a newly discovered metallic substance, chem. *Ann*, pages 387–403, 1789.

[47] R Clark, D Bradley, and P Thornton. *The Chemistry of Titanium, Zirconium and Hafnium: Pergamon Texts in Inorganic Chemistry*, volume 19. Elsevier, 2018.

[48] W Pauli and N Bohr. the development of physics. *London, 1955PauliNeils Bohr and the Development of Physics1955*, 1955.

[49] NN Greenwood and A Earnshaw. *Chemistry of the Elements*. Elsevier, 2012.

[50] R Nielsen, J Schlewitz, H Nielsen, and Updated by Staff. Zirconium and zirconium compounds. *Kirk-Othmer Encyclopedia of Chemical Technology*, pages 1–46, 2000.

[51] A Loonam. Principles and applications of the iodide process. *Journal of The Electrochemical Society*, 106(3):238–244, 1959.

[52] W Robb. Zirconium coating of uranium by the iodide process. *Journal of The Electrochemical Society*, 106(2):126–129, 1959.

[53] N Veigel, E Sherwood, and I Campbell. Preparation of high-purity thorium by the iodide process. *Journal of The Electrochemical Society*, 102(12):687–689, 1955.

[54] E Kobayashi, S Matsumoto, H Doi, T Yoneyama, and H Hamanaka. Mechanical properties of the binary titanium-zirconium alloys and their potential for biomedical materials. *Journal of biomedical materials research*, 29(8):943–950, 1995.

[55] S Kass. The development of the zircaloys. In *Corrosion of Zirconium Alloys*. ASTM International, 1964.

[56] C Tian, D Gao, Y Zhang, C Xu, Y Song, and X Shi. Oxidation behaviour of zirconium diboride–silicon carbide ceramic composites under low oxygen partial pressure. *Corrosion Science*, 53(11):3742–3746, 2011.

[57] W Eugene. Ceramic composition for aircraft spark plugs, September 9 1947. US Patent 2,427,034.

[58] M Qian and A Das. Grain refinement of magnesium alloys by zirconium: Formation of equiaxed grains. *Scripta materialia*, 54(5):881–886, 2006.

[59] S Kurtz, S Kocagöz, C Arnholt, R Huet, M Ueno, and W Walter. Advances in zirconia toughened alumina biomaterials for total joint replacement. *Journal of the mechanical behavior of biomedical materials*, 31:107–116, 2014.

[60] P Partridge. The crystallography and deformation modes of hexagonal close-packed metals. *Metallurgical reviews*, 12(1):169–194, 1967.

[61] J Jamieson. Crystal structures of titanium, zirconium, and hafnium at high pressures. *Science*, 140(3562):72–73, 1963.

[62] W Williams. Influence of temperature, strain rate, surface condition, and composition on the plasticity of transition-metal carbide crystals. *Journal of Applied Physics*, 35(4):1329–1338, 1964.

[63] J Sha, J Dai, J Li, Z Wei, J Hausherr, and W Krenkel. Influence of thermal treatment on thermo-mechanical stability and surface composition of carbon fiber. *Applied Surface Science*, 274:89–94, 2013.

[64] K Funatani. Emerging technology in surface modification of light metals. *Surface and Coatings Technology*, 133:264–272, 2000.

[65] B Baranowski, S Zaginaichenko, D Schur, V Skorokhod, and A Veziroglu. *Carbon nanomaterials in clean energy hydrogen systems*. Springer Science & Business Media, 2008.

[66] F Bridier, P Villechaise, and J Mendez. Analysis of the different slip systems activated by tension in a $\alpha/\beta$ titanium alloy in relation with local crystallographic orientation. *Acta Materialia*, 53(3):555–567, 2005.

[67] D Banerjee and JC Williams. Microstructure and slip character in titanium alloys. *Defence Science Journal*, 36:191–206, 1986.

[68] J Albrecht and G Lütjering. Microstructure and mechanical properties of titanium alloys. *Titanium'99: Science and Technology*, pages 363–374, 2000.

[69] J Bishop and R Hill. Cxxviii. a theoretical derivation of the plastic properties of a polycrystalline face-centred metal. *The London, Edinburgh, and Dublin Philosophical Magazine and Journal of Science*, 42(334):1298–1307, 1951.

[70] M Yoo. Slip, twinning, and fracture in hexagonal close-packed metals. *Metallurgical Transactions A*, 12(3):409–418, 1981.

[71] D Lazar, C Menezes, V Ussui, A Bressiani, and J Paschoal. The influence of sulphur on the processing of zirconia based ceramics. *Journal of the European Ceramic Society*, 22(16):2813–2820, 2002.

[72] G Brauer. *Handbook of preparative inorganic chemistry*, volume 2. Elsevier, 2012.

[73] F Venable. An examination of the chlorides of zirconium. *Journal of the American Chemical Society*, 16(7):469–475, 1894.

[74] S Naher and A Haseeb. A technical note on the production of zirconia and zircon brick from locally available zircon in bangladesh. *Journal of materials processing technology*, 172(3):388–393, 2006.

[75] ES Chandrasekaran, RH Grubbs, and CH Brubaker Jr. Polymer-supported organometallic compounds of titanium, zirconium and hafnium as hydrogenation catalysts. *Journal of Organometallic Chemistry*, 120(1):49–63, 1976.

[76] A Clearfield and Ph A Vaughan. The crystal structure of zirconyl chloride octahydrate and zirconyl bromide octahydrate. *Acta Crystallographica*, 9(7):555–558, 1956.

[77] NN Greenwood and A Earnshaw. *Chemistry of the Elements 2nd Edition*. Butterworth-Heinemann, 1997.

[78] N Kijima and Y Oguri. Ceramic implant and process for its production, January 8 1991. US Patent 4,983,182.

[79] N Kimura, H Okamura, and J Morishita. High density alumina zirconia ceramics and a process for production thereof, September 20 1988. US Patent 4,772,576.

[80] Z Deng, C Wang, and Y Li. New hydrolytic process for producing zirconium dioxide, tin dioxide, and titanium dioxide nanoparticles. *Journal of the American Ceramic Society*, 85(11):2837–2839, 2002.

[81] R Nielsen and G Wilfing. Zirconium and zirconium compounds. *Ullmann's Encyclopedia of Industrial Chemistry*, 2000.

[82] A Jones and P Chalker. Some recent developments in the chemical vapour deposition of electroceramic oxides. *Journal of Physics D: Applied Physics*, 36(6):R80, 2003.

[83] M Mamivand, M Zaeem, H El Kadiri, and L Chen. Phase field modeling of the tetragonal-to-monoclinic phase transformation in zirconia. *Acta Materialia*, 61(14):5223–5235, 2013.

[84] J Valdez, M Tang, Z Chi, M Peters, and K Sickafus. Characterization of an ion irradiation induced phase transformation in monoclinic zirconia. *Nuclear Instruments and Methods in Physics Research Section B: Beam Interactions with Materials and Atoms*, 218:103–110, 2004.

[85] I Denry and J Kelly. State of the art of zirconia for dental applications. *Dental materials*, 24(3):299–307, 2008.

[86] H Boysen, F Frey, and T Vogt. Neutron powder investigation of the tetragonal to monoclinic phase transformation in undoped zirconia. *Acta Crystallographica Section B: Structural Science*, 47(6):881–886, 1991.

[87] R Hannink, P Kelly, and B Muddle. Transformation toughening in zirconia-containing ceramics. *Journal of the American Ceramic Society*, 83(3):461–487, 2000.

[88] W Burger, HG Richter, C Piconi, R Vatteroni, A Cittadini, and M Boccalari. New y-tzp powders for medical grade zirconia. *Journal of Materials Science: Materials in Medicine*, 8(2):113–118, 1997.

[89] R Garvie and P Nicholson. Phase analysis in zirconia systems. *Journal of the American Ceramic Society*, 55(6):303–305, 1972.

[90] D Hanaor, W Xu, M Ferry, and C Sorrell. Abnormal grain growth of rutile tio2 induced by zrsio4. *Journal of Crystal Growth*, 359:83–91, 2012.

[91] L Thomé, J Fradin, J Jagielski, A Gentils, S Enescu, and F Garrido. Radiation damage in ion-irradiated yttria-stabilized cubic zirconia single crystals. *The European Physical Journal-Applied Physics*, 24(1):37–48, 2003.

[92] K Otsuka, K Matsunaga, A Nakamura, S Ii, A Kuwabara, T Yamamoto, and Y Ikuhara. Effects of dislocations on the oxygen ionic conduction in yttria stabilized zirconia. *Materials transactions*, 45(7):2042–2047, 2004.

[93] N Suh. New theories of wear and their implications for tool materials. *Wear*, 62(1):1–20, 1980.

[94] F Seitz. *The modern theory of solids*. McGraw-Hill Book Company, Inc; New York, 1940.

[95] G Vasudevamurthy, T Knight, W Travis, E Roberts, and T Adams. Laboratory production of zirconium carbide compacts for use in inert matrix fuels. *Journal of Nuclear Materials*, 374(1-2):241–247, 2008.

[96] D Franklin, G Lucas, and A Bement. *Creep of zirconium alloys in nuclear reactors*. Number 815. ASTM International, 1983.

[97] L Wang, X Zhao, M Ding, H Zheng, H Zhang, B Zhang, X Li, and G Wu. Surface modification of biomedical aisi 316l stainless steel with zirconium carbonitride coatings. *Applied Surface Science*, 340:113–119, 2015.

[98] C Hu, J Huang, B Sumpter, E Meletis, and T Dumitrica. Ab initio predictions of hexagonal zr (b, c, n) polymorphs for coherent interface design. *The Journal of Physical Chemistry C*, 121(46):26007–26018, 2017.

[99] X Yu, G Thompson, and C Weinberger. Influence of carbon vacancy formation on the elastic constants and hardening mechanisms in transition metal carbides. *Journal of the European Ceramic Society*, 35(1):95–103, 2015.

[100] U Seelam, G Barkhordarian, and C Suryanarayana. Is there a hexagonal-close-packed (hcp)- face-centered-cubic (fcc) allotropic transformation in mechanically milled group ivb elements? *Journal of Materials Research*, 24(11):3454–3461, 2009.

[101] I Manna, P Chattopadhyay, F Banhart, and H Fecht. Formation of face-centered-cubic zirconium by mechanical attrition. *Applied physics letters*, 81(22):4136–4138, 2002.

[102] I Manna, P Chattopadhyay, P Nandi, F Banhart, and H Fecht. Formation of face-centered-cubic titanium by mechanical attrition. *Journal of applied physics*, 93(3):1520–1524, 2003.

[103] A Scarano, M Piattelli, S Caputi, G Favero, and A Piattelli. Bacterial adhesion on commercially pure titanium and zirconium oxide disks: an in vivo human study. *Journal of periodontology*, 75(2):292–296, 2004.

[104] C Nowierski, J Noël, D Shoesmith, and Z Ding. Correlating surface microstructures with reactivity on commercially pure zirconium using scanning electrochemical microscopy and scanning electron microscopy. *Electrochemistry Communications*, 11(6):1234–1236, 2009.

[105] J Piascik, S Wolter, and B Stoner. Development of a novel surface modification for improved bonding to zirconia. *dental materials*, 27(5):e99–e105, 2011.

[106] H Tsuchiya, J Macak, I Sieber, and P Schmuki. Self-organized high-aspect-ratio nanoporous zirconium oxides prepared by electrochemical anodization. *Small*, 1(7):722–725, 2005.

[107] H Porte, J Schnizlein, R Vogel, and D Fischer. Oxidation of zirconium and zirconium alloys. *Journal of the Electrochemical Society*, 107(6):506–515, 1960.

[108] H Weidinger. Raman spectroscopy study of the tetragonal-to-monoclinic transition in zirconium oxide scales and determination of overall oxygen diffusion by nuclear microanalysis of o18. In *Zirconium in the Nuclear Industry: Proceedings of the... International Conference*, volume 9, page 416. ASTM, 1991.

[109] W Xue, Q Zhu, Q Jin, and M Hua. Characterization of ceramic coatings fabricated on zirconium alloy by plasma electrolytic oxidation in silicate electrolyte. *Materials Chemistry and Physics*, 120(2):656–660, 2010.

[110] M Opeka, I Talmy, E Wuchina, J Zaykoski, and S Causey. Mechanical, thermal, and oxidation properties of refractory hafnium and zirconium compounds. *Journal of the European Ceramic Society*, 19(13):2405–2414, 1999.

[111] A Lyapin, L Jeurgens, and E Mittemeijer. Effect of temperature on the initial, thermal oxidation of zirconium. *Acta Materialia*, 53(10):2925–2935, 2005.

[112] A Alansari and Y Sun. Surface finish effect on dry sliding wear behavior of thermally oxidized commercially pure zirconium. *Transactions of Nonferrous Metals Society of China*, 29(1):88–97, 2019.

[113] A Zaimovskii. Zirconium alloys in nuclear power. *Atomic Energy*, 45(6):1165–1168, 1978.

[114] T Kutty, K Ravi, and C Ganguly. Studies on hot hardness of zr and its alloys for nuclear reactors. *Journal of nuclear materials*, 265(1-2):91–99, 1999.

[115] R Krishnan and M Asundi. Zirconium alloys in nuclear technology. *Proceedings of the Indian Academy of Sciences Section C: Engineering Sciences*, 4(1):41–56, 1981.

[116] B Cox. Some thoughts on the mechanisms of in-reactor corrosion of zirconium alloys. *Journal of Nuclear materials*, 336(2-3):331–368, 2005.

[117] T Ahmed and LH Keys. The breakaway oxidation of zirconium and its alloys a review. *Journal of the Less Common Metals*, 39(1):99–107, 1975.

[118] J Baek and Y Jeong. Breakaway phenomenon of zr-based alloys during a high-temperature oxidation. *Journal of Nuclear Materials*, 372(2-3):152–159, 2008.

[119] M Steinbrück, N Vér, and M Große. Oxidation of advanced zirconium cladding alloys in steam at temperatures in the range of $600 - 1200^{o}c$. *Oxidation of metals*, 76(3-4):215–232, 2011.

[120] K Östhagen and P Kofstad. Oxidation of zirconium and zirconium-oxygen alloys at $800^{o}c$. *Journal of the Electrochemical Society*, 109(3):204–207, 1962.

[121] M Steinbrueck. Oxidation of zirconium alloys in oxygen at high temperatures up to $1600^{o}c$. *Oxidation of Metals*, 70(5-6):317–329, 2008.

[122] DH Bradhurst and PM Heuer. The influence of oxide stress on the breakaway oxidation of zircaloy-2. *Journal of nuclear materials*, 37(1):35–47, 1970.

[123] P Stratton and M Graf. Case hardening of zirconium. *International Heat Treatment and Surface Engineering*, 3(3):121–124, 2009.

[124] A Kuriakose and J Margrave. The oxidation kinetics of zirconium diboride and zirconium carbide at high temperatures. *Journal of the Electrochemical Society*, 111(7):827–831, 1964.

[125] G Murtaza, S Hussain, N Rehman, S Naseer, M Shafiq, and M Zakaullah. Carburizing of zirconium using a low energy mather type plasma focus. *Surface and Coatings Technology*, 205(8):3012–3019, 2011.

[126] J Williams. *Engineering tribology*. Cambridge University Press, 1994.

[127] B Bhushan and B Gupta. Handbook of tribology: materials, coatings, and surface treatments. 1991.

[128] J Davis. *Surface engineering for corrosion and wear resistance*. ASM international, 2001.

[129] J Takadoum. *Materials and surface engineering in tribology*. John Wiley & Sons, 2008.

[130] D Talbot and J Talbot. *Corrosion science and technology*. CRC press, 2018.

[131] M Pourbaix. *Lectures on electrochemical corrosion*. Springer Science & Business Media, 2012.

[132] L Shreir, R Jarman, and G Burstein. Corrosion control (volume 2), 1994.

[133] D Landolt, S Mischler, and M Stemp. Electrochemical methods in tribocorrosion: a critical appraisal. *Electrochimica Acta*, 46(24):3913–3929, 2001.

[134] A Fischer and S Mischler. Tribocorrosion: fundamentals, materials and applications. *Journal of Physics D: Applied Physics*, 39(15):null, 2006.

[135] Y Yan, A Neville, and D Dowson. Tribo-corrosion properties of cobalt-based medical implant alloys in simulated biological environments. *Wear*, 263(7-12):1105–1111, 2007.

[136] S Mischler, S Debaud, and D Landolt. Wear-accelerated corrosion of passive metals in tribocorrosion systems. *Journal of the Electrochemical Society*, 145(3):750–758, 1998.

[137] M Mathew, P Srinivasa Pai, R Pourzal, A Fischer, and M Wimmer. Significance of tribocorrosion in biomedical applications: overview and current status. *Advances in tribology*, 2009, 2010.

[138] N Chelliah and S Kailas. Synergy between tribo-oxidation and strain rate response on governing the dry sliding wear behavior of titanium. *Wear*, 266(7-8):704–712, 2009.

[139] J Sánchez-López, A Contreras, S Domínguez-Meister, A García-Luis, and M Brizuela. Tribological behaviour at high temperature of hard craln coatings doped with y or zr. *Thin Solid Films*, 550:413–420, 2014.

[140] P Ponthiaux, F Wenger, D Drees, and J Celis. Electrochemical techniques for studying tribocorrosion processes. *Wear*, 256(5):459–468, 2004.

[141] D Déforge, F Huet, RP Nogueira, P Ponthiaux, and F Wenger. Electrochemical noise analysis of tribocorrosion processes under steady-state friction regime. *Corrosion*, 62(6):514–521, 2006.

[142] D Landolt. Electrochemical and materials aspects of tribocorrosion systems. *Journal of Physics D: applied physics*, 39(15):3121, 2006.

[143] S Mischler. Triboelectrochemical techniques and interpretation methods in tribocorrosion: a comparative evaluation. *Tribology International*, 41(7):573–583, 2008.

[144] M Fazel, HR Salimijazi, MA Golozar, et al. A comparison of corrosion, tribocorrosion and electrochemical impedance properties of pure ti and ti6al4v alloy treated by micro-arc oxidation process. *Applied Surface Science*, 324:751–756, 2015.

[145] R Priya, C Mallika, and U Mudali. Wear and tribocorrosion behaviour of 304l ss, zr-702, zircaloy-4 and ti-grade2. *Wear*, 310(1-2):90–100, 2014.

[146] R Wood. Tribo-corrosion of coatings: a review. *Journal of Physics D: Applied Physics*, 40(18):5502, 2007.

[147] SC Ferreira, E Ariza, LA Rocha, JR Gomes, Ph Carvalho, F Vaz, AC Fernandes, L Rebouta, L Cunha, E Alves, et al. Tribocorrosion behaviour of zroxny thin films for decorative applications. *Surface and coatings technology*, 200(22-23):6634–6639, 2006.

[148] L Benea. Electrodeposition and tribocorrosion behaviour of zro 2–ni composite coatings. *Journal of Applied Electrochemistry*, 39(10):1671, 2009.

[149] N Hua, Z Liao, W Chen, Y Huang, and T Zhang. Effects of noble elements on the glass-forming ability, mechanical property, electrochemical behavior and tribocorrosion resistance of ni-and cu-free zr-al-co bulk metallic glass. *Journal of Alloys and Compounds*, 725:403–414, 2017.

[150] S Watson, F Friedersdorf, B Madsen, and S Cramer. Methods of measuring wear-corrosion synergism. *Wear*, 181:476–484, 1995.

[151] MG Gee, A Gant, I Hutchings, R Bethke, K Schiffman, K Van Acker, S Poulat, Y Gachon, and J Von Stebut. Progress towards standardisation of ball cratering. *Wear*, 255(1-6):1–13, 2003.

[152] J Walls, D Hall, and D Sykes. Composition–depth profiling and interface analysis of surface coatings using ball cratering and the scanning auger microprobe. *Surface and Interface Analysis*, 1(6):204–210, 1979.

[153] M Holmboe, S Wold, and M Jonsson. Porosity investigation of compacted bentonite using xrd profile modeling. *Journal of Contaminant Hydrology*, 128(1-4):19–32, 2012.

[154] A Monshi, M Foroughi, and M Monshi. Modified scherrer equation to estimate more accurately nano-crystallite size using xrd. *World journal of nano science and engineering*, 2(3):154–160, 2012.

[155] J Kacher, C Landon, B Adams, and D Fullwood. Bragg's law diffraction simulations for electron backscatter diffraction analysis. *Ultramicroscopy*, 109(9):1148–1156, 2009.

[156] Y Sun and T Bell. Glow discharge depth profiling a powerful analytical technique in surface engineering. *International Journal of Engineering*, 10(2):111–119, 1997.

[157] A Perry. Scratch adhesion testing of hard coatings. *Thin Solid Films*, 107(2):167–180, 1983.

[158] F Attar and T Johannesson. Adhesion evaluation of thin ceramic coatings on tool steel using the scratch testing technique. *Surface and Coatings Technology*, 78(1-3):87–102, 1996.

[159] M Balaceanu, T Petreus, V Braic, CN Zoita, A Vladescu, CE Cotrutz, and M Braic. Characterization of zr-based hard coatings for medical implant applications. *Surface and Coatings Technology*, 204(12-13):2046–2050, 2010.

[160] S Kun Lee, R Tandon, M Readey, and B Lawn. Scratch damage in zirconia ceramics. *Journal of the American Ceramic Society*, 83(6):1428–1432, 2000.

[161] T Maekawa and B Ishii. Oxidation of zirconium in air. *Transactions of the Japan Institute of Metals*, 3(4):203–209, 1962.

[162] K Holmberg, A Laukkanen, H Ronkainen, K Wallin, and S Varjus. A model for stresses, crack generation and fracture toughness calculation in scratched tin-coated steel surfaces. *Wear*, 254(3-4):278–291, 2003.

[163] Y Xie and H Hawthorne. A model for compressive coating stresses in the scratch adhesion test. *Surface and Coatings Technology*, 141(1):15–25, 2001.

[164] F Svahn, A Kassman-Rudolphi, and E Wallen. The influence of surface roughness on friction and wear of machine element coatings. *Wear*, 254(11):1092–1098, 2003.

[165] M Hanief and MF Wani. Effect of surface roughness on wear rate during running-in of en31-steel: model and experimental validation. *Materials Letters*, 176:91–93, 2016.

[166] RG Bayer and JL Sirico. The influence of surface roughness on wear. *Wear*, 35(2):251–260, 1975.

[167] M Federici, C Menapace, A Moscatelli, S Gialanella, and G Straffelini. Effect of roughness on the wear behavior of hvof coatings dry sliding against a friction material. *Wear*, 368:326–334, 2016.

[168] M Rahaman, L Zhang, M Liu, and W Liu. Surface roughness effect on the friction and wear of bulk metallic glasses. *Wear*, 332:1231–1237, 2015.

[169] J Jiang and R Arnell. The effect of substrate surface roughness on the wear of dlc coatings. *Wear*, 239(1):1–9, 2000.

[170] J Takadoum and H Bennani. Influence of substrate roughness and coating thickness on adhesion, friction and wear of tin films. *Surface and Coatings Technology*, 96(2-3):272–282, 1997.

[171] K Kubiak, T Liskiewicz, and T Mathia. Surface morphology in engineering applications: Influence of roughness on sliding and wear in dry fretting. *Tribology International*, 44(11):1427–1432, 2011.

[172] S Lee, W Ho, and F Lai. Effect of substrate surface roughness on the characteristics of crn hard film. *Materials chemistry and physics*, 43(3):266–273, 1996.

[173] SJ Bull, PR Chalker, C Johnston, and V Moore. The effect of roughness on the friction and wear of diamond thin films. *Surface and Coatings Technology*, 68:603–610, 1994.

[174] A Alansari and Y Sun. Effect of oxidation time on the tribological behavior of thermally oxidized commercially pure zirconium under dry sliding conditions. *Surface and Coatings Technology*, 309:195–202, 2017.

[175] Y Sun, P Dearnley, and B Mallia. Response of duplex cr (n)/s and cr (c)/s coatings on 316l stainless steel to tribocorrosion in 0.89% nacl solution under plastic contact conditions. *Journal of Biomedical Materials Research Part B: Applied Biomaterials*, 105(6):1503–1513, 2017.

[176] K Mao, Y Sun, and T Bell. A numerical model for the dry sliding contact of layered elastic bodies with rough surfaces. *Tribology transactions*, 39(2):416–424, 1996.

[177] K Mao, Y Sun, A Bloyce, and T Bell. Surface coating effects on contact stress and wear: an approach of surface engineering design and modelling. *Surface Engineering*, 26(1-2):142–148, 2010.

[178] AV Byeli, VA Kukareko, and AG Kononov. Titanium and zirconium based alloys modified by intensive plastic deformation and nitrogen ion implantation for biocompatible implants. *Journal of the mechanical behavior of biomedical materials*, 6:89–94, 2012.

[179] M Gepreel and M Niinomi. Biocompatibility of ti-alloys for long-term implantation. *Journal of the mechanical behavior of biomedical materials*, 20:407–415, 2013.

[180] M Niinomi. Recent metallic materials for biomedical applications. *Metallurgical and materials transactions A*, 33(3):477, 2002.

[181] A Bloyce, H Dong, and T Bell. Surface modification of titanium alloys for combined improvements in corrosion and wear resistance. *Surface and Coatings Technology*, 107(2-3):125–132, 1998.

[182] T Bell, H Dong, and Y Sun. Realising the potential of duplex surface engineering. *Tribology International*, 31(1-3):127–137, 1998.

[183] H Güleryüz and H Çimenoğlu. Effect of thermal oxidation on corrosion and corrosion–wear behaviour of a ti–6al–4v alloy. *Biomaterials*, 25(16):3325–3333, 2004.

[184] S Kumar, T Narayanan, S Raman, and S Seshadri. Thermal oxidation of ti6al4v alloy: Microstructural and electrochemical characterization. *Materials Chemistry and Physics*, 119(1-2):337–346, 2010.

[185] O Yamamoto, K Alvarez, T Kikuchi, and M Fukuda. Fabrication and characterization of oxygen-diffused titanium for biomedical applications. *Acta biomaterialia*, 5(9):3605–3615, 2009.

[186] S Wang, Y Liu, C Zhang, Z Liao, and W Liu. The improvement of wettability, biotribological behavior and corrosion resistance of titanium alloy pretreated by thermal oxidation. *Tribology International*, 79:174–182, 2014.

[187] M Lieblich, S Barriuso, M Multigner, G González-Doncel, and J González-Carrasco. Thermal oxidation of medical ti6al4v blasted with ceramic particles: Effects on the microstructure, residual stresses and mechanical properties. *Journal of the mechanical behavior of biomedical materials*, 54:173–184, 2016.

[188] H Dong and T Bell. Designer surfaces for titanium components. *Industrial Lubrication and Tribology*, 50(6):282–289, 1999.

[189] A Biswas and J Majumdar. Surface characterization and mechanical property evaluation of thermally oxidized ti-6al-4v. *Materials Characterization*, 60(6):513–518, 2009.

[190] Y Sun, T Hu, H Fan, Y Zhang, and L Hu. Thermal oxidation behavior and tribological properties of textured tc4 surface: Influence of thermal oxidation temperature and time. *Tribology International*, 94:479–489, 2016.

[191] D Krishna, Y Brama, and Y Sun. Thick rutile layer on titanium for tribological applications. *Tribology International*, 40(2):329–334, 2007.

[192] S Wang, Z Liao, Y Liu, and W Liu. Influence of thermal oxidation temperature on the microstructural and tribological behavior of ti6al4v alloy. *Surface and Coatings Technology*, 240:470–477, 2014.

[193] K Aniolek, M Kupka, and A Barylski. Sliding wear resistance of oxide layers formed on a titanium surface during thermal oxidation. *Wear*, 356:23–29, 2016.

[194] A Leto, W Zhu, M Matsubara, and G Pezzotti. Bioinertness and fracture toughness evaluation of the monoclinic zirconia surface film of oxinium™ femoral head by raman and cathodoluminescence spectroscopy. *Journal of the mechanical behavior of biomedical materials*, 31:135–144, 2014.

[195] P Dearnley and G Aldrich-Smith. Corrosion–wear mechanisms of hard coated austenitic 316l stainless steels. *Wear*, 256(5):491–499, 2004.

[196] J Jiang, M Stack, and A Neville. Modelling the tribo-corrosion interaction in aqueous sliding conditions. *Tribology International*, 35(10):669–679, 2002.

[197] Y Sun and V Rana. Tribocorrosion behaviour of aisi 304 stainless steel in 0.5 m nacl solution. *Materials Chemistry and Physics*, 129(1-2):138–147, 2011.

[198] C Jeon, CP Kim, S-H Joo, HS Kim, and S Lee. High tensile ductility of ti-based amorphous matrix composites modified from conventional ti–6al–4v titanium alloy. *Acta Materialia*, 61(8):3012–3026, 2013.

[199] H Dong, A Bloyce, PH Morton, and T Bell. Surface engineering to improve tribological performance of ti–6al–4v. *Surface engineering*, 13(5):402–406, 1997.

[200] Y Luo, H Jiang, G Cheng, and H Liu. Effect of carburization on the mechanical properties of biomedical grade titanium alloys. *Journal of Bionic Engineering*, 8(1):86–89, 2011.

[201] A Alansari and Y Sun. A comparative study of the mechanical behaviour of thermally oxidised commercially pure titanium and zirconium. *Journal of the mechanical behavior of biomedical materials*, 74:221–231, 2017.